

Review

Progress in focal plane array technologies

Antoni Rogalski*

Institute of Applied Physics, Military University of Technology, 2 Kaliskiego St., 00-908 Warsaw, Poland

Available online 13 July 2012

Abstract

Development of focal plane arrays started in seventies last century and has revolutionized imaging systems in the next decades. This paper presents progress in optical detector technology of focal plane arrays during the past twenty years. At the beginning of paper, emphasises are given on integrated detector assembly and cooling requirements of different types of detectors. Next, the classification of two types of detectors (photon detectors and thermal detectors) is done on the basis of their principle of operation. This topic is followed by general overview of focal plane array architectures.

The main subject of paper is concentrated on describing of material systems and detectors operated in different spectral ranges. Special attention is given on recent progress in their detector technologies. Discussion is focused mainly on current and the most rapidly developing focal plane arrays including: CdZnTe detectors, AlGaIn photodiodes, visible CCD and CMOS imaging systems, HgCdTe heterostructure photodiodes, quantum well AlGaAs/GaAs photoresistors, and thermal detectors. Emphasis is also given on far-infrared and sub-millimetre wave detector arrays. Finally, the outlook for near-future trends in optical detector technologies is presented.

© 2012 Elsevier Ltd. All rights reserved.

Keywords: X-ray detectors; Ultraviolet detectors; Visible detectors; Infrared detectors; Monolithic and hybrid focal plane arrays

Contents

1. Introduction	343
2. Integrated detector assembly.	346

*Tel./fax: +48 22 6839109.

E-mail address: rogan@wat.edu.pl

2.1.	Detector operating temperature	347
2.2.	Cooler technologies	348
2.2.1.	Cryocoolers	349
2.2.2.	Peltier coolers	356
3.	Classification of detectors	358
3.1.	Photon detectors	358
3.2.	Thermal detectors	367
4.	Overview of focal plane array architectures	372
4.1.	Monolithic arrays	373
4.1.1.	CCD devices	374
4.1.2.	CMOS devices	375
4.2.	Hybrid arrays	378
4.2.1.	Interconnect techniques	379
4.3.	Performance of focal plane arrays	383
5.	X-ray detector arrays	385
5.1.	Phosphors, scintillators, and microchannel plates	385
5.2.	Direct and indirect X-ray detection	387
5.3.	Silicon detector arrays	388
5.4.	CdZnTe hybrid array	391
6.	Ultraviolet detector arrays	394
7.	Visible detector arrays	398
8.	Infrared detector arrays	404
8.1.	InGaAs arrays	404
8.2.	Schottky-barrier photoemissive arrays	407
8.3.	Lead salt arrays	409
8.4.	InSb arrays	411
8.5.	HgCdTe arrays	413
8.6.	QWIP arrays	418
8.7.	Type II superlattice arrays	421
8.8.	Thermal detector arrays	426
8.9.	Third generation infrared detectors	431
8.10.	Readiness level of LWIR detector technologies	436
9.	Far-IR and sub-mm-wave detector arrays	438
9.1.	Schottky barrier arrays	444
9.2.	Silicon and germanium extrinsic photoconductor arrays	446
9.3.	Pair braking photon detector arrays	452
9.4.	Semiconductor bolometer arrays	455
9.5.	Superconducting HEB and TES arrays	458
9.6.	Field effect transistor detector arrays	463
10.	Conclusions	464
	References	466

1. Introduction

Developments in source and detection of electromagnetic radiation have a very long history. First humans relied on the radiation from the Sun. Cave men used torches (approximately 500,000 years ago). Candles appeared around 1000 BC, followed by gas

lighting (1772), and incandescent bulbs (Edison, 1897). Radio (1886–1895), X-rays (1895), UV radiation (1901), and radar (1936) were invented in the end of the 19-th and the beginning of the 20-th centuries. The terahertz (THZ) region of electromagnetic spectrum (see Fig. 1) is often described as the final unexplored area of spectrum and still presents a challenge for both electronic and photonic technologies.

Looking back over the past several hundreds of years we notice that following the invention and evolution of optical systems (telescopes, microscopes, eyeglasses, cameras, etc.) the optical image was formed on the human retina, photographic plate, or films. The birth of photodetectors can be dated back to 1873 when Smith discovered photoconductivity in selenium [1]. Progress was slow until 1905, when Einstein explained the newly observed photoelectric effect in metals, and Planck solved the blackbody emission puzzle by introducing the quanta hypothesis. Applications and new devices soon flourished, pushed by the dawning technology of vacuum tube sensors developed in the 1920s and 1930s culminating in the advent of television. Zworykin and Morton, the celebrated fathers of videonics, on the last page of their legendary book *Television* (1939) concluded that: “when rockets will fly to the moon and to other celestial bodies, the first images we will see of them will be those taken by camera tubes, which will open to mankind new horizons.” Their foresight became a reality with the Apollo and Explorer missions. Photolithography enabled the fabrication of silicon monolithic imaging focal planes for the visible spectrum beginning in the early 1960s. Some of these early developments were intended for a picturephone, other efforts were for television cameras, satellite surveillance, and digital imaging. Infrared imaging has been vigorously pursued in parallel with visible imaging because of its utility in military applications. More recently (1997), the CCD camera aboard the Hubble space telescope delivered a deep-space picture, a result of 10 day’s integration, featuring galaxies of the 30th magnitude—an unimaginable figure even for astronomers of our generation. Probably, the next effort will be in the big-band age. Thus, photodetectors continue to open to mankind the most amazing new horizons.

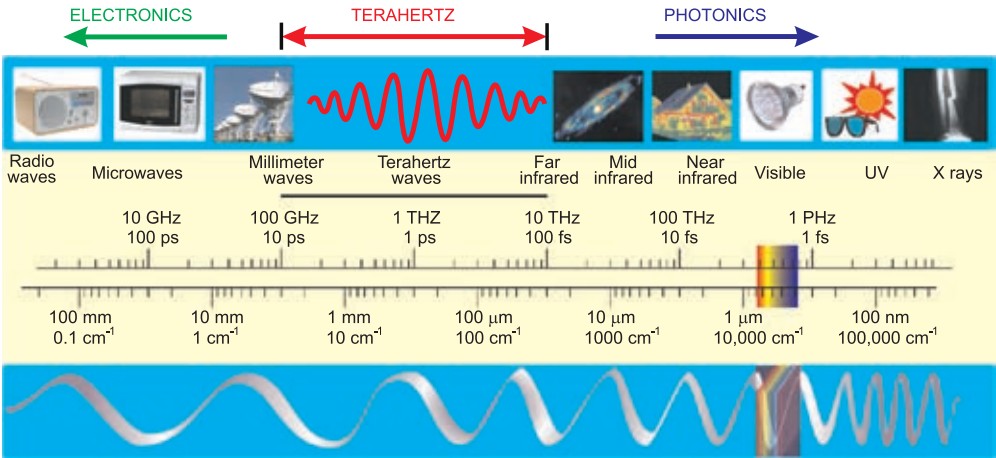


Fig. 1. The electromagnetic spectrum.

In this paper optical radiation is considered as a radiation over the range from vacuum ultraviolet to the submillimeter wavelength (25 to 3000 μm):

25–200 nm	Vacuum ultraviolet	VUV
200–400 nm	Ultraviolet	UV
400–700 nm	Visible	VIS
700–1000 nm	Near infrared	NIR
1–3 μm	Short wavelength infrared	SWIR
3–5 μm	Medium wavelength infrared	MWIR
5–14 μm	Long wavelength infrared	LWIR
14–30 μm	Very long wavelength infrared	VLWIR
30–100 μm	Far infrared	FIR
100–3000 μm	Submillimeter	SubMM

THz radiation is frequently treated as the spectral region within frequency range $\nu \approx 0.1\text{--}10$ THz ($\lambda \approx 3\text{ mm--}30\text{ }\mu\text{m}$) and it is partly overlapping with loosely treated submillimeter (sub-mm) wavelength band $\nu \approx 0.1\text{--}3$ THz ($\lambda \approx 3\text{ mm--}100\text{ }\mu\text{m}$).

Both ultraviolet (UV), visible, as well as infrared (IR) detectors technologies have undergone significant maturation, and high-performance detectors are available across most spectral bands from 0.2- to 100- μm . Significant improvements were possible for sensor systems by adding functionality, such as multi- and hyper-spectral response, polarimetric sensitivity, dynamic resolution and sensitivity adaptation, as well as reductions in size, weight, power and cost. The increase in digital processing capabilities, fuelled by the semiconductor industry, is a trend that will continue to have a major effect on sensor system.

Development in detector focal plane array (FPA) technology has revolutionized many kinds of imaging [2]. From γ rays to the infrared and even radio waves, the rate at which images can be acquired has increased by more than a factor of a million in many cases. Fig. 2 illustrates the trend in array size over the past 40 years. Imaging FPAs have developed in proportion to the ability of silicon integrated circuit (ICs) technology to read and process the array signals, and with ability to display the resulting image. The progress in arrays has been steady and has paralleled the development of dense electronic structures such as dynamic random access memories (DRAMs). FPAs have nominally the same growth rate as DRAM ICs, which have had a doubling-rate period of approximately 18 months; it is a consequence of Moore's Law, but lag behind in size by about 5–10 years. The graph in insert of Fig. 2 shows the log of the number of pixels per a sensor chip assembly (SCA) as a function of the year first used on astronomy for MWIR SCAs. Charge coupled devices (CCDs) with close to 2 gigapixels offer the largest formats.

There are many excellent texts at both introductory and advanced levels that deal the fundamentals and applications of optical detectors [3–5]. Our intent is to provide a progress in optical detector FPA technology in the last two decades. In this context, the paper acquires topicality of previously published papers devoted FPA [2,6]. In comparison with the previous papers, this paper presents additional information devoted development of integrated FPA detector assemblies.

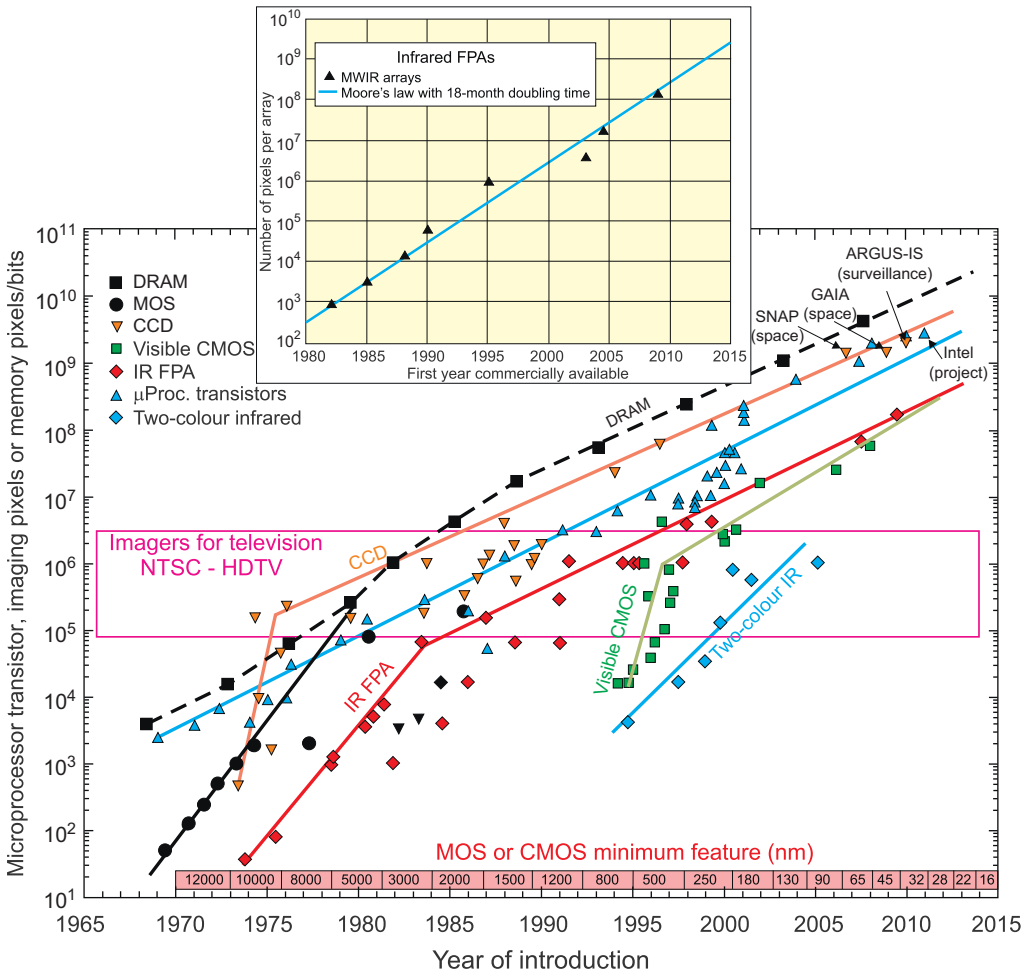


Fig. 2. Imaging array formats compared with the complexity of silicon microprocessor technology and dynamic access memory (DRAM) as indicated by transistor count and memory bit capacity (adapted after Ref. [2] with completions). The timeline design rule of MOS/CMOS features is shown at the bottom. CCDs with close to 2 gigapixels offer the largest formats. Note the rapid rise of CMOS imagers which are challenging CCDs in the visible spectrum. The number of pixels on an infrared array has been growing exponentially, in accordance with Moore's Law for 30 years with a doubling time of approximately 18 months. In infrared 147 megapixel arrays are now available for astronomy applications. Imaging formats of many detector types have gone beyond that required for high definition TV.

2. Integrated detector assembly

A FPA is created by arranging individual elements in a lattice-like array. Typically each pixel has one independent contact and shares the second contact with other pixels in the array. The distribution of the common contacts impacts electrical and readout speed.

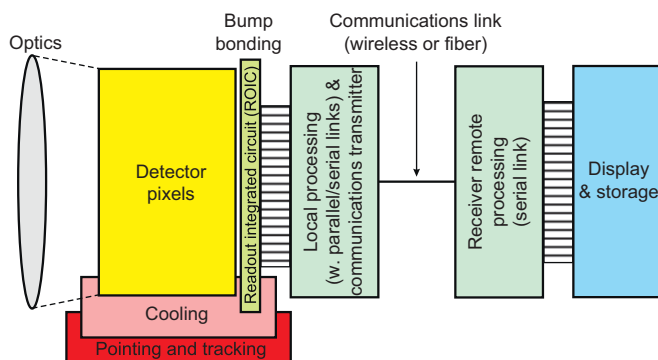


Fig. 3. Schematic representation of an imaging system showing important sub-systems (after Ref. [7]).

A serious limitation in the development of arrays of detectors is that light is easily coupled to neighbouring pixels in an array which lead to the developments of false counts, or crosstalk. There are approaches to mitigate this limitation, but they add additional complexity to the manufacturing.

Detectors are only a part of usable sensor systems. Military sensor systems include optics, coolers, pointing and tracking systems, electronics, communication, processing together with information-extraction sub-systems, and displays (see Fig. 3) [7]. So, the process of developing sensor system is significantly more challenging than fabricating a detector array.

In IR systems, two-dimensional (2-D) arrays of detectors connected with indium bumps to a readout integrated circuit (ROIC) chip as a hybrid structure are often called a sensor chip assembly (SCA). The FPA industry is not sufficiently large to support the development of a complete set of unique tools. The evolution of the silicon industry can lead to divergence and to gaps in the FPA tool set. One simple example is that the silicon industry has standardized on a field size of $22 \times 33 \text{ mm}^2$ for its lithography tools. The drive to larger pixel counts for FPAs often requires much larger overall FPA sizes which can only be accomplished by abutting multiple fields. Tiling large arrays from smaller chips addresses the practical and economic limits of making larger detector chips.

Generally, there are two main types of detectors; cooled and uncooled. Cooled detectors require cooling below ambient temperature. Although uncooled sensors offer significant advantages in terms of cost, lifetime, size, weight and power, cooled sensors offer significantly enhanced range, resolution, and sensitivity as a result of the lower noise operation.

In the infrared industry the housing with detector installed is known as and integrated detector assembly (or IDA). The housing on an IDA is basically a fancy dewar. The detector is located on the base of the inner wall with a window in the base of the outer wall. There are many design considerations and challenges that go into developing an IDA.

2.1. Detector operating temperature

Fig. 4 is a chart depicting infrared operating temperature and wavelength regions spanned by a variety of available infrared detector technologies. Typical operating temperatures range from 4 K to just below room temperature, depending on the detector technology. Most modern cooled detectors operate in the temperature range from <10 to 150 K, depending on the detector type and performance level. 77 K is a very

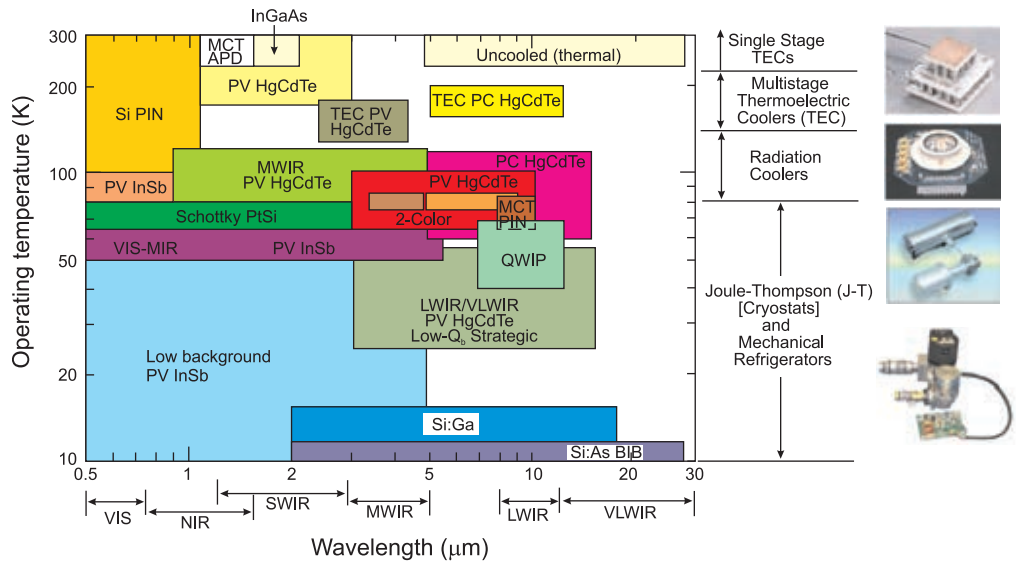


Fig. 4. The operating temperature and wavelength regions spanned by a variety of available IR detector technologies.

common temperature because this is relatively easily achievable with liquid nitrogen. Uncooled detectors, despite their title, typically incorporate some degree of temperature control near or slightly below room temperature ($\sim 250\text{--}300\text{ K}$) to minimize noise, optimize resolution, and maintain stable operating temperature.

For space mission detectors with the very long wavelength cutoff wavelengths are also required. Due to small photon energy activation, the extrinsic detector materials are used. In comparison with intrinsic photoconductivity, the extrinsic photoconductivity is far less efficient because of limits in the amount of impurity that can be introduced into semiconductor without altering the nature of the impurity states. Implicit in the treatment of low background detectors is that the generation of free carriers is dominated by photon absorption, not by thermal excitation. As a result, lower temperature is required as the long wavelength cutoff of the detector increases, what can be approximated as [8]

$$T_{\text{max}} = \frac{300\text{ K}}{\lambda_c[\mu\text{m}]} \tag{1}$$

This general trend is illustrated in Fig. 5 for six high performance detector materials suitable for low-background applications: Si, InGaAs, InSb, HgCdTe photodiodes, Si:As (Si:Sb) impurity band conductor (IBC) detectors also called as the blocked impurity band (BIB) detectors, and Ge:Ga stressed photoconductive detectors. The operating temperature range can be fairly broad due to the wide range of system backgrounds.

2.2. Cooler technologies

The method of cooling varies according to the operating temperature and the system’s logistical requirements [9,10]. The two technologies currently available for addressing the

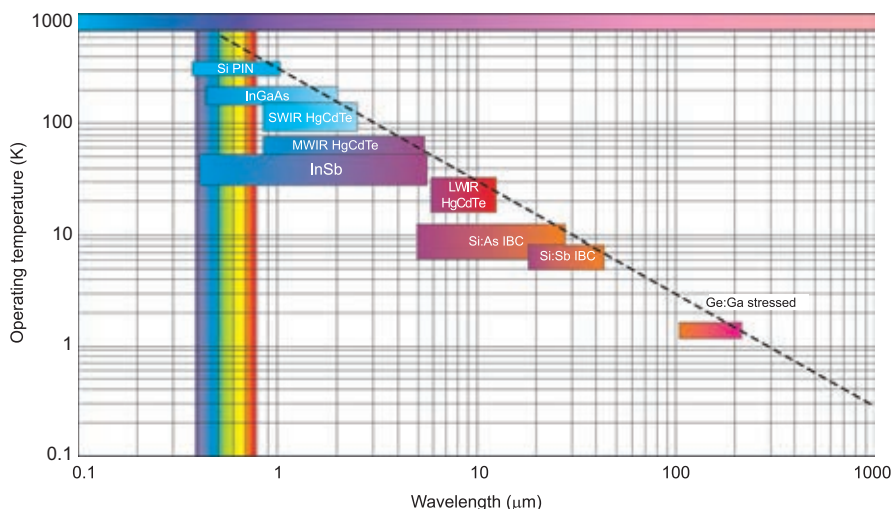


Fig. 5. Operating temperatures for low-background material systems with their spectral band of greatest sensitivity. The dashed line indicates the trend toward lower operating temperature for longer wavelength detection.

cooling requirements of IR and visible detectors are closed cycle refrigerators and thermoelectric coolers. Closed cycle refrigerators can achieve the cryogenic temperatures required for cooled IR sensors, while thermoelectric coolers are generally the preferred approach to temperature control for uncooled visible and IR sensors. The major difference between the thermoelectric and mechanical cryocoolers is the nature of the working fluid. A thermoelectric cooler is a solid-state device that uses charge carriers (electrons or holes) as a working fluid, whereas mechanical cryocoolers use a gas such as helium as the working fluid.

The selection of a cooler for a specific application depends on cooling capacity, operating temperature, procurement, cost and maintenance, and servicing requirements. A survey of currently operating cryogenic systems for commercial, military, and space applications are summarized in Fig. 6.

2.2.1. Cryocoolers

Cryocoolers can be classified as either recuperative or regenerative. In recuperative systems, gas flows in a single direction. The gas is compressed at ambient fixed temperature and pressure and allowed to expand through an orifice to the desired cryogenic fixed temperature and pressure. The Joule Thompson and Brayton cycle refrigerators are examples of recuperative systems.

In a regenerative system, the gas flow oscillates back and forth between hot and cold regions driven by a piston, diaphragm or compressor, with the gas being compressed at the hot end and expanded on the cold end. Stirling, Gifford-McMahon and Pulse Tube cryocoolers are the most common types of regenerative cryocooler systems.

Fig. 7 presents a map of the major cryocooler applications in terms of the temperature and net refrigeration power required. The major commercial applications include cryopumps for semiconductor fabrication facilities, magnetic resonance imaging magnet

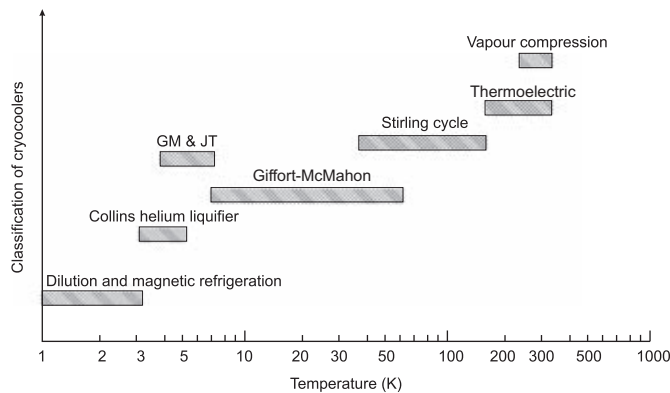


Fig. 6. Temperature ranges for commercial refrigerators (after Ref. [9]).

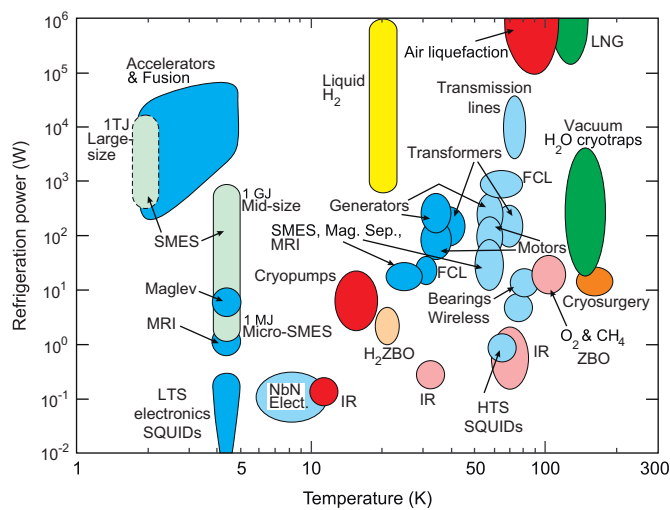


Fig. 7. Map of cryocooler applications in plane of refrigeration power versus temperature (after Ref. [10]). Note: SMES—Superconducting Magnetic Energy Storage, MRI—Magnetic Resonance Imaging, LTS—Low Temperature Superconductivity, SQUIDs—Superconducting Quantum Interference Devices, LNG—Liquid Natural Gas, FCL—Freon Coolant Line, IR—Infrared, ZBO—zero boil-off, and HTC—High-Temperature Superconductivity.

cooling, and gas separation and liquefaction. The largest low-power application of cryocoolers is covered by IR sensors.

The performance of a cryocooler is specified by coefficient of performance (COP), which is defined as the ratio of cooling power achieved at a particular temperature to total electrical input power to the cryocooler. The COP is often given as a fraction of the Carnot efficiency. Fig. 8 compares the relative performance of the different technologies as a fraction of the limiting ideal efficiency. For lower temperatures the efficiency drops significantly. At 4 K typical efficiency is about 1% or less. Generally, recuperative systems have advantages in terms of reduced noise and vibration, whereas the regenerative systems

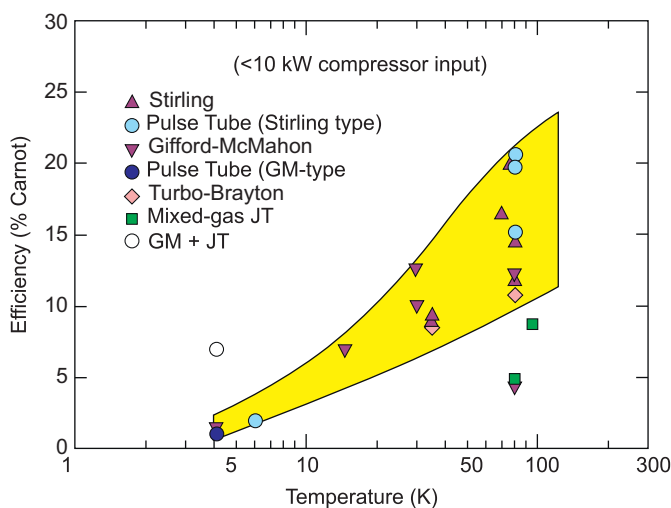


Fig. 8. Efficiency of small cryocoolers as a function of cold end temperature (after Ref. [10]).

tend to obtain higher efficiencies and greater reliability at the temperatures of interest for many IR detector applications.

Ever since the late 1970s, military systems have overcome the problem of LN_2 operation by utilizing Stirling closed-cycle refrigerators to generate the cryogenic temperatures necessary for critical IR detector components. These refrigerators were designed to produce operating temperatures of 77 K directly from DC power. Early versions were large and expensive, and suffered from microphonic and electromagnetic interference (EMI) noise problems. The use of cooling engines has increased considerably due to their efficiency, reliability, and cost reduction. Today, smaller and more efficient cryocoolers have been developed and refined. The development of novel adsorber materials and designs as well as improved sealing techniques for maintaining the high pressures required for cryocooler operation have significantly contributed to the improved lifetimes [mean time before failure (MTBF)] now achievable in many cryocooler systems (5000–10,000 h). Lifetime of ten years are now possible in space cryocoolers, and five years lifetimes are possible in similar cryocoolers developed for commercial applications [11]. A comparison of cryocooler efficiencies near 80 K is shown in Fig. 9. Efficiency as high as about 20% is achieved for large best space cryocoolers, whereas 10–20% is typical for the best commercial cryocoolers. Improvements in heat exchanger, recuperator designs and materials have given COP values in the range to 10% for small cryocoolers. However, despite these advances, the cryocooler remains a major failure point for the integrated IR sensor system.

Below we briefly describe different type of FPA coolers [12]. Table 1 presents advantages and disadvantages of different cryocoolers for space applications. More information can be found in Refs. [11,13].

2.2.1.1. Cryogenic dewars. Most 8–14- μm detectors operate at approximately 77 K and can be cooled by liquid nitrogen. Cryogenic liquid pour-filled dewars are frequently used for detector cooling in laboratories. They are rather bulky and need to be refilled with

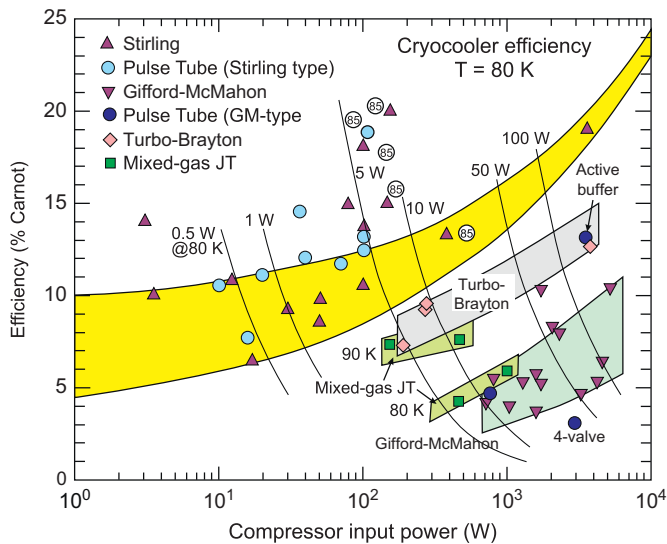


Fig. 9. Efficiencies of various types of cryocoolers at 80 K (after Ref. [10]).

Table 1
Cryocoolers for space applications (after Ref. [12]).

Cooler	Typical temperature (K)	Typical heat lift	Advantages	Disadvantages
Radiator	80	0.5 W	Reliable, low vibration, long lifetime	Complicates orbit
Stirling—1 stage	80	0.8 W	Efficient, heritage	Vibrations
Stirling—2 stage	20	0.06 W	Intermediate temp	Under development
Pulse tube	80	0.8 W	Lower vibrations, efficiency comparable to Stirling	Difficulties in scaling down to small sizes while maintaining high efficiency, larger diameter cold finger
Joule–Thompson	4	0.01 W	Low vibrations	Requires hybrid design
Sorption	10	0.1 W	Low vibrations	Low efficiency, under development
Brayton	65	8W	High capacity	Complex
ADR	0.05	0.01 mW	Only way to reach these temps.	Large magnetic field
Peltier	170	1W	Lightweight	High temp, low efficiency

liquid nitrogen every few hours. For many applications, especially in the field LN₂, pour-filled dewars are impractical, so many manufacturers are turning to alternative coolers that do not require cryogenic liquids or solids.

2.2.1.2. Stirling cycle. Stirling coolers are based on causing a working gas to undergo a Stirling cycle which consists of two constant volume processes and two isothermal processes. Devices consist of a compressor pump and a displacer unit with a regenerative

heat exchanger, known as a regenerator. Stirling engines require several minutes of cool-down time; the working fluid is helium. The development of two-stage devices extend the lower temperature range from 60–80 to 15–30 K.

Both Joule–Thompson and engine-cooled detectors are housed in precision-bore dewars into which the cooling device is inserted (see Fig. 10). The detector, mounted in the vacuum space at the end of the inner wall of the dewar and surrounded by a cooled radiation shield compatible with the convergence angle of the optical system, looks out through an IR window. In some dewars, the electrical leads to detector elements are embedded in the inner wall of the dewar to protect them from damage due to vibration. After 3000 to 5000 h of operation, Stirling cooler requires factory service to maintain performance. Because the dewar and cooler is one IDA unit, the entire unit must be serviced together.

Split Stirling coolers are also fabricated. The detector is mounted on the dewar bore, and the cold finger of the cooler is thermally connected to the dewar by a bellows. A fan is necessary to dissipate the heat. The cooler can be easily removed from the detector/dewar for replacement.

Fig. 11 shows the four sizes of Stirling cryocoolers used for military tactical applications. The refrigeration powers listed for each cooler are for a temperature of about 77 to 80 K, except the 1.75 W system, which is for a temperature of 67 K [13]. Their COPs range from about 3 to 6% of Carnot as the size increases. All of the shown coolers use linear drive motors with a dual-opposed arrangement to reduce vibration. The displacer driven pneumatically with the oscillating pressure in the system gives rise to considerable vibration (because only one displacer is used). Space applications of Stirling cryocoolers require greatly improved reliabilities, and a MTBF of 10 years is now usually specified for these applications.

2.2.1.3. Pulse tube. The moving displacer in the Stirling cryocoolers has several disadvantages. It is a source of vibration, has a limited lifetime, and contributes to axial heat conduction as well as to a shuttle heat loss. Pulse tube coolers are similar to Stirling coolers. However, their thermodynamic processes are quite different. The proper gas motion in phase with the pressure is achieved by the use of an orifice, along with a reservoir volume to store the gas during a half cycle. The reservoir volume is large enough that negligible pressure oscillation occurs in it during the oscillating flow. The oscillating flow through the orifice separates the heating and cooling effects just as the displacer does for the Stirling refrigerator.

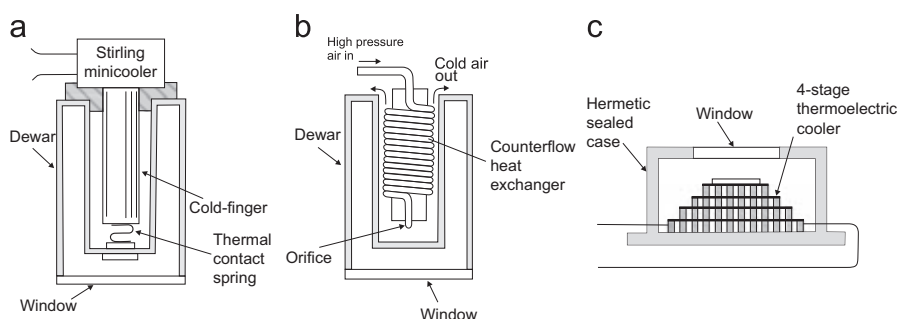


Fig. 10. Three ways of cooling IR detectors: (a) Stirling-cycle engine, (b) Joule–Thompson cooler, and (c) four-stage thermoelectric cooler (Peltier cooling).



Fig. 11. Four sizes of Stirling cryocoolers with dual-opposed linear compressors (after Ref. [12]). The refrigeration powers listed for each cooler are for a temperature of about 77 to 80 K, except the 1.75 W system, which is for a temperature of 67 K.

Since there are no moving parts at the cold-end reliability is theoretically higher than Stirling cycle machines. Efficiencies approaching Stirling cycle coolers can be achieved (see Fig. 9) and several recent missions have demonstrated their usefulness in space.

2.2.1.4. Joule–Thompson (J – T) coolers. The design of Joule–Thompson coolers is based on the fact that as a high-pressure gas expands upon leaving a throttle valve, it cools and liquefies (leading to isenthalpic cooling). The coolers require a high-pressure gas supply from bottles and compressors. Although this is an irreversible process, with correspondingly low efficiency, Joule–Thompson coolers are simple, reliable, and have low electrical and mechanical noise levels.

Using compressed air, temperatures of the order 80 K can be achieved in one or two minutes. The gas used must be purified to remove water vapour and carbon dioxide that could freeze and block the throttle valve. Specially designed Joule–Thompson coolers using argon are suitable for ultrafast cool-down (a few second cooling time). Recent advances in J – T cryocoolers have been associated with the use of mixed-gases as the working fluid rather than pure gases.

Fig. 12 shows a typical Joule–Thompson cryocooler used for missile guidance, where miniature finned tubing is used for the heat exchanger. An explosive valve is used to start the flow of gas from the high-pressure bottle, and after flowing through the system, the gas is vented to the atmosphere.

2.2.1.5. Sorption. This type of cooler is essentially J – T cooler which use a thermo-chemical process to provide gas compression with no moving parts. Powdered sorbent materials (e.g. metal hydrides) are electrically heated and cooled to pressurize, circulate, and adsorb a working fluid such as hydrogen. Disadvantage of sorption coolers is low efficiency, which may be increased by the use of mixed working gases. These coolers are expected to be useful in long-life space missions where very low vibration levels are required.

2.2.1.6. Brayton. In Brayton cryocoolers (sometimes referred to as the reverse-Brayton cycle to distinguish it from a heat engine) cooling occurs as the expanding gas does work. Coolers consist of a rotary compressor, a rotary turbo-alternator (expander), and a



Fig. 12. Open-cycle Joule–Thomson cryocooler for missile guidance (after Ref. [12]).

counterflow heat exchanger (as opposed to the regenerator found in Stirling or pulse tube coolers). The compressor and expander use high-speed miniature turbines on gas bearings and small machines are thus very difficult to build. Brayton coolers have high efficiencies and are practically vibration free. This low vibration is often required with sensitive telescopes in satellite applications. These coolers are primarily useful for low temperature experiments (less than 10 K), where a large machine is inevitable or for large capacity devices at higher temperatures (although these requirements are quite rare). The expansion engine provides for good efficiency over a wide temperature range, although not as high as some Stirling and pulse tube cryocoolers at temperatures above about 50 K.

2.2.1.7. Adiabatic demagnetization. Adiabatic demagnetization refrigeration (ADR) has been used on the ground for many years to achieve milli-Kelvin temperatures after a first stage cooling process. The process utilizes the magneto-caloric effect with a paramagnetic salt. These coolers are currently under development for space use.

2.2.1.8. ^3He coolers. When a mixture of two isotopes of helium is cooled below approximately 870 mK, the mixture undergoes spontaneous phase separation to form a ^3He -rich phase and a ^3He -poor phase.

A helium-3 (^3He) refrigerator is a simple device used for obtaining temperatures down to about 250 mK. By evaporative cooling of helium-4 (^4He) (the more common isotope of helium), a 1-K pot liquefies a small amount of ^3He in a small vessel called a ^3He pot. Evaporative cooling of the liquid ^3He , usually driven by adsorption (an internal charcoal sorption pump) cools the ^3He pot to a fraction of a kelvin.

Using dilution refrigerators a temperature above 50 mK can be received. A two stage Gifford-McMahon cryocooler can be used for ^3He condensation.

2.2.1.9. Passive coolers. Passive coolers require no input power and have been used for many years in space science applications due to their relatively high reliability and low vibration levels. To passive coolers belong radiators and stored cryogens.

Radiators are panels radiating heat and are the workhorse of satellite cooling due to their extremely high reliability. They have low mass and a lifetime limited only by surface contamination and degradation. Radiators have severe limitations on the heat load and temperature (typically in the milliwatt range at 70 K). Usually two and three stages are used to baffle the lowest temperature stage, or patch. In this case the first stage consists of a highly reflective baffle (e.g., a cone), to shield the patch from the spacecraft, Earth or shallow-angle sun-light.

Stored cryogens are dewars contained a cryogen such as liquid helium or solid neon. They are used to achieve temperatures below those offered by radiators (heat is absorbed by either boiling or sublimation, respectively) and provide excellent temperature stability with no exported vibrations. However, stored cryogens substantially increase the launch mass of the vehicle and limit the lifetime of the mission to the amount of cryogen stored. They have also proved to be of limited reliability.

2.2.2. Peltier coolers

Thermoelectric (TE) cooling of detectors is simpler and less costly than closed-cycle cooling. Thermoelectric coolers work by exploiting the Peltier effect that refers to the creation of heat flux at the junction of two dissimilar conductors in the presence of current flow. The optimal performance of thermoelectrical material in a device is determined by the dimensionless figure of merit

$$ZT = \frac{S^2 \sigma}{k}, \quad (1)$$

where S is the Seebeck coefficient, σ is the electrical conductivity, k is the thermal conductivity, and T is the average temperature.

It appears that the Peltier cooler's coefficient of performance (COP) is a function of ZT and the overall temperature difference between the hot side and cold side of the cooler. The typical maximum temperature difference between the hot side and the cold side of a single stage TE cooler, referred to as ΔT_{max} , is around 70 °C (see Fig. 13). At maximum temperature difference, the COP goes to zero. Conversely, at zero ΔT , a TE cooler achieves maximum heat pumping capacity. Therefore, TE coolers typically operate at the minimal ΔT that provides acceptable detector performance. In order to achieve ΔT of 70 K or more, TE coolers are stacked in "stages". The theoretical range for ΔT_{max} achievable using existing commercial materials is plotted in Fig. 14 as a function of the number of stages [14].

Commercially available coolers do not go beyond 6 stages. They are based on alloys of bismuth telluride and antimony telluride materials exhibiting ZT -values close to one, but

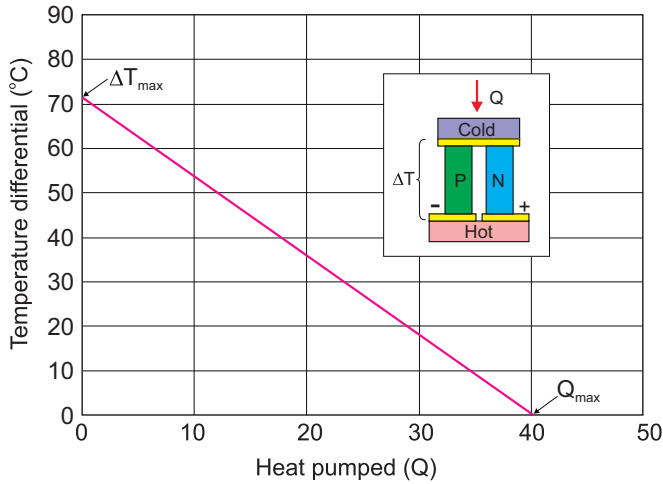


Fig. 13. Typical load profile of a one stage TE cooler.

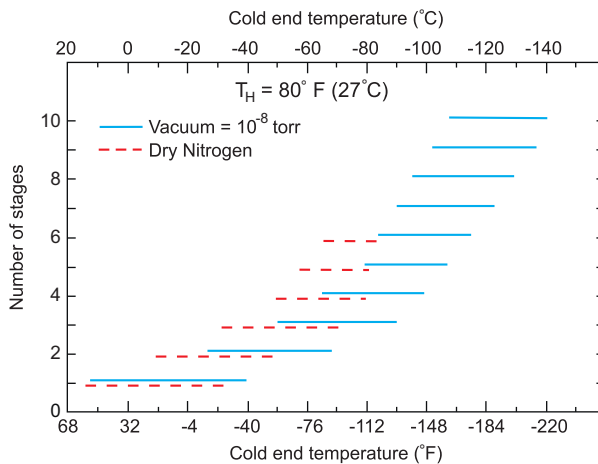


Fig. 14. Typical performance range of thermoelectric modules (after Ref. [14]).

in a device configuration ZT -value is closer to 0.7. Recently, the enhancement in ZT -value has been achieved in low dimensional solids via nanostructuring in thin film materials. Similar investigations in bulk materials have indicated that bulk TE performance in the range of ZT is about 1.5 near room temperature and approaching 2.0 at higher temperatures [15]. The modest improvements in bulk materials are transitioning to commercial TE products [16].

In the case of Peltier coolers, detectors are usually mounted in a hermetic encapsulation with a base designed to make good contact with a heat sink. TE coolers can achieve temperatures to ≈ 200 K, have about 20-year operating life, are small and rugged, and have low input power (<1 W for a 2-stage device and <3 W for a 3-stage device). Their main disadvantage is low efficiency (see Table 1).

The TE coolers used for IR FPA operation include 1-stage (TE1, down to -20°C or 253 K), 2-stage (TE2, down to -40°C or 233 K), 3-stage (TE3, down to -65°C or 208 K), and 4-stage (TE4, down to -80°C or 193 K). Peltier coolers are also the preferred approach to temperature control at the required level, e.g., for uncooled visible and IR sensors.

3. Classification of detectors

The majority of optical detectors can be classified in two broad categories: photon detectors (also called quantum detectors) and thermal detectors.

3.1. Photon detectors

In photon detectors the radiation is absorbed within the material by interaction with electrons either bound to lattice atoms or to impurity atoms or with free electrons. The observed electrical output signal results from the changed electronic energy distribution. The fundamental optical excitation processes in semiconductors are illustrated in Fig. 15. The photon detectors show a selective wavelength dependence of response per unit incident radiation power (see Fig. 16). They exhibit both good signal-to-noise performance and a very fast response. But to achieve this, the photon IR detectors require cryogenic cooling. This is necessary to prevent the thermal generation of charge carriers. The thermal transitions compete with the optical ones, making non-cooled devices very noisy.

The spectral current responsivity of photon detectors is equal to

$$R_i = \frac{\lambda \eta}{hc} qg, \quad (2)$$

where λ is the wavelength, h is the Planck's constant, c is the velocity of light, q is the electron charge, and g is the photoelectric current gain. The current that flows through the contacts of the device is noisy due to the statistical nature of the generation and recombination processes—fluctuation of optical generation, thermal generation, and radiative and nonradiative recombination rates. Assuming that the current gain for the

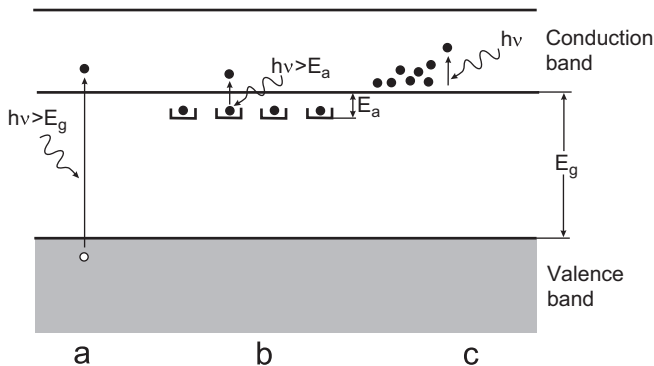


Fig. 15. Fundamental optical excitation processes in semiconductors: (a) intrinsic absorption, (b) extrinsic absorption, (c) free carrier absorption.

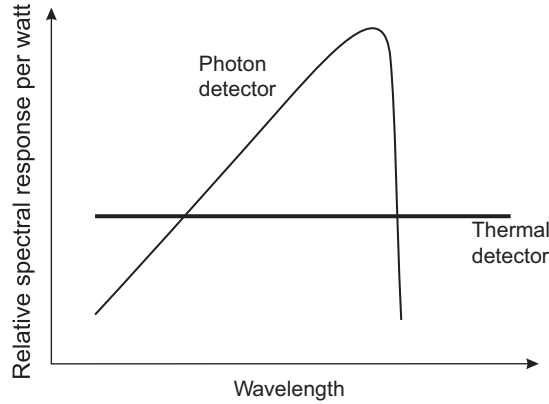


Fig. 16. Relative spectral response for a photon and thermal detector.

photocurrent and the noise current are the same, the noise current is

$$I_n^2 = 2q^2 g^2 (G_{\text{op}} + G_{\text{th}} + R) \Delta f, \quad (3)$$

where G_{op} is the optical generation rate, G_{th} is the thermal generation rate, R is the resulting recombination rate, and Δf is the frequency band.

It was found by Jones [17], that for many detectors the noise equivalent power (NEP) is proportional to the square root of the detector signal that is proportional to the detector area, A_d . A normalized detectivity D^* (or D -star) suggested by Jones [5,17] is defined as

$$D^* = \frac{(A_d)^{1/2}}{NEP}. \quad (4)$$

Detectivity, D^* , is the main parameter to characterize normalized signal-to-noise performance of detectors, and can be also defined as

$$D^* = \frac{R_i (A_d \Delta f)^{1/2}}{I_n}. \quad (5)$$

The importance of D^* is that this figure of merit permits comparison of detectors of the same type, but having different areas. Either a spectral or blackbody D^* can be defined in terms of corresponding type of NEP .

At equilibrium, the generation and recombination rates are equal. In this case

$$D^* = \frac{\lambda \eta}{2hc(Gt)^{1/2}}. \quad (6)$$

Background radiation frequently is the main source of noise in an infrared detector. Assuming no contribution due to recombination,

$$I_n^2 = 2\Phi_B A_d \eta q^2 g^2 \Delta f, \quad (7)$$

where Φ_B is the background photon flux density. Therefore, at the background limited performance conditions (BLIP performance)

$$D_{\text{BLIP}}^* = \frac{\lambda}{hc} \left(\frac{\eta}{\Phi_B} \right)^{1/2} . \quad (8)$$

Once background-limited performance is reached, quantum efficiency, η , is the only detector parameter that can influence a detector's performance.

When detectors are operated in conditions where the background flux is less than the signal flux, the ultimate performance of detectors is determined by the signal fluctuation limit (SFL). It is achieved in practice with photomultipliers operating in the visible and ultraviolet region, but it is rarely achieved with solid-state devices, which are normally detector-noise or electronic noise limited. This limit is also applicable to longer wavelength detectors when the background temperature is very low. The *NEP* and detectivity of detectors operating in this limit have been derived by a number of authors (see e.g., Kruse et al. [18,19]).

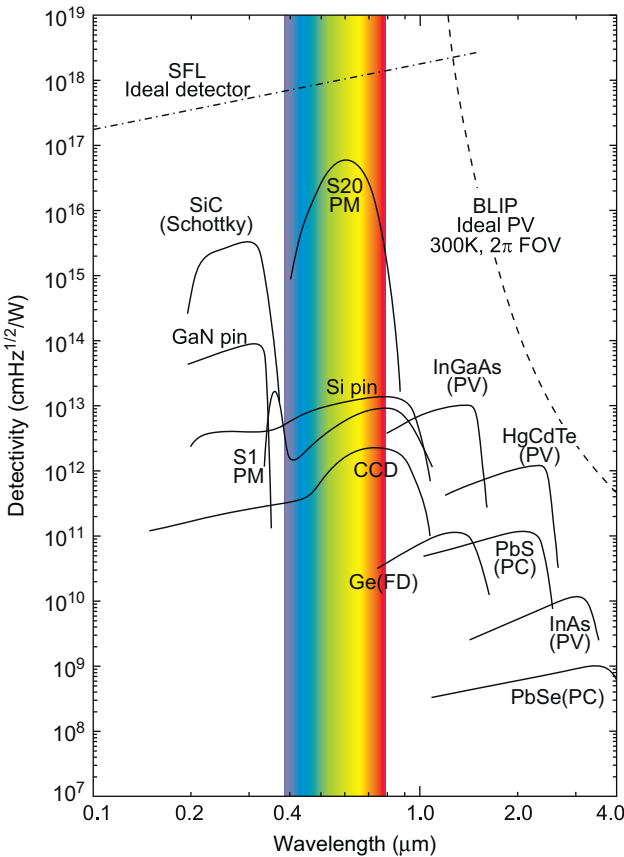


Fig. 17. Detectivity vs wavelength values of 0.1–4 μm photodetectors. PC indicates a photoconductive detector, PD—photodiode, and PM indicates a photomultiplier.

It is interesting to determine the composite signal fluctuation and background fluctuation limits. Fig. 17 illustrates the spectral detectivities over the wavelength range from 0.1 to 4 μm assuming a background temperature of 290 K and a 2π steradian field of view (FOV) (applicable only to the background fluctuation limit). Note that the intersections of curves for signal fluctuation and background fluctuation limits lie about 1.2 μm . At wavelengths below 1.2 μm the SFL dominates; the converse is true above 1.2 μm . Below 1.2 μm the wavelength dependence is small. Above 1.2 μm it is very large, due to steep dependence of detectivity upon wavelength of the short wavelength end of the 290 K background spectral distribution.

Depending on the nature of the interaction, the class of photon detectors is further sub-divided into different types. The most important are: intrinsic detectors, extrinsic detectors, photoemissive (Schottky barriers). Different types of detectors are described in details in monograph *Infrared Detectors* [5] and are briefly characterized in Table 2. Fig. 18 shows spectral detectivity curves for a number of commercially available IR detectors.

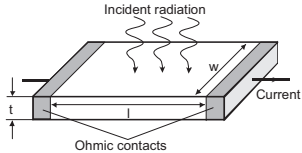
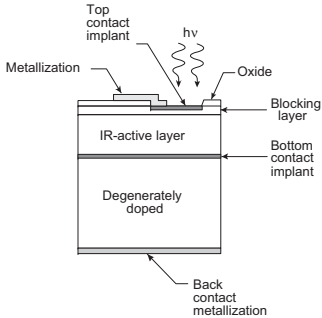
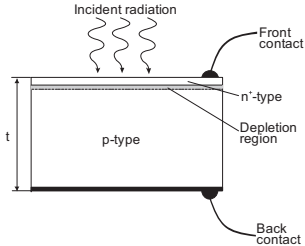
The most widely used photovoltaic detector is the p–n junction, where a strong internal electric field exists across the junction. Photons incident on the junction produce free hole–electron pairs which are separated by the internal electric field across the junction, causing a change in voltage across the open-circuit cell or a current to flow in the short-circuited case. Due to the absence of recombination noise, the limiting p–n junction's noise level can ideally be $\sqrt{2}$ times lower than that of the photoconductor.

Photoconductors that utilize excitation of an electron from the valence to conduction band are called intrinsic detectors. Instead those which operate by exciting electrons into the conduction band or holes into the valence band from impurity states within the band (impurity-bound states in energy gap, quantum wells or quantum dots), are called extrinsic detectors. A key difference between intrinsic and extrinsic detectors is that extrinsic detectors require much cooling to achieve high sensitivity at a given spectral response cutoff in comparison with intrinsic detectors. Low-temperature operation is associated with longer-wavelength sensitivity in order to suppress noise due to thermally induced transitions between close-lying energy levels. Intrinsic detectors are most common at the short wavelengths, below 20 μm . In the more long wavelength region the photoconductors are operated in extrinsic mode. One advantage of photoconductors is their current gain which is equal to the recombination time divided by the majority-carrier transit time. This current gain leads to higher responsivity than is possible with nonavalanching photovoltaic detectors. However, series problem of photoconductors operated at low temperature is nonuniformity of detector element due to recombination mechanisms at the electrical contacts and its dependence on electrical bias.

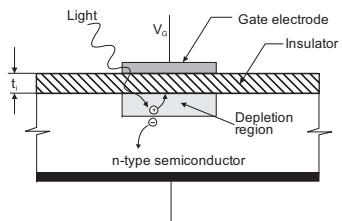
Recently, interfacial workfunction internal photoemission (IWIP) detectors [20], quantum well [21] and quantum dot detectors [22], which can be included to extrinsic photoconductors, have been proposed especially for IR and THz spectral bands [5]. The very fast time response of quantum well and quantum dot semiconductor detectors make them attractive for heterodyne detection.

In general, quantum dot infrared photodetectors (QDIPs) are similar to quantum well infrared photodetectors (QWIPs) but with the quantum wells replaced by quantum dots, which have size confinement in all spatial directions. The energy position of QD (also QW) level essentially depends on geometrical sizes and even one monolayer variation of the size can significantly affect the energy of optical transition. Fluctuations of the geometrical parameters results in corresponding fluctuation of the quantum level over the array

Table 2
Photon detectors.

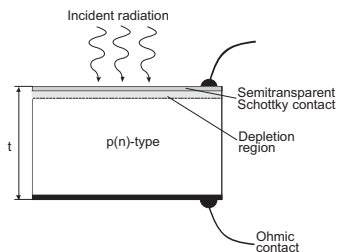
Mode of operation	Schematic of detector	Operation and properties
Photoconductor		It is essentially a radiation-sensitive-resistor, generally a semiconductor, either in thin-film or bulk form. A photon may release an electron–hole pair or an impurity-bound charge carrier, thereby increasing the electrical conductivity. In almost all cases the change in conductivity is measured by means of electrodes attached to the sample. For low resistance material, the photoconductor is usually operated in a constant current circuit. For high resistance photoconductors, a constant voltage circuit is preferred and the signal is detected as a change in current in the bias circuit.
Blocked impurity band detector		The active region of BIB detector structure, usually based on epitaxially grown n-type material, is sandwiched between a higher doped degenerate substrate electrode and an undoped blocking layer. Doping of active layer is high enough for the onset of an impurity band in order to display a high quantum efficiency for impurity ionization (in the case of Si:As BIB, the active layer is doped to $\approx 5 \times 10^{17} \text{ cm}^{-3}$). The device exhibits a diode-like characteristic, except that photoexcitation of electrons takes place between the donor impurity and the conduction band. The heavily doped n-type IR-active layer has a small concentration of negatively charged compensating acceptor impurities. In the absence of an applied bias, charge neutrality requires an equal concentration of ionized donors. Whereas the negative charges are fixed at acceptor sites, the positive charges associated with ionized donor sites (D^+ charges) are mobile and can propagate through the IR-active layer via the mechanism of hopping between occupied (D^0) and vacant (D^+) neighbouring sites. A positive bias to the transparent contact creates a field that drives the pre-existing D^+ charges towards the substrate, while the undoped blocking layer prevents the injection of new D^+ charges. A region depleted of D^+ charges is therefore created, with a width depending on the applied bias and on the compensating acceptor concentration.
p–n junction photodiode		It is the most widely used photovoltaic detector, but rather rarely used as THz detector. Photons with energy greater than the energy gap create electron–hole pairs in the material on both sides of the junction. By diffusion, the electrons and holes generated within a diffusion length from the junction reach the space-charge region where they are separated by the strong electric field; minority carriers become majority carriers on the other side. This way a photocurrent is generated causing a change in voltage across the open-circuit cell or a current to flow in the short-circuited case. The limiting noise level of photodiodes can ideally be $\sqrt{2}$ times lower than that of the photoconductor, due to the absence of recombination noise. Response times are generally limited by device capacitance and detector-circuit resistance.

MIS photodiode



The MIS device consists of a metal gate separated from a semiconductor surface by an insulator of thickness t_i and dielectric constant ϵ_i . By applying a negative voltage V_G to the metal electrode, electrons are repelled from the I–S interface, creating a depletion region. When incident photons create hole–electron pairs, the minority carriers drift away to the depletion region and the volume of the depletion region shrinks. The total amount of charge that a photogate can collect is defined as its well capacity. The total well capacity is decided by the gate bias, the insulator thickness, the area of the electrodes, and the background doping of the semiconductor. Numerous such photogates with proper clocking sequence form a CCD imaging array.

Schottky barrier photodiode



Schottky barrier photodiode reveal some advantages over p–n junction photodiode: fabrication simplicity (deposition of metal barrier on n(p)-semiconductor), absence of high-temperature diffusion processes, and high speed of response. Since it is a majority carrier device, minority carrier storage and removal problems do not exist and therefore higher bandwidths can be expected. The thermionic emission process in Schottky barrier is much more efficient than the diffusion process and therefore for a given built-in voltage, the saturation current in a Schottky diode is several orders of magnitude higher than in the p–n junction.

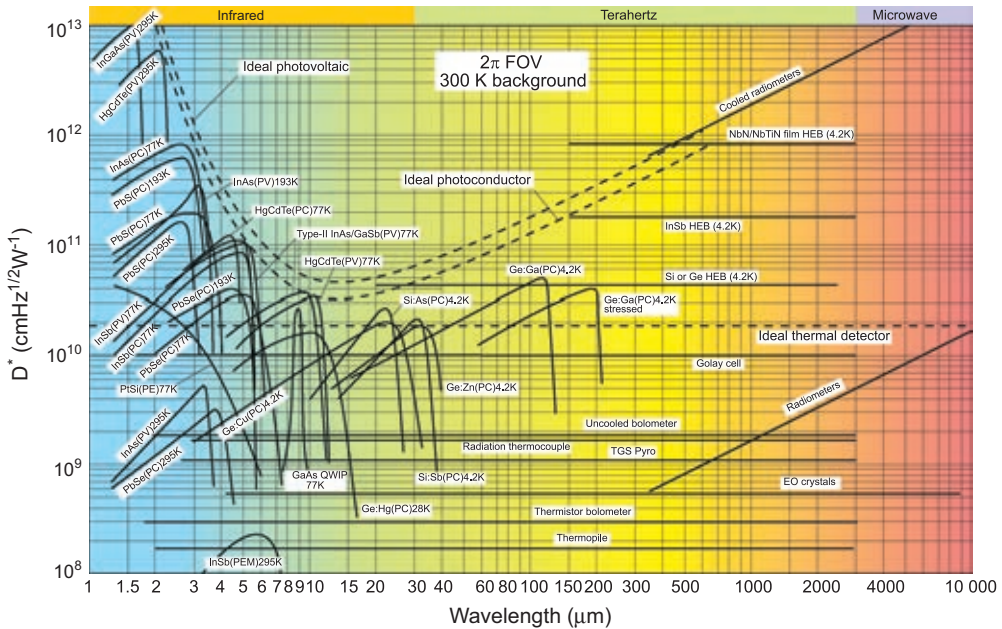


Fig. 18. Comparison of the D^* of various available detectors when operated at the indicated temperature. Chopping frequency is 1000 Hz for all detectors except the thermopile (10 Hz), thermocouple (10 Hz), thermistor bolometer (10 Hz), Golay cell (10 Hz) and pyroelectric detector (10 Hz). Each detector is assumed to view a hemispherical surrounding at a temperature of 300 K. Theoretical curves for the background-limited D^* (dashed lines) for ideal photovoltaic and photoconductive detectors and thermal detectors are also shown. PC—photoconductive detector, PV—photovoltaic detector, PEM—photoelectromagnetic detector, and HEB—hot electron bolometer.

of dots. Random fluctuations also affect the density of states on nonuniform array of QDs.

The quantum well AlGaAs/GaAs structures are mainly grown by MBE on semi-insulating GaAs substrate [see Fig. 19(a)]. Process technology starts with epitaxial growth of structure with a periodic array of Si-doped GaAs quantum wells and sequential growth of an etch-stop layer (usually AlGaAs) used for substrate removal. The QWIP active region is sandwiched between two n-type heavily doped GaAs contact layers about 1- μ m-thick, and an etch stop followed by a sacrificial layer for the grating. For optical coupling, usually 2D reflective diffraction gratings are fabricated. Further process technology includes etching mesas through the superlattice to the bottom contact layer, followed by ohmic contacts to the n⁺-doped GaAs contact layers. These steps can be accomplished using wet chemical or dry etching techniques. In selective etching usually ion beam etching is practical for patterning the grating coupler into each pixel.

The self-assembling method for fabricating QDs has been recognized as one of the most promising methods for forming QDs. In the crystal growth of highly lattice-mismatched materials system, self-assembling formation of nanometer-scale 3D islands has been reported. The lattice mismatch between a QD and the matrix is the fundamental driving force of self-assembling. In(Ga)As on GaAs is the most commonly used material system because lattice mismatched can be controlled by the In alloy ratio up to about 7%.

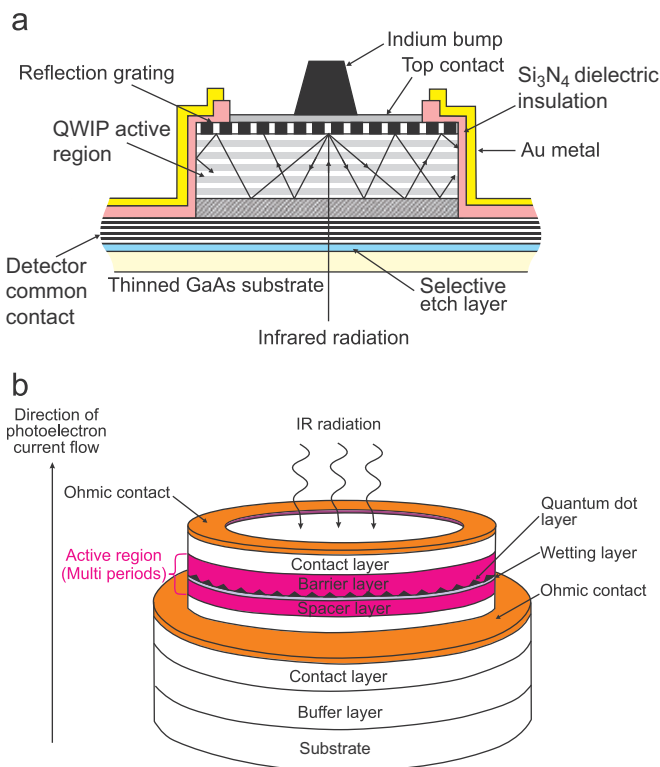


Fig. 19. Schematic diagram of QWIP (a) and QDIP (b).

In a vertical QDIP [Fig. 19(b)], the photocurrent is collected through the vertical transport of carriers between top and bottom contacts. The device heterostructure comprises repeated InAs QD layers buried between GaAs barriers with top and bottom contact layers at active region boundaries. The mesa height can vary from 1 to 4 μm depending on the device heterostructure. The quantum dots are directly doped (usually with silicon) in order to provide free carriers during photoexcitation, and an AlGaAs barrier can be included in the vertical device heterostructure in order to block dark current created by thermionic emission.

A wide variety of detector materials have been adapted for fabrication of photon and thermal detectors, what is shown in Fig. 20(a). Large bandgap materials such as AlGaAs are being actively developed for solar blind and visible blind detection. The traditional material systems for cooled detectors are InSb for MWIR and HgCdTe for SWIR, MWIR, and LWIR. Extrinsic doped and deeply-cooled semiconductors, such as silicon and germanium, are operated in far-infrared spectral region. Emerging material systems include strained layer superlattice (SLS) antimonides and intersubband transition QWIPs and QDIPs in the AlGaAs system. Both of these have the advantage of epitaxial growth on GaAs and possibly Si substrates. However, they are at a much earlier stage of development and technology readiness [7].

Fig. 20(b) shows the quantum efficiency of some of the detector materials used to fabricate arrays of ultraviolet (UV), visible and infrared detectors. Photocathodes and

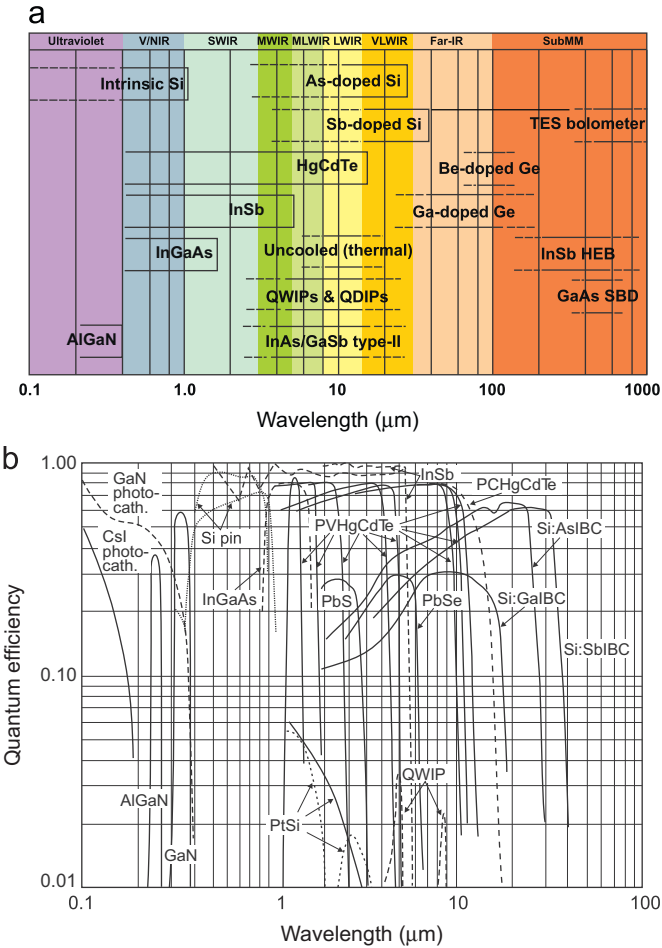


Fig. 20. UV, visible, and infrared detectors: (a) different material systems (adapted after Ref. [7]) and (b) quantum efficiency of detectors (adapted after Ref. [2]).

AlGaAs detectors are being developed in the UV region. Silicon p–i–n diodes are shown with and without antireflection coating. Lead salts (PbS and PbSe) have intermediate quantum efficiencies, while PtSi Schottky barrier types and quantum well infrared photodetectors (QWIPs) have low values. InSb can respond from the near UV out to $5.5\,\mu\text{m}$ at 80 K. A suitable detector material for near-IR ($1.0\text{--}1.7\,\mu\text{m}$) spectral range is InGaAs lattice matched to the InP. Various HgCdTe alloys, in both photovoltaic and photoconductive configurations, cover from 0.7 to over $20\,\mu\text{m}$. Impurity-doped (Sb, As, and Ga) silicon impurity-blocked conduction (IBC) detectors operating at 10 K have a spectral response cut-off in the range of 16 to $30\,\mu\text{m}$. Impurity-doped Ge detectors can extend the response out to $100\text{--}200\,\mu\text{m}$.

UV, visible, and infrared arrays most commonly employ a photodiode structure. Photodiodes are preferred to photoconductors because of their relatively high impedance, which matches directly into the high input impedance stage of an FET readout circuit and

also allows lower power dissipation. Mesa photodiodes are used in AlGaIn, InSb, and HgCdTe detectors, whereas planar photodiodes are used in Si, PtSi, Ge, HgCdTe, InGaAs, and InSb detectors. A third photodiode structure – used exclusively with HgCdTe detectors – is the high-density vertically-integrated photodiode, or loop-hole photodiode [5].

3.2. Thermal detectors

The second class of detectors is composed of thermal detectors. In a thermal detector shown schematically in Fig. 21, the incident radiation is absorbed to change the material temperature, and the resultant change in some physical property is used to generate an electrical output. The detector is suspended on links, which are connected to the heat sink. The signal does not depend upon the photonic nature of the incident radiation. Thus, thermal effects are generally wavelength independent (see Fig. 16); the signal depends upon the radiant power (or its rate of change) but not upon its spectral content. Since the radiation can be absorbed in a black surface coating, the spectral response can be very broad. Attention is directed toward three approaches which have found the greatest utility in infrared technology, namely, bolometers, pyroelectric and thermoelectric effects. The thermopile is one of the oldest IR detector, and is a collection of thermocouples connected in series in order to achieve better temperature sensitivity. In pyroelectric detectors a change in the internal electrical polarization is measured, whereas in the case of thermistor bolometers a change in the electrical resistance is measured. For a long time, thermopiles were slow, insensitive, bulky and costly devices. But with developments in semiconductor technology, thermopiles can be optimized for specific applications. Recently, thanks to conventional CMOS processes, the thermopile's on-chip circuitry technology has opened the door to mass production.

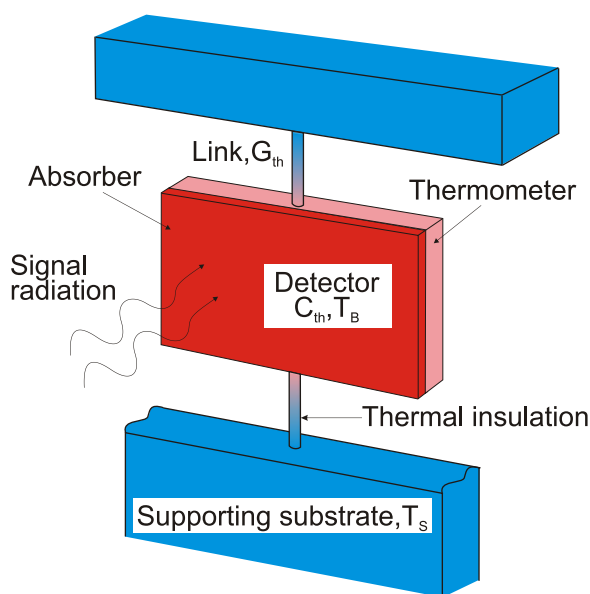


Fig. 21. Schematic diagram of thermal detector.

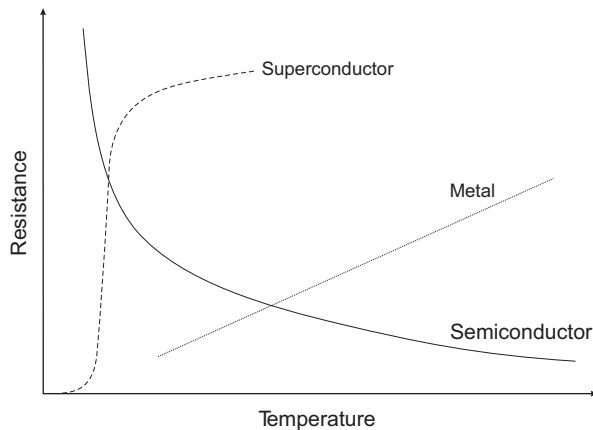


Fig. 22. Temperature dependence of resistance of three bolometer material types.

Usually bolometer is a thin, blackened flake or slab, whose impedance is highly temperature dependent. Bolometers may be divided into several types. The most commonly used are the metal, the thermistor, and the semiconductor bolometers. A fourth type is the superconducting bolometer. This bolometer operates on a conductivity transition in which the resistance changes dramatically over the transition temperature range. Fig. 22 shows schematically the temperature dependence of resistance of different types of bolometers.

Many types of thermal detectors are operated in wide spectral range of electromagnetic radiation. The operation principles of thermal detectors are described in many books; see e.g., Refs. [18,23,24] and briefly described in Table 3.

In the simplest representation of the thermal detector shown in Fig. 21, the detector is represented by an absorbing element with heat capacity, C_{th} , which converts the incident radiation to heat, and which is attached to a heat sink (thermal reservoir) at temperature T_S via thermal conductance G_{th} . In the absence of a radiation input the average temperature of the detector is constant, although it exhibits a fluctuation about this value. When a radiation input power, P , is received by the detector, the temperature T_B of absorbing element initially increases with time at rate $dT_B/dt = P/C_{th}$ and approaches the limiting value $T_B = T_S + P/G_{th}$ with the thermal time constant $\tau_{th} = C_{th}/G_{th}$. When the radiation is turned off, it relaxes back to T_S with time constant τ_{th} . Thermal detectors are frequently used to give a periodic response to a signal which is modulated at a frequency $\omega \approx 1/\tau_{th}$.

The key trade-off with respect to conventional uncooled thermal detectors is between sensitivity and response time. The detector sensitivity is often expressed by noise equivalent temperature difference ($NEDT$) represented by the temperature change, for incident radiation, that gives an output signal equal to the rms noise level. The thermal conductance is an extremely important parameter, since the $NEDT$ is proportional to $(G_{th})^{1/2}$, but the thermal response time of the detector, τ_{th} , is inversely proportional to G_{th} . Therefore, a change in thermal conductance due to improvements in material processing technique improves sensitivity at the expense of time response. Typical calculations of the trade-off between $NEDT$ and time response carried out in Ref. [25] are shown in Fig. 23.

Table 3
Thermal detectors.

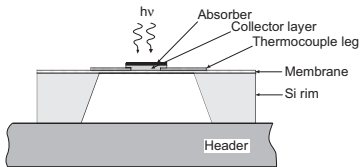
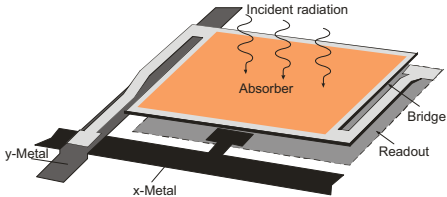
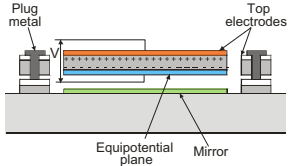
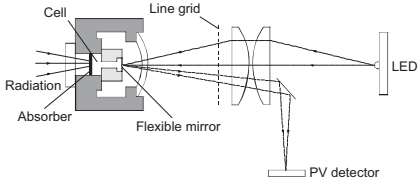
Mode of operation	Schematic of detector	Operation and properties
Thermopile		<p>The thermocouple is usually a thin, blackened flake connected thermally to the junction of two dissimilar metals or semiconductors. Heat absorbed by the flake causes a temperature rise of the junction, and hence a thermoelectric electromotive force is developed which can be measured. Although thermopiles are not as sensitive as bolometers and pyroelectric detectors, they will replace these in many applications due to their reliable characteristics and good cost/performance ratio. Thermocouples are widely used in spectroscopy.</p>
Bolometer Metal Semiconductor Superconductor Hot electron		<p>The bolometer is a resistive element constructed from a material with a very small thermal capacity and large temperature coefficient so that the absorbed radiation produces a large change in resistance. The change in resistance is like to the photoconductor, however, the basic detection mechanisms are different. In the case of a bolometer, radiant power produces heat within the material, which in turn produces the resistance change. There is no direct photon–electron interaction.</p> <p>Most bolometers in use today are of the thermistor type made from oxides of manganese, cobalt, or nickel. Their construction is very rugged for system applications. Some extremely sensitive low-temperature semiconductor and superconductor bolometers are used in THz region.</p>
Pyroelectric detector		<p>The pyroelectric detector can be considered as a small capacitor with two conducting electrodes mounted perpendicularly to the direction of spontaneous polarization. During incident of radiation, the change in polarization appears as a charge on the capacitor and a current is generated, the magnitude of which depends on the temperature rise and the pyroelectrical coefficient of the material. The signal, however, must be chopped or modulated. The detector sensitivity is limited either by amplifier noise or by loss-tangent noise. Response speed can be engineered making pyroelectric detectors useful for fast laser pulse detection, however with proportional decrease in sensitivity.</p>
Golay cell		

Table 3 (continued)

Mode of operation	Schematic of detector	Operation and properties
		<p>The Golay cell consists of an hermetically sealed container filled with gas (usually xenon for its low thermal conductivity) and arranged so that expansion of the gas under heating by a photon signal distorts a flexible membrane on which a mirror is mounted. The movement of the mirror is used to deflect a beam of light shining on a photocell and so producing a change in the photocell current as the output. In modern Golay cells the photocell is replaced by a solid state photodiode and light emitting diode is used for illumination.</p> <p>The performance of the Golay cell is only limited by the temperature noise associated with the thermal exchange between the absorbing film and the detector gas, consequently the detector can be extremely sensitive with $D^* \approx 3 \times 10^9 \text{ cm Hz}^{1/2}/\text{W}$, and responsivities of 10^5 to 10^6 V/W. The response time is quite long, typically 15 ms.</p>

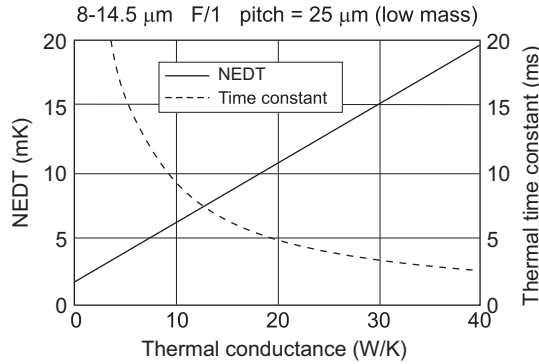


Fig. 23. Trade-off between sensitivity and response time of uncooled thermal imaging systems (after Ref. [25]).

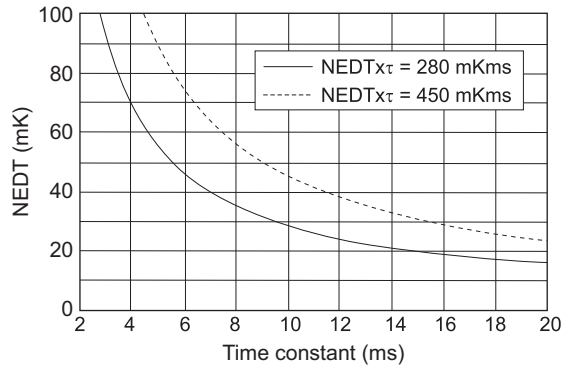


Fig. 24. Calculated microbolometer $NEDT$ and thermal time constant, τ_{th} , for two $NEDT \times \tau_{th}$ products (after Ref. [26]).

If the $NEDT$ is dominated by a noise source that is proportional to G_{th} , what has place when Johnson and $1/f$ noises are dominated, and since $\tau_{th} = C_{th}/G_{th}$, then the Figure of Merit given by

$$FOM = NEDT \times \tau_{th} \quad (9)$$

can be introduced for long wavelength IR bolometers [26].

Users are interested not only in the sensitivity, but also in their thermal time constants and the FOM described by Eq. (9) recognizes the tradeoffs between thermal time constant and sensitivity. Fig. 24 shows the dependence of $NEDT$ on thermal time constant for two $NEDT \times \tau_{th}$ products.

Bolometers, as other thermal devices, for a long time traditionally were treated as slow devices. In many applications, their performance is limited by a trade-off between speed and sensitivity. For conventional uncooled microbolometers operated in wavelength range 10–100 μm at room temperature, the typical value of heat capacity is about of 2×10^{-9} J/K (for bolometer with dimensions $50 \times 50 \times 0.5 \mu\text{m}$) and thermal conductance of 10^{-7} W/K (a-Si or VO_x bolometers). Both parameters define time constant, τ_{th} , equal about 20 ms. The upper limit of NEP for a bolometer limited only by radiation exchange with the environment is $NEP_R \approx 2.7 \times 10^{-13}$ W/Hz^{1/2}. At present however, the bolometer is also

used as a THz mixer, where has to be fast enough to follow the intermediate frequency, i.e., the overall time constant of the processes involved in the mixing has to be a few tens of picoseconds at maximum. In other words, high heat conductivity and small heat capacity are required [27]. These requirements can be fulfilled by such subsystem as electrons in semiconductor or superconductor interacting with the lattice (phonons). Electron heat capacity is many orders lower compared to the lattice one.

Whenever a pyroelectric crystal undergoes a change of temperature, surface charge is produced in a particular direction as a result of the change in its spontaneous polarization with temperature. The choice of pyroelectric materials is not an obvious one as it will depend on many factors including the size of the detector required, the operating temperature and the frequency of operation. An ideal material should have large pyroelectric coefficient, low dielectric constant, low dielectric loss and low volume specific heat. The possibility of satisfying these requirements in a single material is not promising. While it is generally true that a large pyroelectric coefficient and a small dielectric constant are desirable, it is also true that these two parameters are not independently adjustable. Thus, the materials having a high pyroelectric coefficient also have a high dielectric constant, and materials having a low dielectric constant also have a low pyroelectric coefficient. This means that different detector-preamplifier sizes and configurations will be optimized with different materials [28,29].

4. Overview of focal plane array architectures

Detector arrays are available in wide spectral range of electromagnetic spectrum. A variety of detector array formats are elaborated in the ultraviolet, visible, infrared and far-infrared (terahertz) regions. Fewer options are available in the shorter or longer wavelength regions. The most spectacular array technology achievements in different spectral ranges are presented in the next sections. We will survey a sample of the types that have been built to address the various portions of the optical spectrum.

In the last four decades, different types of detectors are combined with electronic readouts to make detector arrays. The progress in integrated circuit design and fabrication techniques has resulted in continued rapid growth in the size and performance of these solid state arrays. In the infrared technique, these devices are based on a combination of a readout array connected to an array of detectors.

The term “focal plane array” (FPA) refers to an assemblage of individual detector picture elements (“pixels”) located at the focal plane of an imaging system. Although the definition could include one-dimensional (“linear”) arrays as well as two-dimensional (2D) arrays, it is frequently applied to the latter. Usually, the optics part of an optoelectronic images device is limited only to focusing of the image onto the detectors array. These so-called “staring arrays” are scanned electronically usually using circuits integrated with the arrays. The architecture of detector-readout assemblies has assumed a number of forms which are discussed below. The types of readout integrated circuits (ROICs) include the function of pixel deselecting, antiblooming on each pixel, subframe imaging, output preamplifiers, and may include yet other functions. Infrared imaging systems, which use 2D arrays, belong to so-called “second generation” systems.

A number of architectures are used in the development of FPAs. In general, they may be classified as hybrid and monolithic, but these distinctions are often not as important as proponents and critics state them to be. The central design questions involve performance

advantages versus ultimate producibility. Each application may favour a different approach depending on the technical requirements, projected costs and schedule.

4.1. Monolithic arrays

In the monolithic approach, both detection of light and signal readout (multiplexing) is done in the detector material rather than in an external readout circuit. The integration of detector and readout onto a single monolithic piece reduces the number of processing steps, increases yields, and reduces costs. Common examples of these FPAs in the visible and near infrared (0.7–1.0 μm) are found in camcorders and digital cameras. Two generic types of silicon technology provide the bulk of devices in these markets: charge coupled devices (CCDs) and complementary metal-oxide-semiconductor (CMOS) imagers. CCD technology has achieved the highest pixel counts or largest formats with numbers above 10^9 (see Fig. 2). This approach to image acquisition was first proposed in 1970 in a paper written by Bell Lab researchers Boyle and Smith [30]. CMOS imagers are also rapidly moving to large formats and at present are competed with

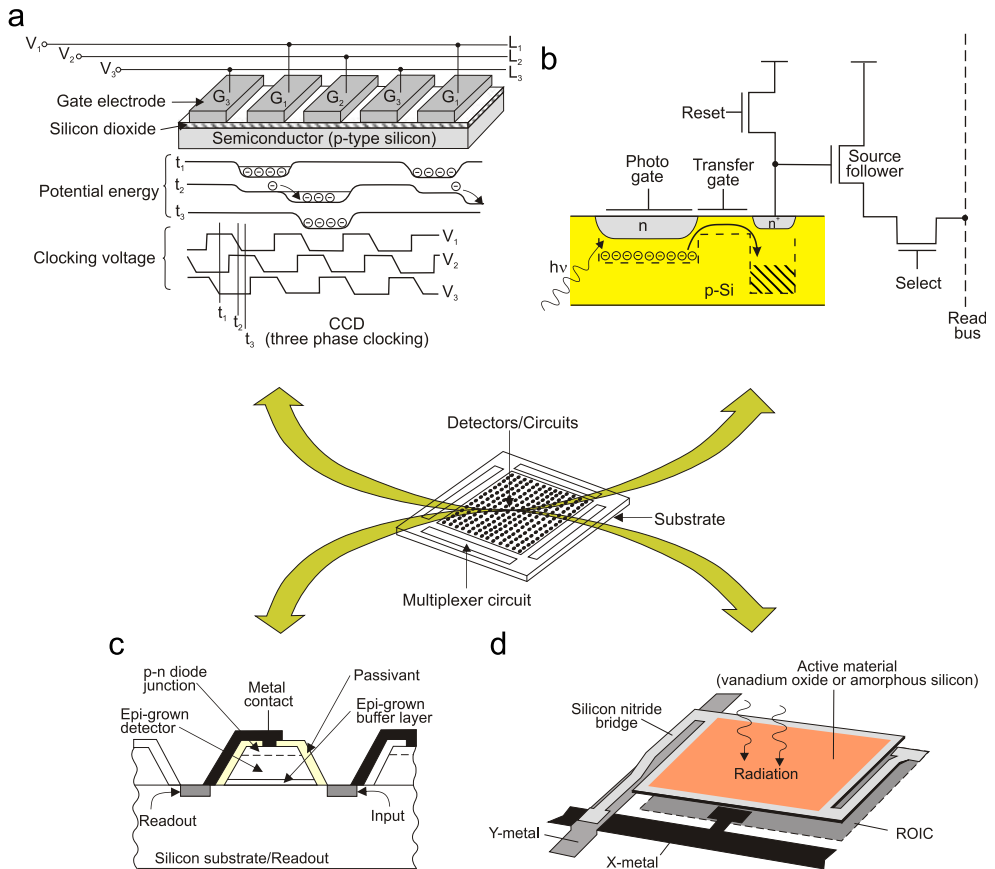


Fig. 25. Monolithic focal plane arrays: (a) CCD, (b) CMOS, (c) heteroepitaxy-on-silicon, and (d) microbolometer.

CCDs for the large format applications. Fig. 25 shows different architectures of monolithic FPAs.

4.1.1. CCD devices

The basic element of a monolithic CCD array is a metal-insulator-semiconductor (MIS) structure. Used as part of a charge transfer device, a MIS capacitor detects and integrates the generated photocurrent [31,32]. Although most imaging applications tend to require high charge handling capabilities in the unit cells, an MIS capacitor fabricated in a narrow-gap semiconductor material (e.g., HgCdTe and InSb) has a limited charge capacity because of its low background potential as well as more severe problems involving noise, tunnelling effects and charge trapping when shifting charge through the narrow bandgap CCD to accomplish the readout function. Because of the non-equilibrium operation of the MIS detector, much larger electric fields are set up in the depletion region than in the p–n junction, resulting in defect-related tunnelling current that is orders of magnitude larger than the fundamental dark current. The MIS detector required much higher material quality than p–n junction detectors, which still has not been achieved. So, although efforts have been made to develop monolithic FPAs using narrow-gap semiconductors, silicon based FPA technology is the only mature technology with respect to fabrication yield and attainment of near-theoretical sensitivity.

A MOS capacitor typically consists of an extrinsic silicon substrate on which is grown an insulating layer of silicon dioxide (SiO_2). When a bias voltage is applied across p-type MOS structure, majority charge carriers (holes) are pushed away from the Si– SiO_2 interface directly below the gate, leaving a region depleted of positive charge and available as a potential energy well for any mobile minority charge carriers (electrons); see Fig. 25(a). Electrons generated in the silicon through absorption (charge generation) will collect in the potential-energy well under the gate (charge collection). Linear or two-dimensional arrays of these MOS capacitors can therefore store images in the form of trapped charge carriers beneath the gates. The accumulated charges are transferred from potential well to the next well by using sequentially shifted voltage on each gate (charge transfer). One of the most successful voltage-shifting schemes is called three-phase clocking. Column gates are connected to the separate voltage lines (L_1 , L_2 , L_3) in contiguous groups of three (G_1 , G_2 , G_3). The setup enables each gate voltage to be separately controlled.

Fig. 26(a) shows the schematic circuit for a typical CCD imager. The photogenerated carriers are first integrated in an electronic well at the pixel and subsequently transferred to slow and fast CCD shift registers. At the end of the CCD register, a charge carrying information on the received signal can be readout and converted into a useful signal (charge measurement).

At present, the following readout techniques are used in CCD devices:

- floating diffusion amplifier in each pixel,
- system with correlated double sampling (CDS),
- floating gate amplifier.

which are described in details, e.g., in Refs. [5,32,33].

The first CCD imager sensors were developed about 40 years ago primarily for television analog image acquisition, transmission, and display. With increasing demand for digital image data, the traditional analog raster scan output of image sensors is of limited use, and there is a strong motivation to fully integrate the control, digital interface, and image sensor on a single

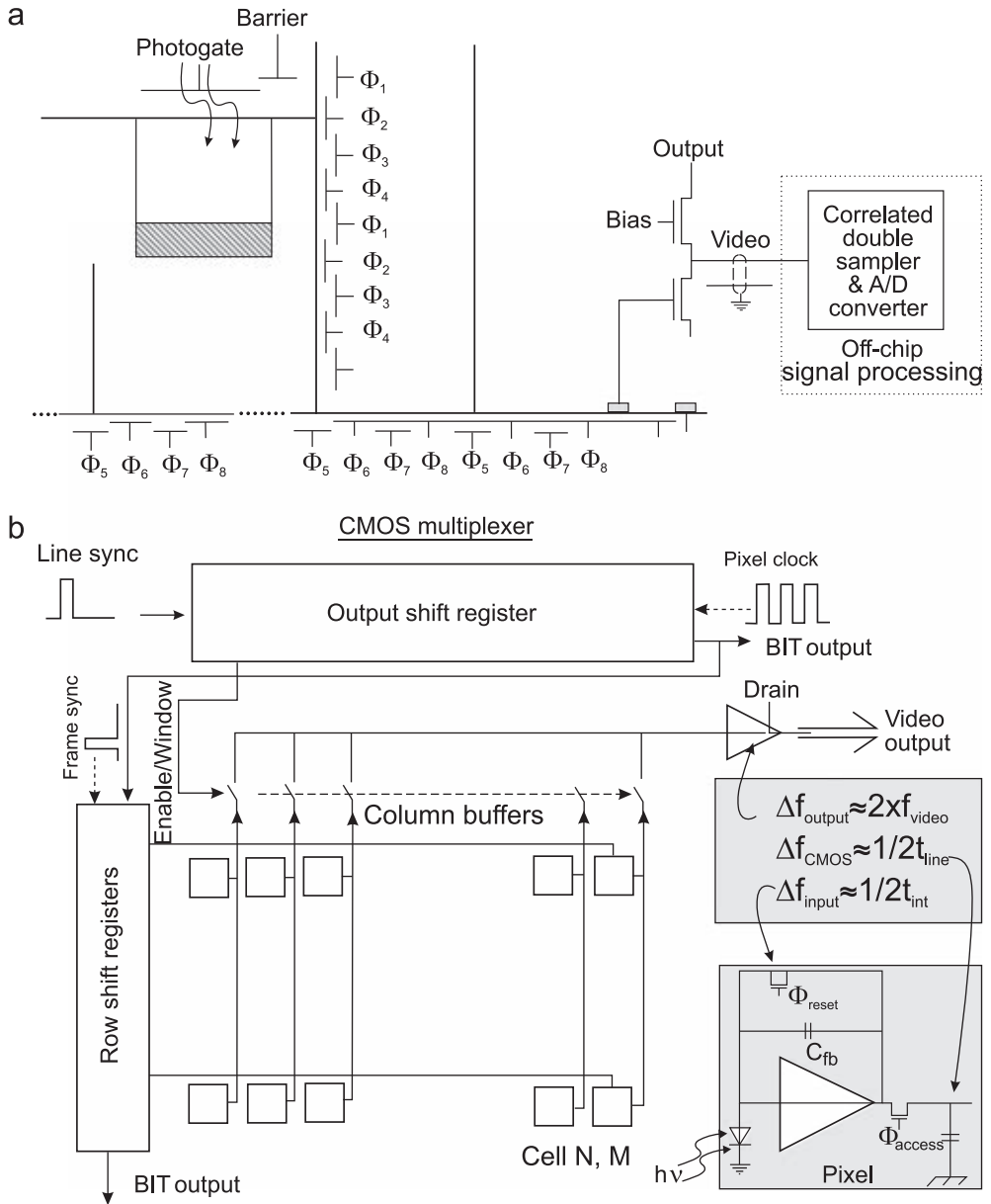


Fig. 26. Typical readout architecture of CCD (a) and CMOS (b) images.

chip. In particular, silicon fabrication advances now permit the implementation of CMOS transistor structures that are considerably smaller than the wavelength of visible light and have enabled the practical integration of multiple transistors within a single picture.

4.1.2. CMOS devices

An attractive alternative to the CCD readout is coordinative addressing with CMOS switches. The configuration of CCD devices requires specialized processing, unlike CMOS imagers which

can be built on fabrication lines designed for commercial microprocessors. CMOS have the advantage that existing foundries, intended for application specific integrated circuits (ASICs), can be readily used by adapting their design rules. Design rules of 28 nm are currently in production, with pre-production runs of 22 nm design rules. As a result of such fine design rules, more functionality has been designed into the unit cells of multiplexers with smaller unit cells, leading to large array sizes. Fig. 2 shows the timelines for minimum circuit features and the resulting CCD, IR FPA and CMOS visible imager sizes with respect to number of imaging pixels. Along the horizontal axis is also a scale depicting the general availability of various MOS and CMOS processes. The ongoing migration to even finer lithography will thus enable the rapid development of CMOS-based imagers having even higher resolution, better image quality, higher levels of integration and lower overall imaging system cost than CCD-based solutions. At present, CMOS with minimum features of $\leq 0.1 \mu\text{m}$, makes possible monolithic visible CMOS imagers because the denser photolithography allows for low-noise signal extraction and high performance detection with high optical fill-factor within each pixel. The silicon wafer production infrastructure which has put high performance personal computers into many homes makes CMOS-based imaging in consumer products such as video and digital still cameras widely available.

A typical CMOS multiplexer architecture [see Fig. 26(b)] consists of fast (column) and slow (row) shift registers at the edges of the active area, and pixels are addressed one by one through the selection of a slow register, while the fast register scans through a column, and so on. Each image-sensor is connected in parallel to a storage capacitor located in the unit cell. A column of diodes and storage capacitors is selected one at a time by a digital horizontal scan register and a row bus is selected by the vertical scan register. Therefore, each pixel can be individually addressed.

CMOS-based imagers use active and passive pixels [34–36] as shown, in simplified form, in Fig. 25(b). In comparison with passive pixel sensors (PPSs), active pixel sensors (APSs) apart from read functions exploit some form of amplification at each pixel. The PPS consists of three transistors: a reset FET, a selective switch, and a source follower (SF) for driving the signal onto the column bus. As a result, circuit overhead is low and the optical collection efficiency [fill factor (FF)] is high even for monolithic devices. Microlenses, typically used in CCD and CMOS APS imagers for visible application, concentrate the incoming light into the photosensitive region when they are accurately deposited over each pixel (see Fig. 27). In the case of the per-pixel electronics, the area available in the pixel for the detector is reduced, so fill factor is often limited to 30 to 60%. When the FF is low and microlenses are not used, the light falling elsewhere is either lost or, in some cases, creates artifacts in the imagery by generating electrical currents in the active circuitry. Unfortunately micro-lenses are less effective when used in low $F/\#$ imaging systems, and may not be appropriate for all applications.

In the APS three of the metal-oxide-semiconductor field-effect transistors (MOSFETs) have the same function as in PPS. The fourth transistor works as a transfer gate that moves charge from the photodiode to the floating diffusion. Usually, both pixels operate in rolling shutter mode. The APS is capable of performing correlated double sampling (CDS) to eliminate the reset noise (kTC noise) and the pixel offsets. The PPS can only be used with noncorrelated double sampling, which is sufficient to reduce the pixel-to-pixel offsets but does not eliminate the temporal noise (temporal noise can be addressed by other methods like soft reset or tapered reset). Adding these components, however, reduces the FF of monolithic imagers to about 30–50% in $0.5\text{-}\mu\text{m}$ processes at a $5\text{--}6\text{-}\mu\text{m}$ pixel pitch or in $0.25\text{-}\mu\text{m}$ processes at a $3.3\text{--}4.0\text{-}\mu\text{m}$ pixel pitch [37]. The MOSFETs incorporated in each

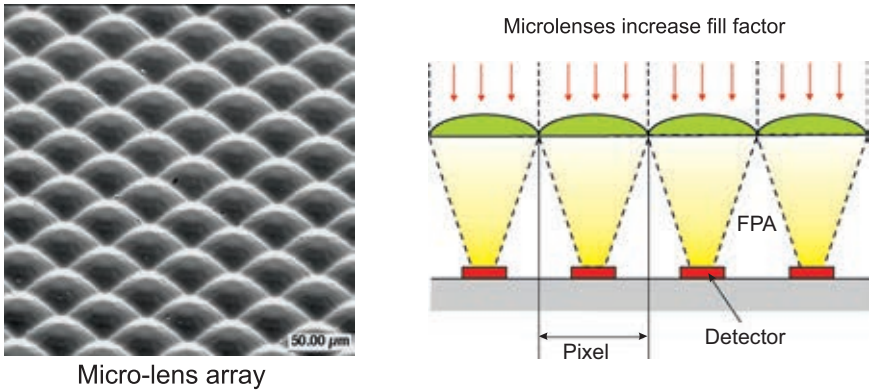


Fig. 27. Micrograph and cross-sectional drawing of microlensed FPA.

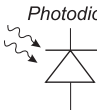
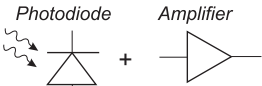
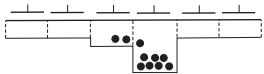
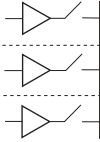
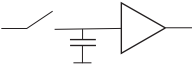
	CCD approach	CMOS approach
Pixel	<div>Photodiode</div>  <div>Charge generation and charge integration</div>	<div>Photodiode + Amplifier</div>  <div>Charge generation, charge integration and charge-to-voltage conversion</div>
Array readout	 <div>Charge transfer from pixel to pixel</div>	 <div>Multiplexing of pixel voltages: Successively connect amplifiers to common bus</div>
Sensor output	 <div>Output amplifier performs charge-to-voltage conversion</div>	<div>Various options possible:</div> <ul style="list-style-type: none">- no further circuitry (analog out)- add. amplifiers (analog output)- A/D conversion (digital output)

Fig. 28. Comparison between the CCD-based and CMOS-based image sensor approach (after Ref. [36]).

pixel for readout are optically dead. CMOS sensors also require several metal layers to interconnect MOSFETs. The busses are stacked and interleaved above the pixel, producing an “optical tunnel” through which incoming photons must pass. In addition, most CMOS imagers are front side illuminated. This limits the visible sensitivity in the red because of a relatively shallow absorption material. For comparison, CCD pixels are constructed so that the entire pixel is sensitive, with a 100% FF.

To increase a number of transistors into a small area of a pixel, a more deeply scaled CMOS processes are used [7]. However, these processes have limitations, such as

maximum voltages limited to 1- to 2-volts for 34- to 180-nm processes, which adversely affect imager performance by reducing the dynamic range of the imager.

Fig. 28 compares the principle of CCDs and CMOS sensors. Both detector technologies use a photosensor to generate and separate the charges in the pixel. Beyond that, however, the two sensor schemes differ significantly. During CCD readout, the collected charge is shifted from pixel to pixel all the way to the perimeter. Finally, all charges are sequentially pushed to one common location (floating diffusion), and a single amplifier generates the corresponding output voltages. On the other hand, CMOS detectors have an independent amplifier in each pixel (APS). The amplifier converts the integrated charge into a voltage and thus eliminates the need to transfer charge from pixel to pixel. The voltages are multiplexed onto a common bus line using integrated CMOS switches. Analog and digital sensor outputs are possible by implementing either a video output amplifier or an analog-to-digital (A/D) converter on the chip.

The processing technology for CMOS is typically two to three times less complex than standard CCD technology. In comparison with CCDs, the CMOS multiplexers exhibit important advantages due to high circuit density, fewer drive voltages, fewer clocks, much lower voltages (low power consumption) and packing density compatible with many more special functions, lower cost for both digital video and still camera applications. The minimum theoretical read noise of a CCD is limited in large imagers by the output amplifier's thermal noise after CDS is applied in off-chip support circuits. The alternative CMOS paradigm offers lower temporal noise because the relevant noise bandwidth is fundamentally several orders of magnitude smaller and better matches the signal bandwidth. While CCD sensitivity is constrained by the limited design space involving the sense node and the output buffer, CMOS sensitivity is limited only by the desired dynamic range and operating voltage. CMOS-based imagers also offer practical advantages with respect to on-chip integration of camera functions including command and control electronics, digitisation and image processing. CMOS is now suitable also for TDI-type multiplexers because of the availability from foundries of design rules lower than 1.0 μm , more uniform electrical characteristics and lower noise figures.

4.2. Hybrid arrays

In the case of hybrid technology (see Fig. 29), we can optimize the detector material and multiplexer independently. Other advantages of hybrid-packaged FPAs are near-100% fill factors and increased signal-processing area on the multiplexer chip. Photodiodes with their very low power dissipation, inherently high impedance, negligible $1/f$ noise, and easy multiplexing via the ROIC, can be assembled in 2-D arrays containing a very large number of pixels, limited only by existing technologies. Photodiodes can be reverse-biased for even higher impedance, and can therefore better match electrically with compact low-noise silicon readout preamplifier circuits. The photo-response of photodiodes remains linear for significantly higher photon flux levels than that of photoconductors, primarily because of higher doping levels in the photodiode absorber layer and because the photogenerated carriers are collected rapidly by the junction.

Development of hybrid packaging technology began in the late 1970s [38] and took the next decade to reach volume production. In the early 1990s, fully 2-D imaging arrays provided a means for staring sensor systems to enter the production stage. In the hybrid architecture, indium bump bonding with readout electronics provides for multiplexing the

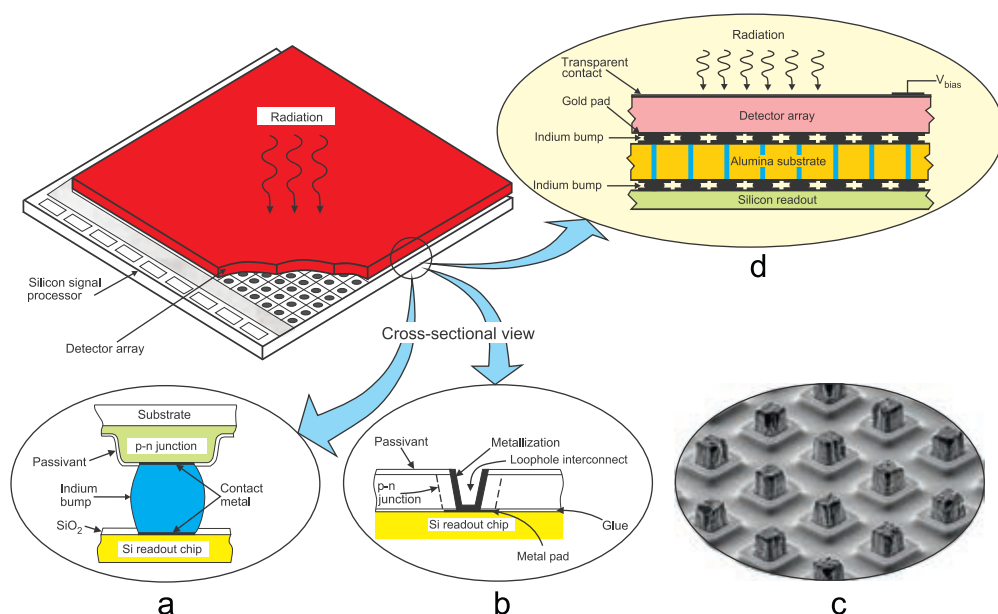


Fig. 29. Hybrid IR FPA interconnect techniques between a detector array and silicon multiplexer: (a) indium bump technique, (b) loophole technique, (c) SEM photo shows mesa photodiode array with indium bumps, and (d) layered-hybrid design suitable for large format far IR and sub-mm arrays.

signals from thousands or millions of pixels onto a few output lines, greatly simplifying the interface between the vacuum-enclosed cryogenic sensor and the system electronics.

4.2.1. Interconnect techniques

Different hybridization approaches are in use today. The most popular is flip-chip interconnect using bump bond [see Fig. 29(a) and (c)]. In this approach, indium bumps are formed on both the detector array and the ROIC chip. The array and the ROIC are aligned and force is applied to cause the indium bumps to cold-weld together. In the other approach, indium bumps are formed only on the ROIC; the detector array is brought into alignment and proximity with the ROIC, the temperature is raised to cause the indium to melt, and contact is made by reflow.

Infrared hybrid FPA detectors and multiplexers are also fabricated using loophole interconnection—see Fig. 29(b) [39]. In this case, the detector and the multiplexer chips are glued together to form a single chip before detector fabrication. The photovoltaic detector is formed by ion implantation and loopholes are drilled by ion-milling and electrical interconnection between each detector and its corresponding input circuit is made through a small hole formed in each detector. The junctions are connected down to the silicon circuit by cutting the fine, few μm in diameter holes through the junctions by ion milling, and then backfilling the holes with metallization. A similar type of hybrid technology called VIPTM (vertically integrated photodiode) was reported by DRS Infrared Technologies (former Texas Instruments) [40].

It is difficult to make small pixel pitches (below 10 μm) using bump-bonding interconnect technique, especially when high yield and 100% pixel operability are required. A new facility

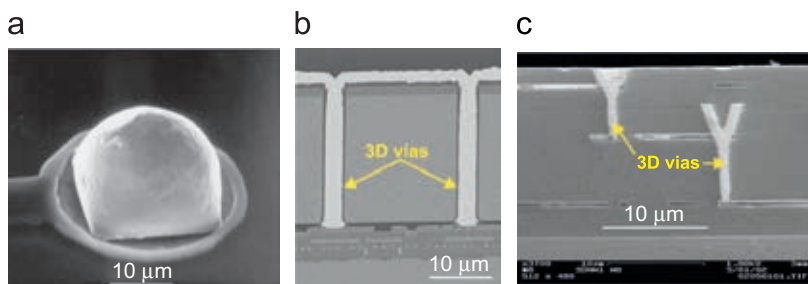


Fig. 30. Approaches to 3-D integration: (a) bump bond used to flip-chip interconnect two circuit layers, (b) two-layer stack with insulated vias through thinned bulk Si, (c) two-layer stack using Lincoln's SOI-based vias (after Ref. [41]).

gives 3-D integration process using wafer bonding, where such materials as Si and InP have been monolithically integrated with pixels size down to $6\ \mu\text{m}$ [7,41,42]. Fig. 30 compares three methods of vertically interconnect circuit layers: (a) bump bond, (b) insulated through-silicon vias, and (c) Lincoln Laboratory's SOI based via. The Lincoln integration method enables the dense vertical interconnection of multiple circuit layers and is capable of achieving far smaller pixel sizes than possible with bump bonding.

The detector array can be illuminated from either the frontside (with the photons passing through the transparent silicon multiplexer) or backside (with photons passing through the transparent detector array substrate). In general, the latter approach is most advantageous, as the multiplexer will typically have areas of metallization and other opaque regions, which can reduce the effective optical area of the structure. The epoxy is flowed into the space between the readout and the detectors to increase the bonding strength. In the case of backside detector illumination, a transparent substrates are required. When using opaque materials, substrates must be thinned to below $10\ \mu\text{m}$ to obtain sufficient quantum efficiencies and reduce crosstalk. In some cases the substrates are completely removed. In the “direct” backside illuminated configuration both the detector array and the silicon ROIC chip are bump mounted side-by-side onto a common circuit board. The “indirect” configuration allows the unit cell area in the silicon ROIC to be larger than the detector area and is usually used for small scanning FPAs, where stray capacitance is not an issue.

Readout circuit wafers are processed in standard commercial foundries and can be constrained in size by the die-size limits of the photolithography step and repeat printers. Because of field size limitations in those photography systems, CMOS imager chip sizes must currently be limited to standard lithographic field sizes of less than $32 \times 22\ \text{mm}$ for submicron lithography. To build larger sensor arrays, a new photolithographic technique called *stitching* can be used to fabricate detector arrays larger than the reticle field of photolithographic steppers. The large array is divided into smaller subblocks. Later, the complete sensor chips are stitched together from the building blocks in the reticle as shown in Fig. 31. Each block can be photocomposed on the wafer by multiple exposures at appropriate locations. Single blocks of the detector array are exposed at one time, as the optical system allows shuttering, or selectively exposing only a desired section of the reticle.

It should be noted that stitching creates a seamless detector array, as opposed to an assembly of closely butted sub-arrays [43,44]. The butting technique is commonly used in

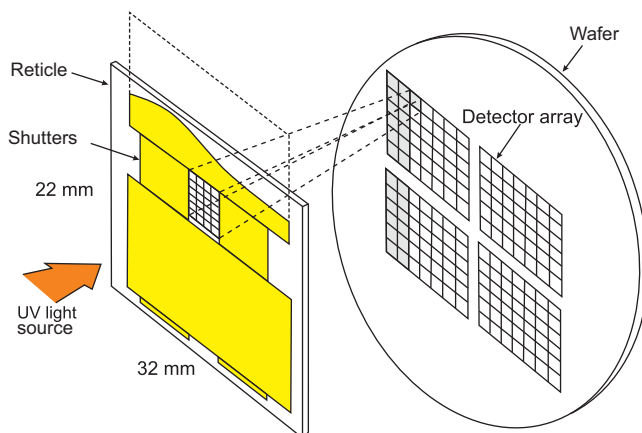


Fig. 31. The photocomposition of a detector array die using array stitching based on photolithographic stepper.

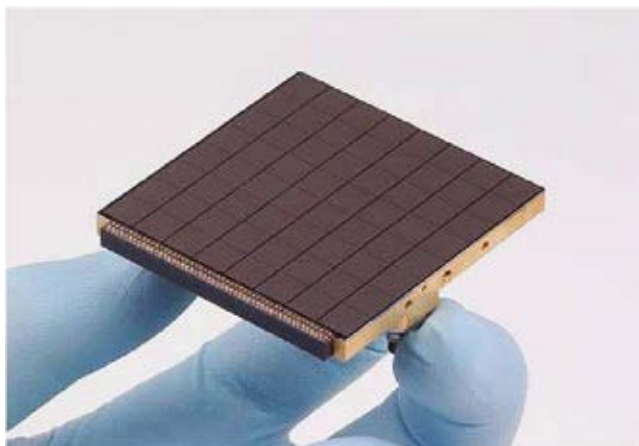


Fig. 32. One of the 64 orthogonal transfer array (OTA) devices used in PanSTARRS camera. The OTA consists of an 8×8 array of 600×600 CCD devices, each of which can be controlled and read out independently (after Ref. [44]).

the fabrication of very large format sensor arrays due to the limited size of substrate wafers. For example, the 1.4 gigapixel (Gpixel) orthogonal transfer array (OTA) CCD imager (spread over an area about 40 cm^2) used in Panoramic Survey Telescope And Rapid Response System (PanSTARRS) is comprised of 64 chips, each of 22 megapixels (Mpixels). Fig. 32 shows one of the 64 OTA devices. This above 1 gigapixel imager could not be made monolithically since it exceeds the size of the largest silicon wafers used by the IC industry. Currently silicon wafer sizes do not exceed the 300-mm diameter although the silicon integrated circuit industry is actively exploring a transition to 450 mm diameter wafers. Due to both cost and technological reasons, many imaging chips are made typically using process technologies being run on 200-mm diameter wafers. Gaps between are reduced to as little as a few tens of micrometers, especially for monolithic technologies. In the future, greater use of 4-side buttable designs is expected.

Key to the development of ROICs has been the evolution in input preamplifier technology. This evolution has been driven by increased performance requirements and silicon processing technology improvements. A discussion of the various circuits is given e.g., in Refs. [5,33,45–47].

The direct injection (DI) circuit was one of the first integrated readout preamplifiers and has been used as an input to CCDs and visible imagers for many years. The direct injection is also commonly used input circuit for infrared tactical applications, where the backgrounds are high and detector resistances are moderate. The goal is to fit as large a capacitor as possible into the unit cell, where signal-to-noise ratios can be obtained through longer integration times.

The DI circuit is widely used for simplicity; however, it requires a high impedance detector interface and is not generally used for low IR backgrounds due to injection efficiency issues. Many times the strategic applications have low backgrounds and require low noise multiplexers interfaced to high resistance detectors. A commonly used input circuit for strategic applications is the capacitive transimpedance amplification (CTIA) input circuit.

Besides the DI and CTIA inputs mentioned above, we can distinguish other multiplexers; the most important are: source follower per detector (SFD), buffered direct injection (BDI), and gate modulation input (GMI) circuits. Table 4 provides a description of the advantages and disadvantages of DI, CTIA and SFD circuit. As is mentioned above, the DI circuit is used in higher-flux situations. The CTIA is more complex and higher power but is extremely linear. The SFD is most commonly used in large-format hybrid astronomy arrays as well as commercial monolithic CMOS cameras.

The development of FPAs using IC techniques together with development of new material growth techniques and microelectronic innovations began about 40 years ago. The combination of the last two techniques gives many new possibilities for imaging

Table 4
Comparison of attributes of the three most common input circuits (after Ref. [41]).

Circuit	Advantages	Disadvantages	Comments
Direct injection (DI)	Large well capacity Gain determined by ROIC design (C_{int}) Detector bias remains constant Low FET glow Low power	Poor performance at low flux	Standard circuit for high flux
Capacitance transimpedance amplifier (CTIA)	Very linear Gain determined by ROIC design (C_f) Detector bias remains constant	More complex circuit FET glow Higher power	Very high gains demonstrated
Source follower per detector (SFD)	Simple Low noise Low FET glow Low power	Gain fixed by detector and ROIC input capacitance Detector bias changes during integration Some nonlinearity	Most common circuit in IR astronomy

systems with increased sensitivity and spatial resolution. Moreover, a number of other important advantages are accrued in terms of simplicity, reliability and reduced costs. Fifteen years ago, high quality single element IR detectors often were priced over \$2000, but now some current IR FPA production costs are less than \$0.1 per detector, and even greater reductions are expected in the near future. As the commercial market for uncooled imagers expand, the cost of commercial systems will inevitably decrease. At present, the cost of 320×240 bolometer arrays for thermal imagers is below \$5 000.

4.3. Performance of focal plane arrays

Imaging system specifications partially depend on their applications. Because the array is the basic building block of the imaging system, so imaging system terminology is often used for array specifications.

Different array parameters are determined. The most common are read noise, charge well capacity, and responsivity. Having these parameters the minimum and maximum signals, signal-to-noise ratio, and dynamic range can be calculated. However, full characterization includes quantifying the various noise sources, spectral quantum efficiency, linearity, and pixel nonuniformity (in the case of CCD devices—also charge transfer efficiency).

For IR imaging systems, the relevant figure of merit for determining the ultimate performance is not the detectivity, D^* , but the noise equivalent difference temperature (*NEDT*) and the minimum resolvable difference temperature (*MRDT*). There are considered the primary performance metrics to thermal imaging systems: thermal sensitivity and spatial resolution. Thermal sensitivity is concerned with the minimum temperature difference that can be discerned above the noise level. The *MRDT* concerns the spatial resolution and answers on question—how small an object can be imaged by the system? The general approach of system performance is given by Lloyd in his fundamental monograph [48]. In spite of its widespread use in infrared literature, *NEDT* is applied to different systems, in different conditions, and with different meanings [49].

NEDT of a detector represents the temperature change, for incident radiation, that gives an output signal equal to the rms noise level. While normally thought of as a system parameter, detector *NEDT* and system *NEDT* are the same except for system losses. *NEDT* is defined

$$NEDT = \frac{V_n(\partial T / \partial Q)}{(\partial V_s / \partial Q)} = V_n \frac{\Delta T}{\Delta V_s}, \quad (10)$$

where V_n is the rms noise, Q is the spectral photon flux density (photons/cm²/s) incident on a focal plane, and ΔV_s is the signal measured for the temperature difference ΔT .

Usually, the performance of MW and LWIR FPAs is limited by the readout circuits (by storage capacity of the ROIC). In this case [47]

$$NEDT = \left(\tau C \eta \sqrt{N_w} \right)^{-1}, \quad (11)$$

where N_w is the number of photogenerated carriers integrated for one integration time, t_{int}

$$N_w = \eta A_d t_{\text{int}} Q_B. \quad (12)$$

It results from the above formulas that the charge handling capacity of the readout, the integration time linked to the frame time, and dark current of the sensitive material become the major issues of IR FPAs. The *NEDT* is inversely proportional to the square root of the integrated charge and therefore the greater the charge, the higher the performance. The well charge capacity is the maximum amount of the charge that can be stored in the storage capacitor of each cell. The size of the unit cell is limited to the dimensions of the detector element in the array.

These considerations are valid assuming that the temporal noise of the detector is the main source of noise. However, this assertion is not true to staring arrays, where the nonuniformity of the detectors response is a significant source of noise. This nonuniformity appears as a fixed pattern noise (spatial noise). It is defined in various ways in the literature, however, the most common definition is that it is the dark signal nonuniformity arising from electronic source (i.e., other than thermal generation of the dark current); e.g., clock breakthrough or from offset variations in row, column or pixel amplifiers/switches. So, estimation of IR sensor performance must include a treatment of spatial noise that occurs when FPA nonuniformities cannot be compensated correctly.

Mooney et al. [50] have given a comprehensive discussion of the origin of spatial noise. The total noise of a staring arrays is the composite of the temporal noise and the spatial noise. The spatial noise is the residual nonuniformity u after application of nonuniformity compensation, multiplied by the signal electrons N . Photon noise, equal $N^{1/2}$, is the dominant temporal noise for the high IR background signals for which spatial noise is significant. Then, the total *NEDT* is

$$NEDT_{\text{total}} = \frac{(N + u^2 N^2)^{1/2}}{\partial N / \partial T} = \frac{(1/N + u^2)^{1/2}}{(1/N)(\partial N / \partial T)} \quad (13)$$

where $\partial N / \partial T$ is the signal change for a 1 K source temperature change. The denominator, $(\partial N / \partial T) / N$, is the fractional signal change for a 1 K source temperature change. This is the relative scene contrast.

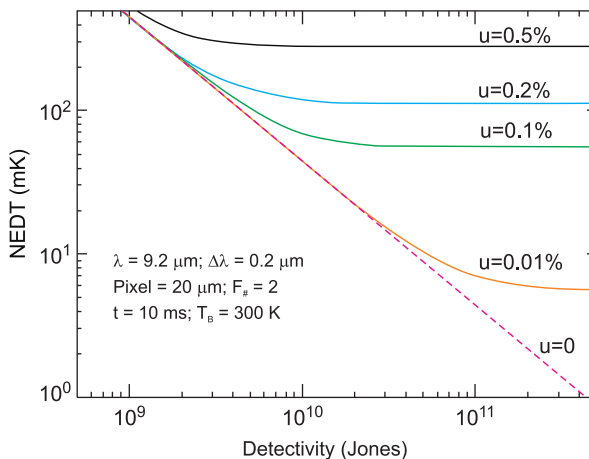


Fig. 33. *NEDT* as a function of detectivity. The effects of nonuniformity are included for $u=0.01\%$, 0.1% , 0.2% and 0.5% . Note that for $D^* > 10^{10} \text{ cm Hz}^{1/2}/\text{W}$, detectivity is not the relevant figure of merit.

The dependence of the total *NEDT* on detectivity for different residual nonuniformity is plotted in Fig. 33 for 300 K scene temperature and set of parameters shown insert the figure. When the detectivity is approaching a value above $10^{10} \text{ cm Hz}^{1/2}/\text{W}$, the FPA performance is uniformity limited prior to correction and thus essentially independent of the detectivity. An improvement in nonuniformity from 0.1% to 0.01% after correction could lower the *NEDT* from 63 to 6.3 mK.

5. X-ray detector arrays

In the course of the past hundred years the X-ray detection has migrated from film to digital cameras for dental and medical applications. Several classes of X-ray sensor arrays have been developed including [2]:

- phosphors,
- scintillators,
- microchannel plates,
- silicon detector arrays (CCD and CMOS devices, hybrid p–i–n structures, thin film silicon panels), and
- CdZnTe hybrid detector arrays.

5.1. Phosphors, scintillators, and microchannel plates

Phosphors absorb X-ray photons and emit visible photons as a result of returning of the excited electrons in the material to their ground state. Phosphors are generally used in a thin film layer of polycrystalline material and hence provide excellent spatial resolution, but absorb X-rays relatively weakly. Usually, phosphors were combined with photographic films, but today they can be combined with a visible detector array to improve an X-ray detective system.

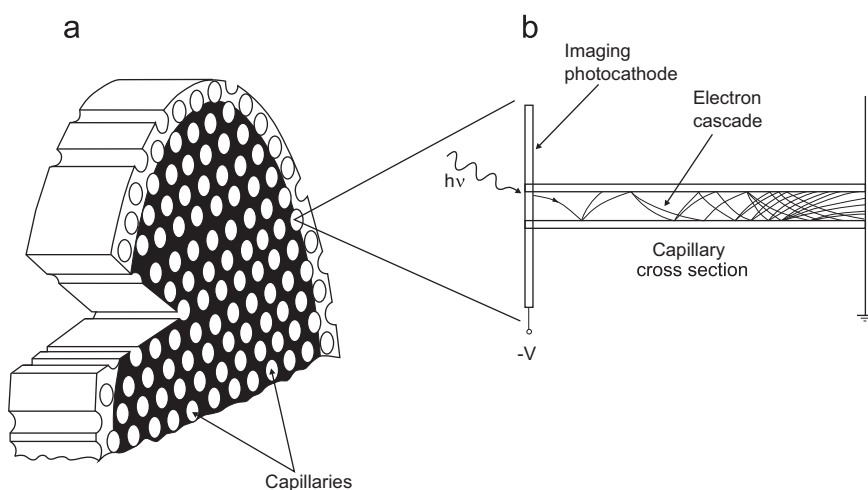


Fig. 34. Schematic cutaway view of microchannel plate (a) and a single capillary (b) in a multichannel plate.

Also scintillator crystals convert X-ray photons to visible light. To maximize the density of available electrons to interact with X-rays, large and optically transparent single crystals of high-Z materials are used. Examples include the alkali halide materials (NaI and CsI is doped with small amounts of Tl) and more dense with higher stopping power BGO ($\text{Bi}_4\text{Ge}_3\text{O}_{12}$) crystals [51]. The alkali halide are typically 5-mm thick to absorb incident energies from 20 to 100 keV with conversion efficiency (the fraction of X-ray energy converted to visible light) around 10%. Scintillators are combined with a visible detector array.

The microchannel plate (MCP) is a disk consisting of millions of micro glass tubes (channels) fused in parallel with each other (see Fig. 34). The channels made of combination of oxides of silicon, lead, and alkali compounds in mixture are used to obtain design resistivity in the approximate range of 10^{10} – $10^{15} \Omega \text{ cm}^2$. Each channel acts as an independent electron multiplier. Its diameter is typically $10 \mu\text{m}$ and length of 0.5 mm and then is possible incorporate 3 million of them in a 25 mm plate. They are operated at approximately 1 kV with a typical amplification of 3000. The electron gain of the channel depends on the applied voltage, the ratio of the channel length to the diameter and the secondary emission characteristics of the channel surface. The gain up to 10^8 for 3 keV applied field is achieved. Quantum efficiency can vary considerably from as low as 1% to as high as 60%. It depends upon energy, angle of incidence, and coating of the channel walls and channel entrance. The MCP offers faster time response; temporal resolution is 10^{-10} s under favourable conditions. It also features good immunity from magnetic fields and 2-D detection ability when multiple anodes are used.

MCP arrays are used in the UV and visible spectral regions as well as for X-rays. An X-ray-sensitive MCP is illustrated in Fig. 35(a), which is used in the high-resolution camera on board the Advanced X-ray Astrophysics Facility (AXAF) satellite renamed Chandra after its 1999 launch. It is the most sophisticated X-ray observatory built to date. As we can see in the figure, two MCP stages amplify the electron stream which is collected by a crossed grid of wires connected to charge-sensitive amplifiers. Each of two MCPs consist of a 10-cm square cluster of 69 million tiny lead-oxide glass tubes that are about $10 \mu\text{m}$ in diameter (1/8 the thickness of a human hair) and 1.2 mm long. Fig. 35(b) shows another instruments installed in Chandra satellite—the advanced CCD imaging spectrometer (ACIS) used for studying the temperature variation across X-ray sources such as vast clouds of hot gas in intergalactic space.

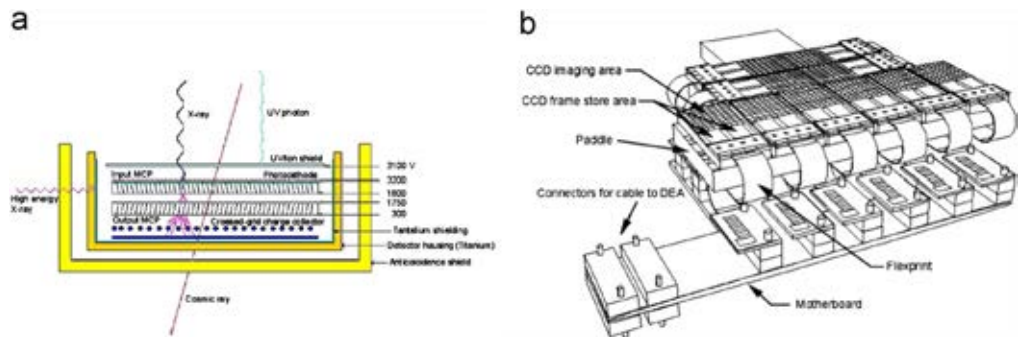


Fig. 35. Science instruments on the Advanced X-ray Astrophysics Facility (AXAF) satellite renamed Chandra: (a) a diagram of MCP detector in the high resolution camera (HRC) and (b) a diagram of the Chandra advanced CCD imaging spectrometer (ACIS) (after Ref. [52]).

5.2. Direct and indirect X-ray detection

There are two primary X-ray imaging technologies in use today: direct and indirect detections. Their schematic designs are shown in Fig. 36(a). The most common method, the indirect detection uses scintillators to convert X-Rays to visible light. CCD devices were the first detectors introduced in radiology approximately 40 years ago. Since traditionally CCDs are physically much smaller than the image area, so the light generated by the scintillator is imaged onto a CCD sensor using a bulky lens system which is some kind of optics reducing the size of the image. However, this optical system reduces the number of photons that reaches the CCD and moreover, geometric distortions and light scatter are another consequence of the use of optical reduction. As a result, the CCD-based indirect X-ray detectors are bulky and not flat-panel detectors, what is their most important inconvenience. This drawback of CCD-based indirect system is successively omitted due to development of large format CCDs.

In indirect conversion thin-film transistor (TFT)-based detectors X-ray photons are converted into visible light in the scintillator layer. A photodiode converts the visible light into electrical charges which the TFT array reads out row after row.

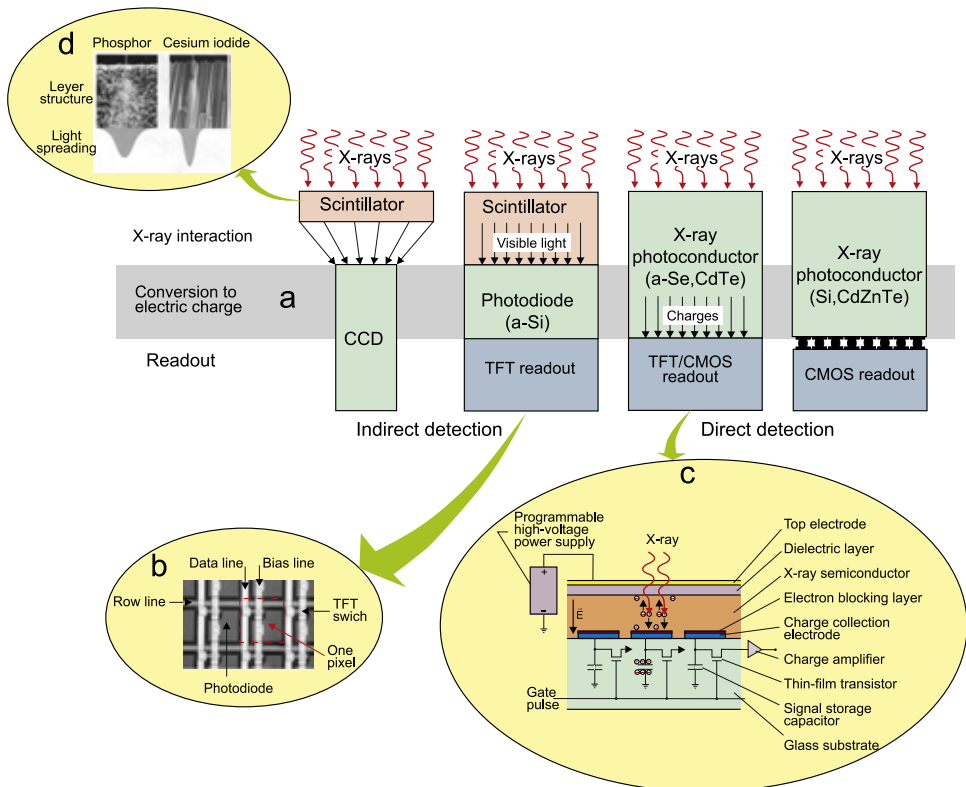


Fig. 36. Direct and indirect X-ray detection: (a) different types of X-ray image systems, (b) pixel structure of indirect conversion imager, (c) operative design of direct conversion detector used in flat-panel imagers, and (d) light diffusion in phosphor and CsI.

One potential inconvenience of transforming X-rays into visible light is that lateral diffusion of the light [see Fig. 36(d)] reduces sharpness and spatial resolution of the image. To overcome this problem, some indirect conversion detectors use structured scintillators, consisting of CsI crystals that are grown perpendicularly to the detector surface with diameter of approximately 5–10 μm . A column like structure significantly reduce lateral diffusion of the scintillator light, much like fiber optics. The reduction of light diffusion in turn allows to use thicker scintillator layers, thus increasing the detective quantum efficiency of the detector system.

Direct conversion is used in flat-panel detectors and in recently developed hybrid arrays with CMOS readout. Flat-panel detectors usually use an amorphous selenium (a-Se) layer to convert X-ray photons directly to electrons for immediate image capture. The generated charge migrates to the pixel electrode in accordance with the polarity of the bias being applied to the X-ray photodetector, and is stored in a storage capacitor within the TFT array [see Fig. 36(c)]. By subsequently scanning the TFTs line by line, the charge information stored in the storage capacitors can be read out from the data bus lines. The data bus line terminations connect to a charge amplifiers and A/D converters, and the scanned charge information is converted to digital image signals and output sequentially.

Selenium has relatively low X-ray absorption and requires about 50 electronvolts to produce a hole–electron pair. These restrict both the minimum dose needed and the size of the signal generated. In addition, an important drawback of selenium is the instability of the material over time and at elevated temperatures, as well as the environmental impact during production and repair or disposal. Other materials with lower energy requirements and higher x-ray absorption are under development.

5.3. Silicon detector arrays

Between different silicon detector arrays in the X-ray region the most important are CCD and CMOS devices. Many manufactures offer indirect detectors working with different scintillators and coupling fibre-optics to CCD and CMOS imagers. Large, buttable CMOS tiles are assembled into panels of size more than 30×24 cm with less than one pixel spacing in between individual sensors. For example, next two figures (Figs. 37 and 38) show large CCD and CMOS arrays fabricated by Simens and Teledyne Dalsa.

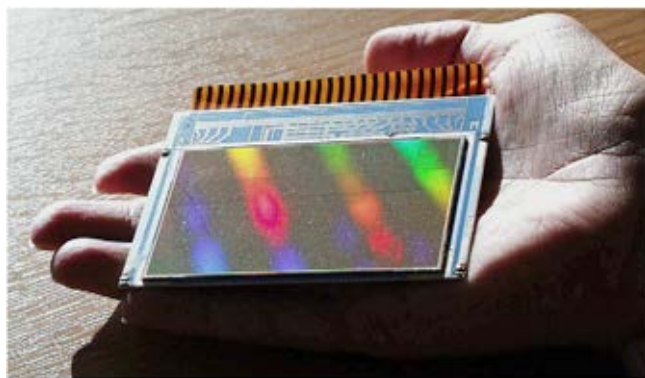


Fig. 37. Very high spatial resolution Simens CCD X-ray matrix with $4k \times 4k$ pixels, pixel size 12 μm , total area 49×86 mm.

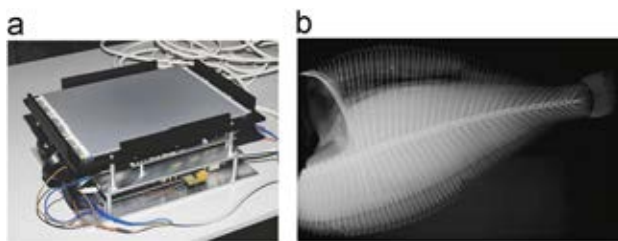


Fig. 38. 3-side buttable CMOS APS Dalsa mammography image sensor with the final 232×290 mm detector comprises 2×3 butted CMOS tiles with $33.55 \times 33.55 \mu\text{m}$ pixel pitch, total 60 megapixels: (a) sensor assembly with a fibre optic plate+scintillator, and (b) “first patient result” obtained on a total detector (after Ref. [53]).

CCD detectors are susceptible to radiation damage and failure when operated for extended periods in space environments. The main reason of that is CCD surface inversion from accumulated surface charge build up. The advantages of CMOS in comparison to CCD include programmable readout modes, faster readout, lower power, radiation hardness, and the ability to put specialized processing within each pixel.

CMOS imagers are growing in popularity for many small area imaging applications. These include medical imaging in the fields of dental, extremities imaging, veterinary and industrial X-ray applications. The main advantage of CMOS imagers over a-Si flat-panel imagers is higher read out speed. The electron mobility in crystalline silicon is about $1400 \text{ cm}^2/\text{Vs}$ while it is less than $1 \text{ cm}^2/\text{Vs}$ in amorphous silicon, what limits readout speed of imaging pixels. For comparison a 2000×3000 pixel a-Si based array can be read out about 3 times in a second, the same size CMOS array can be read out about 30 times [54]. The 10 times faster speed is especially useful for the high resolution computer tomography (CT). The second advantage of CMOS imagers is their low noise especially in comparison with large flat-panel detectors. CMOS circuitry eliminates influence of noise because each pixel contains an active circuit. This low noise provides a huge advantage at low X-ray dose imaging, such as low dose CT application.

Thin-film silicon panels are usually used for medical imaging when a very large area and high-resolution arrays are needed. Usually, as an active material the thin-film of amorphous silicon is deposited on a substrate using chemical vapour deposition (CVD) method. Each pixel of the array, photolithographically processed, consists of a photodiode and an addressable switch to read out the photocurrent [see Fig. 36(a,b)].

In modern flat-panel detectors, the scintillator output is captured by either an amorphous silicon TFT panel or CMOS sensor which convert the image to digital format. For example, this second solution is used by Dexela. The Dexela CMOS image sensor consists of a photodiode array with a pixel size of $75\text{-}\mu\text{m}$. The detector is capable of multi-resolution readout with pixels binned 1×2 , 2×2 , 1×4 , 2×4 and 4×4 . A highly modular technology platform allows produce detectors of different dimensions with sizes up to $35 \times 29 \text{ cm}$ [55].

To convert incident X-rays to visible light, a scintillating material such as $\text{Gd}_2\text{O}_2\text{S:Tb}$ is deposited in proximity over the amorphous silicon array [56,57]. Fig. 39 shows X-ray images taken with this panel. Typical X-ray sensitivity converts the 40- to 150-keV range.

Unfortunately, the X-ray absorption of a-Si is very low so the photodiode needs to be 10 to 20 mm thick. Fabricating such devices of amorphous silicon is not feasible.

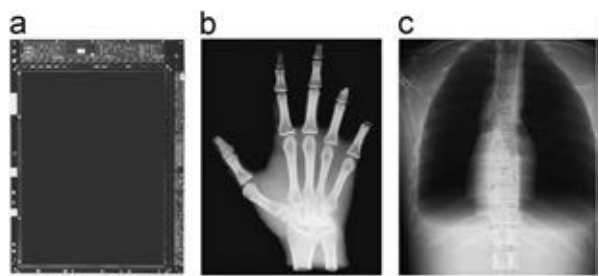


Fig. 39. High-resolution a-Si flat-panel X-ray medical image sensor: (a) a view of 2304 × 3200 pixel array module with a 30 × 40 cm active area (127-μm pixel size, fill factor 57%) connected to gate and data boards bonded to the glass, which is mounted on an aluminium backing plate, (b) a digital X-ray image of a human hand phantom, and (c) a digital X-ray image of a human chest phantom (after Ref. [57]).

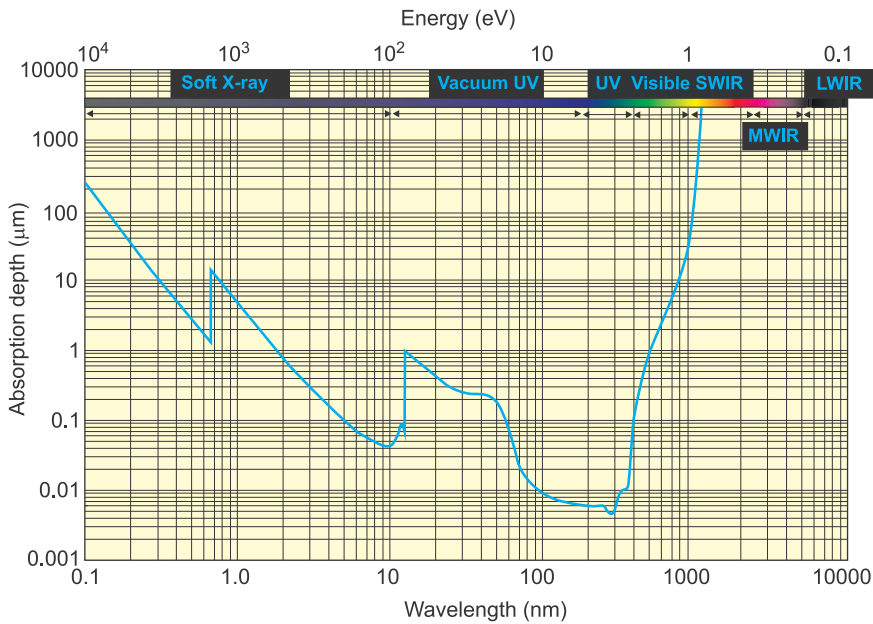


Fig. 40. Absorption depth of photons in silicon as a function of the wavelengths and energy from UV to NIR (after Ref. [58]).

Photoconductive materials with higher X-ray absorption than silicon can be coated on an array of conductive charge collection plates each supplied with a storage capacitor.

Crystalline silicon is an excellent material for direct detection for photons from soft X-ray to the silicon cutoff wavelength in the near infrared (NIR). Due to different absorption mechanisms (see Fig. 40), 5–10 keV X-rays and 850–1000 nm NIR light have a long absorption length in silicon (20–200 μm); while low energy X-rays and UV light are absorbed within 10 to 40 nm of the silicon surface. So, a low loss surface region is required to provide a good response to low energy X-ray photons (< 500 eV).

It appears that hybrid structures with readouts compatible with silicon p–i–n diodes can be hardened to very high radiation doses, and the p–i–n devices itself is also quite resistant

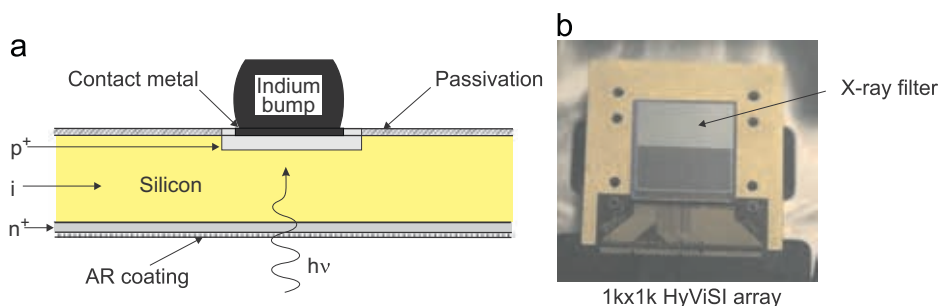


Fig. 41. Hybrid silicon p–i–n photodiode X-ray arrays: (a) cross-section of p–i–n photodiode, and (b) photo of a 1024×1024 pixel HyViSI array with 50 nm Al blocking filter covering half of the active area of the detector surface (after Ref. [59]).

to radiation damage [2]. Fig. 41(a) shows silicon p–i–n diodes fabricated in a lightly doped silicon wafer with a common back electrode and an array of the opposite doping type on the front side. Metal contacts are made to the front-side p^+ -doped regions. These devices give relatively good energy resolution since the total thickness of i-region is fully depleted and all the absorbed charge in the active region is efficiently collected.

Teledyne Imaging Sensors has produced large array hybrid silicon p–i–n CMOS sensors with > 99.9% operability, called HyViSITM, which provide high quantum efficiency for the X-ray through NIR spectral range. The thickness of detectors is between 50 and 250 μm . For X-ray astronomy applications, a 50-nm thick Al optical blocking filter with nearly 100% transmission of X-rays is typically used to decrease the influence of optical light on a noise level. Fig. 41(b) shows a 1024×1024 18- μm /pixel array with a 50-nm thick Al blocking filter covering half of the active area of the detector surface.

5.4. CdZnTe hybrid array

Despite the excellent energy resolution and charge-transport properties of Si and Ge detectors, their low stopping power for high energy photons limits their application to hard X-ray and gamma-ray detection. The room-temperature semiconductors with high atomic numbers and wide band gaps have long been under development. The great potential of these compounds has not been exploited for many decades due mainly to the limited commercial availability of high-quality crystals [60–62]. This situation has changed dramatically during the last decade of XX century with the emergence of a few companies committed to the advancement and commercialization of these materials. Table 5 reports the physical properties of the most common compound semiconductors typically used for radiation detection.

Over the last decade, cadmium telluride (CdTe) and cadmium zinc telluride (CdZnTe) wide band gap semiconductors have become established as perhaps the most suitable materials for the detection of X-rays and gamma-rays. Discrete detectors and arrays fabricated from $\text{Cd}_{1-x}\text{Zn}_x\text{Te}$ (where $x=0.08\text{--}0.3$) are becoming more widely used to detect nuclear radiation in medicine, industry and scientific research. Devices fabricated from the most common detector material, germanium, offer high resolution but require liquid nitrogen cooling. Although NaI(Tl) scintillators do not require cooling, they suffer from low resolution compared to CdZnTe, and are bulky. NaI(Tl) relies on secondary detection;

Table 5
Properties of semiconductors at room temperature (after Ref. [62]).

Material	Si	Ge	GaAs	CdTe	Cd _{0.9} Zn _{0.1} Te	HgI ₂	TlBr
Crystal structure	Cubic	Cubic	Cubic(ZnS)	Cubic(ZnS)	Cubic(ZnS)	Tetragonal	Cubic(CsCl)
Growth method*	C	C	CVD	THM	HPB, THM	VAM	BM
Atomic number	14	32	31, 33	48, 52	48, 30, 52	80, 53	81, 35
Density (g/cm ³)	2.33	5.33	5.32	6.2	5.78	6.4	7.56
Band gap (eV)	1.12	0.67	1.43	1.44	1.57	2.13	2.68
Pair creation energy (eV)	3.62	2.96	4.2	4.43	4.6	4.2	6.5
Resistivity (Ω cm)	10 ⁴	50	10 ⁷	10 ⁹	10 ¹⁰	10 ¹³	10 ¹²
μ _e τ _e (cm ² /V)	> 1	> 1	10 ^{−5}	10 ^{−3}	10 ^{−3} –10 ^{−2}	10 ^{−4}	10 ^{−5}
μ _h τ _h (cm ² /V)	~1	> 1	10 ^{−6}	10 ^{−4}	10 ^{−5}	10 ^{−5}	10 ^{−6}

*The more common growth methods: C=Czochralski, CVD=chemical vapour deposition, THM=travelling heater method, BM=Bridgman method, HPB=high-pressure Bridgman, and VAM=vertical ampoule method.

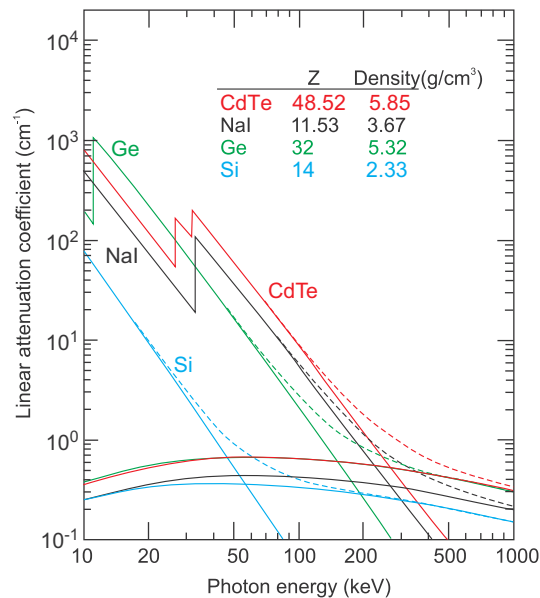


Fig. 42. Linear attenuation coefficients for photoabsorption and Compton scattering in CdTe, Si, Ge, and NaI(Tl) (after Ref. [63]).

photons hit the scintillator, producing light, which is in turn detected by visible detector array. In contrast, photons reaching the CdZnTe detector are directly converted into an electrical signal, which is then amplified by standard electronic circuitry. The relatively high density (5.78 g/cm³) of CdZnTe provides good absorption efficiency. As shown in Fig. 42 [63], CdTe has a high photoelectric attenuation coefficient. Photoelectric absorption is the main process up to 300 keV for CdTe, as compared to 60 keV for Si and 150 keV for Ge. The higher resistivity of CdZnTe (around $3 \times 10^{10} \Omega \text{ cm}$) results in low leakage currents in photovoltaic devices (MSM devices and p–n junctions), and also

allows the use of higher bias voltage. In turn, this improves the charge-collection efficiency and allows the fabrication of large volume detectors.

The current developments in large area/volume CdZnTe detectors and the common constraints on their design are summarized in Refs. [60–62]. The CdZnTe crystals used in fabrication of hybrid focal plane arrays are grown using modified standard or vertical furnaces by the high pressure of inert gas inside the crucible. Generally, compound semiconductors are characterized by poor charge transport properties due to charge trapping—the hole and electron mobility lifetime products ($\mu_e\tau_e$ and $\mu_h\tau_h$) are key parameters in the development of radiation detectors (see Table 5). However, the relatively high mobility and lifetime of the charge carriers in CdZnTe crystals, particularly those of electrons, allows the transport of the carriers through the whole depleted volume of mm- and cm-thick devices with minimum trapping loss.

An example of a CdZnTe X-ray detector structure is shown in Fig. 43. This radiation imaging digital technology combines a dedicated direct conversion detector substrate connected via micro bumps to a dedicated CMOS readout substrate. As an active material, lightly doped, high-resistivity material is used. To solve the problem of forming ohmic contacts to CdZnTe wide-band gap material, the narrower-band-gap both p- and n-type HgCdTe epitaxial layers are used.

Different pixel sizes are used in hybrid CdZnTe/CMOS imaging sensors. For high spatial image resolution the pixel size is typically 50 μm —see Fig. 44(a). Such arrays can yield very high quality, digital X-ray images of small objects. In Ajat solution [see Fig. 44(b)], many hundreds of mega bytes of image information at high frame rate (up to 300 images per second) is reconstructed to the panoramic layer by intensive post acquisition computing like a computed tomography.

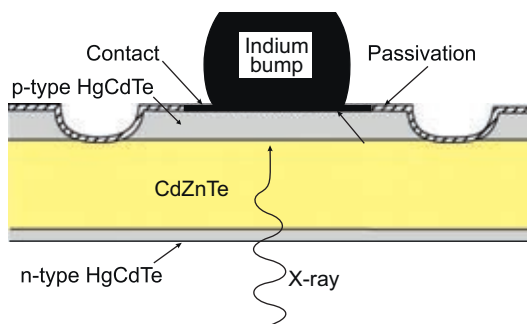


Fig. 43. CdZnTe X-ray detector structure (after Ref. [2]).

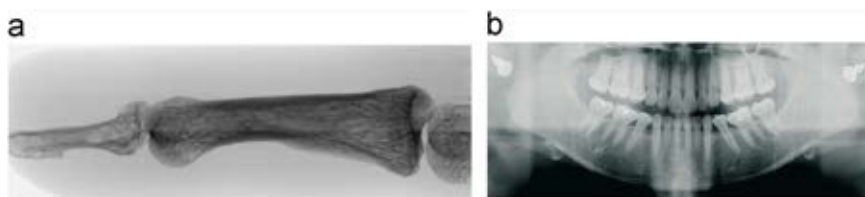


Fig. 44. Digital CdZnTe/CMOS X-ray images: (a) of a human finger phantom taken with a CdZnTe array (192 \times 340 pixels with 50- μm size and 0.15-mm thick CdZnTe detector) (after Ref. [64]) and (b) dental panoramic image (after Ref. [65]).

6. Ultraviolet detector arrays

Ultraviolet (UV) detection technology is classified into two major categories. In the first group a photoemissive device (photocathode) is combined with a gain component, usually with microchannel plate (MCP) [66–68]. The second group consists of solid-state devices based on silicon (CCD and CMOS) or hybrid structure wide bandgap semiconductor-based detectors such as AlGa_N and SiC.

Ternary AlGa_N alloys are excellent photocathode materials due to their low electron affinity, chemical stability and direct bandgap. The quantum efficiency of planar cesiated p-type opaque photocathodes reach 70–80% at 122 nm and steady decline to 10–20% near 360 nm what represents significant improvements over conventional CsI and CsTe photocathodes—see Fig. 45 [69]. Cesium photocathodes are limited to windowed detectors with wavelengths > 105 nm and require sealed tubes to retain the Cs.

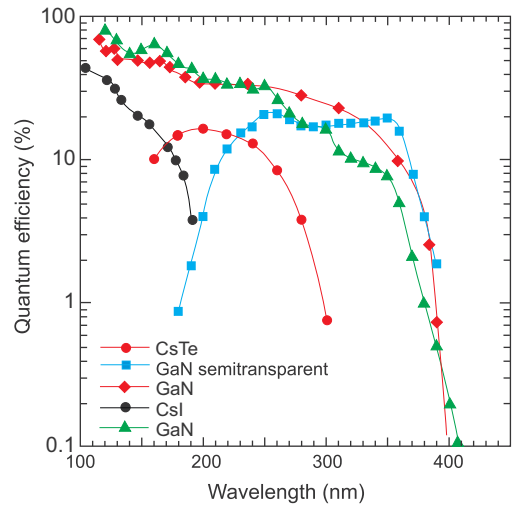


Fig. 45. Quantum efficiencies as a function of wavelength for several photocathodes (after Ref. [69]).

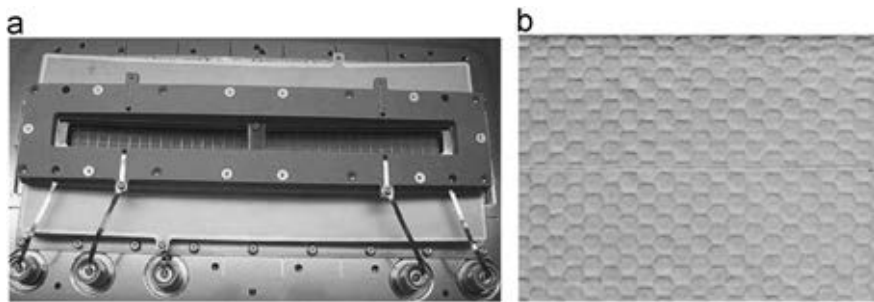


Fig. 46. COS-HST detector: (a) head of detector with two abutting MCP detector segments (each 85 × 10 mm) curved to the focal plane of the spectrograph (after Ref. [68]; (b) flat field image of a 10 × 13 mm area of the MCP detector, the fibre bundles imprint an obvious fixed-pattern noise features in the image (after Ref. [69]).

Improvements of MCP devices have been made in spatial resolution, dynamic range, detector size, quantum efficiency and background together with decreasing the power and mass required to achieve these goals. Especially, there are significant challenges in the implementation of detectors on astrophysics instruments. For example, the Cosmic Origins Spectrograph (COS), installed on the Hubble Space Telescope (HST) in May 2009, contains two segments of far-UV MCP detector, each 85×10 mm active area, separated by 9 mm, and curved to a focal plane of 0.6 m radius for the Rowland circle [see Fig. 46(a)]. The COS detector has a spatial resolution of $\sim 25 \mu\text{m}$ with electronic sub-resolution sampling using a cross delay line readout anode. Encouraging progress has been made on reduction fixed-pattern noise introduced at the “dead zones” at the boundaries of the MCP fibre bundles [see Fig. 46(b)].

With the emergence of photolithographic silicon based microchannel plates and large format high resolution position sensing readouts, considerable progress has been made towards the next generation of microchannel plate detectors. Silicon based MCPs have qualities that make them preferable to glass MCPs (very low intrinsic background, low fixed pattern noise). The fabrication has been scaled to 4” wafers (Fig. 47) so larger MCPs are possible.

Ultraviolet (UV) solid-state imagers are most commonly built with a hybrid structure. An example is $\text{Al}_x\text{Ga}_{1-x}\text{N}$ (AlGaIn) material sensitive to UV radiation while being insensitive to longer wavelength radiation [70–73]. Such devices have applications where there is a need to detect or control the source of UV radiation in an existing background of visible or infrared radiation. Examples of such applications include flame detection, furnace and engine monitoring for the automotive, aerospace and petroleum industry, undersea communications, UV astronomy, space-to-space communications secure from Earth, early missile threat warning and airborne UV countermeasures, and portable battlefield reagent/chemical analysis system. Because of their theoretical intrinsic solar blindness and low dark currents, III-Nitride based devices are expected to work without optical filters and complex electronics, thus significantly reducing the launch weight for space and airborne applications. The goal of this development is to achieve “solar blind” spectral response of 280 nm because ozone in the atmosphere absorbs nearly all sunlight shorter than this wavelength.

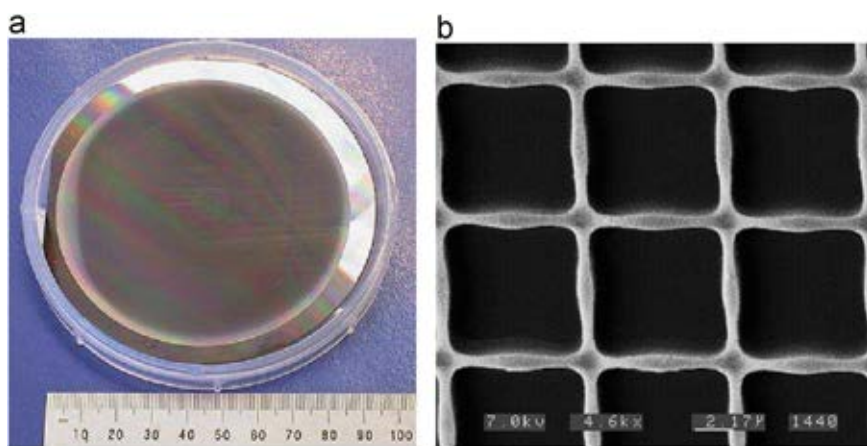


Fig. 47. Silicon MCP detector: (a) produced on 10-cm wafer, and (b) square pore 7- μm pores (after Ref. [66]).

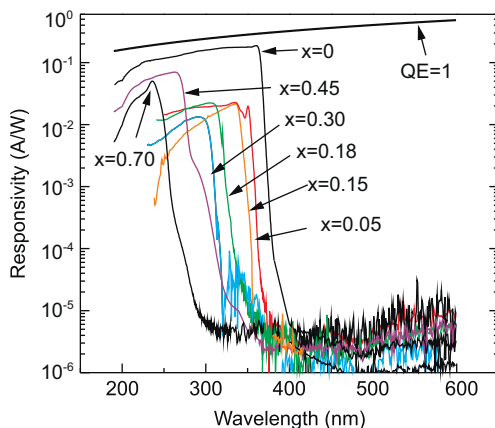


Fig. 48. Responsivity of $\text{Al}_x\text{Ga}_{1-x}\text{N}$ p-i-n photodiodes showing a cut-off wavelength continuously tuneable from 227 to 365 nm, corresponding to an Al concentration in the range 0–70% (after Ref. [73]).

There are different types of AlGaN detectors including photoconductors, MSM diodes, Schottky barrier and p-i-n photodiodes. Most of the research on UV photodetectors has recently been directed toward the demonstration of AlGaN based p-i-n junction photodiodes, which present the capability of tailoring the cut-off wavelength by controlling the alloy composition and thus the bandgap energy of the active layer. A full range of $\text{Al}_x\text{Ga}_{1-x}\text{N}$ p-i-n photodiodes has been demonstrated with a cut-off wavelength continuously tuneable from 227 to 365 nm, corresponding to an Al concentration in the range 0–70%. This can be seen in Fig. 48 where the current responsivity of these detectors at room temperature is shown. Their internal quantum efficiencies were up to 86% when operated in photovoltaic mode (i.e., at zero bias) and they exhibited an UV-to-visible rejection ratio as high as six orders of magnitude. At shorter wavelengths, the penetration depth decrease and the detection of charge carriers is decreased by processes such as surface recombination and photoemission losses. In addition to these front-side illuminated devices, backside illuminated AlGaN UV photodiodes have also recently been reported using sapphire substrates, which are UV transparent. Sapphire has only a moderate thermal coefficient of expansion mismatch with silicon readouts.

Hybrid AlGaN FPAs have been produced by several groups, e.g., with 256×256 pixels [74,75] and 320×256 pixels [76–79]. These devices employ deposition of the array structure on a transparent substrate and illumination from the back side (back-illumination) through the substrate. However, for shorter wavelengths than the transmission cut-off of the substrate material, e.g., in the vacuum UV (VUV) front-side illumination of the device is required. Further in the extreme UV (EUV) below ≈ 30 nm, the back-side illumination is again possible with a device that is back-side thinned (e.g., removing the Si substrate [80]; sapphire absorbs the low wavelengths below approximately 170 nm) making it transparent to the EUV and X-ray radiation ranges.

Fig. 49(a) shows cross section of the back-illuminated AlGaN p-i-n photodiodes [74]. The first Si-doped n-type AlGaN window bottom layer serves as the common n-side contact to all elements in the array. Its alloy composition determines the cut-on wavelength. Next the absorber layer is an unintentionally-doped (uid) n-type AlGaN, with a smaller band gap, that forms an

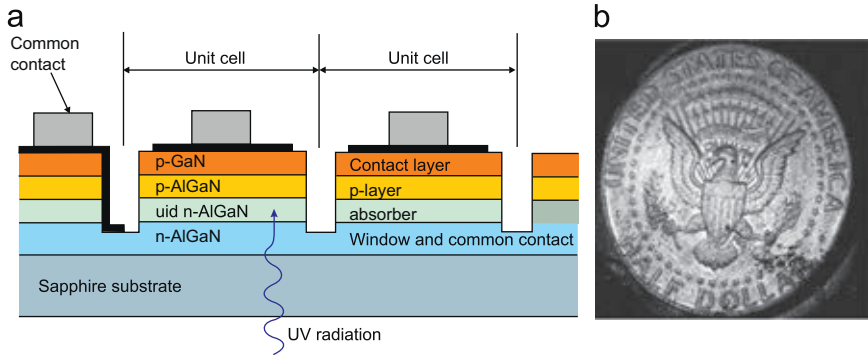


Fig. 49. Hybrid 256×256 AlGaIn p-i-n photodiode FPA with $30 \times 30\text{-}\mu\text{m}$ unit pixels: (a) cross section of the back-illuminated photodiode array, and (b) UV reflection image of a US half-dollar coin taken with this array (after Ref. [74]).

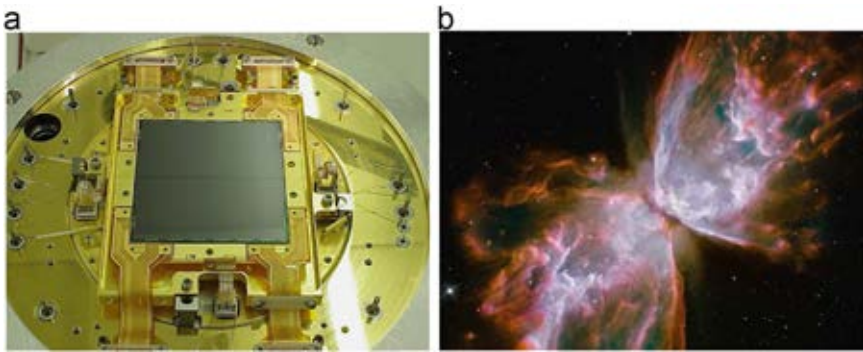


Fig. 50. The WFC3 CCD, developed by e2v (formerly Marconi): (a) mounted on its TEC cooler, (b) WFC3 butterfly emerge snapped from stellar demise in planetary Nebula NG C 6302, more popularly called the Bug Nebula or the Butterfly Nebula.

isotype n-N heterojunction with the window layer. The alloy composition of the absorber layer determines the cut-off wavelength. Next layer, a Mg-doped AlGaIn p-type layer forms a p-n homojunction with the n-type absorber layer. The final layer is a thin heavily-doped Mg-doped GaN cap layer that facilitates the p-side contact.

Fig. 49(b) shows a UV reflection image of a US half-dollar coin (3-cm diameter) taken with a 256×256 AlGaIn FPA with $30 \times 30\text{-}\mu\text{m}$ unit pixels. The UV detector array was hybridized to a BAE Systems 256×256 silicon CMOS ROIC chip with CTIA input circuits.

It should be mentioned that silicon sensor response is being extended into the UV using delta doping and antireflection coating [81]. Using molecular beam epitaxy, fully-processed thinned CCDs are modified for UV enhancement by growing 2.5-nm thick boron-doped silicon on the back surface. The sharply-spiked dopant profile in the thin epitaxial layer improves device stability and external quantum efficiency to 50–90% at wavelengths of 200–300 nm.

Fig. 50(a) shows the $4k \times 4k$ CCD array installed in Wide Field Camera 3 (WFC3) on the Hubble Space Telescope (HST) that covers the near-UV and near-IR wavelength ranges. This array has readnoise level of $< 3e^-$ and quantum efficiency of 30–60% between 200 and 300 nm [82]. WFC3 was installed by NASA astronauts in May 2009, during the Servicing Mission to upgrade and repair the 19-year-old Hubble. An image taken by the WFC3 is shown in Fig. 50(b).

In comparison with existing silicon based technology, the wide-bandgap semiconductors are significantly more radiation tolerant. Apart from AlGaIn, other material systems such as SiC, MgZnO and diamond are good candidates to compete with silicon. Photodetectors based on diamond material have recently progressed due to success in producing high-quality thin films with sufficiently low defects and concentrations of n-type and p-type dopants [83]. The first two types of diamond detectors showing high responsivity around 200 nm, p–i–n photodiode and MSM detector [84], are flown on a space mission in the solar XUV-VUV radiometer LYRA (Large Yield Radiometer) aboard the PROBA-2 satellite.

7. Visible detector arrays

Silicon is the semiconductor that has dominated the electronic industry for over 40 years. While the first transistor fabricated in Ge and III–V semiconductor material compounds may have higher mobilities, higher saturation velocities, or larger bandgaps, silicon devices account for over 97% of all microelectronics [85]. The main reason is that silicon is the cheapest microelectronic technology for integrated circuits. The reason for the dominance of silicon can be traced to a number of natural properties of silicon but more importantly, two insulators of silicon, SiO₂ and Si₃N₄, allow deposition and selective etching processes to be developed with exceptionally high uniformity and yield.

Photodetectors are perhaps the oldest and best understood silicon photonic devices [86]. Silicon photodiodes are widely applied in spectral range below 1.1 μm and even are used for X-ray and gamma ray detectors. The main types are as followed:

- p–n junctions generally formed by diffusion (ion implantation is also used),
- p–i–n junctions (because of thicker active region, they have enhanced near-IR spectral response),

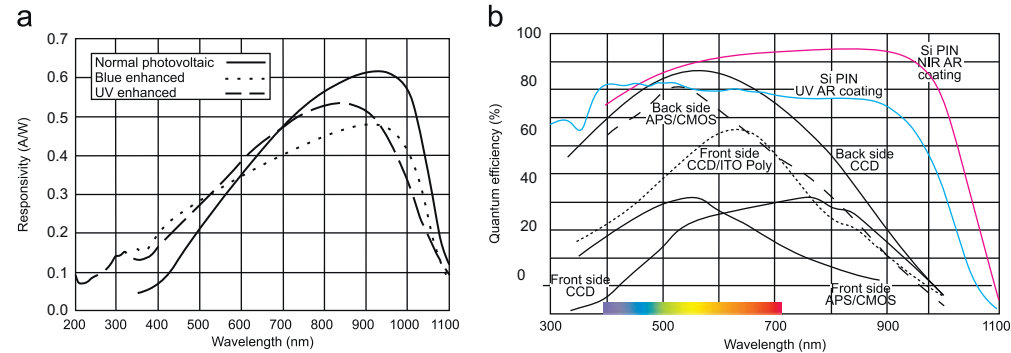


Fig. 51. Silicon photodetectors: (a) typical current responsivity of several different types of planar diffused silicon photodiodes (after Ref. [87]), and (b) quantum efficiency comparison of different technologies.

- UV- and blue-enhanced photodiodes, and
- avalanche photodiodes.

Typical spectral characteristics of planar diffusion photodiodes are shown in Fig. 51(a). The time constant of p–n junction silicon photodiodes is generally limited by RC constant rather than by the inherent speed of the detection mechanism (drift and/or diffusion) and is on the order of microsecond. Detectivity is typically between mid- 10^{12} and 10^{13} cm Hz^{1/2}/W usually amplifier-limited for small area detectors.

The p–i–n detector is faster but is also less sensitive than conventional p–n junction detector and has slightly extended red response. It is a consequence of extension of the depletion layer width, since longer wavelength photons will be absorbed in the active device region. Incorporation of a very lightly doped region between the p and n regions and a modest reverse bias form a depletion region the full thickness of the material (≈ 500 μ m for a typical silicon wafer). Higher dark current collected from generation within the wider depletion layer results in lower sensitivity.

High absorption coefficient of silicon in the blue and UV spectral regions causes generation of carriers within the heavily doped p⁺ (or n⁺) contact surface of p–n and p–i–n photodiodes, where the lifetime is short due to the high and/or surface recombination. As a result, the quantum efficiency degrades rapidly in these regions. Blue- and UV-enhanced photodiodes optimize the response at short wavelengths by minimizing near-surface carrier recombination. This is achieved by using very thin and highly graded p⁺ (or n⁺ or metal Schottky) contacts, by using lateral collection to minimize the percentage of the surface area which is heavily doped, and/or passivating the surface with a fixed surface charge to repel minority carriers from the surface.

The avalanche photodiodes are especially useful where both fast response and high sensitivity are required. An optimum gain exists below which system is limited by receiver noise and above which shot noise dominates receiver noise and the overall noise increases faster than the signal. Noise is a function of detector area and increases as gain increases. Typical detectivity is $(3\text{--}5) \times 10^{14}$ cm Hz^{1/2}/W.

Visible imaging sensors use three basic architectures:

- Monolithic CCD (both front side and back side illuminated),
- Monolithic CMOS, for which the photodiodes are included within the silicon readout integrated circuit (ROIC),
- Hybrid CMOS that uses a detector layer for detection of light and collection of photocharge into pixels and a CMOS ROIC for signal amplification and readout.

At present two monolithic technologies provide the bulk of devices in the markets of camcorders and digital cameras: CCD and CMOS imagers. The fundamental performance parameters common to both CCD and CMOS imagers have been compared by Janesick [88,89]. Compared to CCD, CMOS performance is currently preventing the technology from scientific and high end use.

Monolithic imaging FPAs for the visible spectrum began in the early 1970s. Further development is shown in Fig. 52, where the trend in image sensor migration of CCD and CMOS devices for various market applications is presented [90]. CCDs dominate in high

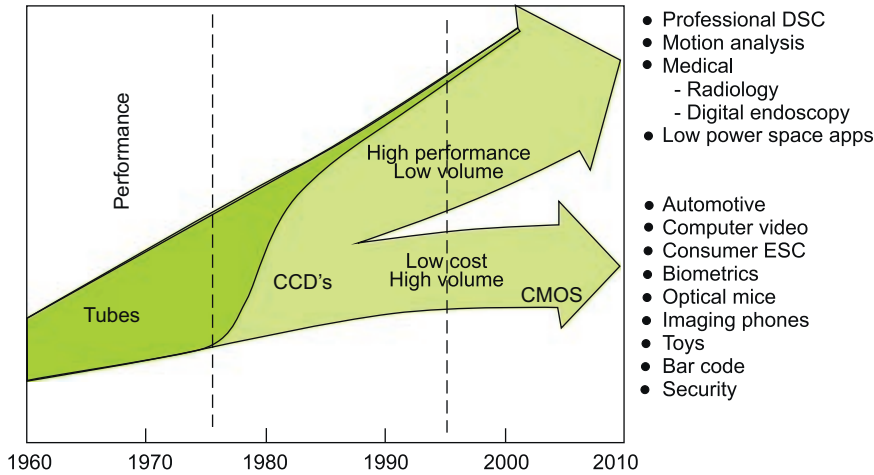


Fig. 52. Trend in image sensor migration of CCD and CMOS devices for various market applications (after Ref. [90]).

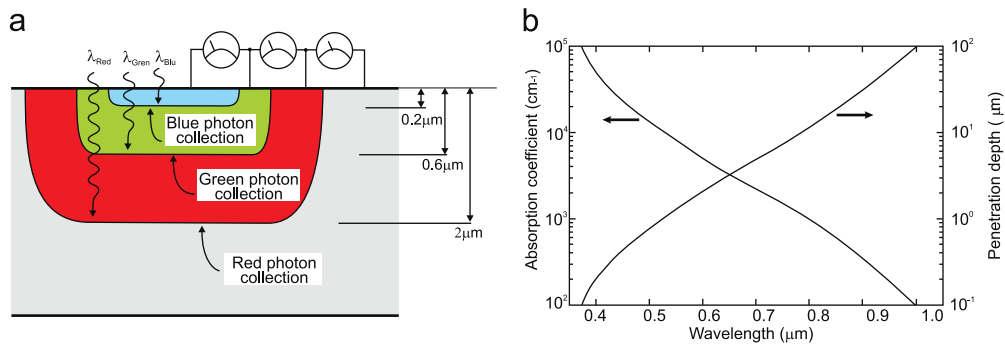


Fig. 53. Schematic illustration of Foveon's sensor stack: (a) cross section of the sensor, (b) absorption coefficient and penetration depth in silicon (after Ref. [92]).

performance, low-volume segments, such as professional digital still cameras, machine vision, medical, and scientific applications. However, due to low power consumption; ability to integrate timing, control, and other signal processing circuitry on chip; and single supply and master clock operation, CMOS emerges the winner in low-cost, high-volume applications, particularly where low power consumption and small system size are key. The majority of growth comes from new products enabled by CMOS imaging technology, such as automotive, computer video, optical mice, imaging phones, toys, biometrics, and a host of hybrid products.

Digital CCD silicon image sensors were developed approximately 30 years ago, ushering in the era of digital photography. In visible imaging CCD arrays integrate the readout and sensor in a combined pixel and an integrated red-green-blue (RGB) colour filters are included. The most common checkerboard filter pattern dedicates 2 out of 4 pixels to green, and 1 pixel each to red and blue. As a result, the sensor gathers only 50% of the green light, and 25% of the red and blue. Digital post-processing interpolates to fill in the

blanks, so more than half of the image is artificially generated and innately imperfect. In this case the fill factor is only a fraction of the pixel area; e.g., about 70% [91]. Unfortunately, the rich, warm tones and detail of colour film that the world came to expect suffered over the convenience and immediacy of digital. This was due to the fact that CCD digital image sensors were only capable of recording just one colour at each point in the captured image instead of the full range of colours at each location.

Foveon has introduced an innovative design of visible image sensor [91]. This is accomplished by X3 direct image sensors which have three layers of pixels, just like film has three layers of chemical emulsion (see Fig. 53) [92]. This silicon sensor is fabricated on a standard CMOS processing line. Foveon's layers are embedded in silicon to take advantage of the fact that red, green, and blue light penetrate silicon to different depths (the photodetectors sensitive to blue light are on top, the green sensitive detectors are in the middle, and the red on the bottom) forming the image sensor that captures full colour at every point in the captured image. This is 100% full colour with no interpolation. Fig. 53 plots the absorption coefficient as a function of depth, which is an exponential function of depth for any wavelength. Since the higher energy photons interact more strongly, they have a smaller space constant, and thus the exponential falloff with depth is more rapid.

Recently, the Sigma Corporation has fabricated the new SIGMA SD1 Digital SLR Camera, incorporating a 46 megapixel ($4800 \times 3200 \times 3$ layers) 24×16 mm APS-C X3 image sensor [93]. This camera ensures the high resolution images which are processed quickly with high definition and a smooth and subtle graduation of colour.

Today, CMOS image sensors are the dominant imaging device, having overtaken CCDs a few years ago [94]. CMOS devices do not employ pixel-to-pixel charge transfer cross the detector area as CCDs do, so they are inherently more radiation tolerant. The megapixel race has pushed manufacturers towards a continuous decrease in pixel size, the image sensor equivalent of the well-known Moore's law. It has been recognized that the smallest pixel available in a specific technology lies between 10 and 20 times the minimum feature

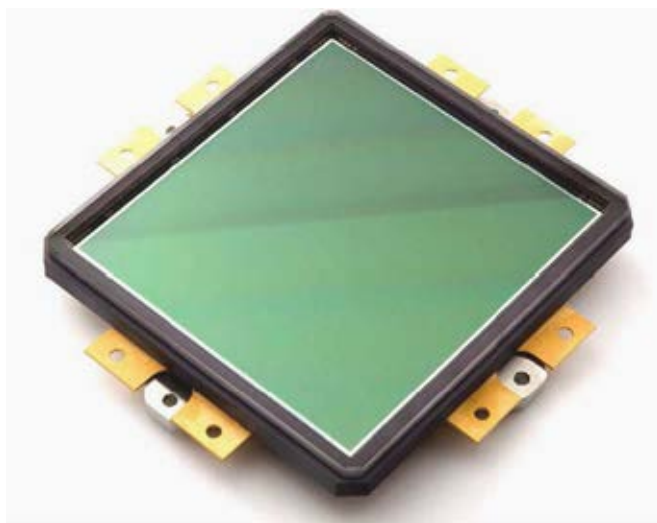


Fig. 54. DALSA 252 megapixel CCD-array with 17216×14656 pixels (96.4×82.1 mm) with $5.6 \mu\text{m}$ size (after Ref. [96]).

size of that technology node [95] and their size is in the micron range, with some examples below $1\ \mu\text{m}$. In general, systems operating at shorter wavelengths are more likely to benefit from small pixel sizes because of the smaller diffraction-limited spot size.

CCD for scientific applications are routinely made with pixel counts exceeding 20 megapixels and the trend to ever larger single chips will continue. Visible 50 megapixel arrays are now available with digital outputs having ROIC noise levels of less than 10 electrons and offering a sensitivity advantage over consumer products. At present, the largest single chip CCD arrays exceed 100 megapixels. DALSA announces that it has successfully produced a 252 megapixel CCD (see Fig. 54). The active area measures approximately 4×4 inches and 17216×14656 pixels with $5.6\ \mu\text{m}$ size [96]. The record-breaking chip are developed for the astronomy applications to assist them in the determination of the positions and motions of stars, solar system objects, and the establishment of celestial reference frames. The large CCD sensors are now starting to be produced in large quantities to meet the demands of astronomers. In particular, recent development of but table CCD arrays could be of considerable interest to the photogrammetric and remote sensing communities.

The development of mosaics of area arrays to produce large format (above 1 gigapixel) frame image is an intriguing idea [97]. One of them, the 1.4 gigapixel CCD imager used in PanSTARRS is comprised of 60 chips, each of 22 megapixel (see Fig. 32). An another example is a wide area persistent surveillance program such as the Autonomous Real-time Ground Ubiquitous Surveillance—Imaging System (ARGUS-IS) [98], where extremely large mosaics of visible FPAs is used (see Fig. 55). The 1.8 gigapixel video sensor produces more than 27 gigapixels per second running at a frame rate of 15 Hz. The airborne processing subsystem is modular and scalable providing more than 10 teraops of processing.

Another milestone step in the development of large CCD arrays is Gaia camera for space mission. Gaia, funded by ESA with EADS Astrium as the prime contractor, is an



Fig. 55. Sample of ARGUS-IS imagery. Mounted under a YEH-60B helicopter at 17,500 ft. over Quantico, Va., Argus-IS images an area more than 4 km wide and provides multiple 640×480 -pixel real-time video windows (after Ref. [7]).

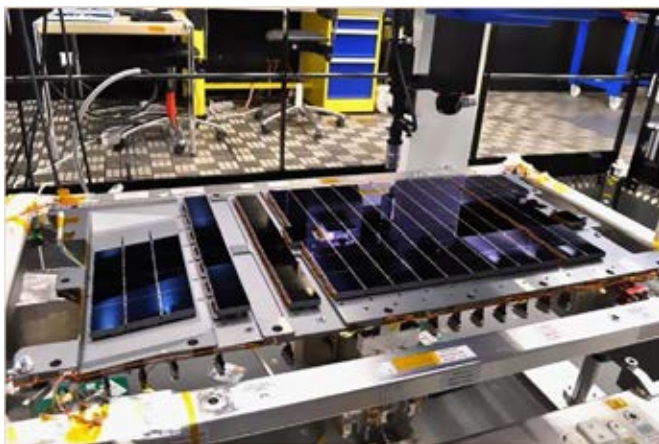


Fig. 56. The photo, taken at the Astrium France facility in Toulouse, shows the complete set of 106 CCDs that make up Gaia's focal plane. The CCDs are bolted to the CCD support structure (CSS). The CSS (the grey plate underneath the CCDs) weighs about 20 kg and is made of silicon carbide, a material that provides remarkable thermal and mechanical stability. The focal plane measures 1×0.5 m (after Ref. [99]).

ambitious space observatory designed to measure the positions of around one billion stars with unprecedented accuracy. In order to meet this challenge, Gaia has enlisted the services of e2v Technologies of Chelmsford, UK, the world's leading scientific CCD manufacturer. This FPA is populated with 106 back-illuminated devices, each with an active area of $45 \times 59 \text{ mm}^2$ corresponding to 4500×1966 pixels, each $10 \times 30 \text{ }\mu\text{m}^2$ in size (see Fig. 56). All of the Gaia CCDs are large area, back-illuminated, full frame devices. They all have a 4-phase electrode structure in the image section and a 2-phase structure in the readout register, leading to a single, high-performance, two-stage, buffered output node. A noise performance better than 10 electrons RMS is expected.

The Gaia telescope and camera is set for launch in 2013. The Gaia spacecraft will end up parked at the Earth-Sun L2 Lagrange point, which is a spot 1.5 million kilometers (932,057 miles) behind the earth, when viewed from the sun. Gaia will operate at a temperature of minus 115°C . This low temperature will be maintained by passive thermal control, including the cold radiator on the focal plane assembly and a giant sunshade attached to the top of the spacecraft.

Large visible light detection CCD and CMOS imagers are also fabricated by Fairchild Imaging [100] and Teledyne Imaging Sensors (TIS). TIS use both monolithic and hybrid MOS detectors [59]. These highest performance silicon-based image arrays are addressed to the astronomical community. Monolithic image sensors as large as 59 million pixels characterized by low noise (2.8 e^- readout noise) and low dark current ($<10 \text{ pA/cm}^2$ at 295 K) are being produced with $>99.9\%$ operability. Teledyne's monolithic CMOS sensors are fully digital system-on-chip, with all bias generation, clocking, and analog-to-digital conversion included with the image array.

Until recently, CMOS imagers have been at a disadvantage relative to CCDs for readout noise, since the CMOS's readout circuit is inherently higher noise than a CCD amplifier. One reason for higher noise is the capacitance of the sense node of the three transistor CMOS pixel. For a typical pixel size of $5 \text{ }\mu\text{m}$ in a $0.25 \text{ }\mu\text{m}$ CMOS image sensor process, the sense node capacitance is about 5 fF, corresponding to a responsivity of $32 \text{ }\mu\text{V/electron}$, which limits the

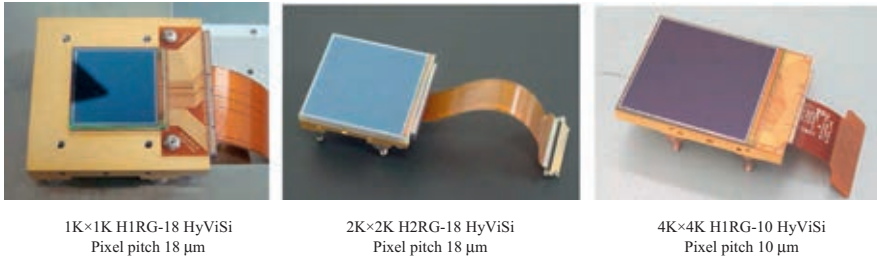


Fig. 57. Teledyne's hybrid silicon p-i-n CMOS sensors with 18- and 10- μm pixel pitch (after Ref. [59]).

lowest readout noise to about 10 electrons. With the development of the four transistor pixel, monolithic CMOS can achieve the lowest noise levels required by astronomy [59].

Visible hybrids have also been built for special applications to take advantage of the materials flexibility and larger surface area with nearly 100% fill factor [59,101]. Recently, Si p-i-n detector arrays for the astronomy and civil space communities in hybrid configuration with size as large as 4096×4096 have been demonstrated [59]. The prototype arrays demonstrated a high pixel interconnectivity ($>99.9\%$) and high pixel operability ($>99.8\%$). This design is scalable to an array format up to 16×16 K. It should be added that due to thin oxides used in fabrication of CMOS ROICs, the FPAs are inherently radiation hard and do not suffer from charge transfer inefficiency that is problematic for CCDs.

During 2007, three types of Teledyne's hybrid silicon p-i-n CMOS sensors, called HyViSiTM (H1RG-19, H2RG-18, H4RG-10; see Fig. 57), were tested on the 2.1 m telescope on Kitt Peak (Arizona) [59].

Even though silicon imagers are routinely manufactured with megapixel resolution and excellent reproducibility and uniformity, they are not sensitive to radiation longer than about $1 \mu\text{m}$. Today, SiGe alloys are widely used in Si CMOS and bipolar technologies. Recently, this technology is adopted to develop a single-chip SWIR image sensor, which integrates germanium photodetectors on a standard Si process [102].

8. Infrared detector arrays

Although efforts have been made to develop monolithic structures using a variety of infrared detector materials (including narrow-gap semiconductors) over the past 40 years, only a few have matured to a level of practical use. These included PtSi, and more recently PbS, PbTe, and uncooled silicon microbolometers. Other infrared material systems (InGaAs, InSb, HgCdTe, GaAs/AlGaAs QWIP, and extrinsic silicon) are used in hybrid configurations. Table 6 contains a description of representative IR FPAs that are commercially available as standard products and/or catalogue items from the major manufacturers.

8.1. InGaAs arrays

The need for high-speed, low-noise $\text{In}_x\text{Ga}_{1-x}\text{As}$ (InGaAs) photodetectors for use in lightwave communication systems operating in the $1\text{--}1.7 \mu\text{m}$ wavelength region ($x=0.53$) is well established. $\text{In}_{0.53}\text{Ga}_{0.47}\text{As}$ alloy is lattice matched to the InP substrate. Having lower dark current and noise than indirect-bandgap germanium, the competing near-IR material, the

Table 6
Representative IR FPAs offered by some major manufactures.

Manufacturer/Web site	Size/architecture	Pixel size (μm)	Detector material	Spectral range (μm)	Operating temperature (K)	$D^*(\lambda_p)$ ($\text{cm Hz}^{1/2}/\text{W}$) <i>NETD</i> (mK)
Goodrich Corporation http://www.sensorsinc.com	320 × 240/H	25 × 25	InGaAs	0.9–1.7	300	1×10^{13}
	640 × 512/H	25 × 25	InGaAs	0.4–1.7	300	$> 6 \times 10^{12}$
Raytheon Vision Systems http://www.raytheon.com/businesses/ncs/rvs/index.html	1,024 × 1,024/H	30 × 30	InSb	0.6–5.0	50	
	2,048 × 2,048/H(Orion II)	25 × 25	HgCdTe	0.6–5.0	32	23
	2,048 × 2,048/H(Virgo-2k)	20 × 20	HgCdTe	0.8–2.5	4–10	
Teledyne Imaging Sensors http://teledynesi.com/imaging/	2,048 × 2,048/H	15 × 15	HgCdTe/Si	3.0–5.0	78	
	1,024 × 1,024/H	25 × 25	Si:As	5–28	6.7	
Sofradir/ http://www.sofradir.com/	2,048 × 1,024/H	25 × 25	Si:As	5–28		
	4,096 × 4,096/H(H4RG)	10 × 10 or 15 × 15	HgCdTe	1.0–1.7	120	
	4,096 × 4,096/H(H4RG)	10 × 10 or 15 × 15	HgCdTe	1.0–2.5	77	
Selex http://www.selexsas.com/SelexGalileo/EN/index.sdo	4,096 × 4,096/H(H4RG)	10 × 10 or 15 × 15	HgCdTe	1.0–5.4	37	
	2,048 × 2,048/H(H2RG)	18 × 18	HgCdTe	1.0–1.7	120	
	2,048 × 2,048/H(H2RG)	18 × 18	HgCdTe	1.0–2.5	77	
	2,048 × 2,048/H(H2RG)	18 × 18	HgCdTe	1.0–5.4	37	
IAM www.aim-ir.com	1,000 × 256/H(Saturn)	30 × 30	HgCdTe	0.8–2.5	≤200	
	1,280 × 1,024/H(Jupiter)	15 × 15	HgCdTe	3.7–4.8	77–110	18
	384 × 288/H(Venus)	25 × 25	HgCdTe	7.7–9.5	77–80	17
	640 × 512/H	20 × 20	QWIP	8.0–9.0	73	31
	640 × 512/H	24 × 24	HgCdTe	MW(dual)	77–80	15–20
SCD www.scd.co.il	640 × 512/H	24 × 24	HgCdTe	MW/LW(dual)	77–80	20–25
DRS Technologies	1,024 × 768/H(Merlin)	16 × 16	HgCdTe	3–5	Up to 140	15
	640 × 512/H(Eagle)	24 × 24	HgCdTe	8–10	Up to 90	24
	640 × 512/H(CondorII)	24 × 24	HgCdTe	MW/LW(dual)	80	28/28
	640 × 512/H	24 × 24	HgCdTe	3–5		25
DRS Technologies	640 × 512/H	15 × 15	HgCdTe	8–9		40
	384 × 288/H	40 × 40	Type II SL	MW(dual)		35/25
	1280 × 1024/H	15 × 15	InSb	3–5	77	20
	2,048 × 2,048/H	18 × 18	Si:As	5–28	7.8	
	1,024 × 1,024/H	25 × 25	Si:As	5–28	7.8	
	2,048 × 2,048/H	18 × 18	Si:Sb	5–40	7.8	

H—hybrid

material is addressing both entrenched applications including low light level night vision and new applications such as remote sensing, eye-safe range finding and process control.

The InAs/GaAs ternary system bandgaps span 0.35 eV (3.5 μm) for InAs to 1.43 eV (0.87 μm) for GaAs. By changing the alloy composition of the InGaAs absorption layer, the photo detector responsivity can be maximized at the desired wavelength of the end user to enhance the signal to noise ratio. Fig. 58 shows the spectral response of three such InGaAs detectors at room temperature, whose cutoff wavelength is optimized at 1.7, 2.2 and 2.5 μm , respectively.

The spectral response of an $\text{In}_{0.53}\text{Ga}_{0.47}\text{As}$ focal plane array (FPA) to the night spectrum makes it a better choice for use in a night-vision camera in comparison with the current state-of-art technology for enhancing night vision—GaAs Gen III image-intensifier tubes. Fig. 58 also marks the key laser wavelengths.

InGaAs-detector processing technology is similar to that used with silicon, but the detector fabrication is different. The InGaAs detector’s active material is deposited onto a substrate using chloride VPE or MOCVD techniques adjusted for thickness, background doping, and other

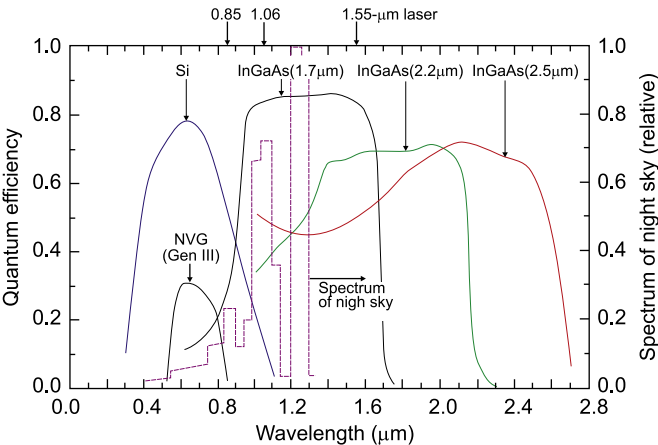


Fig. 58. Quantum efficiency of silicon, InGaAs, and night vision tube detectors in the visible and SWIR. Key laser wavelengths are also noted. $\text{In}_{0.53}\text{Ga}_{0.47}\text{As}$ photodiode has nearly three times higher quantum efficiency than GaAs Gen III photocathodes; InGaAs also overlaps the illumination spectrum of the night sky more.

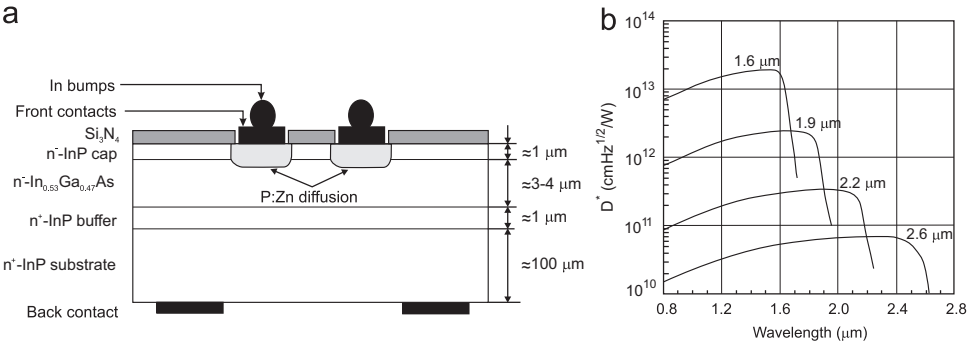


Fig. 59. InGaAs photodiodes: (a) cross section of a planar back side illuminated p-i-n InGaAs photodiode (after Ref. [103]), (b) room-temperature spectral detectivity of photodiodes with different cutoff wavelength.

requirements. Planar technology evolved from the older mesa technology and at present is widely used due to its simple structure and processing as well as the high reliability and low cost.

Fig. 59(a) shows the structure of a InGaAs backside-illuminated p–i–n photodiode. The starting substrate is n^+ -InP on which is deposited approximately 1 μm of n^+ -InP as a buffer layer. 3–4 μm of the n^- -InGaAs active layer is then deposited followed by a 1- μm n^- -InP cap layer. The structure is covered with Si_3N_4 . The p-on-n photodiodes are formed by the diffusion of zinc through the InP cap into the active layer. Ohmic contacts were formed by the sintering of a Au/Zn alloy. At this point, the substrate is thinned to approximately 100 μm and a sintered Au/Ge alloy is used as the back ohmic contact. The last step is the deposition of a 20 μm columns of indium on the front contacts.

Standard $\text{In}_{0.53}\text{Ga}_{0.47}\text{As}$ photodiodes have detector-limited room temperature detectivity of $\sim 10^{13} \text{ cm Hz}^{1/2}/\text{W}$. With increasing cutoff wavelength, detectivity decreases. Fig. 59(b) shows the spectral response of three such InGaAs detectors at room temperature, whose peak responsivity is optimized at 1.5, 1.7, 2.0, and 2.4 μm , respectively.

The arrays of photodiodes are hybridized to CMOS readout integrated circuits (ROICs) and then integrated into cameras for video-rate output to a monitor or for use with a computer for quantitative measurements and machine vision.

At present, InGaAs FPAs are fabricated by several manufacturers including Goodrich Corporation (previously Sensors Unlimited) [104,105], Indigo Systems (merged with FLIR Systems) [106], Teledyne Judson Technologies [107], Aerious Photonics [108], and XenICs [109].

Detector dark current and noise are low enough that InGaAs detectors can be considered for astronomy where bandwidth of interest is between 0.9 to 1.7 μm and a high operating temperature for the focal plane is important. In a recently published paper, the low temperature performance of a 1.7 μm cutoff wavelength $1\text{k} \times 1\text{k}$ InGaAs photodiode against similar $2\text{k} \times 2\text{k}$ HgCdTe imagers has been compared [110]. The data indicates that InGaAs detector technology is well behaved and comparable to those obtained for state-of-the-art HgCdTe imagers.

The InGaAs FPAs achieves very high sensitivity in the shortwave IR bands in addition to the visible response added via substrate removal process post hybridization. The visible InGaAs detector structure is very similar to that shown in Fig. 59(a), except that an InGaAs stop layer is added into the epi-wafer structure to allow complete removal of InP substrate [111]. The substrate is removed using a combination of mechanical and wet chemical etching techniques. The remaining InP contact layer thickness must be controlled to within 10 nm for consistent visible quantum efficiency. Thicker InP layers lead to lower quantum efficiency in the visible spectrum, as well as to image retention.

The largest and finest pitched imager in $\text{In}_{0.53}\text{Ga}_{0.47}\text{As}$ material system has been demonstrated recently. The arrays with more than one million detector elements (1280×1024 and 1024×1024 formats) for low background applications have been developed by RVS with detectors provided by Goodrich. The detector elements are as small as 15 μm pitch [105]. The array with capacitive transimpedance amplification (CTIA) readout unit cells was designated to achieve a noise level of less than 50 electrons, due to its small integration capacitor. Total measured noise with the detector was 114 electrons using double sampling. Fig. 60 shows the image taken with the imager, after nonuniformity correction [105].

8.2. Schottky-barrier photoemissive arrays

In 1973, Shepherd and Yang of Rome Air Development Center proposed the concept of silicide Schottky-barrier detector FPAs as much more reproducible alternative to HgCdTe



Fig. 60. Image of the development team of an 1280×1024 InGaAs visible/SWIR imager taken by their camera (after Ref. [105]).

FPA's for IR thermal imaging [112]. Since then, the development of the Schottky-barrier technology progressed continuously and has been commercialized for about 15 years, and both monolithic and hybrid versions have been produced [113].

The most popular Schottky-barrier detector is the PtSi detector, which can be used for the detection in the $3\text{--}5\text{ }\mu\text{m}$ spectral range. Fig. 61 shows the basic construction and operation of the PtSi detector integrated with a silicon CCD [114]. It is typically operated in backside illumination mode. Radiation is transmitted through the p-type silicon and is absorbed in the metal PtSi (not in the semiconductor), producing hot holes which are then emitted over the potential barrier into the silicon, leaving the silicide charged negatively. Negative charge of silicide is transferred to a CCD by the direct charge injection method.

For improving the monolithic array performance, Kimata and co-workers from Mitsubishi Corporation have developed a readout architecture called the charge sweep device (CSD) used in series of IR image sensors with array sizes up to 1040×1040 elements [115]. At the beginning of 90s last century, the 1040×1040 element array had the smallest pixel size ($17 \times 17\text{ }\mu\text{m}^2$) among 2-dimensional IR FPA's. Fig. 62 shows a photograph of this first mega-pixel array mounted in a 40-lead ceramic package. The chip size of the device is $20.6 \times 19.4\text{ mm}^2$. Although PtSi detectors has quite low quantum efficiency in the $3\text{--}5\text{ }\mu\text{m}$ atmospheric window (of the order of 1%), but excellent imagery of objects at room temperature (with temperature resolution as low as 0.033 K with f/1.2 optics for 512×512 arrays) is obtained by means of near full frame integration in area arrays [116].

Current PtSi Schottky barrier FPA's are mainly manufactured in 300 mm wafer process lines with around $0.1\text{ }\mu\text{m}$ lithography technologies. However, the performance of monolithic PtSi Schottky-barrier FPA's has reached a plateau about ten years ago, and further slow progress is expected [116,117].

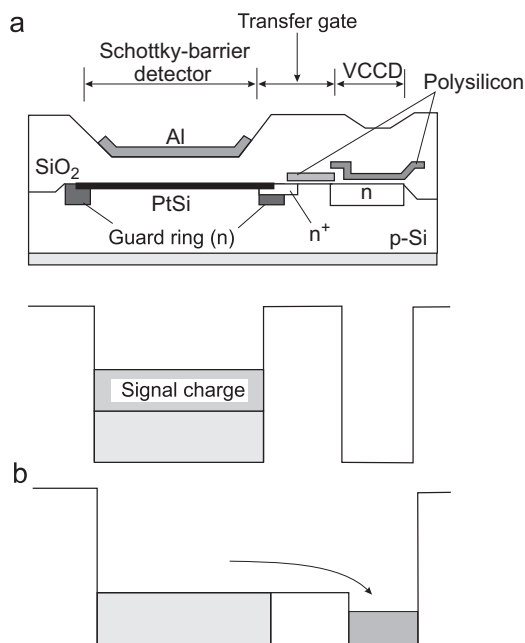


Fig. 61. Typical construction and operation of PtSi Schottky-barrier IR FPA designed with interline transfer CCD readout architecture. (a) and (b) show the potential diagrams in the integration and readout operations, respectively (after Ref. [114]).

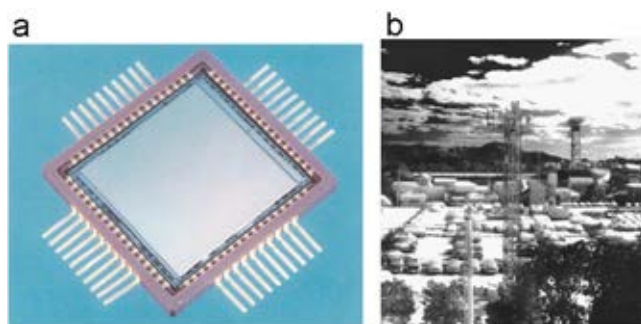


Fig. 62. 1040 × 1040 element PtSi/p-Si Schottky-barrier CSD FPA: (a) photograph of array mounted in a 40-lead ceramic package, and (b) the first mega-pixel infrared image with this array (after Ref. [115]).

8.3. Lead salt arrays

Lead salt thin film photoconductors were first produced in Germany and next in the United States at Northwestern University in 1944 and, in 1945, at the Admiralty Research Laboratory in England [118]. After 60 years, low-cost, versatile PbS and PbSe polycrystalline thin films remain the photoconductive detectors of choice for many applications in the 1–3 and 3–5 μm spectral range.

Lead salt chalcogenides are deposited on silicon or silicon oxide from wet chemical baths, or are grown epitaxially (usually using MBE technique) on silicon through the use of suitable buffer layers (usually CaF_2 - BaF_2 layers) to overcome large thermal mismatch problems between silicon readout substrates and lead salt detectors [119]. Such monolithic solution avoids the use of a thick slab of these materials mated to silicon, as is done with typical hybrids. In the case of using chemical deposition, the detector material is deposited from a wet chemical solution to form polycrystalline photoconductive islands on CMOS multiplexer. Northrop Grumman elaborated monolithic PbS FPAs in a 320×240 format with pixel size of $30 \mu\text{m}$ [120]. Although PbS photoconductors may be operated satisfactorily at ambient temperature, performance is enhanced by utilizing a self-contained thermoelectric cooler.

The research group at the Swiss Federal Institute of Technology has demonstrated the first realization of monolithic PbTe FPA (96×128) on a Si-substrate containing the active addressing electronics [121]. Large lattice mismatches between the detector active region and the Si did not impede fabrication of the high-quality layers because the easy plastic deformation of the IV-VIs by dislocation glide on their main glide system without causing structural deterioration.

A schematic cross-section of a PbTe pixel grown epitaxially by MBE on a Si readout structure is shown in Fig. 63(a). A 2–3-nm thick CaF_2 buffer layer is employed for compatibility with the Si substrate. Active layers of 2–3- μm thickness suffice to obtain only a near-reflection-loss limited quantum efficiency. Typical quantum efficiencies are around 50% without an AR coating. Metal-semiconductor Pb/PbTe detectors are employed. Each Pb-cathode contact is fed to the drain of the access transistor while the anode (sputtered Pt) is common for all pixels. Fig. 63(b) shows a complete array.

Currently, single-element lead salt devices or linear arrays of chemically deposited detectors serve the low-cost military and commercial moderate-performance markets such as guided anti-armor munitions and industrial controls. Commercial companies such as SensArray [123], currently manufacture multiplexed linear arrays of lead salt detectors. However, staring FPAs have not become a reality due to the difficulty in designing a ROIC that can effectively handle the high dark current associated with high operation temperature.

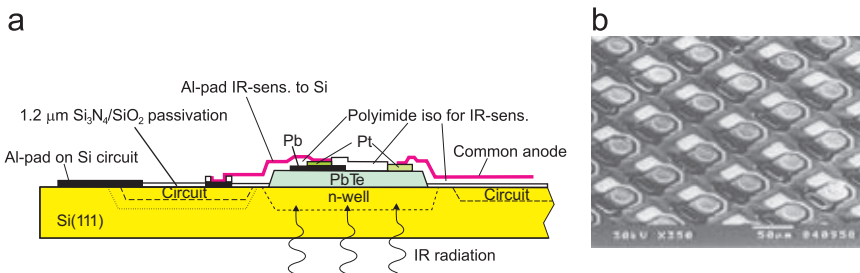


Fig. 63. Monolithic 96×128 PbTe-on-Si MWIR FPA: (a) schematic cross-section of one pixel showing the PbTe island as a backside-illuminated photovoltaic IR detector, the electrical connections to the circuit (access transistor), and a common anode (after [121]); (b) part of the completely processed array with pixel pitch of $75 \mu\text{m}$ (after Ref. [122]).

8.4. InSb arrays

InSb photodiodes have been available since the late fifties last century and are generally fabricated by impurity diffusion and ion implantation. They are used in the 1- to 5- μm spectral region and must be cooled to approximately 77 K. InSb photodiodes can also be operated in the temperature range above 77 K. The quantum efficiency optimized for this temperature range remains unaffected up to 160 K [124].

In InSb photodiode fabrication, epitaxy is not used; instead, the standard manufacturing technique begins with bulk n-type single crystal wafers with donor concentration about 10^{15} cm^{-3} . InSb material is far more mature than HgCdTe and good-quality 10 cm diameter bulk substrates are commercially available. Staring arrays of backside illuminated, direct hybrid InSb photodiodes in formats up to $4\text{k} \times 4\text{k}$ with 15- μm pitch are in fabrication. Such large arrays are possible because the InSb detector material is thinned to less than 10 μm (after surface passivation and hybridization to a readout chip) which allows it to accommodate the InSb/silicon thermal mismatch. Recently, also growing of InSb and related alloys by MBE together with doping of substrate to induce transparency has been demonstrated. In the last case the thinning of the detector material is not required.

In the last decade many manufacturers have made significant process improvements in the fabrication in both InSb detectors and readout electronic chips. In-bumps are deposited on both detector array and silicon ROIC dies, which are then hybridized together using a flip-chip bonder. The gap between bumps is backfilled with epoxy. These improvements in yield and quality have resulted from the implementation of innovative passivation techniques, from specialized antireflection coatings to unique thinning processes.

The first InSb array to exceed one million pixels was the ALADDIN array first produced in 1993 by Santa Barbara Research Center (SBRC) and demonstrated on a telescope by National Optical Astronomy Observations (NOAO), Tucson, Arizona, in 1994 [125]. This array had 1024×1024 pixels spaced on 27 μm centers and was divided into four independent quadrants, each containing 8 output amplifiers. This solution was chosen due to uncertain yield of large arrays at that time. A total of 16 devices were produced in 1996 completing the development program [126].

A chronological history of the Raytheon Vision Systems (RVS) astronomical focal plane arrays is shown in Fig. 64. The next step in the development of InSb FPAs for astronomy

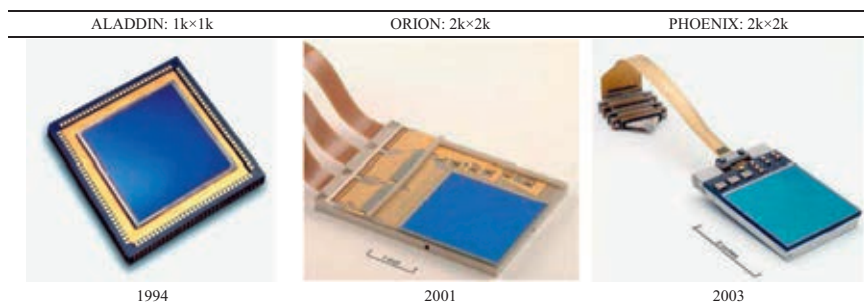


Fig. 64. Timeline and history development of the InSb RVS astronomy arrays (after Ref. [127]).

was the 2048×2048 ORION SCA (see Fig. 65) [128]. Four ORION SCAs were deployed as a 4096×4096 focal plane in the NOAO near-IR camera, currently in operation at the Mayall 4-m telescope on Kit Peak [129]. This array has 64 outputs, allowing up to a 10 Hz frame rate. A challenge for large focal planes is maintaining optical focus, and in consequence maintaining the flatness of the detector surface over a large area. Many of the packaging concepts used on the ORION program are shared with the 3-side buttable $2k \times 2k$ FPA InSb modules developed by RVS for the James Webb Space Telescope (JWST) mission [130].

PHOENIX SCA is another $2k \times 2k$ FPA InSb array that has been fabricated and tested. This detector array is identical to ORION (25- μm pixels), however it readout is optimized for lower frames rates and lower power dissipation. With only 4 outputs, the full frame

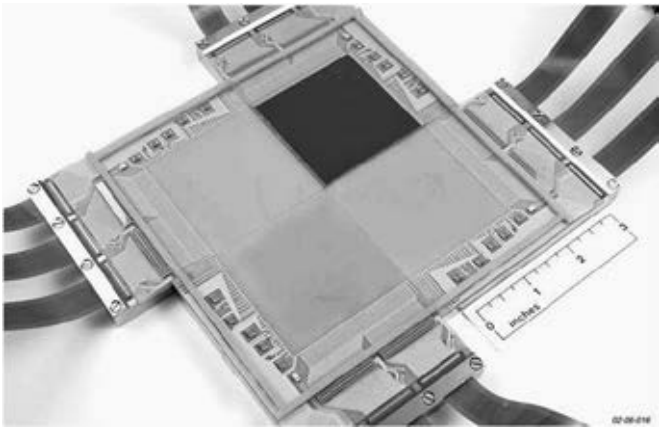


Fig. 65. A demonstration of the 2-sided buttable ORION modules to create a $4k \times 4k$ focal plane. One module contains an InSb SCA while the others have bare readouts (after Ref. [128]).

Table 7
Performance of commercially available megapixel InSb FPAs.

Parameter	Configuration		
	1024 \times 1024 (L-3 communications)	1024 \times 1024 (Santa Barbara Focalplane)	1280 \times 1024 (SCD)
Pixel pitch (μm)	25	19.5	15
Dynamic range (bits)		14	15
Pixel capacity (electrons)	1.1×10^7	8.1×10^6	6×10^6
Power dissipation (mW)	<100	<150	<120
NETD (mK)	<20	<20	20
Frame rate (Hz)	1 to 10	120	120
Operability (%)	>99	>99.5	>99.5
References	www.raytheon.com	www.sbfpc.com	www.scd.co.il

read time is typically 10 s. The smaller number of outputs allows a smaller module package that is 3-side buttable [129]. Three-side buttable modules allow the possibility to realize large detection area.

Different formats of InSb FPAs have found also many high background applications including missile systems, interceptor systems, and commercial imaging camera systems. With an increasing need for higher resolution, several manufacturers have developed megapixel detectors. Table 7 compares performance of commercially available megapixel InSb FPAs fabricated by L-3 Communications (Cincinnati Electronics), Santa Barbara Focalplane, and SCD. Recently, Santa Barbara Focalplane has developed a new large format InSb detector with 1280×1024 elements and a pixel size of $12 \mu\text{m}$ [131].

8.5. HgCdTe arrays

HgCdTe photodiodes are available to cover the spectral range from 1 to $20 \mu\text{m}$ [5,132]. Spectral cutoff can be tailored by adjusting the HgCdTe alloy composition. Most applications are concentrated in the SWIR ($1\text{--}3 \mu\text{m}$), MWIR ($3\text{--}5 \mu\text{m}$), and LWIR ($8\text{--}12 \mu\text{m}$). Also development work on improving performance of very LWIR (VLWIR) photodiodes in the $13\text{--}18 \mu\text{m}$ region for important earth-monitoring applications are undertaken.

Epitaxy is the preferable technique to obtain device-quality HgCdTe epilayers for IR devices. The epitaxial techniques offer the possibility to grow large area epilayers and sophisticated layered structures with abrupt and complex composition and doping profiles.

Among the various epitaxial techniques, the LPE is the most matured method. The recent efforts are mostly on low growth temperature techniques; MBE and MOCVD. MBE offers unique capabilities in material and device engineering including the lowest growth temperature, superlattice growth and potential for the most sophisticated composition and doping profiles. The growth temperature is less than 200°C for MBE but around 350°C for MOCVD, making it more difficult to control the p-type doping in the MOCVD due to the formation of Hg vacancies.

Different HgCdTe photodiode architectures have been fabricated that are compatible with backside and frontside illuminated hybrid FPA technology [5]. Fig. 66 shows the schematic band profiles of the most commonly used unbiased homo- (n^+ -on-p) and

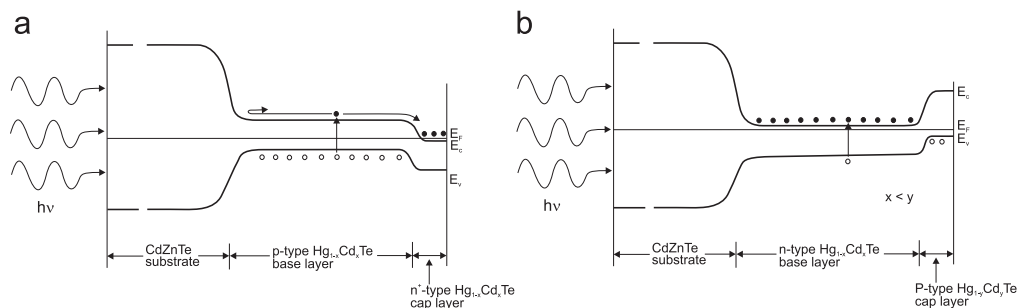


Fig. 66. Schematic band diagrams of n^+ -on-p (a) and p-on-n (b) HgCdTe photodiodes.

heterojunction (p-on-n) photodiodes. To avoid contribution of the tunneling current, the doping concentration in the base region below 10^{16} cm^{-3} is required. In both photodiodes, the lightly doped narrow gap absorbing region [“base” of the photodiode: p(n)-type carrier concentration of about $5 \times 10^{15} \text{ cm}^{-3}$ ($5 \times 10^{14} \text{ cm}^{-3}$)], determines the dark current and photocurrent. The internal electric fields at interfaces are “blocking” for minority carriers and influence of surface recombination is eliminated. Also suitable passivation prevents the influence of surface recombination. Indium is most frequently used as a well-controlled dopant for n-type doping due to its high solubility and moderately high diffusion. Elements of the VB group are acceptors substituting Te sites. They are very useful for fabrication of stable junctions due to very low diffusivity. Arsenic proved to be the most successful p-type dopant to date. The main advantages are stability in lattice, low activation energy and possibility to control concentration over 10^{15} – 10^{18} cm^{-3} range. Intensive efforts are currently underway to reduce a high temperature (400°C) required to activate As as an acceptor.

n-on-p junctions are fabricated in two different manners using Hg vacancy doping and extrinsic doping. Hg vacancies (V_{Hg}) provide intrinsic p-type doping in HgCdTe. In this case, the doping level depends on only one annealing temperature. However, the use of Hg vacancy as p-type doping is known to kill the electron lifetime, and the resulting detector exhibits a higher current than in the case of extrinsic doping using. However, for very low doping ($<10^{15} \text{ cm}^{-3}$), the hole lifetime becomes SR limited and does not depend on doping anymore. V_{Hg} technology leads to low minority diffusion length of the order of 10 – $15 \mu\text{m}$, depending on doping level. Generally, n-on-p vacancy doped diodes give rather high diffusion currents but lead to a robust technology as its performance weakly depend on doping level and absorbing layer thickness. Simple modeling manages to describe dark current behavior of V_{Hg} doped n-on-p junctions over a range of at least eight orders of magnitude (see Fig. 67). In the case of extrinsic doping, Cu, Au, and As are often used.

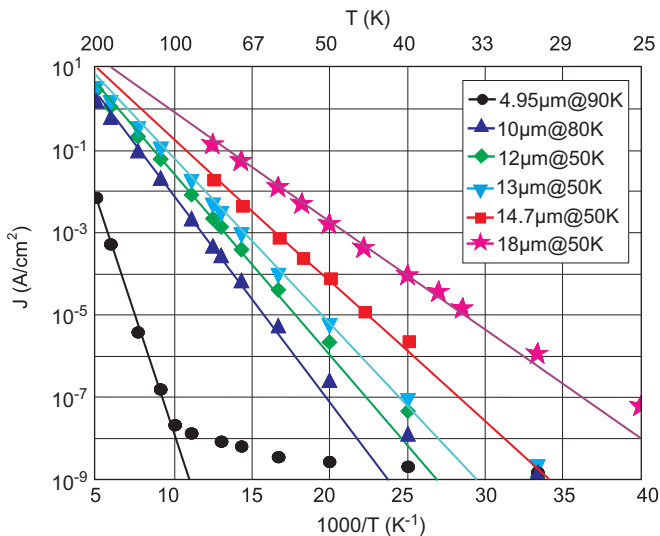


Fig. 67. Mercury vacancy dark current modelling for n-on-p HgCdTe photodiodes with different cutoff wavelengths (after Ref. [133]).

Due to higher minority carrier lifetime, extrinsic doping is used for low dark current (low flux) applications. The extrinsic doping usually leads to larger diffusion length and allows lower diffusion current but might exhibit performance fluctuations, thus affecting yield and uniformity.

Fig. 68 is an accumulation of R_0A -data with different cutoff wavelength, taken from LETI LIR using both V_{Hg} and extrinsic doping n-on-p HgCdTe photodiodes compared with P-on-n data from other laboratories, extracted from various recent literature reports, using various techniques and different diode structures. It is clearly shown, that extrinsic doping of n-on-p photodiodes leads to higher R_0A product (lower dark current) whereas mercury vacancy doping remains on the bottom part of the plot. p-on-n structures are characterized by the lowest dark current (highest R_0A product)—see trend line calculated with Teledyne (formerly Rockwell Scientific) empirical model [134].

Up to the present, photovoltaic HgCdTe FPAs have been mainly based on p-type material. 2-D scanning arrays with time delay and integration (TDI) and 2-D staring formats up to 4096×4096 pixels have been made. The best results have been obtained using hybrid architecture. For example, Fig. 69 shows the timeline for HgCdTe FPA development at Raytheon Vision Systems (RVS, formerly Santa Barbara Research Center, SBRC) starting from the initial bulk HgCdTe crystal wafers of 3 cm^2 , and progressing through LPE on CdZnTe substrates of 30 cm^2 up to today's MBE on alternate substrates of 180 cm^2 .

Sapphire buffered with CdZnTe became a standard substrate for SWIR and MWIR devices. LWIR devices are typically based on CdZnTe. However, near lattice matched CdZnTe substrates have severe drawbacks such as lack of large area, high production cost and, more importantly, a difference in thermal expansion coefficient (TEC) between the CdZnTe substrates and the silicon readout integrated circuit. Currently, readily producible CdZnTe substrates are limited to areas of approximately 50 cm^2 . Large semiconductor

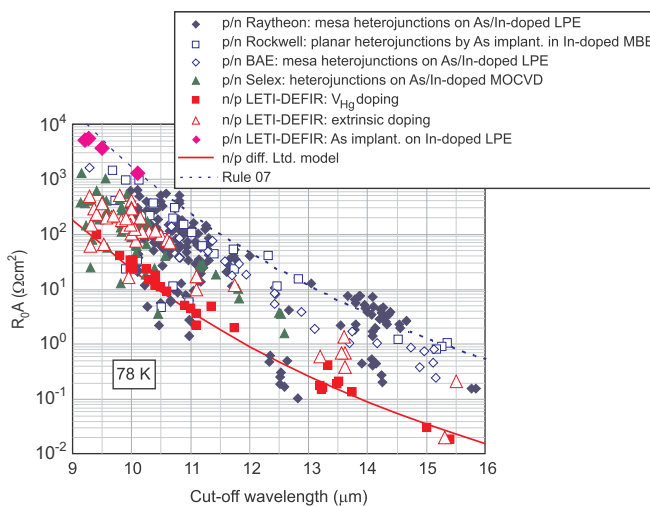


Fig. 68. R_0A product vs. cut-off wavelength at 78 K, summarized with bibliographic data (after Ref. [133]).

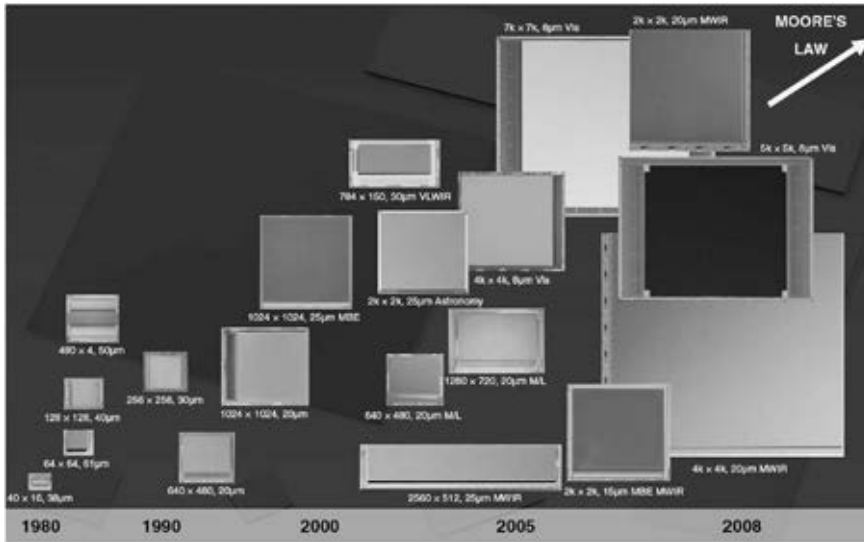


Fig. 69. Timeline for HgCdTe development at Raytheon Vision Systems (after Ref. [135]).

wafers for IR detector fabrication enable lower cost through printing more die per wafer or enable larger single piece detector arrays.

The progress on GaAs-based substrates has not progressed as fast as had been hoped. However, most of the MOCVD work on silicon has used a GaAs layer to buffer lattice mismatch between silicon and HgCdTe. The use of Si substrates is very attractive in IR FPA technology because it is less expensive (the cost of 6 in. Si substrates is \approx \$100 vs. \$10,000 for the $7 \times 7 \text{ cm}^2$ CdZnTe), significant advantages of HgCdTe/Si are evident and available in large area wafers, and because the coupling of the Si substrates with Si readout circuitry in an FPA structure allows fabrication of very large arrays exhibiting long-term thermal cycle reliability. Despite the large lattice mismatch ($\approx 19\%$) between CdTe and Si, MBE has been successfully used for the heteroepitaxial growth of MWIR HgCdTe photodiodes on composite CdTe/Si substrates. However, it has proved difficult to attain the best LW photodiode performance when grown on Si by MBE, such as is observed on lattice matched CdZnTe substrates.

For over six years RVS has fabricated HgCdTe FPAs on 6 inch silicon substrates. Utilizing fabrication processes identical to those used for HgCdTe/CdZnTe, FPAs are the largest reported for any IR detector fabrication method. Fig. 70 shows 6-inch diameter HgCdTe/Si detector wafer. HgCdTe/Si FPA operabilities greater than 99.9% and the technology readiness provide affordable large format arrays for current and future IR applications.

Pixel sizes as small as $10 \mu\text{m}$ have been demonstrated. A general trend has been to reduce pixel sizes, and this trend is expected to continue. Systems operating at shorter wavelengths are more likely to benefit from small pixel sizes because of the smaller diffraction-limited spot size. Diffraction-limited optics with low f-numbers (e.g., $f/1$) could benefit from pixels on the order of one wavelength across; about $10 \mu\text{m}$ in the LWIR. Over sampling the diffractive spot may provide some additional resolution for smaller pixels, but this

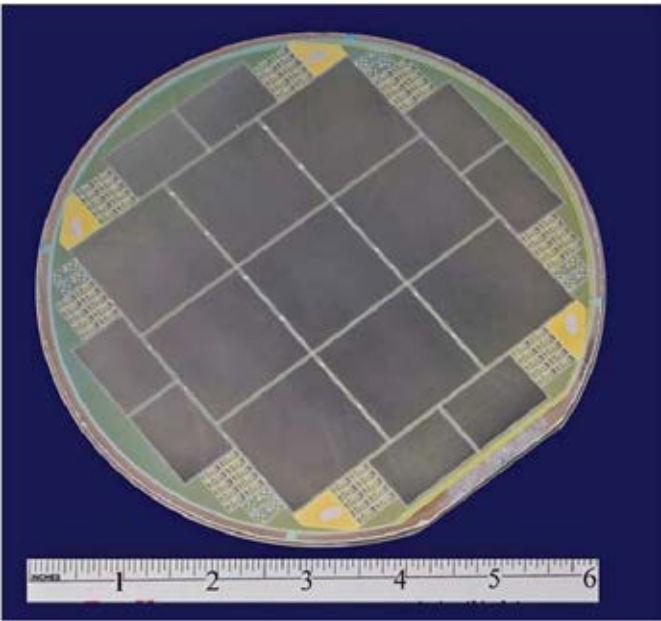


Fig. 70. 6-inch diameter HgCdTe/Si detector (after Ref. [136]).

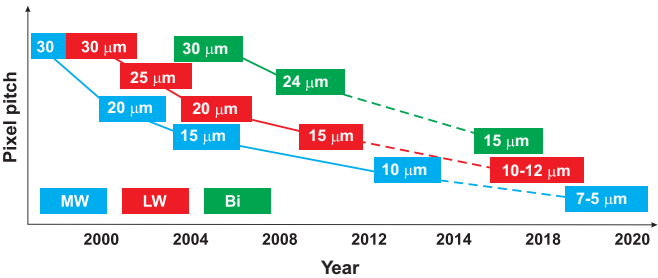


Fig. 71. Pixel pitch for HgCdTe photodiodes have continued to decrease due to technological advancements (after Ref. [137]).

saturates quickly as the pixel size is decreased. Pixel reduction is mandatory also to cost reduction of a system (reduction of the optics diameter, dewar size and weight, together with the power and increase the reliability). The pitch of 15 μm is in production today at Sofradir and pitches of 10- μm and less will be scheduled in short term (see Fig. 71) [137].

SWIR, MWIR and LWIR electronically scanned HgCdTe arrays with CMOS multiplexer are commercially available from several manufactures. Table 6 presents the representative IR FPAs offered by some major manufactures. Most manufactures produce their own multiplexer designs because these often have to be tailored to the applications. Fig. 72 shows an example of large HgCdTe FPAs [138,139]. While the size of individual arrays continues to grow, the very large FPAs required for many space missions by

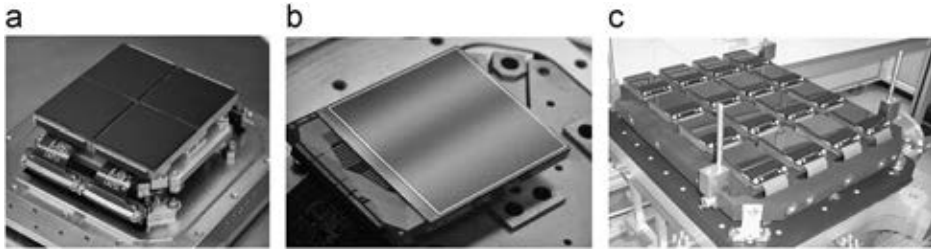


Fig. 72. Large HgCdTe FPAs: (a) a mosaic of four Hawaii-2RG-18s (4096×4096 pixels, $18\text{-}\mu\text{m}$ pitch) and (b) Hawaii-4RG-10 (4096×4096 pixels, $10\text{-}\mu\text{m}$ pitch) as is being used for astronomy observations (after Ref. [138]), (c) 16 2048×2048 HgCdTe arrays assembled for the VISTA telescope (after Ref. [139]).

mosaicking a large number of individual arrays. An example of a large mosaic developed by Teledyne Imaging Sensors, is a 147 megapixel FPA that is comprised of 35 arrays, each with 2048×2048 pixels. This is currently the world's largest IR focal plane [138].

HgCdTe as an attractive material for room-temperature APDs operate at SWIR and MWIR wavelengths. Important APD application is LADAR (laser radar) whereby a pulsed laser system is obtained 3-D imagery. 3-D imagery has been traditionally obtained with scanned laser systems. The gated active/passive system promises target detection and identification at longer ranges compared to conventional passive only imaging systems (typically about 10 km). Baker et al. at Selex were the first to demonstrate laser gated imaging in a 320×256 $24\text{-}\mu\text{m}$ pitch MWIR APD FPA [140]. More recently, a first MW 320×256 passive amplified imaging with $30\text{-}\mu\text{m}$ pitch and operability of 99.8% has been demonstrated [141].

8.6. QWIP arrays

An alternative hybrid detector for the middle and long wavelength IR region are the quantum well infrared photoconductors (QWIPs). Despite large research and development efforts, large photovoltaic LWIR HgCdTe FPAs remain expensive, primarily because of the low yield of operable arrays. The low yield is due to sensitivity of LWIR HgCdTe devices to defects and surface leakage, which is a consequence of basic material properties. With respect to HgCdTe detectors, GaAs/AlGaAs quantum well devices have a number of advantages, including the use of standard manufacturing techniques based on mature GaAs growth and processing technologies, highly uniform and well-controlled MBE growth on greater than 6 in. GaAs wafers, high yield and thus low cost, more thermal stability, and extrinsic radiation hardness. To cover the MWIR range, a strained-layer InGaAs/AlGaAs material system is used. InGaAs in the MWIR stack produces high in-plane compressive strain, which enhances the responsivity.

Fig. 73 shows two detector configurations used in fabrication of QWIP FPAs. The major advantage of the bound-to-continuum QWIP [Fig. 73(a)] is that the photoelectron can escape from the quantum well to the continuum transport states without being required to tunnel through the barrier. As a result, the voltage bias required to efficiently collect the photoelectrons can be reduced dramatically, thereby lowering the dark current. A miniband transport QWIP contains two bound states, the higher-energy one being in resonance with the ground state miniband in the superlattice barrier [see Fig. 73(b)]. In this approach, IR radiation is absorbed in

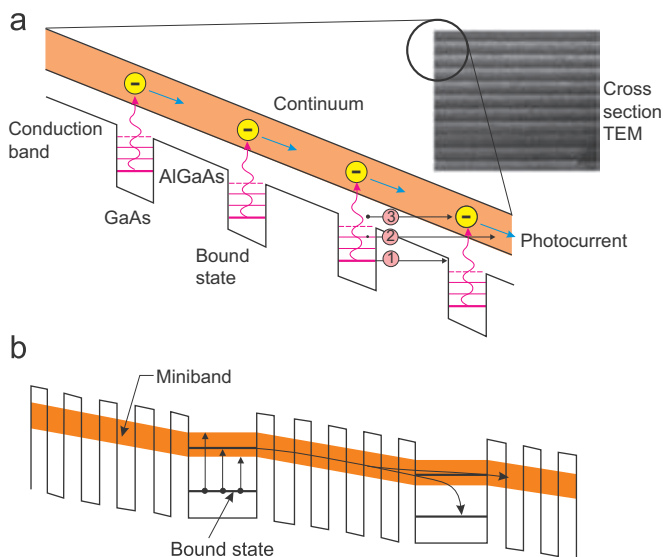


Fig. 73. Band diagram of demonstrated QWIP structures: (a) bound-to-extended (after Ref. [142] and (b) bound-to-miniband. Three mechanisms creating dark current are also shown in Fig. (a): ground-state sequential tunnelling (1), intermediate thermally assisted tunnelling (2), and thermionic emission (3).

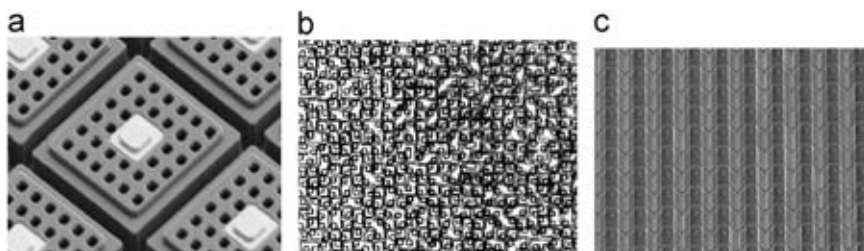


Fig. 74. Gratings light-coupling mechanisms used in QWIPs: (a) gratings with optical cavity, (b) random scattered reflector and (c) corrugated quantum wells.

the doped quantum wells, exciting an electron into the miniband which provides the transport mechanism, until it is collected or recaptured into another quantum well.

A distinct feature of n-type QWIPs is that the optical absorption strength is proportional to the electric-field polarization component of an incident photon in a direction normal to the plane of the quantum wells. For imaging, it is necessary to couple light uniformly to 2-D arrays of these detectors, so a diffraction grating is incorporated on one side of the detectors to redirect a normally incident photon into propagation angles more favorable for absorption (see Fig. 74).

LWIR QWIP cannot compete with HgCdTe photodiode as the single device, especially at higher temperature operation (>70 K) due to fundamental limitations associated with intersubband transitions [143]. QWIP detectors have relatively low quantum efficiencies, typically less than 10%. The spectral response band is also narrow for this detector, with a full-width, half-maximum of about 15%. All the QWIP data with cut-off wavelength about $9\text{ }\mu\text{m}$ is clustered between 10^{10} and $10^{11}\text{ cm Hz}^{1/2}/\text{W}$ at about 77 K operating temperature.

Table 8
Essential properties of LWIR HgCdTe, type II SL photodiodes, and QWIPs at 77 K.

Parameter	HgCdTe	QWIP (n-type)	InAs/GaInSb SL
IR absorption	Normal incidence	$E_{\text{optical}} \perp$ plane of well required Normal incidence: no absorption	Normal incidence
Quantum efficiency	$\geq 70\%$	$\leq 10\%$	$\approx 30\text{--}40\%$
Spectral sensitivity	Wide-band	Narrow-band (FWHM $\approx 1\text{ }\mu\text{m}$)	Wide-band
Optical gain	1	0.2–0.4 (30–50 wells)	1
Thermal generation lifetime	$\approx 1\text{ }\mu\text{s}$	$\approx 10\text{ ps}$	$\approx 0.1\text{ }\mu\text{s}$
R_oA product ($\lambda_c = 10\text{ }\mu\text{m}$)	$300\text{ }\Omega\text{ cm}^2$	$10^4\text{ }\Omega\text{ cm}^2$	$10^3\text{ }\Omega\text{ cm}^2$
Detectivity ($\lambda_c = 10\text{ }\mu\text{m}$, FOV=0)	$2 \times 10^{12}\text{ cm Hz}^{1/2}/\text{W}$	$2 \times 10^{10}\text{ cm Hz}^{1/2}/\text{W}$	$5 \times 10^{11}\text{ cm Hz}^{1/2}/\text{W}$

However, the advantage of HgCdTe is less distinct in temperature range below 50 K due to the problems involved in an HgCdTe material (p-type doping, Shockley-Read recombination, trap-assisted tunneling, surface and interface instabilities). Table 8 compares the essential properties of three types of devices at 77 K.

Even though QWIPs are photoconductors, several its properties such as high impedance, fast response time, and low power consumption comply well with the requirements for large FPAs fabrication. The main drawbacks of LWIR QWIP FPA technology are the performance limitation for low integration time applications and low operating temperature. Their main advantages are linked to performance uniformity and to availability of large size arrays. The large industrial infrastructure in III–V materials/device growth, processing, and packaging brought about by the utility of GaAs-based devices in the telecommunications industry gives QWIPs a potential advantage in producibility and cost HgCdTe material system

State-of-the-art QWIP and HgCdTe FPAs provide similar performance figure of merit, because they are predominantly limited by the readout circuits. The very short integration time of LWIR HgCdTe devices of typically below 300 μs is very useful to freeze a scene with rapidly moving objects. QWIP devices achieve, due to excellent homogeneity and low photoelectrical gain, an even better *NEDT*, however, the integration time must be 10–100 times longer for that, and typically it is 5–20 ms [144]. Decision of the best technology is therefore driven by the specific needs of a system.

QWIP detectors are used for large formats (e.g., 1024×1024 and larger) with low frame rates and large integration time. 1 megapixel hybrid MWIR and LWIR QWIPs with 18- μm pixel size have been demonstrated with excellent imaging performance [145,146]. The MWIR detector arrays has demonstrated a *NEDT* of 17 mK at a 95 K operating temperature with f/2.5 optics at 300 background and the LWIR detector array has demonstrated a *NEDT* of 13 mK at a 70 K operating temperature with the same optical and background conditions as the MWIR detector array. Fig. 75 shows frames of video images taken with both 5.1 and 9 μm cutoff 1024×1024 pixel cameras. At present, this technology is extended to a $2\text{k} \times 2\text{k}$ array. The GaAs/AlGaAs QWIPs are also well situated to multi-color IR sensors. This topic is considered in Section 8.9.

The success of quantum well structures for infrared detection applications has stimulated the development of quantum dot infrared photodetectors (QDIPs). In general, QDIPs are similar to QWIPs but with the quantum wells replaced by quantum dots (QDs), which have size confinement in all spatial directions. QDIPs presents some

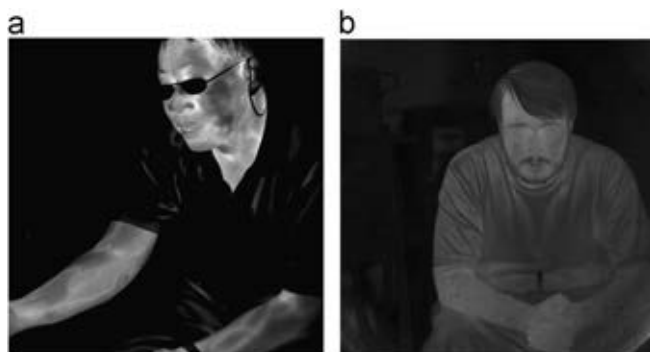


Fig. 75. One frame of video taken with (a) the 5.1 μm and (b) 9 μm cutoff 1024 \times 1024 pixel QWIP cameras (after Ref. [146]).

promise at the research stage, but remains unproved for commercial and military applications [147].

8.7. Type II superlattice arrays

The three semiconductors InAs, GaSb, and AlSb form an approximately lattice-matched set around 6.1 Å, with (room temperature) energy gaps ranging from 0.36 eV (InAs) to 1.61 eV (AlSb). Their heterostructures combining InAs with the two antimonides offers band lineups that are drastically different from those of the more widely studied AlGaAs system. The most exotic lineup is that of InAs/GaSb heterojunctions with a broken gap lineup: at the interface the bottom of conduction band of InAs lines up below the top of the valence band of GaSb with a break in the gap of about 150 meV. In such a heterostructure, with partial overlapping of the InAs conduction band with the GaSb-rich solid solution valence band, electrons and holes are spatially separated and localized in self-consistent quantum wells formed on both sides of the heterointerface. This leads to unusual tunnelling-assisted radiative recombination transitions and novel transport properties. From the viewpoint of producibility, III-V materials offer much stronger chemical bonds and thus higher chemical stability compared to HgCdTe. The 6.1 Å materials can be epitaxially grown on GaSb and InAs substrates. In particular, 4-inch diameter GaSb substrates became commercially available in 2009 offering improved economy of scale for fabrication of large format FPAs arrays.

InAs/Ga_{1-x}In_xSb (InAs/GaInSb) strained layer superlattices (SLSs) can be considered as an alternative to the HgCdTe and GaAs/AlGaAs IR material systems (see Table 8). The InAs/GaInSb material system is however in an early stage of development. Problems exist in material growth, processing, substrate preparation, and device passivation. Optimization of SL growth is a trade-off between interface roughness, with smoother interfaces at higher temperature, and residual background carrier concentrations, which are minimized on the low end of this range.

The staggered band alignment of type-II superlattice shown in Fig. 76(a) creates a situation in which the energy band gap of the superlattice can be adjusted to form either a semimetal (for wide InAs and GaInSb layers) or a narrow band gap (for narrow layers) semiconductor material. In the SL, the electrons are mainly located in the InAs layers, whereas holes are confined to the GaInSb layers. This suppresses Auger recombination

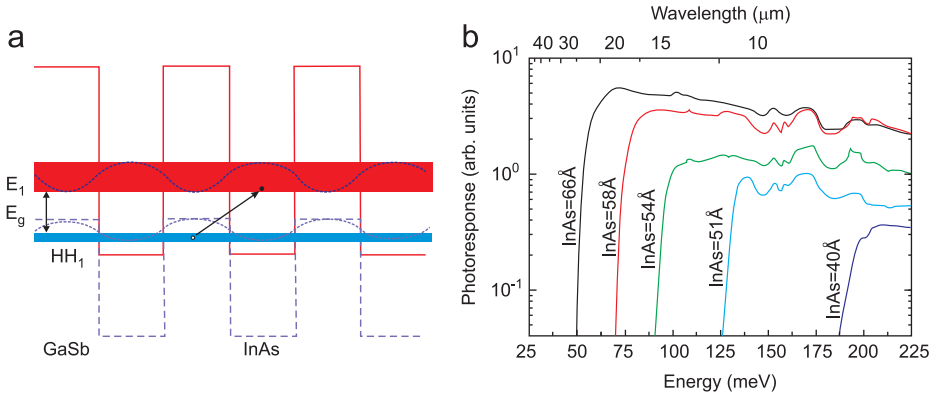


Fig. 76. InAs/GaSb strained layer superlattice: (a) band edge diagram illustrating the confined electron and hole minibands which form the energy band gap; (b) experimental data of type II SLS cutoff wavelengths change with the InAs thickness while GaSb is fixed at 40 Å (after Ref. [148]).

mechanisms and thereby enhances carrier lifetime. Optical transitions occur spatially indirectly and, thus, the optical matrix element for such transitions is relatively small. The band gap of the SL is determined by the energy difference between the electron miniband E_1 and the first heavy hole state HH_1 at the Brillouin zone centre and can be varied continuously in a range between 0 and about 250 meV. One advantage of using type-II superlattice in LW and VLWIR is the ability to fix one component of the material and vary the other to tune wavelength. An example of the wide tunability of the SL is shown in Fig. 76(b).

It has been suggested that InAs/Ga_{1-x}In_xSb SLs material system can have some advantages over bulk HgCdTe, including lower leakage currents and greater uniformity [149]. Electronic properties of SLs may be superior to those of the HgCdTe alloy. The electron effective mass of InAs/GaInSb SLS is larger ($m^*/m_0 \approx 0.02\text{--}0.03$, compared to $m^*/m_0 = 0.009$ in HgCdTe alloy with the same band gap $E_g \approx 0.1$ eV). Thus, diode tunnelling currents in the SL can be reduced compared to the HgCdTe alloy. While mobilities in these SLs are found to be limited by the same interface roughness scattering mechanism, detailed band structure calculations reveal a much weaker dependence on layer thickness, in reasonable agreement with experiment.

Theoretical analysis of band-to-band Auger and radiative recombination lifetimes for InAs/GaInSb SLs showed that in these objects the Auger recombination rates are suppressed by several orders, compared to those of bulk HgCdTe with similar band-gap [150]. However, the promise of Auger suppression has not yet to be observed in practical device material. At present time, the measured carrier lifetime is below 100 ns and is limited by Shockley-Read mechanism in both MWIR and LWIR compositions [151]. It is interesting to note that InSb has had a similar SR lifetime issue since its inspection in 1950s. In a typical LWIR superlattice, the doping density is on the order of 1 to $2 \times 10^{16} \text{ cm}^{-3}$, which is considerably higher than the doping level found in the LWIR HgCdTe (typically low 10^{15} cm^{-3}). This is possible because of tunnelling current suppression in superlattices. The higher doping compensates for the shorter lifetime, resulting in relatively low diffusion dark current.

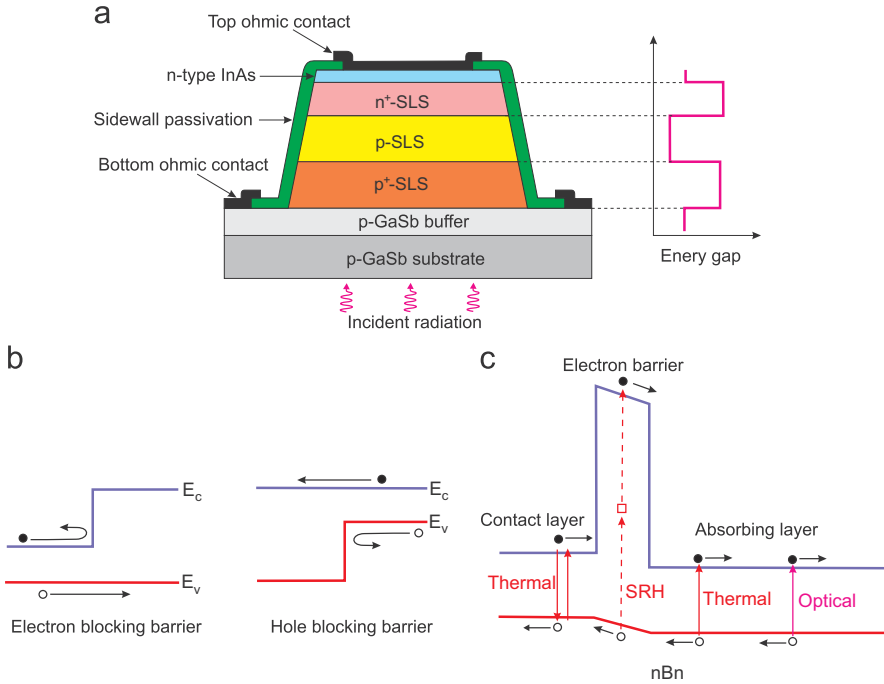


Fig. 77. Schematic illustrations of type-II superlattice devices: (a) p-i-n photodiode and barrier detectors: (b) electron- and hole-blocking unipolar barriers and (c) band gap diagram of nBn barrier detector.

InAs/GaInSb SL photodiodes are typically based on p-i-n structures with an unintentionally doped, intrinsic region between the heavily doped contact portions of the device. A cross section scheme of a mesa detector is presented in Fig. 77(a). The layers are usually grown by MBE at substrate temperatures around 400 °C on undoped (0 0 1) oriented two-inch GaSb substrates. The lower periods of the SLs are p-doped with $1 \times 10^{17} \text{ cm}^{-3}$ Be in the GaSb layers. These acceptor doped SL layers are followed by several micron thick nominally undoped, SL region. The upper of the SL stack is doped with silicon (1×10^{17} to $1 \times 10^{18} \text{ cm}^{-3}$) in the InAs layers and is typically 0.5 μm thick. The top of the SL stack is then capped with an InAs:Si ($n \approx 10^{18} \text{ cm}^{-3}$) layer to provide good ohmic contact.

The main technological challenge for the fabrication of photodiodes is the growth of thick SLS structures without degrading the materials quality. High-quality SLS materials thick enough to achieve acceptable quantum efficiency is crucial to the success of the technology. Surface passivation is also serious problem. Considerable surface leakage is attributed to the discontinuity in the periodic crystal structure caused by mesa delineation. Several materials and processes have been explored for device passivation. Some of the more prominent thin films studied have been silicon nitride, silicon oxides, ammonium sulphide, and aluminium gallium antimonide alloys [152]. The best results have been recently obtained using inductively coupled plasma dry etching and polyimide passivation [153].

Optimization of the SL photodiode architectures is still an open area. Additional design modifications dramatically improve the photodiode performance. For example, Aifer et al. have reported W-structured type II superlattice [154]. Another type II superlattice

photodiode design is structure with the M-structure barrier [155]. The modification of the structures confines the electron wavefunctions, reducing the tunnelling probability, increasing the electron effective mass, and effectively decreasing the dark current.

Introducing of unipolar barriers in various designs based on type-II SLs drastically changed the architecture of infrared detectors. Unipolar barriers are used to impede the flow of majority carrier dark current in photoconductors [see Fig. 77(b)]. The nBn detector is designed to reducing dark current (associated with SRH processes) and noise without impeding photocurrent (signal). In particular, the barrier serves to reduce surface leakage current. The nBn band gap diagram is shown in Fig. 77(c). It somewhat resembles the typical p–n photodiode, except that the junction (space charge region) is replaced by an electron blocking unipolar barrier (B), and that the p-contact is replaced by an n-contact. It can be stated, that the nBn design is a hybrid between photoconductor and photodiode. While the idea of nBn design was originated with bulk materials [156], its demonstration using type-II SL based materials facilitates the experimental realization of the nBn concept with better control of band edge alignments.

Different structures of photovoltaic barrier detector family has been proposed, including pMp and pBn detectors. However, a key feature of the devices is a pair of complementary barriers, namely, an electron barrier and a hole barrier formed at different depths in the growth sequence. Such structure is known as complementary barrier infrared device (CBIRD) and was invented by Ting and others at JPL [157]. Fig. 78(a) shows a band gap diagram at equilibrium and a schematic device structure of the CBIRD. An electron barrier (eB) appears in the conduction band and a hole barrier (hB) in the valence band toward the left. The two barriers complement one another to impede the flow of dark current. The substrate is toward the right. The absorber region, where the band gap is smallest, is p-type and the top contact region at the left is n-type, making an n-on-p polarity for the detector element. In sequence from the top (left) the first three regions are composed of superlattice material: the n-type cap, the p-type absorber, and the p-type eB. The highly doped InAsSb layer below the eB is an alloy. Further to the right (not shown) are a GaSb buffer layer and the GaSb substrate.

Usually, R_0A values are plotted for devices with near zero-bias turn-on. However, since the detector is expected to operate at a higher bias, a more relevant quantity is the effective

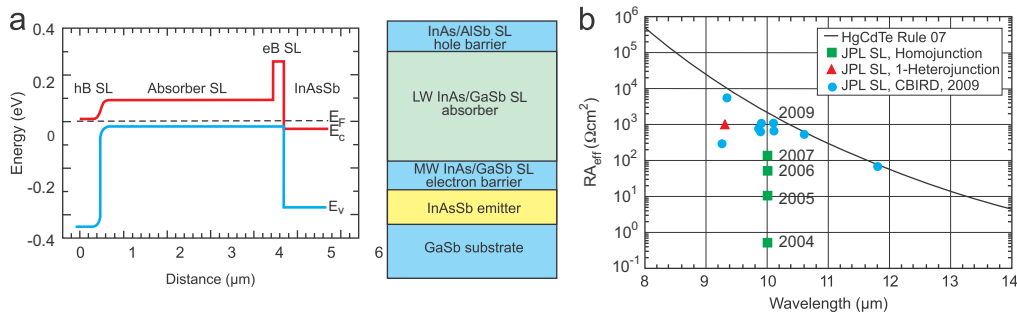


Fig. 78. The complementary barrier infrared detector (CBIRD): (a) zero-bias band diagram and a schematic device structure and (b) the 77 K effective resistance-area product plotted against the detector cutoff wavelength for a number of LWIR InAs/GaSb superlattice detectors (after Ref. [157]).

resistance area product. Fig. 78(b) plots the RA_{eff} values for a set of selected antimonide superlattice devices made at JPL. For reference, the HgCdTe “Rule 07” trend line is also shown. Of note is the steady performance gains achieved in the past few years. In particular, the introduction of device designs containing unipolar barriers has taken the LWIR superlattice detector performance close to the “Rule 07” trend line. The barriers prove to be very effective in suppressing the dark current. In the case of a detector having a cut-off wavelength of $9.24\ \mu\text{m}$, the value of $R_0A > 10^5\ \Omega\ \text{cm}^2$ at 78 K was measured, as compared with about $100\ \Omega\ \text{cm}^2$ for an InAs/GaSb homojunction of the same cut-off. For good photoresponse, the device must be biased to typically 200 mV; the estimated internal quantum efficiency is greater than 50%, while the RA_{eff} remains above $10^4\ \Omega\ \text{cm}^2$.

Fig. 79 shows tremendous progress made in past few years in the performance of type-II superlattice single element detectors or mini-arrays from USA major institutions: Northwestern University (NWU), Naval Research Laboratory (NRL), Jet Propulsion Laboratory (JPL), and Teledyne Imaging Scientific (TIS) [158]. This figure shows superlattice detector performance measured by dark current density as a multiple of Rule 07 versus time in years (Rule 07 is a simple empirical relationship that describes the dark current behaviour with temperature and wavelengths for the better Teledyne HgCdTe diodes and arrays [134]). The best SL device is within three times the value of HgCdTe Rule 07. Most of the devices cited here have an absorber thickness of 2–4 μm , which limits its quantum efficiency to less than 40%. At the FPA level the dark current density is about

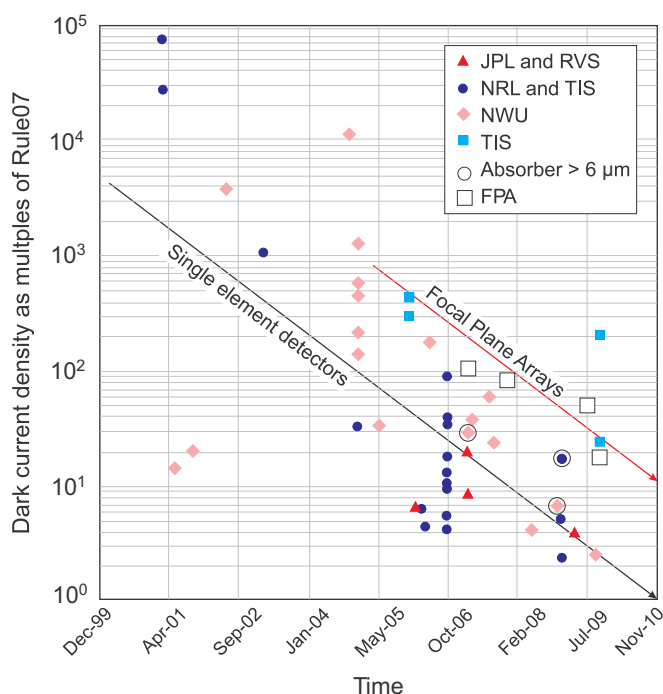


Fig. 79. Detector dark current density as a multiple of Rule 07. The black line is drawn as an eye aid to show the trend line of dark current reduction along time for single element-detector, and the red line helps to show the trend for FPAs (after Ref. [158]). (For interpretation of the references to color in this figure legend, the reader is referred to the web version of this article.)

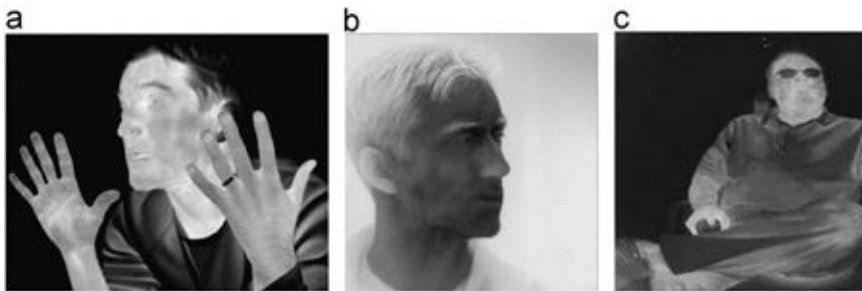


Fig. 80. Images taken with nBn 640×512 MWIR FPA (a), megapixel MWIR (b) and LWIR (b) Sb-based photovoltaic FPAs (after Refs. [159,160]).

one order of magnitude higher than that of single-element detectors, and within a factor of 20 of Rule 07.

In the last two year the first megapixel MWIR and LWIR type-II SL FPAs have been demonstrated with excellent imaging [159–161]. At about 78 K *NEDT* value below 20 mK has been presented for MW arrays; instead for LWIR – above 20 mK. Fig. 80 presents imagers taken with MWIR 640×512 nBn array and two (MWIR and LWIR) megapixel photovoltaic arrays.

Above described very promising results confirm that the antimonide SL technology is now a direct competitor to HgCdTe IR detector technology. To establish US industry capability of producing high-quality type-II superlattice FPAs, a new 4-year program was established in 2009 [158].

8.8. Thermal detector arrays

In the beginning of the 1970s in US started research programmers to develop uncooled infrared detectors for practical military applications. The efforts were mainly concentrated on ferroelectric barium strontium titanate detectors [(BST) in Texas Instruments (TI)] and micromachining bolometer technology [Honeywell (Morristown, NJ)]. Vanadium oxide microbolometers developed by Honeywell were subsequently licensed to numerous others. As a result of the limitations of BST, TI began an independent microbolometer development based on amorphous silicon (a-Si) instead of VO_x . TI also developed a thin-film ferroelectric (TFFE) technology as a simple upgrade to overcome the limitations of BST. After Raytheon acquired TI's defense business, microbolometers captured an increasing share of the rapidly growing market. In 2004 Raytheon sold the TI uncooled IR group with its BST, TFFE, and microbolometer technologies to L-3 Communications, who eventually discontinued BST production in 2009. TFFE technology development was discontinued about the same time because of manufacturing difficulties (most ferroelectrics tend to lose their interesting properties as the thickness is reduced).

In the mid 1990s the amorphous silicon technology was developed in other countries, especially in France. During this time, the big advantage of using a-Si was their fabrication in a silicon foundry. The VO_x technology was controlled by the US military and export license was required for microbolometer cameras that were sold outside the US. Today, VO_x bolometers can be also produced in a silicon foundry and above both reasons disappeared.

At present large scale integration combined with micromachining has been used for manufacturing of large 2-D arrays of uncooled IR sensors. This enables fabrication of low cost and high-quality thermal imagers. Although developed for military applications, low-cost IR imagers are used in nonmilitary applications such as: drivers aid, aircraft aid, industrial process monitoring, community services, firefighting, portable mine detection, night vision, border surveillance, law enforcement, search and rescue, etc.

Microbolometers are the dominant uncooled IR detector technology with more than 95% of the market in 2010. At present, VO_x microbolometer arrays are clearly the most used technology for uncooled detectors (see Fig. 81). VO_x is winner the battle between the technologies and VO_x detectors are being produced at a lower cost than either of the two other technologies [162]. However in the near future, VO_x will be challenged by a-Si

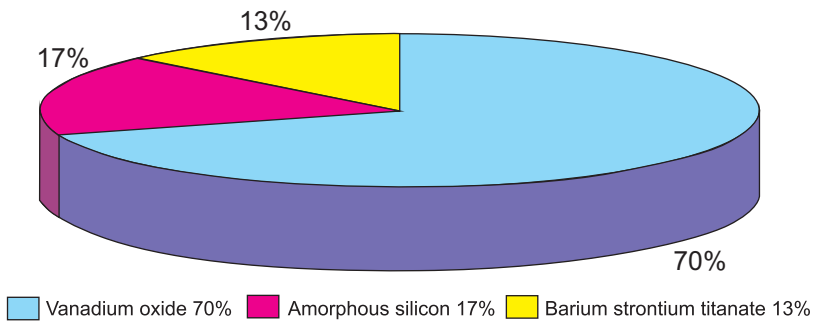


Fig. 81. Estimated market shares for VO_x , a-Si and BST detectors (after Ref. [162]).

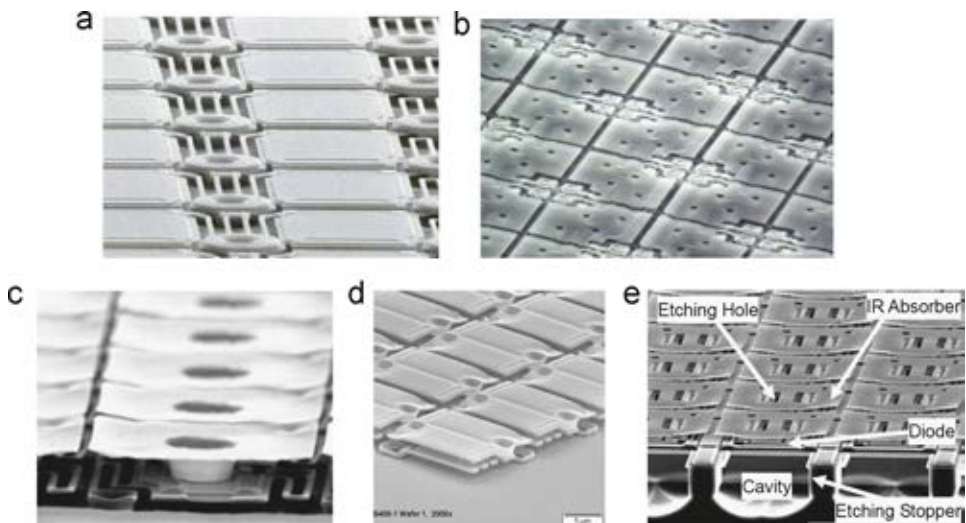


Fig. 82. Commercial bolometer design: (a) VO_x bolometer from BAE, (b) a-Si bolometer from Ullis, (c) VO_x umbrella design bolometer from DRS, (d) VO_x bolometer from Raytheon, and (e) SOI diode bolometer from Mitsubishi.

material and new silicon based materials introduced by new market entrants, thanks to their cost structure, and easier manufacturability.

At present, the commercially available bolometer arrays are either made from VO_x, amorphous silicon (α-Si) or silicon diodes. Fig. 82 shows scanning electron microscope (SEM) images of commercial bolometers fabricated by different manufacturers.

Conventional single-level bolometer arrays typically have a fill factor between 60% and 70%. To increase the fill factor, two-layer bolometer designs have been reported that reach fill factor of up to 90% [163]. Fig. 82(c) shows an example of a two-level (umbrella) design. In this case, the bolometer legs, and in some cases the sensing material are placed underneath the absorbing bolometer membrane [164]. Another way has been chosen by Raytheon, which also implemented an advanced double-layer micromachining fabrication process. In this case, the thermal isolation layer is fabricated on the first level of the structure while the optical absorber level is fabricated on the second level of the structure [see Fig. 82(d)]. These processes have been also successfully implemented for 17-μm pitch FPAs. The Mitsubishi Electric Corporation has made advances in uncooled SOI (silicon-on-insulator) technology in which change in the forward bias voltage of silicon diodes with temperature is used to sense the incident infrared radiation [see Fig. 82(e)]. This technology is very promising for beyond 17-μm/pixel pitch mega-pixel-class uncooled IRFPAs [165].

Table 9
Representative commercial uncooled infrared bolometer array.

Company	Bolometer type	Array format	Pixel pitch (μm)	Detector <i>NEDT</i> (mK) (f/1, 20–60 Hz)
L-3 (USA)	VO _x bolometer	320 × 240	37.5	50
	α-Si Bolometer	160 × 120–640 × 480	30	50
	α-Si/α-SiGe	320 × 240–1024 × 768	17	30–50
BAE (USA)	VO _x bolometer	320 × 240–640 × 480	28	30–50
	VO _x bolometer (standard design)	160 × 120–640 × 480	17	50
	VO _x bolometer (standard design)	1024 × 768	17	
DRS (USA)	VO _x bolometer (standard design)	320 × 240	25	35
	VO _x bolometer (umbrella design)	320 × 240	17	50
	VO _x bolometer (umbrella design)	640 × 480, 1024 × 768	17	
Raytheon (USA)	VO _x bolometer	320 × 240, 640 × 480	25	30–40
	VO _x bolometer (umbrella design)	320 × 240, 640 × 480	17	50
	VO _x bolometer (umbrella design)	1024 × 480, 2048 × 1536	17	
ULIS (France)	α-Si bolometer	160 × 120–640 × 480	25	<60
	α-Si bolometer	640 × 480, 1024 × 768	17	<60
SCD (Israel)	VO _x bolometer	384 × 288	17	35
	VO _x bolometer	640 × 480	25	50
NEC (Japan)	VO _x bolometer	320 × 240	23.5	<75
	VO _x bolometer	640 × 480	23.5	<75

Table 9 contains an overview of the main suppliers and specifications for existing products and for bolometer arrays that are in the R&D stage, whereas Fig. 83(a) presents development efforts for the VO_x FPAs. The microbolometer detectors are now produced in larger volumes than all other IR array technologies together. For future arrays, the $f/1$ NETD performance of $17\text{-}\mu\text{m}$ pitch microbolometer FPAs is projected to be below 20 mK [26,166]. The demonstrated performance is getting closer to the theoretical limit with the advantages regarding weight, power consumption and cost. The 640×480 arrays of $25\text{-}\mu\text{m}$ microbolometers are fabricated on industry-standard wafer (up to 8-in. diameter) complete with monolithic readout circuits integrated into underlying silicon. However, there is a strong system need to reduce the pixel size to achieve several potential benefits [see Fig. 83(b)]. The detection range of many uncooled IR imaging systems is limited by pixel resolution rather than sensitivity.

Fig. 84 presents a trade-off analysis of the detection range and sensor optics for a thermal weapon sight using the NVESD NVTherm IP model, assuming a detector

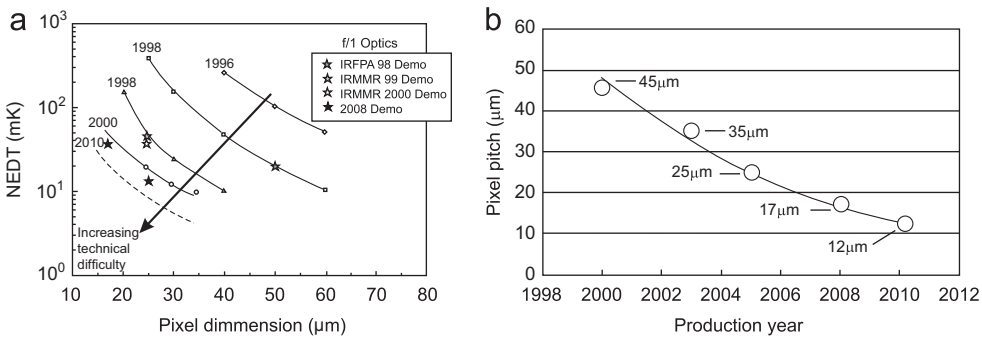


Fig. 83. Development of thermal focal plane arrays: evolution of NETD for VO_x FPAs (a) (adapted after Ref. [166]) and pixel pitch for amorphous silicon microbolometers (after Ref. [167]).

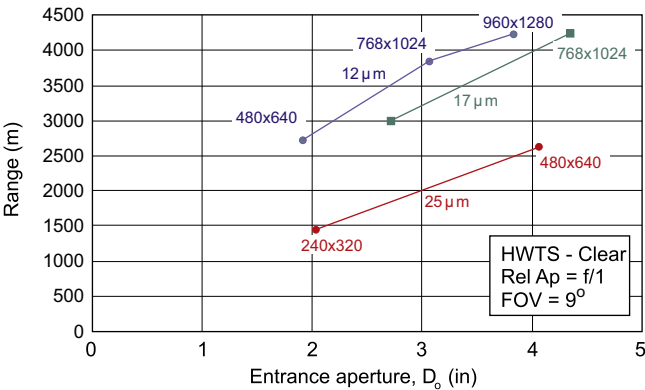


Fig. 84. Calculated detection range as a function of sensor optics and detector pixel size and format using NVESD NV Therm IP modelling, assuming a 35 mK NETD ($f/1$, 30 Hz) for all detectors (after Ref. [168]).

sensitivity of 35 mK *NETD* (f/1, 30 Hz) for the 25, 17, and 12 μm pitch pixel of uncooled FPAs. The advantages of small pixel pitch and large format UFPAs are obvious. By switching to smaller pitch and larger format detectors, the detection range of a weapon sight increases significantly with a fixed optic.

Because the cost of the optics made of Ge, the standard material, depends approximately upon the square of the diameter, so reducing of the pixel size causes reducing cost of the optics. These reductions in optics size would have a major benefit in reducing the overall size, weight and cost of manportable IR systems. In addition the reduction in pixel size allows a significantly larger number of FPAs to be fabricated on each wafer. However, the *NETD* is inversely proportional to the pixel area, thus, if the pixel size is reducing from $50 \times 50\text{-}\mu\text{m}$ to $17 \times 17\text{-}\mu\text{m}$, and everything else remained the same, the *NETD* would increase by the factor of nine. Improvements in the readout electronics are needed to compensate for this.

In the outlook of the next 12- μm pixel node uncooled IR FPA, further improvements in detector technology are necessary. The development of highly sensitive 12- μm microbolometer pixels, however, presents significant challenges in both fabrication process improvements and in pixel design. The current sensitivity (in A/W) of a scaled pixel may be improved by increasing the fill factor (FF), the absorption (ε), the thermal coefficient of the resistance (*TCR*), the applied voltage (V_{bias}) or by reducing the thermal conductance (G_{th}) or the resistance value of the thermistor (R), as is shown by equation

$$R_i = \frac{FF \times \varepsilon \times TCR \times V_{\text{bias}}}{G_{th} \times R} \quad (14)$$

At present stage of technology, the detector fill factor and the absorption coefficient are closed to their ideal value and only a little benefit can be expected from the optimization of these two parameters. More gain can be obtained through improvement of the thermistor material; its *TCR* and R . A promising approach is the development of lower resistance a-Si/a-SiGe thin films [169,170]. *TCR* of Si alloy has been increased to $\approx 3.9\%/K$ from a baseline of $3.2\%/K$ without an increase in material 1/f-noise. Amorphous-silicon technology is particularly susceptible to that, because it is capable of a *TCR* in excess of $5\%/^{\circ}\text{C}$ while maintaining its other excellent properties [171]. With this advantage, it is likely the a-Si microbolometer will soon establish itself as the premium technology for uncooled IR imaging. Also properties of the Si/SiGe single crystalline quantum well as a thermistor material are promising [172].

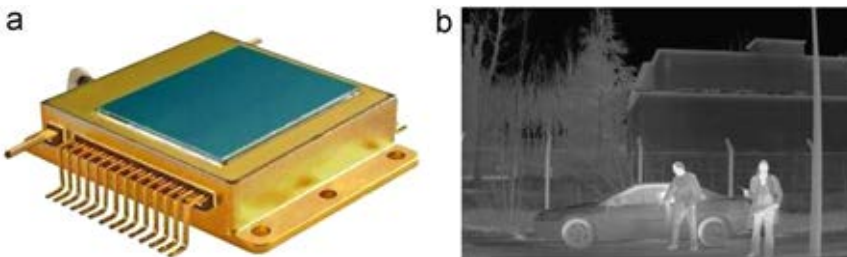


Fig. 85. Unisys 17- μm pitch 1024 \times 768 FPA: (a) packaging and (b) thermal image (after Ref. [167]).

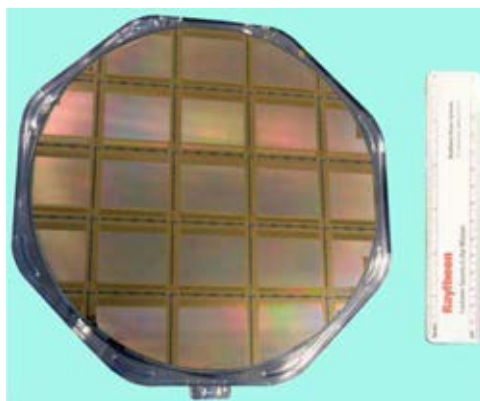


Fig. 86. 2048×1536 uncooled VO_x microbolometers with $17\text{-}\mu\text{m}$ pixel pitch on a 200 mm wafer (after Ref. [173]).

Development of $17\text{-}\mu\text{m}$ pixel pitch FPAs is being extended to both smaller arrays (320×240) and arrays larger than 3 megapixel. Thermal image obtained with 1024×768 a-Si microbolometer detector shows both high sensitivity and resolution what is shown in Fig. 85(b). This device can detect temperature variations smaller than 50 mK.

Currently, the largest microbolometer array fabricated by Raytheon is shown on a wafer in Fig. 86. In the fabrication of 2048×1536 staring arrays and associated ROIC circuits, a stitching technique has been used. Each 200 mm wafer contains nine- 2048×1536 uncooled detector die, which represents an 80% increase in yield over an equivalent 150 mm wafer.

8.9. Third generation infrared detectors

In the infrared spectral region, third generation systems are now being developed. In this class of detector, four detector technologies that are developing multicolor capability are visited here: HgCdTe, QWIPs, antimonide based type-II SLs, and QDIPs [174,175]. Third generation IR systems considered to be those that provide enhanced capabilities like larger number of pixels, higher frame rates, better thermal resolution as well as multicolor functionality and other on-chip functions. Multicolor capabilities are highly desirable for advance IR systems. Systems that gather data in separate IR spectral bands can discriminate both absolute temperature and unique signatures of objects in the scene. By providing this new dimension of contrast, multiband detection also offers advanced color processing algorithms to further improve sensitivity compared to that of single-color devices.

The unit cell of integrated multicolor FPAs consists of several co-located detectors, each sensitive to a different spectral band. Radiation is incident on the shorter band detector, with the longer wave radiation passing through to the next detector. Each layer absorbs radiation up to its cut-off, and hence transparent to the longer wavelengths, which are then collected in subsequent layers. In the case of HgCdTe, this device architecture is realized by placing a longer wavelength HgCdTe photodiode optically behind a shorter wavelength photodiode.

Back-to-back photodiode two-color detectors were first implemented using quaternary III–V alloy ($\text{Ga}_x\text{In}_{1-x}\text{As}_y\text{P}_{1-y}$) absorbing layers in a lattice matched InP structure sensitive to two different SWIR bands [176]. A variation on the original back-to-back concept was

implemented using HgCdTe at Rockwell [177]. Following the successful demonstration of dual-band detectors in LPE-grown HgCdTe devices [178], the MBE and MOCVD techniques have been used for the growth of a variety of multispectral detectors at Raytheon, BAE Systems, Leti, Selex, and QinetiQ, DRS, Teledyne, and NVESD.

Both sequential mode and simultaneous mode detectors are fabricated from multilayer materials. The simplest two-colour HgCdTe detector, and the first to be demonstrated, was the bias selectable n–P–N triple-layer heterojunction (TLHJ), back-to-back photodiode shown in Fig. 87(a) (capital letter means wider band gap structure). When the polarity of the bias voltage applied to the bump contact is positive, the top (LW) photodiode is reverse biased and the bottom (SW) photodiode is forward biased. The SW photocurrent is shunted by the low impedance of the forward biased SW photodiode, and the only photocurrent to emerge in the external circuit is the LW photocurrent. When the bias voltage polarity is reversed, the situation reverses; only SW photocurrent is available. Switching times within the detector can be relatively short, on the order of microseconds, so detection of slowly changing targets or images can be achieved by switching rapidly between the MW and LW modes.

Many applications require true simultaneous detection in the two spectral bands. This has been achieved in a number of ingenious architectures shown in Fig. 87(b–f). Two different architectures are shown. The first one is the classical n–P–N back-to-back

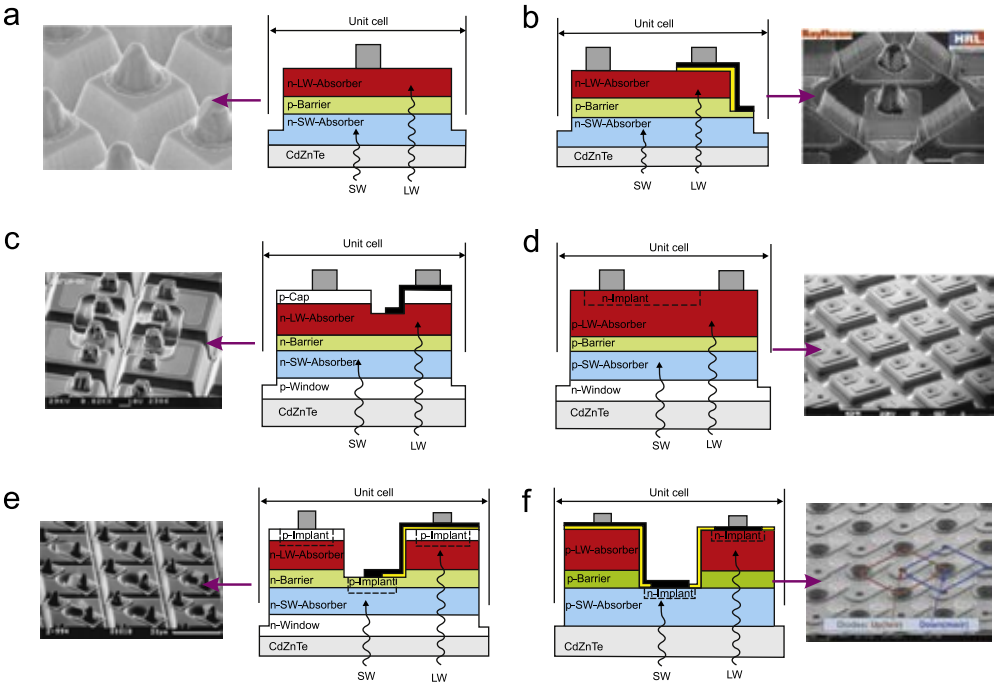


Fig. 87. Cross section views of unit cells for various back-illuminated dual-band HgCdTe detector approaches: (a) bias-selectable n–p–n structure reported by Raytheon [178], (b) simultaneous n–p–n design reported by Raytheon [179], (c) simultaneous p–n–n–p reported by BAE Systems [180], (d) simultaneous n–p–p–p–n design reported by Leti [181], (e) simultaneous structure based on p-on-n junctions reported by Rockwell [182], and simultaneous structure based on n-on-p junctions reported by Leti [183].

photodiode structure [Fig. 87(b)]. In the case of the architecture developed at Leti (Fig. 6d), the two absorption materials are p-type separated by a barrier to prevent any carrier drift between the two n-on-p diodes. Each pixel consists of two standard n-on-p photodiodes, where the p-type layers are usually doped with Hg vacancies. The shorter wavelength diode is realized during epitaxy by simply doping part of the first absorbing layer with In. The longer wavelength junction is obtained by a planar implantation process. It should be noted that the electron mobility is around 100 times greater in n-type material than holes in p-type material and, hence, the n-on-p structures will have a much lower common resistance. This is an important consideration for large area FPAs with detection in the LW range due to the larger incident-photon flux.

The last two architectures showed in Fig. 87(e) and f, called “pseudo-planar”, present totally different approach. They are close to the structure proposed by Lockwood et al. [184] in 1976 for PbTe/PbSnTe heterostructure two-colour photodiodes. They are based on the concept of two p-on-n [Fig. 87(e)] or n-on-p [Fig. 87(f)] diodes fabricated by p-type or n-type implantation, respectively, but on two different levels of a three-layer heterostructure. The architecture developed by Rockwell is a simultaneous two-colour MWIR/LWIR FPA technology based on a double-layer planar heterostructure (DLPH) MBE technology [Fig. 87(e)]. To prevent the diffusion of carriers between two bands, a wide-band gap 1- μm thick layer separates these two absorbing layers. The diodes are formed by implanting arsenic as a p-type dopant and activating it with an anneal. This results in a unipolar operation for both bands. The implanted area of Band 2 is a concentric ring around the Band 1 dimple. Because the lateral carrier-diffusion length is larger than the pixel pitch in the MWIR material, and the Band 1 junction is shallow, each pixel is isolated by dry-etching a trench around it to reduce carrier cross-talk. The entire structure is capped with a layer of material with a slightly wider band gap to reduce surface recombination and simplify passivation. All these simultaneous dual-band detector architectures require an additional electrical contact from an underlying layer in the multijunction structure to both the SW and the LW photodiode. The most important distinction is the requirement of a second readout circuit in each unit cell.

Fig. 88 illustrates examples of the spectral response from different two-color devices. Note that there is minimal crosstalk between the bands, since the short-wavelength detector absorbs nearly 100% of the shorter wavelengths. Test structures indicate that the separate photodiodes in a two-color detector perform exactly like single-color detectors in terms of achievable R_0A variation with wavelength at a given temperature.

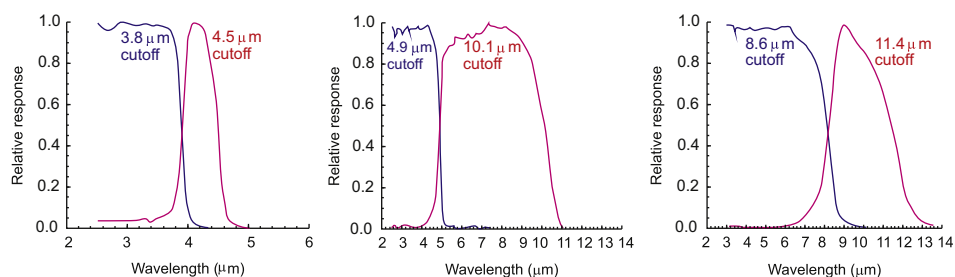


Fig. 88. Spectral response curves for two-colour HgCdTe detectors in various dual-band combinations of MWIR and LWIR spectral bands (after Ref. [132]).

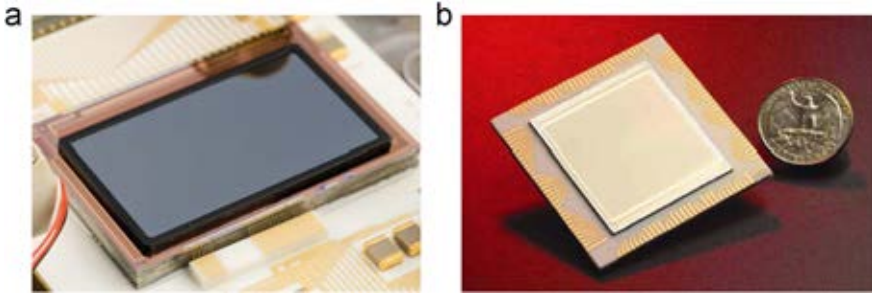


Fig. 89. Dual-band megapixel MW/LW FPAs: (a) RVS 1280×720 format HgCdTe FPAs mounted on dewar platforms (after Ref. [185]), and (b) JPL 1024×1024 format QWIP FPA mounted on a 124-pin lead less chip carrier (after Ref. [190]).

Large two-color FPAs are fabricated by Raytheon [185,186], Sofradir [187,188], and Selex [189]. RVS has developed two-colour, 1280×720 large format MWIR/LWIR FPAs with $20 \times 20 \mu\text{m}$ unit cells [see Fig. 89(a)]. The ROICs share a common chip architecture and incorporate identical unit cell circuit designs and layouts; both FPAs can operate in either dual-band or single-band modes. High quality FPAs with cut-offs ranging out to $11 \mu\text{m}$ at 78 K have demonstrated excellent sensitivity and pixel operabilities exceeding 99.9% in the MW band and greater than 98% in the LW band. Median 300 K *NEDT* values at $f/3.5$ of approximately 20 mK for the MW and 25 mK for the LW have been measured for dual-band time division multiplexed integration (TDMI) operation at 60 Hz frame rate with integration times corresponding to roughly 40% (MW) and 60% (LW) of full well charge capacities. Excellent high resolution IR camera imaging with $f/2.8$ FOV broadband refractive optics at 60 Hz frame rate has been achieved.

Both Sofradir as well as Selex fabricate TV format (640×512) families of $24\text{-}\mu\text{m}$ pixel pitch MWIR/MWIR dual-band FPAs. In Sofradir's ALTAIR arrays two separate input stages are designed into each pixel to allow simultaneous integration and readout of both bands. They show median *NEDT* around 20 mK with operability over 99.5% [188].

QWIPs are also ideal detectors for the fabrication of pixel co-registered simultaneously readable two-colour IR FPAs because a QWIP absorbs IR radiation only in a narrow spectral band and is transparent outside of that absorption band [191]. Thus it provides zero spectral cross-talk when two spectral bands are more than a few microns apart. Devices capable of simultaneously detecting two separate wavelengths can be fabricated by vertical stacking of the different QWIP layers during epitaxial growth. Separate bias voltages can be applied to each QWIP simultaneously via doped contact layers that separate the MQW detector heterostructures. Fig. 90 shows schematically the structure of a two-colour stacked QWIPs and provides additional insight into processing technology developed at JPL with pixels collocated and simultaneously readable [192]. As shown in Fig. 90(b), the carriers emitted from each multi-quantum well (MQW) region are collected separately using three contacts. The middle contact layer [see Fig. 90(c)] is used as the detector common. The electrical connections to the detector common and the LWIR connection are brought to the top of each pixel using via connections. Electrical connections to the common contact and the LWIR pixel connection are brought to the top of each pixel using the gold via connections.

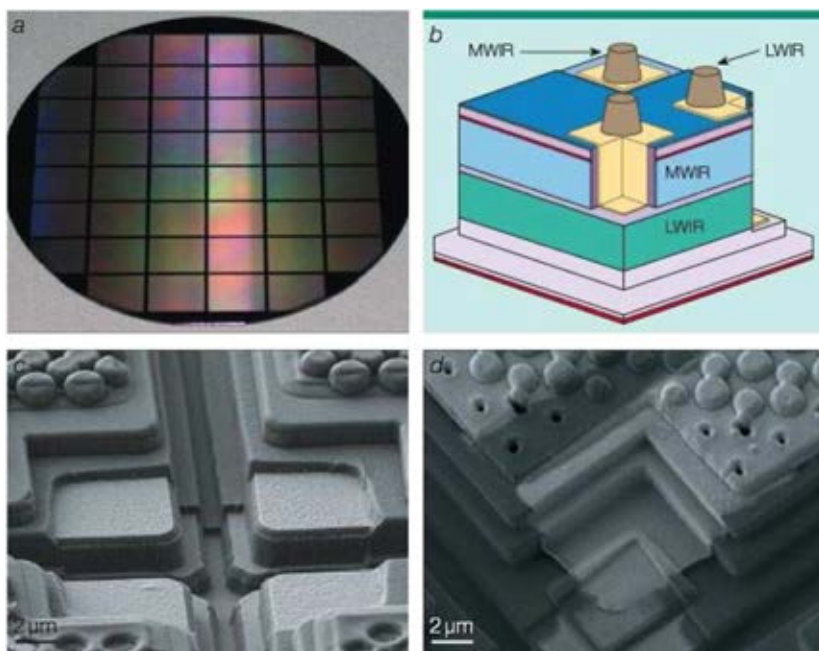


Fig. 90. Two-colour 320×256 MWIR/LWIR QWIP FPA: (a) forty eight FPAs processed on a 4-in. GaAs wafer, (b) 3-D view of pixel structure, (c) electrical connections to the common contact, (d) the pixel connections are brought to the top of each pixel using the gold via connections (after Ref. [192]).

A four-band FPAs has been demonstrated by stacking different multi-quantum well structures, which are sensitive in 4–6, 8.5–10, 10–12, and 13–15 μm bands [193]. The 640×512 format FPA consists of four 640×128 pixel areas which are capable of acquiring images in these bands. Four separate detector bands were defined by a deep trench etch process and the unwanted spectral bands were eliminated by a detector short-circuiting process. Gold-coated reflective 2-D etched gratings electrically shorted the unwanted top detectors.

More recently, the research group from Jet Propulsion Laboratory has implemented a MWIR/LWIR pixel co-registered simultaneously readable 1024×1024 dual-band device structure that uses only two indium bumps per pixel (Fig. 91) compared to three indium bumps per pixel with pixel co-located dual-band devices [194]. In this device structure the detector common (or ground) is shorted to the bottom detector common plane via a metal bridge. Thus, this device structure reduces the number of indium bumps by 30% and has a unique advantage in large format FPAs, since more indium bumps require additional force during the FPA hybridization process. The pitch of the detector array is 30 μm and the actual MWIR and LWIR pixel sizes are $28 \times 28 \mu\text{m}^2$. Fig. 89(b) shows the picture of a 1024×1024 pixel MW/LW dual band QWIP FPA mounted on a 124-pin lead less chip carrier. The estimated *NEDT* based on single pixel data of MWIR and LWIR detectors at 70 K are 22 and 24 mK, respectively. The experimentally measured *NEDT* values are 27 and 40 mK for MWIR and LWIR, respectively.

In most of the two-colour QWIP FPAs three-bump approach is used to assure simultaneous integration of the detector output in different bands. However this design decreases the FPA

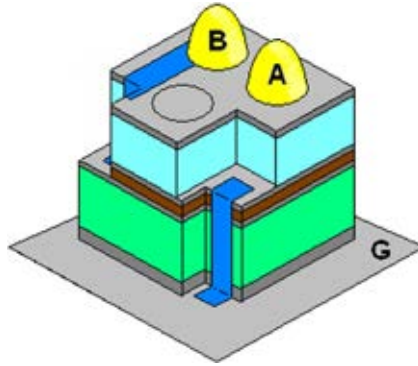


Fig. 91. 3-D view of dual-band QWIP device structure showing via connects for independent access of MWIR and LWIR devices. The colour code is as follows, orange— isolation layer; green—LWIR QWIP; light blue—MWIR QWIP; grey—contact layer; dark blue—metal bridges between MQW regions; yellow—indium bumps (after Ref. [194]). (For interpretation of the references to color in this figure legend, the reader is referred to the web version of this article.)

fill factor and significantly complicates the fabrication process. Recently, the research group from Middle East Technical University in Ankara has demonstrated the voltage tunable two-colour 640×512 MWIR/LWIR FPAs using commercially readout integrated circuits [195]. Dual-band sensors are implemented with conventional FPA fabrication process requiring only one In bump on each pixel making it possible to fabricate large format arrays at the cost and yield of single band detectors.

Results presented in this section indicate that QWIPs have shown significant progress in recent years, especially in their applications to the multiband imaging problem. It is a niche in which they have an intrinsic advantage due to the comparative ease of growing multiband structures by MBE with very low defect density.

Recently, type-II InAs/GaSb SLs has emerged as a candidate for third generation IR detectors [175]. Over the past few years type-II superlattice based detectors have been also made rapid progress in fabrication of dual-band FPAs. Fraunhofer's dual-colour MWIR superlattice detector array technology with simultaneous, co-located detection capability is ideally suited for airborne missile threat warning systems [196,197]. Fig. 92 illustrates a fully processed dual-colour 288×384 FPA. With 0.2 ms integration time and 78 K detector temperature, the superlattice camera achieves an *NEDT* of 29.5 mK for the blue channel ($3.4 \leq \lambda \leq 4.1 \mu\text{m}$) and 14.3 mK for the red channel ($4.1 \leq \lambda \leq 5.1 \mu\text{m}$).

As an example, the excellent imagery delivered by the 288×384 InAs/GaSb dual-colour camera is presented in Fig. 93. The image is a superposition of the images of the two channels coded in the complimentary colours cyan and red for the detection ranges of 3–4 and 4–5 μm , respectively. The red signatures reveal hot CO₂ emissions in the scene, whereas water vapour, e.g., from steam exhausts or in clouds, appear cyan due to the frequency dependency of the Rayleigh scattering coefficient.

The progress towards third generation imaging based on type-II superlattices is going on quickly. Recently, the first MW/LW FPAs have been demonstrated [198].

8.10. Readiness level of LWIR detector technologies

We follow here after Ref. [7]. Table 10 provides a snapshot of the current state development of LWIR detectors fabricated from different material systems. Note that

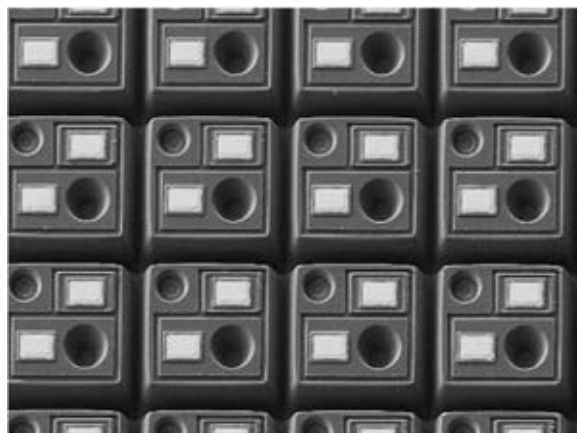


Fig. 92. SEM images illustrating the processing of 288×384 dual colour InAs/GaSb SLS FPAs. At a pixel pitch of $30 \mu\text{m}$, three contact lands per pixel permit simultaneous and spatially coincident detection of both colours (after Ref. [197]). (For interpretation of the references to color in this figure legend, the reader is referred to the web version of this article.)



Fig. 93. Bispectral infrared image of an industrial site taken with a 384×288 dual-colour InAs/GaSb SL camera. The two-colour channels $3\text{--}4 \mu\text{m}$ and $4\text{--}5 \mu\text{m}$ are represented by the complementary colours cyan and red, respectively (after Ref. [196]). (For interpretation of the references to color in this figure legend, the reader is referred to the web version of this article.)

TRL means technology readiness level. The highest level of TRL (ideal maturity) achieves value of 10. The highest level of maturity (TRL=9) is credited to HgCdTe photodiodes and microbolometers. A little less, TRL=8, for QWPs. The type-II InAs/GaInSb SL structure has great potential for LWIR spectral range application with performance comparable to HgCdTe for the same cutoff wavelength, but require a significant investment and fundamental material breakthrough to mature.

QDIP detector technology is at a very early stage of development (TRL=1–2). The bias-dependent spectral response of this type of detector can be exploited to realize spectrally smart sensors whose wavelength and bandwidth can be tuned depending on the desired application. The main disadvantage of QDIPs is the large inhomogeneous linewidth of the QD ensemble variation of dot size in the Stranski–Krastanow growth mode. As a result, the absorption coefficient is reduced what has a deleterious effect on QDIP performance [199].

Table 10
Comparison of LWIR existing state-of-the-art device systems for LWIR detectors (after Ref. [7]).

	Bolometer	HgCdTe	Type-II SLs	QWIP	QDIP
Maturity Status	TRL 9 Material of choice for application requiring medium to low performance	TRL 9 Material of choice for application requiring high performance	TRL 2–3 Research and development	TRL 8 Commercial	TRL 1–2 Research and development
Military system examples	Weapon sight, night vision goggles, missile seekers, small UAV sensors, unattended ground sensors	Missile intercept, tactical ground and air born imaging, hyper spectral, missile seeker, missile tracking, space based sensing	Being developed in university and evaluated industry research environment	Being evaluated for some military applications	Very early stages of development at universities
Limitations	Low sensitivity and long time constants	Performance susceptible to manufacturing variations. Difficult to extend to > 14-μm cutoff	Requires a significant, > \$100 M, investment and fundamental material breakthrough to mature	Narrow bandwidth and low sensitivity	Narrow bandwidth and low sensitivity
Advantages	Low cost and requires no active cooling, leverages standard Si manufacturing equipment	Near theoretical performance, will remain material of choice for minimum of the next 10–15 years	Theoretically better than HgCdTe at > 14-μm micron cut-off, leverages commercial III-V fabrication techniques	Low cost applications. Leverages commercial manufacturing processes. Very uniform material	Not sufficient data to characterize material advantages

Note: TRL—technology readiness level.

9. Far-IR and sub-mm-wave detector arrays

The detection of far-IR and sub-mm-wave radiation is resistant to the commonly employed techniques in the neighbouring microwave and infrared (IR) frequency bands. In THz detection the use of solid state detectors has been hampered for the reasons of transit time of charge carriers being larger than the time of one oscillation period of THz radiation. Also the energy of radiation quanta is substantially smaller than the thermal energy at room temperature and even liquid nitrogen temperature.

Detector development is at the heart of all current plants. There are exist a large variety of traditional deeply cooled mm and sub-mm wavelength detectors (mainly bolometers) as well as new propositions based on optoelectronic quantum devices [200], carbon nanotube bolometers, plasma wave detection by field effect transistors, and hot electron room temperature bipolar semiconductor bolometers [201,202].

Progress in THz detector sensitivity has been impressive in a period more than half century what is shown in Fig. 94(a) in the case of bolometers used in far-IR and sub-mm-wave astrophysics [203]. The NEP value has decreased by a factor of 10¹¹ in 70 years, corresponding improvements by factor of two every two years. Individual detectors achieved photon noise limited performance for ground-based imaging in the 1990s.

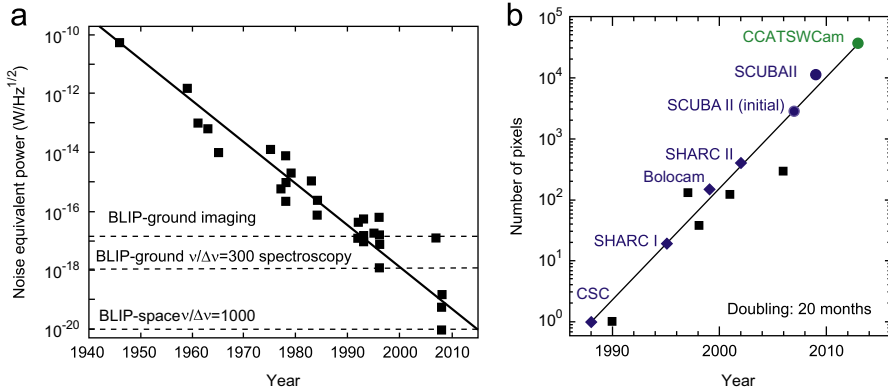


Fig. 94. Trends in development of THz detectors: (a) improvement of the bolometer NEP-value for more than half a century (sensitivity doubled every 2 years over the past 70 years), (b) detector arrays have doubled in format every 20 months over the past 10 years; green symbol indicates current expectation (adapted after Ref. [203]). (For interpretation of the references to color in this figure legend, the reader is referred to the web version of this article.)

The photon noise from astrophysical sources, achievable in space with a cold telescope, $\sim 10^{-18} \text{ W Hz}^{1/2}$, is now within demonstrated sensitivities. In present decade, the studies of inflation via cosmic microwave background (CMB) polarization will be driven not by detector sensitivity but by array formats. Far-infrared spectroscopy from a cold telescope however requires sensitivity $\sim 10^{-20} \text{ W Hz}^{1/2}$ to reach the astrophysical photon noise limit. Achieving this sensitivity in working detector arrays remains a challenge for the coming decade, as the number of the detectors in the array is a key parameter that determines the information capabilities of the system [202] and the speed improvement in obtaining a complete imaging or spectrum when observing galactic objects, as the accumulation time τ_{acc} at each sensitive element is proportional to the number M_e of sensitive elements in the array and inversely proportional to the frame rate f_r , and the number of picture dots M , $\tau_{\text{acc}} = 1/f_r(M_e/M)$.

The development of pixel arrays has been comparably revolutionary [203]. Fig. 94(b) shows increasing in number of pixels in the period over last two decades. Detector arrays have doubled in format every 20 months over the past 10 years producing arrays with pixels now numbering in the thousands. Steady increase in overall observing efficiency is expected in near future, which by now has reached factors in the range of 10^{12} in comparison to capabilities in the early 1960s.

NASA has historically been the leading US agency for promoting the development of long wavelength detector technologies. Fig. 95 shows the sensitivities of currently-planned or active far-IR/sub-mm spectroscopic facilities in near future, instead Table 11 describes shortly several airborne and space-borne platform missions.

As last figure shows, the James Webb Space Telescope (JWST) operates at wavelengths below about $27 \mu\text{m}$. The Atacama Large Millimeter/submillimeter Array (ALMA) operating through a number of submillimeter atmospheric windows as well as $\sim 650 \mu\text{m}$, will have sensitivities at least 100 times higher than Herschel spanning the intervening $60\text{--}650 \mu\text{m}$ wavelength range. ALMA and JWST are currently scheduled to start operations within the next few years. The Space Infrared Telescope for Cosmology and Astrophysics (SPICA), with launch envisioned in 2017, will provide two-to-three

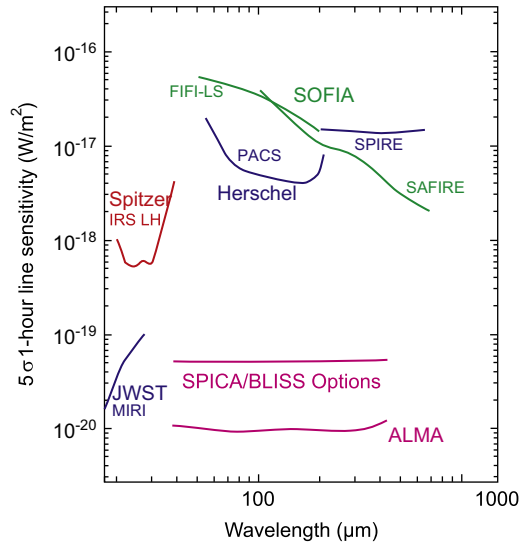


Fig. 95. Sensitivity of far-IR spectroscopy platforms (after Ref. [203]).

orders of magnitude increase in sensitivity in comparison with Herschel that will bring far-IR/sub-mm sensitivity into line with those of JWST and ALMA. The ambitious requirements of future space missions are summarized in Table 12.

All radiation detection systems in THz spectral ranges can be divided into two groups:

- incoherent detection systems (with direct detection sensors), which allow only signal amplitude detection and which, as a rule, are broadband detection systems, and
- coherent detection systems, which allow detecting not only the amplitude of the signal, but also its phase.

Coherent signal detection systems use heterodyne circuit design, since so far, for high radiation frequency range proper amplifiers do not exist. The detected signals are transferred to much lower frequencies ($f \approx 1\text{--}30$ GHz) where they are amplified by low-noise amplifiers. Basically these systems are selective (narrow-band) detection systems.

Detectors with direct signal detection basically are used in spectroscopic and technical vision systems. In sub-mm and mm wavelength bands they are suitable for applications that do not require ultrahigh spectral resolution ($\nu/\Delta\nu \approx 10^6$) that is provided by heterodyne detector spectroscopic systems. But unlike heterodyne detection systems, there do not exist the problem of multielement arrays formation conditioned by local oscillation (LO) power and fast detector response ($\tau \approx 10^{-10}\text{--}10^{-11}$ s).

In direct THz detection systems even room temperature detectors can be used with relatively long response time ($\tau \approx 10^{-2}\text{--}10^{-3}$ s) and modest sensitivity. Among them are Golay cells, pyroelectric detectors, different kind of thermal direct detection detectors (bolometers and microbolometers), which use antennas to couple power to a small thermally absorbing regions. The NEP value for uncooled detectors typically is from 10^{-10} to 10^{-9} W/Hz^{1/2} (see Table 13 [205]).

Table 11
Far-IR spectroscopy platforms.

**Spitzer Space
Telescope 2003**



The **Spitzer Space Telescope** was launched in August 2003. It is the last of NASA's "great observatories" in space. Spitzer is much more sensitive than prior infrared missions and study the universe at a wide range of infrared wavelengths. Spitzer concentrates on the study of brown dwarfs, super planets, protoplanetary and planetary debris disks, ultraluminous galaxies, active galaxies, and deep surveys of the early universe.

SOFIA 2005



SOFIA (Stratospheric Observatory For Infrared Astronomy) was finally completed in 2005. SOFIA, a joint project between NASA and the German Space Agency, incorporates a 2.5 m optical/infrared/sub-millimetre telescope mounted in a Boeing 747. Designed as a replacement for the successful Kuiper Airborne Observatory, SOFIA is the largest airborne telescope in the world.

**Herschel Space
Observatory 2009**



The **Herschel Space Observatory** carried into orbit in May 2009 is a European Space Agency infrared-submillimetre mission. Herschel is perform spectroscopy and photometry over a wide range of infrared wavelengths and is used to study galaxy formation, interstellar matter, star formation and the atmospheres of comets and planets. The Herschel Observatory is capable of seeing the coldest and dustiest objects in space. It is the largest space telescope ever launched carrying a single mirror of 3.5 m in diameter.

ALMA 2011



The **Atacama Large Millimeter/submillimeter Array (ALMA)** is an international partnership between Europe, North America, East Asia and the Republic of Chile to build the largest astronomical project in existence. It is an astronomical interferometer, comprising an array of 66 12-m and 7-m diameter radiotelescopes observing at millimetre and submillimetre wavelengths. It is being built on the Chajnantor plateau at 5000 m altitude in the Atacama desert of northern Chile. ALMA is expected to provide insight on star birth during the early universe and detailed imaging of local star and planet formation. Costing more than a billion dollars, it is the most ambitious ground-based telescope currently under construction. ALMA will begin scientific observations in the second half of 2011 and is scheduled to be fully operational by the end of 2012.

Table 11 (continued)

James Webb Space Telescope 2014

The **James Webb Space Telescope (JWST)** is a large, infrared-optimized space telescope, scheduled for launch in 2014. It is a visible/infrared space mission which will have extremely good sensitivity and resolution, giving us the best views yet of the sky in the near-mid infrared. JWST will be used to study the early universe and the formation of galaxies, stars and planets. Webb will have a large mirror, 6.5 m in diameter and a sunshield the size of a tennis court. Both the mirror and sunshade won't fit onto the rocket fully open, so both will fold up and open once Webb is in outer space. Webb will reside in an orbit about 1.5 million km from the Earth.

SPICA/BLISS 2017

The **Background-Limited Infrared-Submillimeter Spectrograph (BLISS)** is a far-IR spectrograph concept for **Space Infrared Telescope for Cosmology and Astrophysics (SPICA)**. The SPICA mission is a future Japanese infrared astronomical satellite, with launch envisioned in 2017, to explore the universe with a cooled, large telescope.

The philosophy of BLISS is to provide a rapid survey spectroscopy capability over the full far-IR range. The baseline approach is a suite of broadband grating spectrometer modules with transition-edge superconducting (TES) bolometers.

SPICA will use a cooled telescope (3.5 m diameter primary, ~ 5 K) to achieve sensitivities currently inaccessible to existing facilities operating over this wavelength range (SOFIA, Herschel).

Table 12

Requirements for future space applications (after Ref. [204]).

Science	Future opportunities	Requirements		
		NEP [W/Hz]	τ [ms]	Format
CMB polarization	Inflation probe	$(1-5) \times 10^{-18}$	1–30	10^4
Galaxy evolution	SPICA/BLISS	$(3-30) \times 10^{-20}$	100	5000
Star formation	SAFIR/CALISTO imaging	3×10^{-19}	10	10^5
Circumstellar disks	SAFIR/CALISTO spectroscopy	3×10^{-20}	100	10^5
	SPIRIT	1×10^{-19}	0.2	256

Table 13

Parameters of some uncooled THz wave detectors (after Ref. [205]).

Detector type	Modulation frequency (Hz)	Operation frequency (THz)	Noise equivalent power (W/Hz ^{1/2})
Golay cell	≤ 20	≤ 30	10^{-9} – 10^{-10}
Piezoelectric	$\leq 10^2$ (decreases with f increasing and depends on dimensions)	≤ 30	$\approx (1-3) \times 10^{-9}$ (decreases with ν increase)
VO _x microbolometers	$\leq 10^2$	4.3	$> 3 \times 10^{-10}$ (increases with ν increase)
Bi microbolometer	$\leq 10^6$	≤ 3	1.6×10^{-10} (increases with ν increase)
Nb microbolometer	–	≤ 30	5×10^{-11}
Ti microbolometer	530	0.3	4×10^{-11}
Ni microbolometer	30	0.094	1.9×10^{-11}
Schottky diodes	$\leq 10^{10}$	≤ 10	$\geq 10^{-10}$ (increases several orders with ν increase within ~ 0.1 – 10 THz)
Schottky diode (zero biased)	–	–	1.5×10^{-12} (no incident power)
Mott diodes	–	0.1	1×10^{-12}
Si MOSFET	3×10^4	0.645	$\approx 3 \times 10^{-10}$ (depends on gate length and gate voltage)
Si FET	–	≤ 0.7	$> 10^{-10}$ (depends on gate length and gate voltage)
Si CMOS	–	–	5×10^{-11}
SiN membrane	≤ 200	≈ 1.6 – 4.3	10^{-9}
Micro-Golay cell	≤ 30	0.105	3×10^{-7}
HgCdTe HEB	$< 10^8$	≈ 0.03 – 1.5	$\sim 4 \times 10^{-10}$ ($\nu \approx 37$ GHz, increases with ν increase)

In heterodyne detectors the signals with THz frequencies are down-converted to intermediate frequency (IF), preserving the amplitude and phase information of the incoming radiation. In the last several decades the detectors are of choice for high

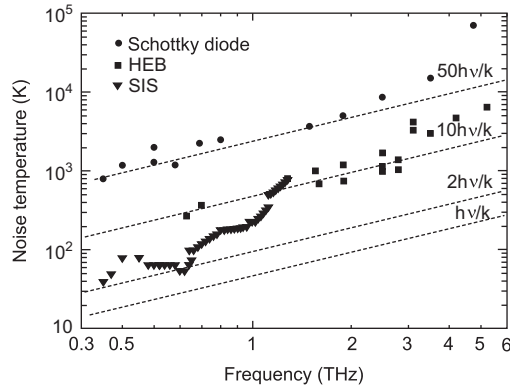


Fig. 96. Noise temperature of Schottky diode mixers, SIS mixers and HEB mixers operated in terahertz spectral band (after Ref. [209]).

resolution spectroscopic studies, cosmic remote sensing, and relatively recently, for mm and sub-mm imaging [206–208].

The technology that has traditionally been available for terahertz receivers utilizes Schottky-barrier diode (SBD) mixers pumped by gas laser local oscillators. The noise temperature of such receivers has essentially reached a limit of about $50h\nu/k$ in frequency range below 3 THz (see Fig. 96). Above 3 THz, there occurs a steep increase, mainly due to increasing losses of the antenna and reduced performance of the diode itself. In the last two decades an impressive improvements in receiver sensitivities have been achieved using superconducting mixers, with both SIS and HEB mixers. In Fig. 96 selected receiver noise temperatures are plotted. Nb-based SIS mixers yield almost quantum limited performance up to gap frequency of 0.7 THz.

Unlike SBD and SIS mixers, the HEB mixer is a thermal detector. Up to 2.5 THz, the noise temperature follows closely the $10h\nu/k$ line. In comparison with Schottky-barrier technology, HEB mixers require three to four orders of magnitude less LO power.

The main advantage of direct-detector systems is that they are less complex than their coherent counterparts. Heterodyne receivers (also called mixers or downconverters), however, provide much higher sensitivity than direct detectors, as well as superior spectral resolution. Below we limit our considerations mainly to direct detector focal plane arrays. Wider treatment of both direct and heterodyne THz detectors is given in Refs. [201,202].

9.1. Schottky barrier arrays

Historically first Schottky-barrier structures were pointed contacts of tapered metal wires (e.g., a tungsten needle) with a semiconductor surface (the so-called crystal detectors). Widely used were, e.g., contacts p-Si/W. At operation temperature $T=300$ K they have $NEP \approx 4 \times 10^{-10} \text{ W/Hz}^{1/2}$. Also pointed tungsten or beryllium bronze contacts to n-Ge, n-GaAs, n-InSb were used (see, e.g., Refs. [210,211]). In the mid 1960s Young and Irvin [212] developed the first lithographically defined whiskered GaAs Schottky diodes for high frequency applications.

Due to limitation of whisker technology, such as constraints on design and repeatability, starting in the 1980s, the efforts were made to produce planar Schottky diodes. Nowadays

the whisker diodes are almost completely replaced by planar diodes. In the case of the discrete diode chip, the diodes are flip-chip mounted into the circuit with either solder or conductive epoxy. Using advanced technology elaborated recently, the diodes are integrated with many passive circuit elements (impedance matching, filters and waveguide probes) onto the same substrate [213]. By improving the mechanical arrangement and reducing loss, the planar technology is pushed well beyond 300 GHz up to several THz. For example, Fig. 97 shows photographs of a bridged Schottky diode and a four-Schottky diodes' chip arrayed in a balanced configuration to increase power handling. The air-bridged fingers replace the now obsolete whisker contact.

Schottky diode mixers in a waveguide configuration have an improved coupling efficiency compared to the open structure mount. To overcome a large shunt capacitance caused by the coplanar contact pads, a surface channel diode, shown in Fig. 98(a), was proposed [215]. The planar diode soldered onto a microstrip circuit (e.g., a thin quartz substrate) is mounted into a waveguide mixer block. The required LO power is about 1 mW. For mixers operating at ≈ 600 GHz, double-sideband (DSB) noise temperature is about 1000 K. To eliminate losses caused by support (influence of surface modes), fabrication of Schottky diodes on thin membrane was developed [216]. In this approach the diodes are integrated with the matching circuit and most of the GaAs substrate is removed from the chip and the entire circuit is fabricated on the remaining GaAs

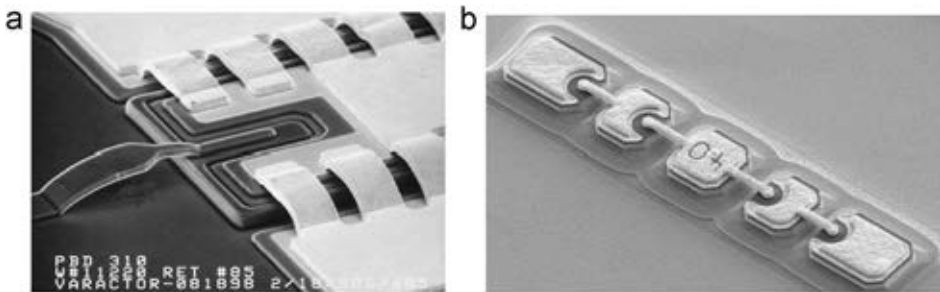


Fig. 97. Photographs of a bridged Schottky diode (a) (after Ref. [214]) and a four-Schottky diodes' chip arrayed in a balanced configuration to increase power handling (b) (after Ref. [213]).

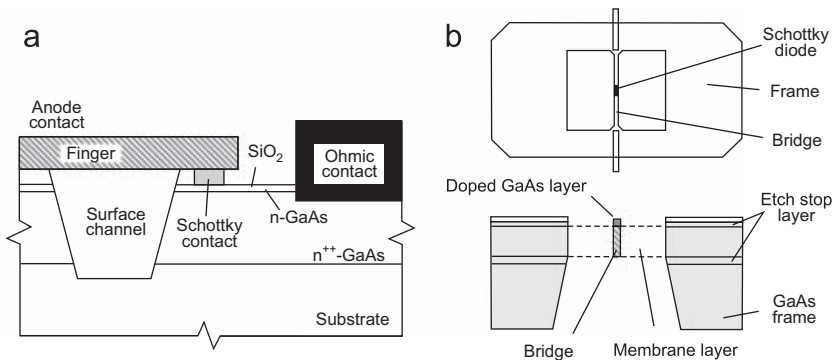


Fig. 98. Designs of planar Schottky diodes: (a) a surface channel design for frequencies below 1 THz, and (b) a GaAs Schottky diode on a membrane (after Ref. [216]).

membrane. Fig. 98(b) shows an example of this type of SBD with 3- μm thick membrane in a $600 \times 1400 \mu\text{m}^2$ GaAs frame.

The typical Schottky diodes usually have high low-frequency noise levels due to introduction of oxides, contaminants, and damage to the junction in the fabrication process. More recently, an alternative method of Schottky barrier formation has been elaborated by molecular beam epitaxy (MBE) in-situ deposition of a semimetal on semiconductor to reduce the imperfections that give rise to excess low-frequency noise, particularly 1/f noise. The semimetal used is an ErAs film grown on Si-doped $(\text{In}_{0.53}\text{Ga}_{0.47}\text{As})_{1-x}(\text{In}_{0.52}\text{Al}_{0.48}\text{As})_x$ on InP substrates [217]. The noise equivalent power (NEP) for these detectors at 639 GHz reach $4 \times 10^{-12} \text{ W/Hz}^{1/2}$, what is about two orders of magnitude better than for typical GaAs Schottky diodes.

The heterodyne SBD receivers are worse compared to cooled HEB receivers and SIS mixers (see Fig. 96). At the same time, SBD receivers operation without cooling gives opportunities for using SBD mixers in different mm and sub-mm applications. Their sensitivity is quite suitable to be used in mm wave spectrometers with moderate resolution [218]. Superconducting mixers typically require microwatt LO powers, which is roughly 3–4 orders of magnitude lower than their SBD predecessors. As a result, a broader range of LO sources can be used. The technologies being used or investigated include diode multipliers, lasers and optoelectronics, and “vacuum tube” oscillators such as klystrons, including novel nano-fabricated versions.

9.2. Silicon and germanium extrinsic photoconductor arrays

The first extrinsic photoconductive detectors were reported in the early 1950s [219]. They were widely used at wavelengths beyond 10 μm prior to the development of the intrinsic detectors. Since the techniques for controlled impurity introduction became available for germanium at an earlier date, the first high performance extrinsic detectors were based on germanium. Today, the problems with producing pure Si have been largely solved, with the exception of boron contamination. Si has several advantages over Ge; for example, three orders of magnitude higher impurity solubilities are attainable, hence thinner detectors with better spatial resolution can be fabricated from silicon. Si has lower dielectric constant than Ge, and the related device technology of Si has now been more thoroughly developed, including contacting methods, surface passivation and mature MOS and CCD technologies. Moreover, Si detectors are characterized by superior hardness in nuclear radiation environments.

Extrinsic silicon detectors can form high impedance photoconductors in a hybrid configuration and can be operated out to about 30 μm . Shallow, hydrogen-like impurities, such as phosphorus, antimony, or arsenic, provide electrons which can be ionised with photon energies in the range of 30–50 meV, depending upon the dopant and concentration used. These devices must be cooled to below 20 K to prevent significant thermal ionization.

The limit to the useful doping which is possible in conventional extrinsic detectors is set by the onset of impurity banding. This occurs when the doping level is sufficiently high that the wavefunctions of neighbouring impurities overlap and their energy level is broadened to a band which can support hopping conduction. When this occurs it limits the detector resistance and photoconductive gain, and also increases the dark current and noise. To overcome the impurity banding effect and in addition, to improve radiation hardness

and reduce the optical cross-talk between adjacent elements of an array, the blocked impurity band (BIB) device was proposed.

A BIB detector structure is displayed in Fig. 99. This structure usually have a thin lightly-doped n^- -region (usually grown epitaxially) between the absorbing n-type region and the common backside implant (p^+ -region) in order to block hopping-conduction currents from reaching the p^+ -contact, which are substantial at the doping levels used in the active detection region. Doping of active layer with a thickness value in the 10- μm range is high enough for the onset of an impurity band in order to display high quantum efficiency for impurity ionization. This also prevents the build of large space-charge regions in n-type active regions, which can otherwise result in a dielectric relaxation response that depends on the illumination history.

BIB detectors do not follow the usual photoconductor model. Because of the presence of the blocking layer, the behavior of BIB detectors is closer to that of a reverse-biased photodiode except that photoexcitation of electrons occurs from the donor impurity band to the conduction band. The gap between the impurity band and the conduction band is narrow; therefore, the response of a Si:As BIB detector extends, in comparison with conventional detector, to the VLWIR region of the spectrum. Fig. 100 illustrates the spectral response for several extrinsic silicon and germanium detectors.

The main application of BIB arrays today is for ground and space-based far-infrared astronomy [222]. The arrays should be operated under the most uniform possible conditions, in the most benign and constant environment possible. Their performance is strongly affected by background levels. Extrinsic silicon arrays for high-background applications are less developed

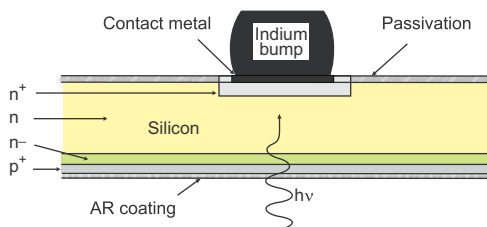


Fig. 99. Blocked impurity band hybrid detector.

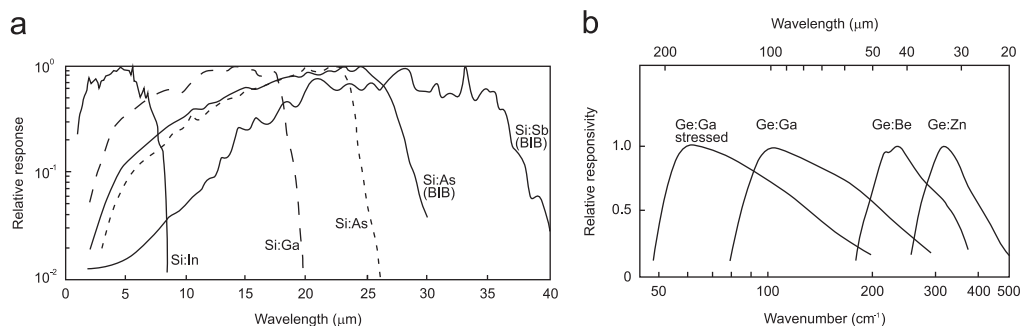


Fig. 100. Relative spectral response of some silicon and germanium extrinsic photoconductors (after Refs. [220,221]).

than that for low-background applications. Detectors in conventional ground-based systems are operated in thermal backgrounds up to 10^9 photons/second.

BIB devices, in large staring array formats are now becoming commercially available. Impressive progress has been achieved especially in Si:As BIB array technology with formats as large as 2048×2048 (pixel size $18\text{-}\mu\text{m}$) operated in spectral band up to $30\text{ }\mu\text{m}$ at $\approx 10\text{ K}$ [223–225]; see Fig. 101 and Table 6.

The readouts for large BIB arrays use a circuit similar to that described shortly in Section 4.2.1. It should be mentioned however, that silicon-based MOSFETs show a number of operational difficulties conditioned by the very low temperatures required for the readout circuits for these detectors. They are related to freeze-out of thermally generated charge carriers, making the circuits unstable, increasing noise, and causing signal hysteresis. They are described in details by Glidden et al. [226].

Silicon detectors have largely supplanted germanium extrinsic detectors for both high and low background applications where comparable spectral response can be obtained. However, for wavelengths longer than $40\text{ }\mu\text{m}$ there are no appropriate shallow dopants for silicon; therefore germanium devices are still of interest for very long wavelengths. Very shallow donors, such as Sb, and acceptors, such as B, In or Ga, provide cut-off wavelengths in the region of $100\text{ }\mu\text{m}$ [see Fig. 100(b)]. The achievement of low NEP values in the range of a few parts $10^{-17}\text{ W/Hz}^{-1/2}$ was made possible by advances in crystal growth development and control the residual minority impurities down to 10^{10} cm^{-3} in a doped crystal. As a result, a high lifetime and mobility value and thus a higher photoconductive gain have been obtained Fig. 101.

However, there are a number of problems with the use of germanium. For example, to control dark current the material must be lightly doped and therefore absorption lengths become long (typically $3\text{--}5\text{ mm}$). Because the diffusion lengths are also large (typically $250\text{--}300\text{ }\mu\text{m}$), pixel dimensions of $500\text{--}700\text{ }\mu\text{m}$ are required to minimize crosstalk. In space applications, large pixels imply higher hit rates for cosmic radiation. This in turn implies very low readout noise for arrays operated in low background limit, what is difficult to achieve for large pixels with large capacitance and large noise. A solution is using the shortest possible exposure time. Due to small energy band gap, the germanium detectors must operated well below the silicon “freeze-out” range—typically at liquid helium temperature.

Application of uniaxial stress along the $[100]$ axis of Ge:Ga crystals reduces the Ga acceptor binding energy, extending the cutoff wavelength to $\approx 240\text{ }\mu\text{m}$ [227]. At the same

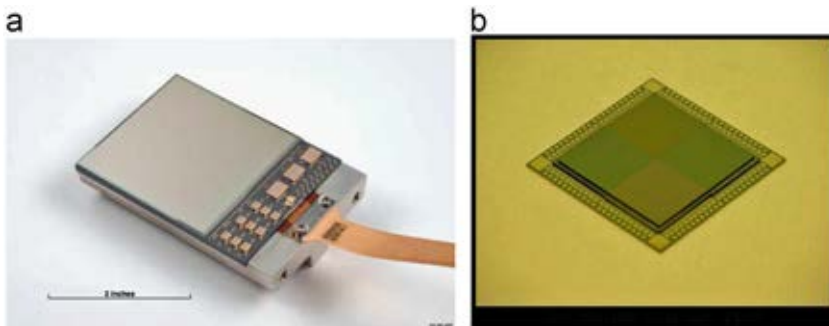


Fig. 101. 2048×2048 Si:As BIB arrays with $25\text{-}\mu\text{m}$ (a) (after Ref. [225]) and $18\text{-}\mu\text{m}$ pitch (after Ref. [224]).

time, the operating temperature must be reduced to less than 2 K. In making practical use of this effect, it is essential to apply and maintain very uniform and controlled pressure to the detector so that the entire detector volume is placed under stress without exceeding its breaking strength at any point. A number of mechanical stress modules have been developed. The stressed Ge:Ga photoconductor systems have found a wide range of astronomical and astrophysical applications [202].

The Infrared Astronomical Satellite (IRAS), the Infrared Space Observatory (ISO), and for the far-infrared channels the Spitzer-Space Telescope (Spitzer) have all used bulk germanium photoconductors. In Spitzer mission a 32×32 -pixel Ge:Ga unstressed array was used for the 70- μm band, while the 160 μm band had a 2×20 array of stressed detectors. The detectors are configured in the so-called Z-plane to indicate that the array has substantial size in the third dimension. The poor absorption of the Ge:Ga detector material requires that the detectors in this array are huge—2 mm long. Due to the long absorption path in germanium, the detectors are illuminated edge-wise with transverse contacts, and the readouts are hidden behind them, what is shown in Fig. 102.

An innovative integral field spectrometer, called the Field Imaging Far-Infrared Line Spectrometer (FIFI-LS) that produces a 5×5 pixel image with 16 spectral resolution elements per pixel in each two bands was constructed at the Max Planck Institut für

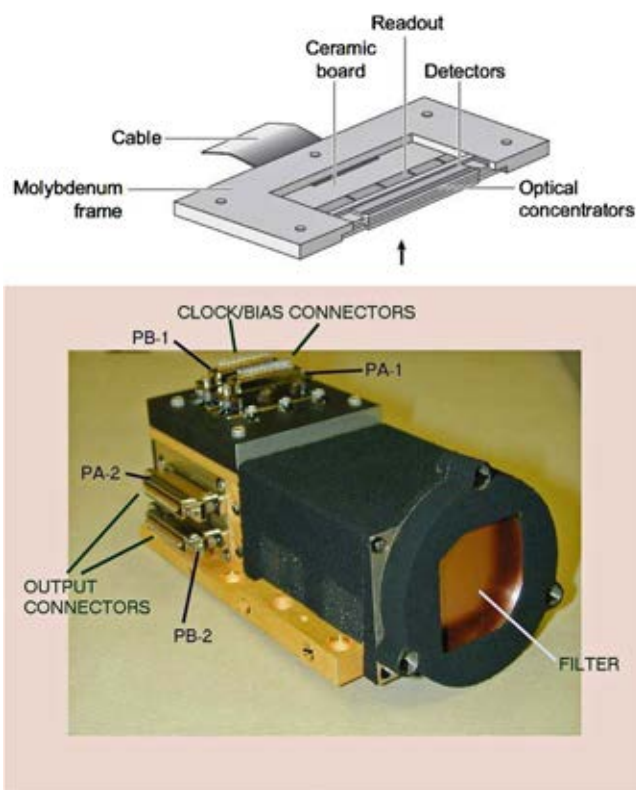


Fig. 102. The Spitzer Space Telescope 70- μm array design of a 4×32 module of the edge-illuminated detectors. Eight such modules are stacked to create the full 32×32 array, which covers the wavelength range 50–110 μm (after Ref. [228]).

Extraterrestrische Physik. This array, shown in Fig. 103, was developed for the Herschel Space Observatory and SOFIA [228,229]. To accomplish this, the instrument has two 16×25 Ge:Ga arrays, unstressed for the 45–110 μm range and stressed for the 110 to 210 μm range. The low-stressed blue detectors has a mechanical stress on the pixels which is reduced to about 10% of the level needed for the long-wavelength response of the red detectors. Each detector pixel is stressed in its own subassembly, and a signal wire is routed to preamplifiers housed nearby what obviously limits this type of array to much smaller formats than are available without this constraints.

The Photodetector Array Camera and Spectrometer (PACS) is one of the three science instruments on ESA's far infrared and sub-millimetre observatory—Herschel Space Laboratory. Apart from two Ge:Ga photoconductor arrays (stressed and unstressed) with 16×25 pixels, each, it employs two filled silicon bolometer arrays with 16×32 and 32×64 pixels, respectively, to perform integral-field spectroscopy and imaging photometry in the 60–210 μm wavelength regime. Fig. 104 shows the spectral response of the filter/detector chain of the PACS photometer in its three bands. Median NEP values are $8.9 \times 10^{-18} \text{ W/Hz}^{1/2}$ for the stressed and $2.1 \times 10^{-17} \text{ W/Hz}^{1/2}$ for the unstressed detectors, respectively. The detectors are operated at $\sim 1.65 \text{ K}$. The readout electronics is integrated into the detector modules—each linear module of 16 detectors is read out by a cryogenic amplifier/multiplexer circuit in CMOS technology but operates at temperature 3–5 K.

Far-infrared photoconductor arrays suffer from the standard bulk photoconductor photometric issues. Especially germanium detectors have complicated responses that affect calibration, observing strategies and data analysis in low background applications. The devices operate at very low bias voltages and even small changes in the operating points of amplifiers can result in unacceptable bias changes on the detectors. More details can be found in Ref. [232].

Usually, the THz arrays have a modular design with many modules stacked together to form a 2-dimensional array. The standard hybrid focal plane array (FPA) architecture is

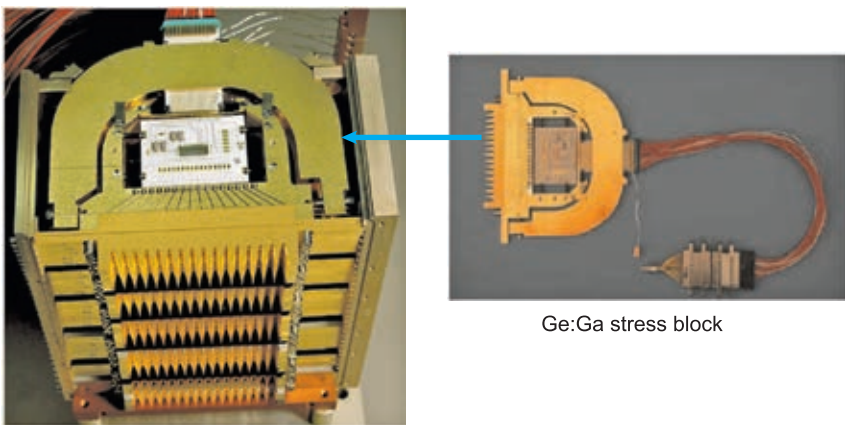


Fig. 103. PACS photoconductor focal plane array. The 25 stressed and low-stress modules of PACS instrument (corresponding to 25 spatial pixels) in the red and blue arrays are integrated into their housing (after Ref. [230]). (For interpretation of the references to color in this figure legend, the reader is referred to the web version of this article.)

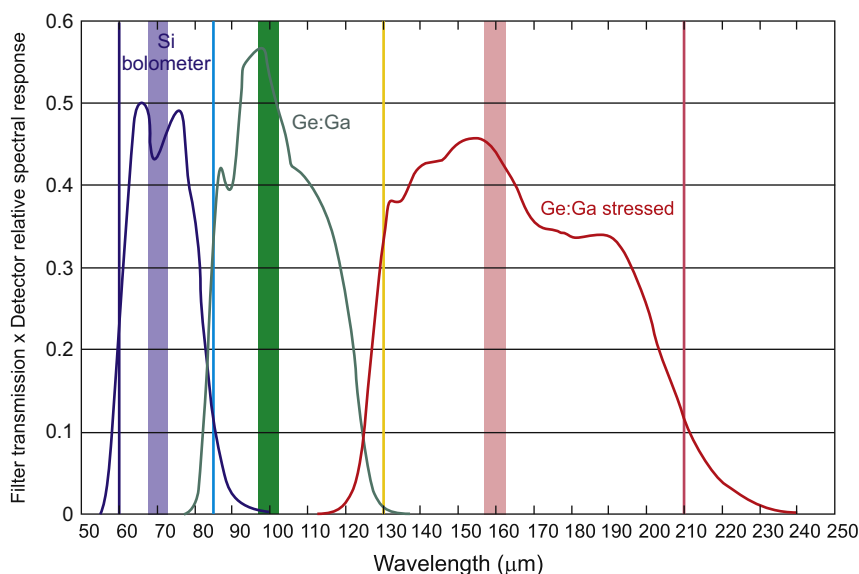


Fig. 104. Effective spectral response of the filter/detector chain of the PACS photometer in its three bands (after Ref. [231]).

not generally suitable for far-IR arrays (although also this architecture is used [233]) primarily because glow from the readout is sensed by the detector, degrading its performance. In response, a new layered-hybrid structure was introduced to alleviate these problems and make possible the construction of large format far-IR FPAs [see Fig. 29(d)] [234,235]. In this design, an intermediate substrate is placed between the detector and the readout, which is pixelized on both sides in a format identical to that of the array and the electrical contact between corresponding pixel pads are made through embedded vias. The substrate material must be chosen to have sufficient IR-blocking property, high thermal conductivity, and an expansion coefficient that is between that of germanium and silicon. Alumina (Al_2O_3) and aluminium nitride (AlN) have these properties and are possible choices as substrate materials. Blocking of the readout glow from reaching the detector, provide more efficient heat dissipation, improve temperature uniformity across the array, and mitigate the thermal mismatch between the detector and the readout. In addition, the substrate serves as a fanout board providing a simple and robust way to connect the FPA to the external electronics with no additional packaging requirement. Fig. 105 shows an assembled Ge:Sb FPA ($\lambda_c \approx 130 \mu\text{m}$) using the layered-hybrid architecture. For low bias voltage photoconductor operated at low temperatures, a capacitive transimpedance amplifier (CTIA) design offers an effective readout solution. It is predicted, that using this structure very large format FPAs with sensitivities better than $10^{-18} \text{ W/Hz}^{1/2}$ could be realized, fulfilling the technology goals of the upcoming astronomical instruments.

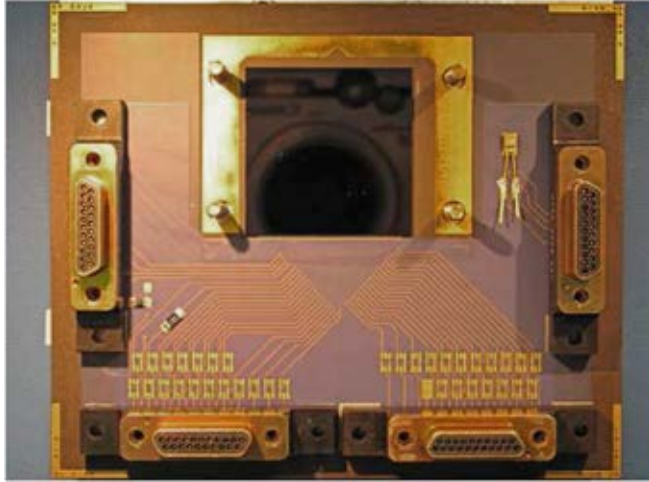


Fig. 105. The fully assembled layered-hybrid Ge:Sb FPA ($\lambda_c \approx 130 \mu\text{m}$) with SB349 readout (CTIA readout). Shown is the readout side; the detector is located on the other side of the fanout board (after Ref. [235]).

9.3. Pair breaking photon detector arrays

One of the methods of photon detection consists in using superconductivity materials. If the temperature is far below the transition temperature, T_c , most of electrons in them are banded into Cooper pairs. Photons with energies exceeding the binding Cooper pair energies in superconductor, 2Δ (each electron must be supplied an energy Δ), can break these pairs producing quasiparticles (electrons) [see inside of Fig. 106(a)]. This process resemble the interband absorption in semiconductors, with the energy gap equal 2Δ , when under the photons absorbed the electron–hole pares are created. One of the advantages of these detectors is that the fundamental noise due to the random generation and recombination of thermal quasiparticles decreases exponentially with temperature as $\exp(-\Delta/k_B T)$ [236]. The best noise temperature of pair breaking detectors can approach nearly the quantum operation limit equal $h\nu/k$ (see Fig. 96).

Several structures of pair braking detectors which use different ways to separate quasiparticles from Cooper pairs have been proposed. Among them are: superconductor-insulator-superconductor (SIS) and superconductor-insulator-normal metal (SIN) detectors and mixers, radio frequency (RF) kinetic inductance detectors, and superconducting quantum interference device (SQUID) kinetic inductance detectors. Superconducting detectors offer many benefits: outstanding sensitivity, lithographic fabrication, and large array sizes, especially through the development of multiplexing techniques. The basics physics of these devices and recent progress in their developments are described in Ref. [237]. Here we concentrate on the most important, SIS detectors.

The SIS detector is a sandwich of two superconductors separated by a thin ($\approx 20 \text{ \AA}$) insulating, what is schematically shown in Fig. 106(c). Nb and NbTiN are almost exclusively used as superconductors for the electrodes. For a standard junction process, the base electrode is 200-nm sputtered Nb, the tunnel barrier is made using a thin 5-nm sputtered Al layer which is either thermally oxidized (Al_2O_3) or plasma nitridized (AlN).

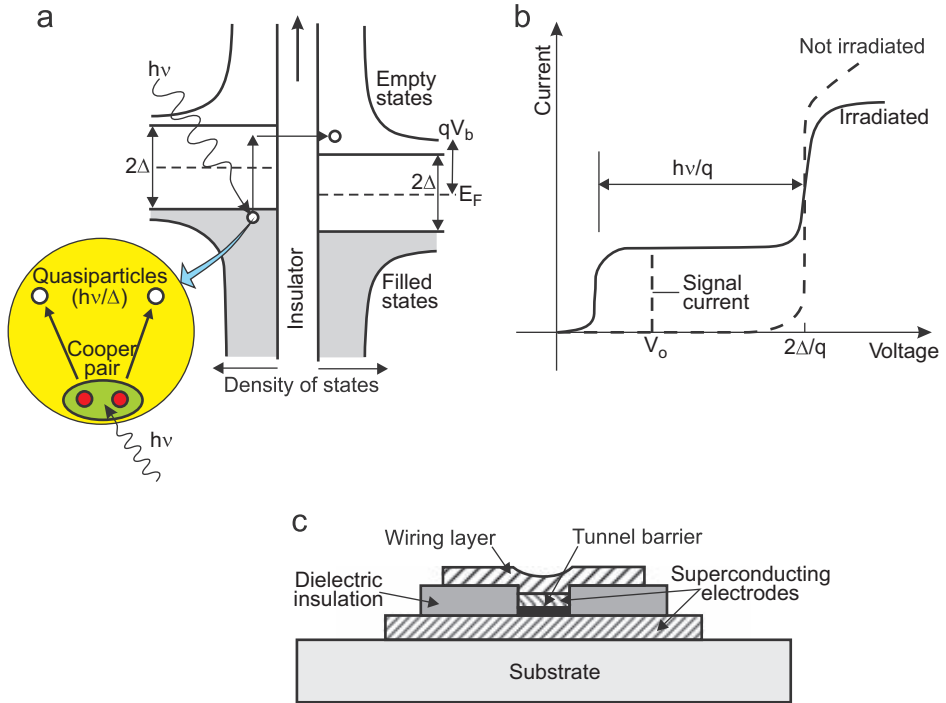


Fig. 106. SIS junction: (a) energy diagram with applied bias voltage and illustration of photon assisted tunnelling, (b) current-voltage characteristic of a non-irradiated and irradiated barrier [the intensity of the incident radiation is measured as an excess of the current at a certain bias voltage V_o —schematic creation of quasiparticle is shown inside (a)], and (c) a cross section of a typical SIS junction.

The counterelectrode is 100-nm sputtered Nb or reactively sputtered NbTiN. Typical junction areas are about $1 \mu\text{m}^2$. The entire SIS structure is deposited in a single deposited run. The junction is defined by photolithography or electron-beam lithography and reactive ion etching of the counterelectrode. Finally, 200-nm thick thermally evaporated SiO or sputtered SiO₂ are deposited. A SiO_x layer insulates the junction and serves as the dielectric for the wiring and RF tuning circuit on top of the junction.

The SIS operation is based on photoassisted tunnelling of quasi-particles through the insulating layer. Its operation can be described by using the energy band representation known for semiconductors. When a bias voltage, V_b , is applied to the junction [see Fig. 106(a)], there is a relative energy shift of qV_b between the Fermi levels of the two superconductors. If qV_b is lower than energy gap, 2Δ , no current flows (electrons may only tunnel into unoccupied states at the same energy). However, if the junction is irradiated, photons of energy $h\nu$ may assist the tunnelling, which now may occur for $qV_b > 2\Delta - h\nu$ [see Fig. 106(b)].

SIS tunnel junctions are mainly used as mixers in heterodyne type mm and sub-mm receivers, because of their strong non-linear I-V characteristic. They can be also used as direct detection detectors. Operating temperature of SIS junctions is below 1 K; typically

$T \leq 300$ mK. However, up to now SIS detectors are difficult to integrate into large arrays. There is only a success in creation of small number element arrays [238].

Progress in detector technology will be connected with successful development of large-format, high-sensitivity focal plane arrays enabling a range of observations from ground-based and orbital platforms. Especially two detector technologies show promise to develop the arrays needed in the next decade: transition-edge superconducting (TES) bolometers (see Section 9.5) and microwave kinetic inductance detectors (MKIDs) based on different



Fig. 107. Prototype MKID camera constructed for the Caltech Submillimeter Observatory with 576 spatial pixels each simultaneously sensitive in four bands at 750, 850, 1100 and 1300 microns.

principles of superconductivity. Multiple instruments are currently in development based on arrays up to 10,000 detectors using both time-domain multiplexing (TDM) and frequency-domain multiplexing (FDM) with superconducting quantum interference devices (SQUIDs) [239]. Both sensors show potential to realize the very low $\sim 10^{-20}$ W/Hz^{1/2} sensitivity needed for space-borne spectroscopy.

A MKID is essentially a high- Q resonant circuit made out of either superconducting microwave transmission lines or a lumped element LC resonator. In the first case a meandered quarter-wavelength strip of superconducting material is coupled by means of a coupling capacitance to a coplanar waveguide through line used for excitation and readout. Lumped element are instead created from an LC series resonant circuit inductively coupled to a microstrip feed line. Photons hitting an MKID break Cooper pairs which changes the surface impedance of the transmission line or inductive element. This causes the resonant frequency and quality factor to shift an amount proportional to the energy deposited by the photon. The readout is almost entirely at room temperature and can be highly multiplexed; in principle hundreds or even thousands of resonators could be read out on a single feedline [240].

MKID devices use superconductors (micro-resonators fabricated from thin aluminium and niobium films) below transition where radiation breaks Cooper pair but with smaller energy gap. Their advantages are: readout of many devices with single coax, simple detector and multiplexer fabrications; but still need ultra low temperatures. For more details see Ref. [241]. Fig. 107 shows prototype MKID camera constructed for the Caltech Submillimeter Observatory with 576 antenna-coupled spatial pixels each simultaneously sensitive in four bands at 750, 850, 1100 and 1300 microns and with a total 2304 detectors [242].

9.4. Semiconductor bolometer arrays

The classic bolometers contain a heavily doped and compensated semiconductor which conduct by a hopping process that yields a resistance $R(T) = R_o \exp(T/T_o)^p$, where R is the resistance at temperature T , and T_o and R_o are constants which depend on the doping and, for R_o , on the thermistor dimensions [243]. The exponent p is a constant, and it is often assumed that $p=0.5$. The thermistors are made by ion implantation in Si, or by neutron transmutations doping (NTD) in Ge [244].

The thermistors are typically fabricated by lithography on membranes of Si or SiN. The impedance is selected to a few M Ω to minimize the noise in JFET amplifiers operated at about 100 K. Limitation of this technology is assertion of thermal mechanical and electrical interface between the bolometers at 100–300 mK and the amplifiers at ≈ 100 K. Usually, JFET amplifiers are sited on membranes which isolate them so effectively that the environment remains at much low temperature (about 10 K)—see Fig. 108. In addition, the equipment at 10 K is itself thermally isolated from nearby components at 0.1–0.3 K. There are not practical approaches to multiplexing many such bolometers to one JFET amplifier. Current arrays require one amplifier per pixel and are limited to a few hundred pixels.

In bolometer metal films that can be continuous or patterned in a mesh absorb the photons. The patterning is designed to select the spectral band, to provide polarization sensitivity, or to control the throughput. Different bolometer architectures are used. In close-packed arrays and spider web, the pop-up structures or two-layer bump bonded structures are fabricated. Agnese et al. have described a different array architecture, which

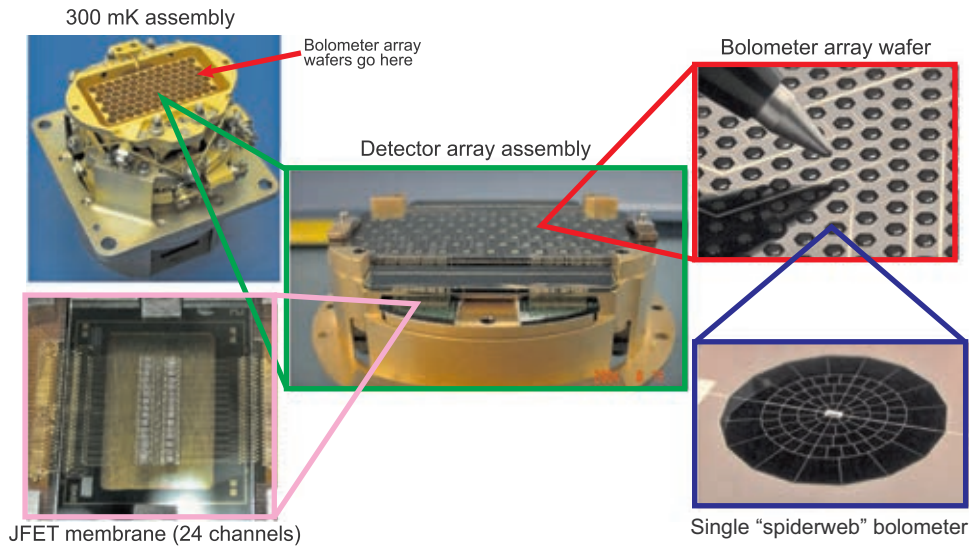


Fig. 108. Bolometer array of the Spectral and Photometric Imaging Receiver (SPIRE) (after Ref. [245]).

Table 14
Requirements for typical astronomic instruments

Instrument	Wavelength range (μm)	NEP (W/Hz ^{1/2})	τ (ms)	$NEP\tau^{1/2}$ ($\times 10^{-19}$ J)	Comments
SCUBA	350–850	1.5×10^{-16}	6	9	High background, needs reasonable τ
SCUBA-2	450–850	7×10^{-17}	1–2	1	Lower background, need faster τ
BoloCAM	1100–2000	3×10^{-17}	10	3	Lower background, slower device okay
SPIRE	250–500	3×10^{-17}	8	2.4	Space background, slower device okay
Planck-HFI	350–3000	1×10^{-17}	5	0.5	Lowest background, need quite fast τ

is assembled from two wafers by indium bump bonds [246]. Other types of bolometers are integrated in horn-coupled arrays. To minimize low frequency noise an AC bias is used. The present day technology exist to produce arrays of hundreds of pixels that are operated in spectral range from 40 to 3000 μm in many experiments including NASA pathfinder ground based instruments, and balloon experiments such as BOOMERANG, MAXIMA and BAM. In Table 14 are gathered requirements for typical astronomic instruments containing bolometers. To fulfil these requirements, the compromise between response time and NEP is needful. A spider web bolometer from the BOOMERANG experiment, which is being used on space experiments (Planck and Herschel missions) is shown inside of Fig. 108.

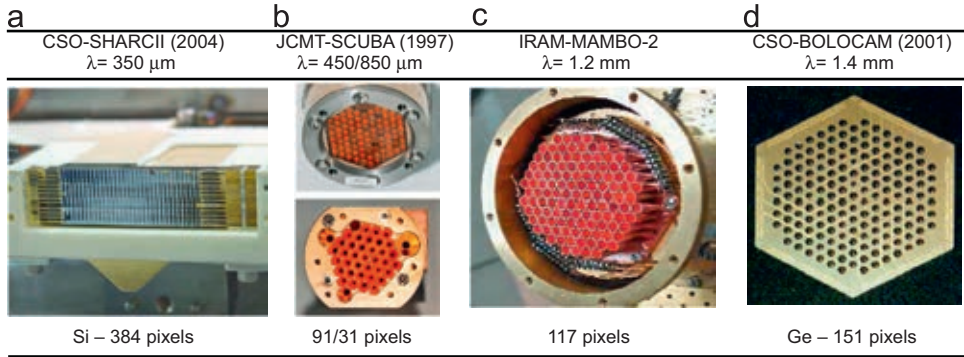


Fig. 109. Arrays installed in ground-based telescopes.

An alternative approach is array for the SHARCII instrument on SOFIA shown in Fig. 109(a) [247]. This array construction, with 12×32 pixels, involves a pop-up configuration, where the absorber is deposited on a dielectric film that is subsequently folded. The 12×32 bolometer array, load resistors, and thermally-isolated JFETs are housed in a structure approximately $18 \times 17 \times 18 \text{ cm}^3$ volume, having a total mass of 5 kg, and heat sink to 4 K. Each bolometer is fabricated on a $1 \mu\text{m}$ silicon membrane and has a collecting area of $1 \times 1 \text{ mm}^2$. The full area is ion implanted with phosphorus and boron, to a depth of $\approx 0.4 \mu\text{m}$, to form a thermistor. Electrical contact between the thermistor and aluminium traces on the silicon frame is accomplished with degenerately-doped leads on the edge of the thermistor and running down the bolometer legs. Each of the four thermally-isolating legs is $16 \mu\text{m}$ wide and $420 \mu\text{m}$ long. Prior to folding, each bolometer is coated with an absorbing $\approx 200 \text{ \AA}$ bismuth film and a protective $\approx 160 \text{ \AA}$ SiO film. At a base temperature of 0.36 K and in the dark, the bolometers have a peak responsivity of approximately $4 \times 10^8 \text{ V/W}$ and a minimum NEP of approximately $6 \times 10^{-17} \text{ W/Hz}^{1/2}$ at 10 Hz. Phonon noise is the dominant contributor, followed by bolometer Johnson noise.

With the development of low-noise readouts that can operate near the bolometer temperature, the first true high-performance bolometer arrays for the far IR and sub-mm spectral ranges are just becoming available. For example, the Herschel/PACS instrument uses a 2048-pixel array of bolometers [232] and is an alternative to JFET amplifiers. The architecture of this array is vaguely similar to the direct hybrid mid-infrared arrays, where one silicon wafer is patterned with bolometers, each in the form of a silicon mesh, as shown in Fig. 110. The development of silicon micromachining has enabled substantial advances in bolometer construction generally and is central to making large-scale arrays. To achieve appropriate response and time constant characteristics, the rods and mesh are designed carefully. The mesh is blackened with a thin layer of titanium nitride with sheet resistance matched to the impedance of free space ($377 \Omega/\square$ section of film) to provide an efficiency of 50% over a broad spectral band. Each bolometer located at the centre of the mesh, containing a silicon-based thermometer doped by ion implantation, is characterized by appropriate temperature-sensitive resistance. Their large resistances ($> 10^{10} \Omega$) are well adjusted to MOSFET readout amplifiers. In final step of hybrid array fabrication, the MOSFET-based readouts and silicon bolometer wafer are joined by indium bump

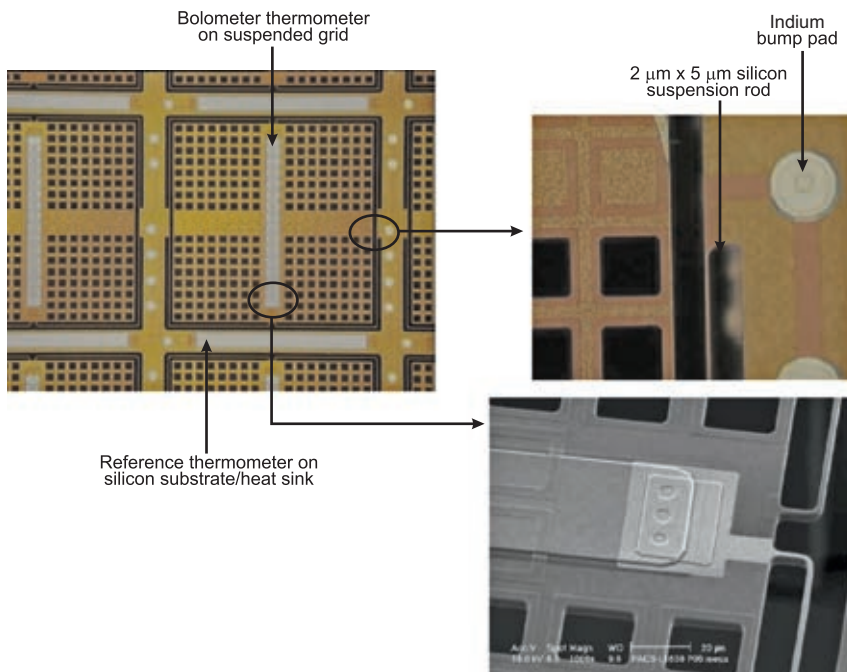


Fig. 110. The Herschel/PACS bolometer array with pixel size $750\text{ }\mu\text{m}$ (after Ref. [222]).

bonding. Performance is currently limited by the noise in the MOSFET amplifiers to the $NEP \approx 10^{-16}$ W/Hz^{1/2} regime, but this technology allows the construction of very large arrays suitable for higher background applications. Further details are in Billot et al. [232].

9.5. Superconducting HEB and TES arrays

Among superconducting detectors used for terahertz downconversion, hot-electron-bolometer (HEB) mixers have attracted the attention. Their low local-oscillator (LO) power consumption (less than $1\text{ }\mu\text{W}$), near-quantum-limited noise performance (see Fig. 96), and ease of fabrication have placed them above competing technologies in the quest for implementation of large-format heterodyne arrays.

In principle, HEB is quite similar to the transition-edge sensor (TES) bolometer, where small temperature changes caused by the absorption of incident radiation strongly influence resistance of biased sensor near its superconducting transition. The main difference between HEBs and ordinary bolometers is the speed of their response. High speed is achieved by allowing the radiation power to be directly absorbed by the electrons in the superconductor, rather than using a separate radiation absorber and allowing the energy to flow to the superconducting TES via phonons, as ordinary bolometers do. After photon absorption, a single electron initially receives the energy $h\nu$, which is rapidly shared with other electrons, producing a slight increase in the electron temperature. In the next step, the electron temperature subsequently relaxes to the bath temperature through emission of phonons.

In comparison with TES, the thermal relaxation time of the HEB's electrons can be made fast by choosing a material with a large electron-phonon interaction. The

development of superconducting HEB mixers has lead to the most sensitive systems at frequencies in the terahertz region, where the overall time constant has to be a few tens of picoseconds. These requirements can be realized with a superconducting microbridge made from NbN, NbTiN, or Nb on a dielectric substrate [237].

Fig. 111(a) presents an example cross-section view of NbN mixer chip. About 150-nm thick Au spiral structure is connected to the contacts pads. The supeconducting NbN film extends underneath the contact layer/antenna. The central area of a mixer chip shown in Fig. 111(b) is manufactured from a 3.5-nm thick superconducting NbN film on a high resistive Si substrate with an e-beam evaporated MgO buffer layer [248]. Ultrathin NbN films are deposited by reactive magnetron sputtering in the Ar+N₂ gas mixture. The active NbN film area is determined by the dimensions of the 0.2- μ m gap between the gold contact pads. The NbN microstrip is integrated with a planar antenna patterned as log-periodic spiral. The NbN critical temperature depends on thickness of film deposited on substrate. An improvement of superconducting properties of NbN films due to the presence of MgO buffer layer on silicon substrates is evident [see Fig. 111(c)]. The superconducting transition temperature is about 9 K and the transition widths are ≈ 0.5 K.

The NbN superconductive HEB mixers are characterized by strong electron–phonon interaction. The response time can achieve value of 10^{-11} s [249], and because of no principal restrictions for operation at $\nu > 1$ THz (the absence of their noticeable capacities), these devices can be effectively used for heterodyne detection in wide spectral range up to the visible one, where operation, e.g., of SIS mixers, is hampered.

HEB mixers can be made either in a waveguide configuration with a horn antenna or as quasi-optical mixers. The more traditional approach is waveguide coupling, in which radiation is first collected by a horn into a single-mode waveguide (typically a rectangular guide), and then, a transition (probe) couples radiation from the waveguide onto a lithographed thin-film transmission line on the detector chip. One major complication of the waveguide approach is that the mixer chip must be very narrow, and must be fabricated on an ultrathin substrate. These requirements are helpful using modern micromachining techniques (see Fig. 112).

Above ~ 1 THz, the quasi-optical coupling is more common. This coupling approach omits the intermediate step of collecting the radiation into a waveguide, and instead uses a

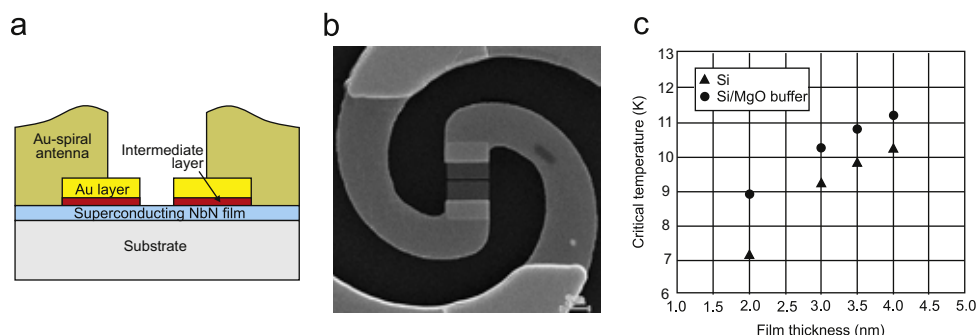


Fig. 111. NbN HEB mixer chip: (a) cross section view, (b) SEM micrograph of the central area of mixer, (c) critical temperature versus thickness for NbN films deposited on Si substrates (triangles) and on Si with MgO buffer layer (circles) (after Ref. [248]).

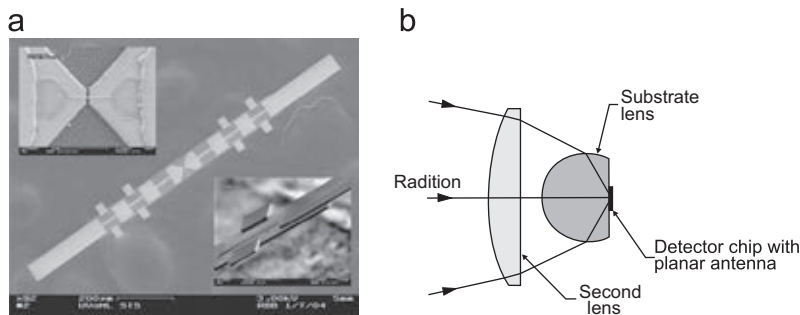


Fig. 112. Configurations of HEB mixers: (a) the waveguide coupling and (b) the quasi-optical coupling. The bridge of 585-GHz HEB mixer chip, shown in figure (a), is 150 nm long and 75 nm wide; the chip itself is 800 μm long, and 3 μm thick. Protruding from the sides and ends of the chip are 2- μm thick gold leads, which provide electrical and thermal contact to the waveguide block, as well as mechanical support for the chip (after Ref. [237]).

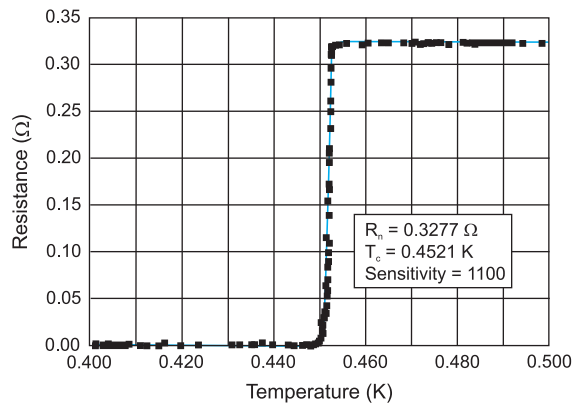


Fig. 113. Resistance vs. temperature for a high-sensitivity TES Mo/Au bilayer with superconducting transition at 444 mK (after Ref. [250]).

lithographed (printed) antenna (e.g., twin-slot or a logarithmic spiral antenna) on the detector chip itself. Such mixers are substantially simpler to fabricate and may be produced using thick substrate [see Fig. 112(b)]. The substrate with the feed antenna and microbridge is mounted to the reverse side of a hyperhemispherical or elliptical lens. The reflection loss at the lens surface can be minimized with a quarter-wavelength antireflection coating.

The name of the transmission-edge sensor (TES) bolometer is derived from its thermometer, which is based on thin superconducting films held within transition region, where it change from the superconducting to the normal state over a temperature range of a few milliKelvin (see Fig. 113). The film has stable but very steep dependence of resistance on temperature in transition region. Changes in temperature transition can be set by using a bilayer film consisting of a normal material and a layer of superconductor. Such design enables diffusion of the Cooper pairs from the superconductor into the normal metal and makes it weakly superconducting—this process is called the proximity effect. As a result,

the transition temperature is lowered relative to that for the pure superconducting film. Thus in principle, the TES bolometers are quite similar to the HEBs.

TES bolometers are superior to current-biased particle detectors in terms of linearity, resolution, and maximum count rate. At present, these detectors can be applied for THz photons counting because of their high sensitivity and low thermal time constant. Membrane isolated TES bolometers are capable of reaching a phonon $NEP \approx 4 \times 10^{-20}$ W/Hz^{1/2} [243]. The current generation of sub-orbital experiments largely rely on TES bolometers. Important feature of this sensor is that it can operate in wide spectral band, between the radio and gamma rays [237,251].

The temperature of a TES can be tailored by using a bilayer film consisting of a thin layer of normal metal and a thin layer of superconductor, resulting in a tuneable transition temperature. Different type of superconducting metal film pairs (bilayers) can be used including thin Mo/Au, Mo/Cu, Ti/Au, etc.). Two metals behave as a single film with a transition temperature between 800 mK (for Mo) and 0 K (for Au). Transition temperature can be tuned within this temperature range. The lower temperature ($T < 200$ mK) is needed because the energy resolution of these devices scales with temperature.

The most ambitious example of TES bolometer array is that used in the submillimeter camera SCUBA (Submillimetre Common-User Bolometer Array)-2 with 10,240 pixels [252,253]. The camera operated at wavelengths of 450 and 850 μm has been mounted on the James Clerk Maxwell Telescope in Hawaii. Each SCUBA-2 array is made of four side-butable sub-arrays, each with 1280 (32×40) transition-edge sensors. The design is illustrated in Fig. 114 together with cross-section of the detector architecture. The detector technology is based on silicon micromachining. Each pixel consists of two silicon wafers bonded together. The upper wafer with its square wells supports the silicon nitride

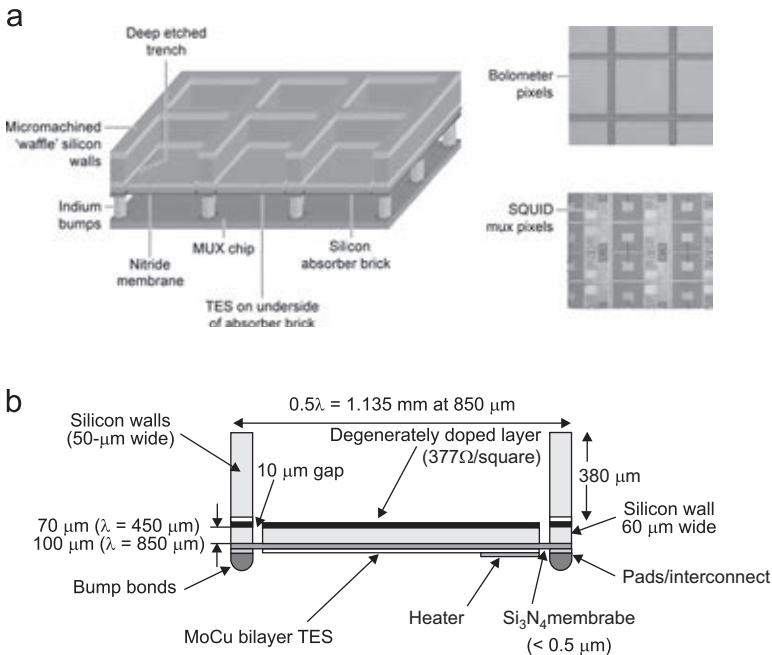


Fig. 114. SCUBA-2 bolometer array: (a) design features, (b) cross-section of single pixel (after Ref. [252]).

membrane on which Mo-Cu bi-layer TES detectors and the absorbing silicon brick are suspended. The lower wafer is thinned to 1/4 wavelength in silicon (70 at 850 μm). The upper surface of this wafer has been previously implanted with phosphorus to match the impedance of free space (377 Ω/square) The detector elements are separated from their heat sinks by a deep etched trench that is bridged by only a thin silicon nitride membrane. The superconducting electronics that read out the bolometers are fabricated on separate wafers (see Fig. 115). The two components are assembled into an array using indium bump bonding. Further details are in Walton et al. [252] and Woodcraft et al. [255].

In addition to the arrays for SCUBA-2, various forms of TES-based bolometers with SQUID readouts are under active development [256]. Large format arrays of antenna-coupled TES bolometers are very attractive candidates for a cosmic microwave background polarization mission. Broadband antennas with RF diplexing and/or interleaved antennas can make efficient use of the focal plane. Antennas are inherently polarization sensitive, and the excellent gain stability provided by the feedback in TES bolometers facilitates polarization differencing.

The fabrication technologies used for TES bolometers are very flexible and specialized detectors are being developed to meet the needs of specific observations. A bolometer design allows the production of large monolithic detector arrays with a very high fill factor by standard planar lithography. Fig. 116 shows the 1024-pixel array structure together with a single pixel [257]. The absorbing element is a square mesh of 1- μm thick low-stress

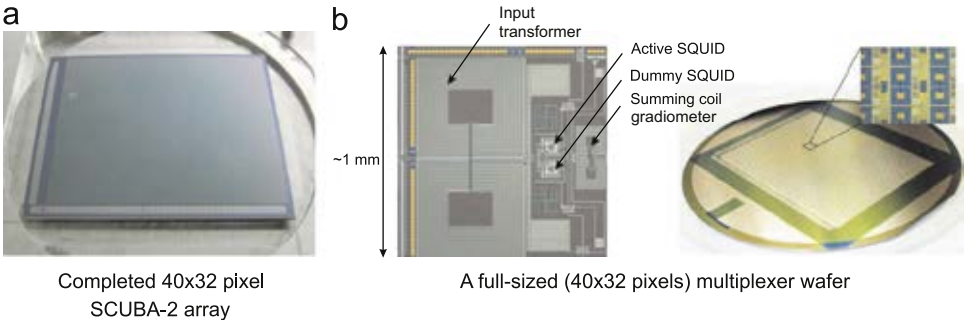


Fig. 115. SCUBA-2: (a) bolometer array and (b) SQUID multiplexer pixel (after Ref. [254]).

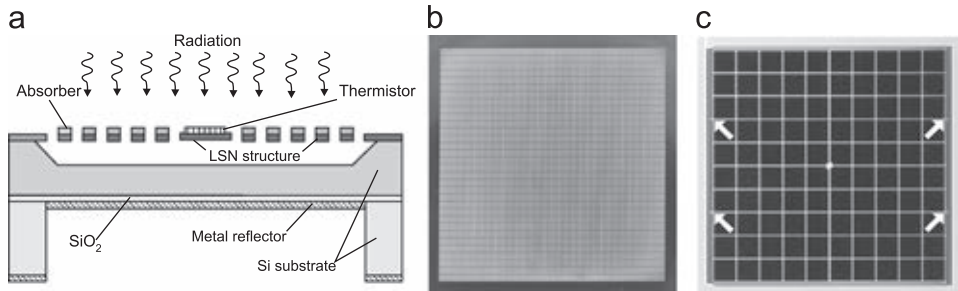


Fig. 116. Monolithic superconducting bolometer array: (a) cross section of pixel, (b) silicon nitride structure for a 1024 element array of bolometers (1.5 \times 1.5 mm² pixel size), (c) complete pixel including sensor and metallization (after Ref. [257]).

(non-stoichiometric) silicon nitride (LSN), which is metallized with gold to produce an average sheet resistance of $377 \Omega/\text{square}$. A conducting backshort is located a distance $\lambda/4$ behind the mesh. This mesh absorber is supported at four points (shown by arrows) by low thermal conductivity beams of LSN. To produce $T_c \approx 400 \text{ mK}$, a proximity-effect sandwich of Al and Ti is made at the centre of the mesh. To connect the thermistors to the edges of the array, fully superconducting Nb leads are used by way of the beams and the dividing strips between pixels. Other designs is using micromachining and folding to bring the leads out of the third dimension [258].

9.6. Field effect transistor detector arrays

Nonlinear properties of plasma wave excitations (the electron density waves) in nanoscale FET channels enable their response at frequencies appreciably higher than the device cutoff frequency, what is due to electron ballistic transport. In the ballistic regime of operation, the momentum relaxation time is longer than the electron transit time. The FETs can be used both for resonant (tuned to a certain wavelength) and non-resonant (broadband) THz detection [259] and can be directly tuneable by changing the gate voltage.

The transistor receivers operate in wide temperature range up to room temperatures. Different material systems are used in fabrication FET, HEMT, and MOSFET devices including: Si, GaAs/AlGaAs, InGaP/InGaAs/GaAs, and GaN/AlGaIn [201,202]. Plasma oscillations can be also observed in a two-dimensional (2-D) electron channel with a reverse-biased Schottky junction and double quantum well FET with a periodic grating gate.

The use FETs as detectors of THz radiation was first proposed by Dyakonov and Shur in 1993 [260] on the basis of formal analogy between the equations of the electron transport in a gated two-dimensional transistor channel and those of shallow water, or acoustic waves in music instruments. As a consequence, hydrodynamic-like phenomena should exist also in the carrier dynamics in the channel. Instability of this flow in the form of plasma waves was predicted under certain boundary conditions.

The physical mechanism supporting the development of stable oscillations lies in the reflection of plasma waves at the borders of transistor with subsequent amplification of the wave's amplitude (see Fig. 117). Plasma excitations in FETs with sufficiently high electron mobility can be used for emission as well as detection of THz radiation [261,262].

The detection by FETs is due to nonlinear properties of the transistor, which lead to the rectification of the ac current induced by the coming radiation. As a result, a

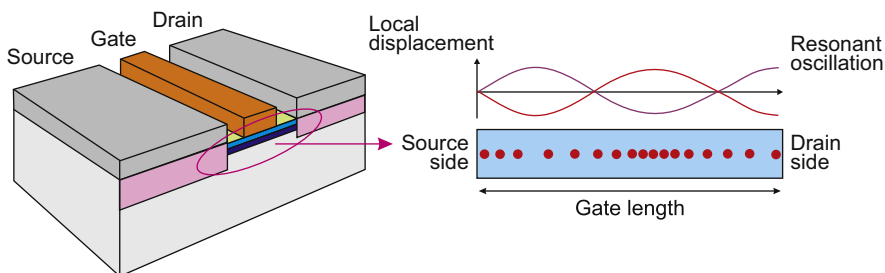


Fig. 117. Plasma oscillations in a field effect transistor.

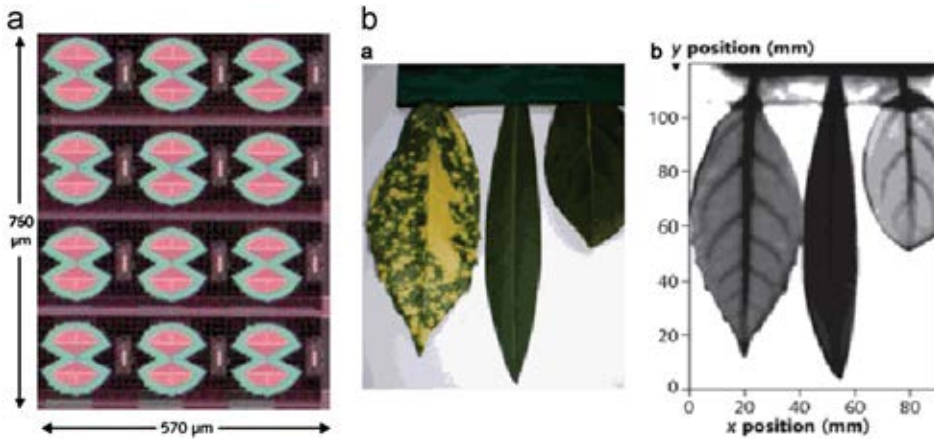


Fig. 118. Room temperature THz imaging: (a) architecture of the 3×4 pixel Si CMOS imager prototype (a bow-tie structure in the metal interconnection layers couples the incoming free-space terahertz radiation to a sub-wavelength transistor), (b) leaves seen in visible light and at 300 GHz in transmission imaging (after Ref. [265]).

photoresponse appears in the form of a dc voltage between source and drain. This voltage is proportional to the radiation intensity (photovoltaic effect). In the simple case (low carrier mobility and density), the process can also be understood in an electronic manner as a special type of resistive self-mixing [259]. Even in the absence of an antenna, the THz radiation is coupled to the FET by contact pads and bonding wires. A big progress in sensitivity can be obtained by adding a proper antenna or a cavity coupling.

An important progress has been reported during last several years. The first silicon CMOS FPAs for imaging at 600 and 645 GHz were demonstrated in 2009 [263]. Further reduction of the system costs was achieved by designing a versatile image sensor that operates at a wide range of THz frequencies. Recently Schuster et al. [264] have presented a prototype THz imager in $0.13 \mu\text{m}$ CMOS with imaging capability from 300 GHz to 1 THz, low-noise in-pixel amplifiers and multiplexing circuitry for single video output. To effectively couple the free-space terahertz wave to the sub-wavelength transistor, an antenna structure is needed. Architecture of the 3×4 pixel image prototype is shown in Fig. 118(a). The best parameters obtained with THz CMOS pixels at room temperature are a NEP of $8 \times 10^{-12} \text{ W/Hz}^{1/2}$ and a responsivity of 5 kV/W at 0.3 THz. The CMOS pixels, mounted in a test package and used with a terahertz source for active illumination, provide images that emphasize the unique characteristics of terahertz radiation. For example, Fig. 118(b) reveals the inner structure of a tree leaves (raster scan image at 300 GHz).

10. Conclusions

This paper offers a rather wide coverage of optical detector array technology. However, for a full understanding of the technical content, the paper requires as a prerequisite the basic courses in material science and fundamentals of semiconductor physics.

The future applications of optical detector systems require:

- Higher pixel sensitivity
- Further increase in pixel density
- Cost reduction in imaging array systems due to less cooling sensor technology combined with integration of detectors and signal processing functions (with much more on-chip signal processing)
- Improvement in functionality of imaging arrays through development of multispectral sensors.

Array sizes will continue to increase but perhaps at a rate that falls below the Moore's Law curve. An increase in array size is already technically feasible. However, the market forces that have demanded larger arrays are not as strong now that the megapixel barrier has been broken. Astronomers, in particular, have eagerly waited for the day when optoelectronic arrays could match the size of photographic film. Development of large format, high sensitivity, mosaic sensors for ground-based astronomy is the goal of many observatories around the world, since large arrays dramatically multiply the data output of a telescope system. This is somewhat surprising given the comparative budgets of the defense market and the astronomical community.

There are many critical challenges for future civilian and military infrared detector applications. For many systems, such as night-vision goggles, the IR image is viewed by the human eye, which can discern resolution improvements only up to about 1 megapixel, roughly the same resolution as high-definition television. Most high-volume applications can be completely satisfied with a format of 1280×1024 . Although wide-area surveillance and astronomy applications could make use of larger formats, funding limits may prevent the exponential growth that was seen in past decades.

Third generation infrared imagers are beginning a challenging road to development. For multiband sensors, boosting the sensitivity in order to maximize identification range is the primary objective. The goal for dual-band MW/LW IR FPAs are 1920×1080 pixels, which due to lower cost should be fabricated on silicon wafers. The challenges to attaining those specifications are material uniformity and defects, heterogeneous integration with silicon, and ultra well capacity (on the order of a billion in the LWIR).

It is predicted that in IR region HgCdTe technology will continue in the future to expand the envelope of its capabilities because of its excellent properties. Despite serious competition from alternative technologies, HgCdTe is unlikely to be seriously challenged for high-performance applications, applications requiring multispectral capability and fast response. However, the nonuniformity is a serious problem in the case of LWIR and VLWIR HgCdTe detectors. For applications that require operation in the LWIR band as well as two-color MWIR/LWIR/VLWIR bands, most probably HgCdTe will not be the optimal solution. Type II InAs/GaInSb superlattice structure is a relatively new alternative IR material system and has great potential for LWIR/VLWIR spectral ranges with performance comparable to HgCdTe with the same cutoff wavelength. The fact that Sb-based superlattices are processed close to standard III-V technology raises the potential to be more competitive due to lower costs in series production.

Near future high performance uncooled thermal imaging will be dominated by VO_x bolometers. However, their sensitivity limitations and the still significant prices will encourage many research teams to explore other IR sensing techniques with the potential for improved performance with reduced detector costs. In the near future, VO_x will be challenged by a-Si material and new silicon based materials introduced by new market entrants, thanks to their cost structure, and easier manufacturability.

The THz detectors will receive increasing importance in a very diverse range of applications including detection of biological and chemical hazardous agents, explosive detection, building and airport security, radio astronomy and space research, biology and medicine. The future sensitivity improvement of THz instruments will come with the use of large format arrays with readouts in the focal plane to provide the vision demands of high resolution spectroscopy. One of promising solution is room temperature THz imaging achieved with low-cost CMOS detectors.

References

- [1] W. Smith, *Nature* 7 (1873) 303.
- [2] P. Norton, Detector focal plane array technology, in: R. Driggers (Ed.), *Encyclopedia of Optical Engineering*, Marcel Dekker Inc., New York, 2003, pp. 320–348.
- [3] E.L. Dereniak, G.D. Boreman, *Infrared Detectors and Systems*, John Wiley and Sons, New York, 1996.
- [4] S. Donati, *Photodetectors. Devices, Circuits, and Applications*, Prentice Hall Inc., 1999.
- [5] A. Rogalski, *Infrared Detectors*, 2nd ed., CRC Press, Boca Raton, 2010.
- [6] A. Rogalski, *Opto-Electronics Review* 12 (2004) 221–245.
- [7] Committee on Developments in Detector Technologies; National Research Council, 2010 <<http://www.nap.edu/catalog/12896.html>>.
- [8] P.J. Love, A.W. Hoffman, N.A. Lum, K.J. Ando, J. Rosbeck, W.D. Ritchie, N.J. Therrien, R.S. Holcombe, E. Corrales, *Proceedings of SPIE* 5902 (2005) 590209-1-9.
- [9] A.R. Jha, *Cryogenic Technology and Applications*, Elsevier, Oxford, 2006.
- [10] P.T. Blotter, J.C. Batty, Thermal and mechanical design of cryogenic cooling systems, in: W.D. Rogatto (Ed.), *The Infrared and Electro-Optical Systems Handbook*, 3, 343–433, Infrared Information Analysis Center, Ann Arbor, MI, and SPIE Press, Bellingham, 1993.
- [11] R. Radebaugh, *Journal of Physics: Condensed Matter* 21 (2009) 164219-1-9.
- [12] Cryocoolers for space applications, Cryogenic Engineering Group. <http://www.eng.ox.ac.uk/cryogenics/research/cryocoolers-for-space-applications>.
- [13] R. Radebaugh, *Proceedings of SPIE* 4130 (2000) 363–379.
- [14] D.M. Rowe, *CRC Handbook of Thermoelectrics*, CRC Press, Boca Raton, 1995.
- [15] B. Poudel, Q. Hao, Y. Ma, Y. Lan, A. Minnich, B. Yu, X. Yan, D. Wang, A. Muto, D. Vashaee, X. Chen, J. Liu, M.S. Dresselhaus, G. Chen, Z. Ren, *Science* 320 (2008) 634–638.
- [16] L.E. Bell, *Science* 321 (2008) 1457–1461.
- [17] R.C. Jones, *Proceedings of the IRE* 47 (1959) 1495–1502.
- [18] P.W. Kruse, L.D. McGlauchlin, R.B. McQuistan, *Elements of Infrared Technology*, Wiley, New York, 1962.
- [19] P.W. Kruse, The photon detection process, in: R.J. Keyes (Ed.), *Optical and Infrared Detectors*, Springer, Berlin, 1977, pp. 5–69.
- [20] A.G.U. Perera, W.Z. Shen, *Opto-Electronics Review* 7 (1999) 153–180.
- [21] H. Schneider, H.C. Liu, *Quantum Well Infrared Photodetectors*, Springer, Berlin, 2007.
- [22] H.C. Liu, *Opto-Electronics Review* 11 (2003) 1–5.
- [23] E.H. Putley, Thermal detectors, in: R.J. Keyes (Ed.), *Optical and Infrared Detectors*, Springer, Berlin, 1977, pp. 71–100.
- [24] P.W. Kruse, *Uncooled Thermal Imaging*, SPIE Press, Bellingham, 2001.
- [25] J.A. Ratches, *Ferroelectrics* 342 (2006) 183–192.
- [26] M. Kohin, N. Butler, *Proceedings of SPIE* 5406 (2004) 447–453.
- [27] G.H. Rieke, *Detection of Light: From the Ultraviolet to the Submillimeter*, Cambridge University Press, Cambridge, 2003.
- [28] W. Whatmore, *Reports on Progress in Physics* 49 (1986) 1335–1386.
- [29] P. Muralt, *Reports on Progress in Physics* 64 (2001) 1338–1339.
- [30] W.S. Boyle, G.E. Smith, *Bell System Technical Journal* 49 (1970) 587–593.
- [31] J.R. Janesick, *Scientific Charge-Coupled Devices*, SPIE Press, Bellingham, 2001.
- [32] B. Burke, P. Jorden, P. Vu, *Experimental Astronomy* 19 (2005) 69–102.
- [33] J.L. Vampola, Readout electronics for infrared sensors, in: W.D. Rogatto (Ed.), *The Infrared and Electro-Optical Systems Handbook*, vol. 3, SPIE Press, Bellingham, 1993, pp. 285–342.
- [34] E.R. Fossum, Active pixel sensors: Are CCD's dinosaurs? *Proceedings of SPIE* 1900, 2–14 (1993).

- [35] J. Janesick, *Proceedings of SPIE* 5167 (2003) 1–18.
- [36] A. Hoffman, M. Loose, V. Suntharalingam, *Experimental Astronomy* 19 (2005) 111–134.
- [37] L.J. Kozlowski, K. Vural, J. Luo, A. Tomasini, T. Liu, W.E. Kleinhan, *Opto-Electronics Review* 7 (1999) 259–269.
- [38] R. Thorn, High density infrared detector arrays, U.S. Patent no. 4,039,833 (1977).
- [39] I.M. Baker, Photovoltaic IR detectors, in: P. Capper (Ed.), *Narrow-gap II-VI Compounds for Optoelectronic and Electromagnetic Applications*, Chapman & Hall, London, 1997, pp. 450–473.
- [40] M.A. Kinch, *Proceedings of SPIE* 4369 (2001) 566–578.
- [41] A. Hoffman, M. Loose, V. Suntharalingam, CMOS detector technology, in: J.E. Beletic, J.W. Beletic, P. Amico (Eds.), *Scientific Detectors for Astronomy 2005*, Springer, Dordrecht, 2006, pp. 307–402.
- [42] P. Garrou, C. Bower, P. Ramm (Eds.), *Handbook of 3D Integration, Technology and Applications of 3D Integrated Circuits*, second ed., Wiley-VCH, Weinheim, 2008.
- [43] <http://pan-starrs.ifa.hawaii.edu/public/design-features/cameras.html>.
- [44] J.W. Beletic, R. Blank, D. Gulbransen, D. Lee, M. Loose, E.C. Piquette, T. Sprafke, W.E. Tennant, M. Zandian, J. Zino, *Proceedings of SPIE* 7021 (2008) 70210H.
- [45] E.R. Fossum, B. Pain, *Proceedings of SPIE* 2020 (1993) 262–285.
- [46] M. Kimata, N. Tubouchi, Charge transfer devices, in: A. Rogalski (Ed.), *Infrared Photon Detectors*, SPIE Optical Engineering Press, Bellingham, 1995, pp. 99–144.
- [47] L.J. Kozlowski, W.F. Kosonocky, Infrared detector arrays, in: M. Bass, E.W. Van Stryland, D.R. Williams, W.L. Wolfe (Eds.), *Handbook of Optics*, McGraw-Hill, Inc., New York, 1995 Chap. 23.
- [48] J.M. Lloyd, *Thermal Imaging Systems*, Plenum Press, New York, 1975.
- [49] J.M. Lopez-Alonso, Noise equivalent temperature difference (NETD), in: R. Driggers (Ed.), *Encyclopedia of Optical Engineering*, Marcel Dekker Inc., New York, 2003, pp. 1466–1474.
- [50] J.M. Mooney, F.D. Shepherd, W.S. Ewing, J. Silverman, *Optical Engineering* 28 (1989) 1151–1161.
- [51] B.D. Milbrath, A.J. Peurrung, M. Bliss, W.J. Weber, *Journal of Materials Research* 23 (2008) 2561–2581.
- [52] http://chandra.harvard.edu/about/science_instruments.html.
- [53] L. Korthout, D. Verbugt, J. Timpert, A. Mierop, W. de Haan, W. Maes, L.J. de Meulmeester, W. Muhammad, B. Dillen, H. Stoldt, I. Peters, E. Fox, A wafer-scale CMOS APS imager for medical X-ray applications, www.teledynedalsa.com/public/.../DALSA_IISW2009_CMOS_Medical.pdf.
- [54] G. Zentai, Comparison of CMOS and a-Si flat panel imagers for X-ray imaging, *IEEE International Conference on Imaging Systems and Techniques*, 194–200 (2011).
- [55] <http://www.dexela.com/cmos.aspx>.
- [56] R.L. Weisfield, M.A. Hartney, R.A. Streetand, R.B. Aptek, *Proceedings of SPIE* 3336 (1998) 442–452.
- [57] R.L. Weisfield, Large-area amorphous silicon TFT-based x-ray image sensors for medical imaging and non destructive testing, http://www.dpix.com/technology/Documents/9805_dpix_tech_paper.pdf.
- [58] http://www-ppd.fnal.gov/EPPOffice-W/Research_Techniques_Seminar/Talks/beletic.pdf.
- [59] Y. Bai, J. Bajaj, J.W. Beletic, M.C. Farris, *Proceedings of SPIE* 7021 (2008) 702102-1-16.
- [60] C. Szeles, *Physica Status Solidi* 241 (2004) 783–790.
- [61] A.E. Bolotnikov, G.S. Camarda, G.A. Carini, G.W. Wright, L. Li, A. Burger, M. Groza, R.B. James, *Physica Status Solidi (c)* 2 (2005) 1495–1503.
- [62] S. Del Sordo, L. Abbene, E. Caroli, A.M. Mancini, A. Zappettini, P. Ubertini, *Sensors* 9 (2009) 3491–3526.
- [63] T. Takahashi, S. Watanabe, *IEEE Transactions on Nuclear Science* 48 (2001) 950–959.
- [64] T.O. Tümer, S. Yin, V. Cajipe, H. Flores, J. Mainprize, G. Mawdsleyb, J.A. Rowlands, M.J. Yaffe, E.E. Gordon, W.J. Hamilton, D. Rhiger, S.O. Kasap, P. Selline, K.S. Shah, *Nuclear Instruments and Methods in Physics Research A* 497 (2003) 21–29.
- [65] http://www.ajat.fi/images/pdf/ajat_art_plus_c_brochure.pdf.
- [66] O.H.W. Siegmund, J.V. Vallerga, J. McPhate, A.S. Tremsin, *Proceedings of SPIE* 5488 (2004) 789–800.
- [67] O.H.W. Siegmund, A.S. Tremsin, J.V. Vallerga, J.B. McPhate, J.S. Hull, J. Malloy, A.M. Dabiran, *Proceedings of SPIE* 7021 (2008) 70211B-1-1-9.
- [68] J.V. Vallerga, J.B. McPhate, A.S. Tremsin, O.H.W. Siegmund, *Astrophysics and Space Science* 320 (2009) 247–250.
- [69] K. Sembach, Technology investments to meet the needs of astronomy at ultraviolet wavelengths in the 21st century, http://www.astro.princeton.edu/~dns/Theia/Sembach_UVtechnology_EOS.pdf.
- [70] M. Razeghi, A. Rogalski, *Journal of Applied Physics* 79 (1996) 7433–7473.
- [71] D. Walker, M. Razeghi, *Opto-Electronics Review* 8 (2000) 25–42.

- [72] F. Monroy, F. Omnes, F. Calle, *Semiconductor Science and Technology* 18 (2003) R33–R51.
- [73] Y.S. Park, *Opto-Electronics Review* 9 (2001) 117–124.
- [74] P. Lamarre, A. Hairston, S.P. Tobin, K.K. Wong, A.K. Sood, M.B. Reine, M. Pophristic, R. Birkham, I.T. Ferguson, R. Singh, C.R. Eddy Jr., U. Chowdhury, M.M. Wong, R.D. Dupuis, P. Kozodoy, E.J. Tarsa, *physica status solidi (a)* 188 (2001) 289–292.
- [75] S. Aslam, F. Yan, D.E. Pugal, D. Franz, L. Miko, F. Herrero, M. Matsumara, S. Babu, C.M. Stahle, *Proceedings of SPIE* 5901 (2005) 59011J-1-12.
- [76] J.P. Long, S. Varadaraajan, J. Matthews, J.F. Schetzina, *Opto-Electronics Review* 10 (2002) 251–260.
- [77] R. McClintock, K. Mayes, A. Yasan, D. Shiell, P. Kung, M. Razeghi, *Applied Physics Letters* 86 (2005) 011117-1-3.
- [78] J.-L. Reverchon, S. Bansropun, J.-P. Truffer, E. Costard, E. Frayssinet, J. Brault, J.-Y. Dubom, *Proceedings of SPIE* 7691 (2010) 769109-1-9.
- [79] E. Cicek, Z. Vashaei, R. McClintock, M. Razeghi, *Proceedings of SPIE* 8155 (2011) 81551O-1-9.
- [80] P.E. Malinowski, J.-Y. Duboz, P. De Moor, J. John, K. Minoglou, P. Srivastava, H. Abdul, M. Patel, H. Osman, F. Semond, E. Frayssinet, J.-F. Hochedez, B. Giordanengo, C. Van Hoof, R. Mertens, *Physica Status Solidi (c)* 8 (2011) 2476–2478.
- [81] S. Nikzad, T.J. Jones, S.T. Elliott, T.J. Cunningham, P.W. Deelman, A.B.C. Walker II, H.M. Oluseyi, *Proceedings of SPIE* 4139 (2000) 250–258.
- [82] <http://www.stsci.edu/hst/wfc3/documents/handbooks/currentIHB/wfc3_cover.html>.
- [83] M. Nesladek, *Semiconductor Science and Technology* 20 (2005) R19–R27.
- [84] A. BenMoussa, J.F. Hochedez, U. Schühle, W. Schmutz, K. Haenen, Y. Stockman, A. Soltani, F. Scholze, U. Kroth, V. Mortet, A. Theissen, C. Laubis, M. Richter, S. Koller, J.-M. Defise, S. Koizumi, *Diamond & Related Materials* 15 (2006) 802–806.
- [85] D.J. Paul, *Semiconductor Science and Technology* 19 (2004) R75–R108.
- [86] L. Pavesi, *Journal of Physics: Condensed Matter* 15 (2003) R1169–R1196.
- [87] UDT Sensors, Inc., Catalog.
- [88] J.R. Janesick, *Scientific Charge-Coupled Devices*, SPIE Press, Bellingham, 2001.
- [89] J.R. Janesick, *Proceedings of SPIE* 5167 (2003) 1–18.
- [90] H. Titus, *Sensors* 18 (2001).
- [91] X-3: New single-chip colour CCD technology *New Technology*, 20–24, March/April 2002.
- [92] R.F. Lyon, P. Hubel, *IS&T/SID Tenth Color Imaging Conference* (2001) 349–355.
- [93] <<http://www.dpreview.com/news/1009/10092129sigmasd1.asp>>.
- [94] Image Sensor, Market Review and Forecast, Strategies Unlimited, PennWell, 2009 September (2009).
- [95] E.R. Fossum, *IEEE Transactions on Electron Devices* 44 (1997) 1689–1698.
- [96] K. Jacobson, Recent developments of digital cameras and space imagery, <http://www.ipi.uni-hannover.de/uploads/tx_tkpublikationen/2011_GISOSTRAVA_KJ.pdf>.
- [97] G. Patrie, *GeoInformatics* 24–29 (2006).
- [98] B. Leininger, J. Edwards, J. Antoniadis, D. Chester, D. Haas, E. Liu, M. Stevens, C. Gershfield, M. Braun, J.D. Targove, S. Weind, P. Brewere, D.G. Madden, K.H. Shafique, *Proceedings of SPIE* 6981 (2008) 69810H-1-11.
- [99] Billion pixel Gaia camera starts to take shape, <<http://sci.esa.int/science-e/www/object/index.cfm?fobjectid=48901>>.
- [100] <<http://www.fairchildimaging.com/products/>>.
- [101] S. Kilcoyne, N. Malone, M. Harris, J. Vampola, D. Lindsay, *Proceedings of SPIE* 7082 (2008) 70820J.
- [102] C.S. Rafferty, C.A. King, B.D. Ackland, I. Aberg, T.S. Sriram, J.H. O'Neill, *Proceedings of SPIE* (2008) 6940-20.
- [103] A.M. Joshi, V.S. Ban, S. Mason, M.J. Lange, W.F. Kosonocky, *Proceedings of SPIE* 1735 (1992) 287–295.
- [104] B.M. Onat, W. Huang, N. Masaun, M. Lange, M.H. Ettenberg, C. Dries, *Proceedings of SPIE* 6542 (2007) 65420L.
- [105] M.D. Enríguez, M.A. Blessinger, J.V. Gropp, T.M. Sudol, J. Battaglia, J. Passe, M. Stern, B.M. Onat, *Proceedings of SPIE* 6940 (2008) 69400O.
- [106] T.R. Hoelter, J.B. Barton, *Proceedings of SPIE* 5074 (2003) 481–490.
- [107] H. Yuan, G. Apgar, J. Kim, J. Laguindanum, V. Nalavade, P. Beer, J. Kimchi, T. Wong, *Proceedings of SPIE* 6940 (2008) 69403C.
- [108] <<http://www.aeriousphotonics.com/>>.
- [109] <<http://www.XenICs.com/>>.

- [110] S. Seshadri, D.M. Cole, B. Hancock, P. Ringold, C. Peay, C. Wrigley, M. Bonati, M.G. Brown, M. Schubnell, G. Rahmer, D. Guzman, D. Figer, G. Tarle, R.M. Smith, C. Bebek, *Proceedings of SPIE* 6690 (2007) 669006.
- [111] T. Martin, R. Brubaker, P. Dixon, M.-A. Gagliardi, T. Sudol, *Proceedings of SPIE* 5783 (2005) 12–20.
- [112] F.D. Shepherd, A.C. Yang, *Technical Digest of IEDM* (1973) 310–313.
- [113] W.F. Kosonocky, *Proceedings of SPIE* 1682 (1992) 2–19.
- [114] M. Kimata, N. Tsubouchi, Schottky barrier photoemissive detectors, in: A. Rogalski (Ed.), *Infrared Photon Detectors*, SPIE Optical Engineering Press, Bellingham, 1995, pp. 299–349.
- [115] M. Kimata, N. Yutani, N. Tsubouchi, T. Seto, *Proceedings of SPIE* 350–360 (1762) 1992.
- [116] M. Kimata, M. Ueno, H. Yagi, T. Shiraishi, M. Kawai, K. Endo, Y. Kosasayama, T. Sone, T. Ozeki, N. Tsubouchi, *Opto-Electronics Review* 6 (1998) 1–10.
- [117] M. Kimata, Silicon infrared focal plane arrays, in: M. Henini, M. Razeghi (Eds.), *Handbook of Infrared Detection Technologies*, Elsevier, Oxford, 2002, pp. 353–392.
- [118] R.J. Cashman, *Proceedings of the IRE* 47 (1959) 1471–1475.
- [119] H. Zogg, *Opto-Electronics Review* 6 (1998) 37–46.
- [120] T. Beysstrum, R. Himoto, N. Jacksen, M. Sutton, *Proceedings of SPIE* 5406 (2004) 287–294.
- [121] K. Alchalabi, D. Zimin, H. Zogg, W. Buttler, *IEEE Electron Device Letters* 22 (2001) 110–112.
- [122] H. Zogg, K. Alchalabi, D. Zimin, K. Kellermann, *IEEE Transactions on Electron Devices* 50 (2003) 209–214.
- [123] <<http://www.sensarrayinfrared.com/>>.
- [124] A. Rogalski, K. Adamiec, J. Rutkowski, J. Narrow-Gap Semiconductor Photodiodes, SPIE Press, Bellingham, 2000.
- [125] A.M. Fowler, D. Bass, J. Heynssens, I. Gatley, F.J. Vrba, H.D. Ables, A. Hoffman, M. Smith, J. Woolaway, *Proceedings of SPIE* 2268 (1994) 340–345.
- [126] A.M. Fowler, I. Gatley, P. McIntyre, F.J. Vrba, A. Hoffman, *Proceedings of SPIE* 2816 (1996) 150–160.
- [127] E. Beuville, D. Acton, E. Corrales, J. Drab, A. Levy, M. Merrill, R. Peralta, W. Ritchie, *Proceedings of SPIE* 6660 (2007) 66600B.
- [128] A.W. Hoffman, E. Corrales, P.J. Love, J. Rosbeck, M. Merrill, A. Fowler, C. McMurtry, *Proceedings of SPIE* 5499 (2004) 59–67.
- [129] A.W. Hoffman, E. Corrales, P.J. Love, J. Rosbeck, M. Merrill, A. Fowler, C. McMurtry, *Proceedings of SPIE* 5499 (2004) 59–67.
- [130] A.M. Fowler, K.M. Merrill, W. Ball, A. Henden, F. Vrba, C. McCreight, Orion: A 1–5 micron focal plane for the 21st century, in: P. Amico (Ed.), *Scientific Detectors for Astronomy: The Beginning of a New Era*, Kluwer, Dordrecht, 2004, pp. 51–58.
- [131] <<http://www.sbfm.com/documents/FPA%20S019-0001-08.pdf>>.
- [132] P. Norton, *Opto-Electronics Review* 10 (2002) 159–174.
- [133] O. Gravrand, L. Mollard, C. Langeron, N. Baier, E. Deborniol, *Journal of Electronic Materials* 38 (2009) 1733–1740.
- [134] W.E. Tennant, D. Lee, M. Zandian, E. Piquette, M. Carmody, *Journal of Electronic Materials* 37 (2008) 1407–1410.
- [135] P.R. Bratt, S.M. Johnson, D.R. Rhiger, T. Tung, M.H. Kalisher, W.A. Radford, G.A. Garwood, C.A. Cockrum, *Proceedings of SPIE* 7298 (2009) 7298-97.
- [136] D. Lindsay, J.W. Bangs, J. Vampola, F. Jaworski, L. Mears, R. Wyles, J. Asbrock, E. Norton, M. Reddy, K. Rybnicek, A. Levy, N. Malone, *Proceedings of SPIE* 8154 (2011) 81540S-1-13.
- [137] G. Destefanis, P. Tribolet, M. Vuillermet, D.B. Lanfrey, *Proceedings of SPIE* 8012 (2011) 801235-1-12.
- [138] J.W. Beletic, R. Blank, D. Gulbransen, D. Lee, M. Loose, E.C. Piquette, T. Sprafke, W.E. Tennant, M. Zandian, J. Zino, *Proceedings of SPIE* 7021 (2008) 70210H.
- [139] A. Hoffman, *Laser Focus World* (2006) 81–84.
- [140] I. Baker, S. Duncan, J. Copley, *Proceedings of SPIE* 5406 (2004) 133–144.
- [141] J. Rothman, E. de Borniol, P. Ballet, L. Mollard, S. Gout, M. Fournier, J.P. Chamonal, G. Destefanis, F. Pistone, S. Courtas, X. Lefouleb, P. Tribolet, *Proceedings of SPIE* 7298 (2009) 7298107.
- [142] S.D. Gunapala, S.V. Bandara, Quantum well infrared photodetectors (QWIP), in: M.H. Francombe (Ed.), *Handbook of Thin Devices*, Vol. 2, Academic Press, San Diego, 2000, pp. 63–99.
- [143] A. Rogalski, *Proceedings of SPIE* 38 (1997) 327–338.
- [144] A. Rogalski, *Journal of Applied Physics* 93 (2003) 4355–4391.
- [145] M. Jhabvala, K. Choi, A. Goldberg, A. La, S. Gunapala, *Proceedings of SPIE* 5167 (2004) 175–185.

- [146] S.D. Gunapala, S.V. Bandara, J.K. Liu, C.J. Hill, B. Rafol, J.M. Mumolo, J.T. Trinh, M.Z. Tidrow, P.D. LeVan, *Semiconductor Science and Technology* 20 (2005) 473–480.
- [147] P. Martyniuk, A. Rogalski, *Progress in Quantum Electronics* 32 (2008) 89–120.
- [148] Y. Wei, M. Razeghi, *Physical Review B* 69 (2004) 085316.
- [149] C. Mailhot, Far-infrared materials based on InAs/GaInSb type II, strained-layer superlattices, in: M.O. Manasreh (Ed.), *Semiconductor Quantum Wells and Superlattices for Long-Wavelength Infrared Detectors*, Artech House, Boston, 1993, pp. 109–138.
- [150] C.H. Grein, P.M. Young, M.E. Flatté, H. Ehrenreich, *Journal of Applied Physics* 78 (1995) 7143–7152.
- [151] D.Z.-Y. Ting, A. Soibel, L. Höglund, J. Nguyen, C.J. Hill, A. Khoshakhlagh, S.D. Gunapala, Type-II superlattice infrared detectors, in: S.D. Gunapala, D.R. Rhiger, C. Jagadish (Eds.), *Semiconductors and Semimetals*, 84, Elsevier, Amsterdam, 2011, pp. 1–57.
- [152] G.J. Brown, *Proceedings of SPIE* 5783 (2005) 65–77.
- [153] M. Razeghi, D. Hoffman, B.M. Nguyen, P.-Y. Delaunay, E.K. Huang, M.Z. Tidrow, V. Nathan, *Proceedings of the IEEE* 97 (2009) 1056–1066.
- [154] E.H. Aifer, J.G. Tischler, J.H. Warner, I. Vurgaftman, W.W. Bewley, J.R. Meyer, C.L. Canedy, E.M. Jackson, *Applied Physics Letters* 89 (2006) 053510.
- [155] B.-M. Nguyen, D. Hoffman, P.-Y. Delaunay, M. Razeghi, *Applied Physics Letters* 91 (2007) 163511.
- [156] S. Maimon, G.W. Wicks, *Applied Physics Letters* 89 (2006) 151109.
- [157] D.Z.-Y. Ting, C.J. Hill, A. Soibel, J. Nguyen, S.A. Keo, M.C. Lee, J.M. Mumolo, J.K. Liu, S.D. Gunapala, *Proceedings of SPIE* 7660 (2010) 76601R-1-12.
- [158] L. Zheng, M. Tidrow, L. Aitcheson, J. O'Connor, S. Brown, *Proceedings of SPIE* 7660 (2010) 7660-1-12.
- [159] C.J. Hill, A. Soibel, S.A. Keo, J.M. Mumolo, D.Z. Ting, S.D. Gunapala, D.R. Rhiger, R.E. Kvaas, S.F. Harris, *Proceedings of SPIE* 7298 (2009) 7294-04.
- [160] S.D. Gunapala, D.Z. Ting, C.J. Hill, J. Nguyen, A. Soibel, S.B. Rafol, S.A. Keo, J.M. Mumolo, M.C. Lee, J.K. Liu, B. Yang, *Phot. Tech. Lett* 22 (2010) 1856–1858.
- [161] P. Manurkar, S. Ramezani-Darvish, B.-M. Nguyen, M. Razeghi, J. Hubbs, *Applied Physics Letters* 97 (2010) 193505-1-3.
- [162] <http://www.flir.com/uploadedFiles/Eurasia/Cores_and_Components/Technical_Notes/uncooled%20detectors%20BST.pdf>.
- [163] D. Murphy, M. Ray, J. Wyles, J. Asbrock, C. Hewitt, R. Wyles, E. Gordon, T. Sessler, A. Kennedy, S. Baur, D. Van Lue, *Proceedings of SPIE* 5406 (2004) 531–540.
- [164] C. Li, G.D. Skidmore, C. Howard, C.J. Han, L. Wood, D. Peysha, E. Williams, C. Trujillo, J. Emmett, G. Robas, D. Jardine, C.-F. Wan, E. Clarke, *Proceedings of SPIE* 6542 (2007) 65421Y.
- [165] D. Takamuro, T. Maegawa, T. Sugino, Y. Kosasayama, T. Ohnakado, H. Hata, M. Ueno, H. Fukumoto, K. Ishida, H. Katayama, T. Imai, M. Ueno, *Proceedings of SPIE* 8012 (2011) 80121E-1-10.
- [166] J. Anderson, D. Bradley, D.C. Chen, R. Chin, K. Jurgelewicz, W. Radford, A. Kennedy, D. Murphy, M. Ray, R. Wyles, J. Brown, G. Newsome, *Proceedings of SPIE* 4369 (2001) 559–565.
- [167] <<http://www.sofradir-ec.com/wp-uncooled-detectors-achieve.asp>>.
- [168] C. Li, G. Skidmore, C. Howard, E. Clarke, C.J. Han, *Proceedings of SPIE* 7298 (2009) 72980S-1-11.
- [169] T. Schimert, C. Hanson, J. Brady, T. Fagan, M. Taylor, W. McCardel, R. Gooch, M. Gohlke, A.J. Syllaios, *Proceedings of SPIE* 7298 (2009) 72980T-1-5.
- [170] J.J. Yon, J.P. Nieto, L. Vandroux, P. Imperinetti, E. Rolland, V. Goudon, C. Vialle, A. Arnaud, *Proceedings of SPIE* 7660 (2010) 76600U-1-7.
- [171] C. Hanson, *Laser Focus World* (2011).
- [172] N. Roxhed, F. Niklaus, A.C. Fischer, F. Forsberg, L. Höglund, P. Ericsson, B. Samel, S. Wissmar, A. Elfving, T.I. Simonsen, K. Wang, N. Hoivik, *Proceedings of SPIE* 7726 (2010) 772611-1-10.
- [173] S.H. Black, T. Sessler, E. Gordon, R. Kraft, T. Kocian, M. Lamb, R. Williams, T. Yang, *Proceedings of SPIE* 8012 (2011) 80121A-1-12.
- [174] A. Rogalski, J. Antoszewski, L. Faraone, *Journal of Applied Physics* 105 (2009) 091101.
- [175] A. Rogalski, *Opto-electronics Review* 16 (2008) 458–482.
- [176] J.C. Campbell, A.G. Dentai, T.P. Lee, C.A. Burrus, *IEEE Journal of Quantum Electronics* QE-16 (1980) 601.
- [177] E.R. Blazejewski, J.M. Arias, G.M. Williams, W. McLevige, M. Zandian, J. Pasko, *Journal of Vacuum Science and Technology* B10 (1992) 1626.
- [178] J.A. Wilson, E.A. Patten, G.R. Chapman, K. Kosai, B. Baumgratz, P. Goetz, S. Tighe, R. Risser, R. Herald, W.A. Radford, T. Tung, W.A. Terre, *Proceedings of SPIE* 2274 (1994) 117–125.

- [179] R.D. Rajavel, D.M. Jamba, J.E. Jensen, O.K. Wu, J.A. Wilson, J.L. Johnson, E.A. Patten, K. Kasai, P.M. Goetz, S.M. Johnson, *Journal of Electronic Materials* 27 (1998) 747–751.
- [180] M.B. Reine, A. Hairston, P. O'Dette, S.P. Tobin, F.T.J. Smith, B.L. Musicant, P. Mitra, F.C. Case, *Proceedings of SPIE* 3379 (1998) 200–212.
- [181] J.P. Zanatta, P. Ferret, R. Loyer, G. Petroz, S. Cremer, J.P. Chamonal, P. Bouchut, A. Million, G. Destefanis, *Proceedings of SPIE* 4130 (2000) 441–451.
- [182] W.E. Tennant, M. Thomas, L.J. Kozlowski, W.V. McLevige, D.D. Edwall, M. Zandian, K. Spariosu, G. Hildebrandt, V. Gil, P. Ely, M. Muzilla, A. Stoltz, J.H. Dinan, *Journal of Electronic Materials* 30 (2001) 590–594.
- [183] G. Destefanis, J. Baylet, P. Ballet, P. Castelein, F. Rothan, O. Gravrand, J. Rothman, J.P. Chamonal, *Journal of Electronic Materials* 36 (2007) 1031–1044.
- [184] A.H. Lockwood, J.R. Balon, P.S. Chia, F.J. Renda, *Infrared Physics* 16 (1976) 509–514.
- [185] D.F. King, J.S. Graham, A.M. Kennedy, R.N. Mullins, J.C. McQuitty, W.A. Radford T.J. Kostrzewa, E.A. Patten, T.F. Mc Ewan, J.G. Vodicka, J.J. Wootana, *Proceedings of SPIE* 6940 (2008) 69402R.
- [186] E.P.G. Smith, A.M. Gallagher, T.J. Kostrzewa, M.L. Brest, R.W. Graham, C.L. Kuzen, E.T. Hughes, T.F. Mc Ewan, G.M. Venzor, E.A. Patten, W.A. Radford, *Proceedings of SPIE* 7298 (2009) 72981Y.
- [187] P. Tribolet, G. Destefanis, P. Ballet, J. Baylet, O. Gravrand, J. Rothman, *Proceedings of SPIE* 6940 (2008) 69402P.
- [188] Y. Reibel, F. Chabuel, C. Vaz, D. Billon-Lanfrey, J. Baylet, O. Gravrand, P. Ballet, G. Destefanis, *Proceedings of SPIE* 8012 (2011) 801238-1-13.
- [189] J.P.G. Price, C.L. Jones, L.G. Hipwood, C.J. Shaw, P. Abbott, C.D. Maxey, H.W. Lau, J. Fitzmaurice, R.A. Catchpole, M. Ordish, P. Thorne, H.J. Weller, R.C. Mistry, K. Hoade, A. Bradford, D. Owton, P. Knowles, *Proceedings of SPIE* 6940 (2008) 69402S.
- [190] S. Gunapala, S.V. Bandara, J.K. Liu, J.M. Mumolo, D.Z. Ting, C.J. Hill, J. Nguyen, B. Simolon, J. Woolaway, S.C. Wang, W. Li, P.D. LeVan, M.Z. Tidrow, *IEEE Journal of Quantum Electronics* 46 (2010) 285–293.
- [191] S.D. Gunapala, S.V. Bandara, J.K. Liu, E.M. Luong, S.B. Rafol, J.M. Mumolo, D.Z. Ting, J.J. Bock, M.E. Ressler, M.W. Werner, P.D. LeVan, R. Chehayeb, C.A. Kukkonen, M. Ley, P. LeVan, M.A. Fauci, *Opto-Electronics Review* 8 (2001) 150–163.
- [192] S. Gunapala, *Compound Semiconductor* 10 (2005).
- [193] S.D. Gunapala, S.V. Bandara, J.K. Liu, B. Rafol, J.M. Mumolo, *IEEE Transactions on Electron Devices* 50 (2003) 2353–2360.
- [194] S. Gunapala, S.V. Bandara, J.K. Liu, J.M. Mumolo, D.Z. Ting, C.J. Hill, J. Nguyen, B. Simolon, J. Woolaway, S.C. Wang, W. Li, P.D. LeVan, M.Z. Tidrow, *IEEE Journal of Quantum Electronics* 46 (2010) 285–293.
- [195] Y. Arslan, S.U. Eker, M. Kaldirim, C. Besicki, *Infrared Physics & Technology* 52 (2009) 399–402.
- [196] F. Rutz, R. Rehm, J. Schmitz, J. Fleissner, M. Walther, *Proceedings of SPIE* 7298 (2009) 72981R-1-10.
- [197] R. Rehm, M. Walther, J. Schmitz, F. Rutz, A. Wörl, R. Scheibner, J. Ziegler, *Proceedings of SPIE* 7660 (2010) 76601G-1-12.
- [198] M. Razeghi, E.K. Huang, B.-M. Nguyen, S. Ramezani-Darvish, S. Abdollahi Pour, G. Chen, A. Haddadi, M.-A. Hoang, *Proceedings of SPIE* 8012 (2011) 80120T-1-13.
- [199] P. Martyniuk, A. Rogalski, *Progress in Quantum Electronics* 32 (2008) 89–120.
- [200] A. Rostami, H. Rasooli, H. Baghban, *Terahertz Technology. Fundamentals and Applications*, Springer, Berlin, 2011.
- [201] F. Sizov, A. Rogalski, *Progress in Quantum Electronics* 34 (2010) 278–347.
- [202] A. Rogalski, F. Sizov, *Opto-Electronics Review* 19 (2011) 346–404.
- [203] M. Harwit, G. Helou, L. Armus, C.M. Bradford, P.F. Goldsmith, M. Hauser, D. Leisawitz, D.F. Lester, G. Rieke, and S.A. Rinehart, *Far-Infrared/Submillimeter astronomy from space tracking an evolving universe and the emergence of life*, <<http://www.ipac.caltech.edu/DecadalSurvey/farir.html>>.
- [204] J.J. Bock, *Superconducting detector arrays for far-infrared to mm-wave astrophysics*, <http://cmbpol.uchicago.edu/depot/pdf/white-paper_j-bock.pdf>.
- [205] F.F. Sizov, V.P. Reva, A.G. Golenkov, V.V. Zabudsky, *Uncooled detector challenges for THz/sub-THz arrays imaging*, *Journal of Infrared, Millimeter and Terahertz Waves* 32 (2011) 1192–1206.
- [206] P.H. Siegel, *IEEE Transactions on Microwave Theory and Techniques* 50 (2002) 910–928.
- [207] P.H. Siegel, R.J. Dengler, *International Journal of Infrared and Millimeter Waves* 27 (2006) 465–480.

- [208] P.H. Siegel, R.J. Dengler, *International Journal of Infrared and Millimeter Waves* 27 (2006) 631–655.
- [209] H.-W. Hübers, *IEEE Journal of Selected Topics in Quantum Electronics* 14 (2008) 378–391.
- [210] H.A. Watson, *Microwave Semiconductor Devices and Their Circuit Applications*, McGraw-Hill, New York, 1969.
- [211] E.J. Becklake, C.D. Payne, B.E. Pruer, *Journal of Physics D: Applied Physics* 3 (1970) 473–481.
- [212] D.T. Young, J.C. Irvin, *Proceedings of the IEEE* 53 (1965) 2130–2132.
- [213] T.W. Crowe, D.P. Porterfield, J.L. Hesler, W.L. Bishop, D.S. Kurtz, K. Hui, *Proceedings of SPIE* 5790 (2005) 271–280.
- [214] I. Mehdi, G. Chattopadhyay, E. Schlecht, J. Ward, J. Gill, F. Maiwald, and A. Maestrini, THz multiplier circuits, *IEEE MTT-S Intern. Microwave Symp. Digest*, 341–344, San Francisco, 2006.
- [215] S.M. Marazita, W.L. Bishop, J.L. Hesler, K. Hui, W.E. Bowen, T.W. Crowe, *IEEE Transactions on Electron Devices* 47 (2000) 1152–1156.
- [216] P. Siegel, R.P. Smith, M.C. Gaidis, S. Martin, *IEEE Transactions on Microwave Theory and Techniques* 47 (1999) 596–604.
- [217] E.R. Brown, A.C. Young, J.E. Bjarnason, J.D. Zimmerman, A.C. Gossard, H. Kazemi, *International Journal of High Speed Electronics and Systems* 17 (2007) 383–394.
- [218] F. Maiwald, F. Lewen, B. Vowinkel, W. Jabs, D.G. Paveljev, M. Winnerwisser, G. Winnerwisser, *IEEE Microwave and Guided Wave Letters* 9 (1999) 198–200.
- [219] E. Burstein, G. Pines, N. Sclar, Optical and photoconductive properties of silicon and germanium,, in: R. Breckenbridge, B. Russell, E. Hahn (Eds.), *Photoconductivity Conference at Atlantic City*, Wiley, New York, 1956, pp. 353–413.
- [220] P.R. Norton, *Optical Engineering* 30 (1991) 1649–1663.
- [221] J. Leotin, *Proceedings of SPIE* 666 (1986) 81–100.
- [222] G.H. Rieke, *Annual Review of Astronomy and Astrophysics* 45 (2007) 77–115.
- [223] A.W. Hoffman, P.J. Love, J.P. Rosbeck, *Proceedings of SPIE* 5167 (2004) 194–203.
- [224] H. Hogue, E. Atkins, D. Reynolds, M. Salcido, L. Dawson, D. Molyneux, M. Murilla, *Proceedings of SPIE* 7780 (2010) 778004-1-10.
- [225] R. Mills, E. Beuville, E. Corrales, A. Hoffman, G. Finger, D. Ives, *Proceedings of SPIE* 8154 (2011) 81540R-1-10.
- [226] R.M. Glidden, S.C. Lizotte, J.S. Cable, L.W. Mason, C. Cao, *Proceedings of SPIE* 1684 (1992) 2–39.
- [227] A.G. Kazanskii, P.L. Richards, E.E. Haller, *Applied Physics Letters* 31 (1977) 496–497.
- [228] E.T. Young, J.T. Davis, C.L. Thompson, G.H. Rieke, G. Rivlis, R. Schnurr, J. Cadien, L. Davidson, G.S. Winters, K.A. Kormos, *Proceedings of SPIE* 3354 (1998) 57–65.
- [229] A. Poglitsch, C. Waekens, O.H. Bauer, J. Cepa, H. Feuchtgruber, T. Henning, C. van Hoof, F. Kerschbaum, O. Krause, E. Renotte, L. Rodriguez, *Proceedings of SPIE* 7010 (2008) 701005.
- [230] <http://fifi-ls.mpg-garching.mpg.de/detector.html>.
- [231] <http://pacs.mpe.mpg.de/p15n.html>.
- [232] N. Billot, P. Agnese, J.L. Augueres, A. Beguin, A. Bouere, O. Boulade, C. Cara, C. Cloue, E. Doumayrou, L. Duband, B. Horeau, I. Le Mer, J.L. Pennec, J. Martignac, K. Okumura, V. Reveret, M. Sauvage, F. Simoens, L. Vigroux, *Proceedings of SPIE* 6265 (2006) 62650D.
- [233] M. Shirahata, S. Matsuura, T. Nakagawa, T. Wada, S. Kamiya, M. Kawada, Y. Sawayama, Y. Doi, H. Kawada, Y. Cretien, B. Okcan, W. Raab, A. Poglitsch, *Proceedings of SPIE* 7741 (2010) 77410B.
- [234] J. Farhoomand, D.L. Sisson, J.W. Beeman, *Infrared Physics & Technology* 51 (2008) 152–159.
- [235] M. Ressler, H. Hogue, M. Muzilla, J. Blacksberg, J. Beeman, E. Haller, J. Huffman, J. Farhoomand, E. Young Development of large format far-infrared detectors, *Astro2010: The Astronomy and Astrophysics Decadal Survey, Technology Development Papers*, no. 18.
- [236] C. Wilson, L. Frunzio, D. Prober, *Physical Review Letters* 87 (2001) 067004.
- [237] J. Zmuidzin, P.L. Richards, *Proceedings of the IEEE* 92 (2004) 1597–1616.
- [238] V.P. Koshelets, S.V. Shitov, L.V. Filippenko, P.N. Dmitriev, A.N. Ermakov, A.S. Sobolev, M. Yu, *Radiophysics and Quantum Electronics* 46 (2003) 618–630.
- [239] J.J. Bock, Superconducting detector arrays for far-infrared to mm-wave astrophysics, <http://cmbpol.uchicago.edu/depot/pdf/white-paper_j_bock.pdf>.
- [240] P. Day, H.G. LeDuc, B.A. Mazin, A. Vayonakis, J. Zmuidzin, *Nature* 425 (2003) 817–821.
- [241] D. Golubev, L. Kuzmin, *Journal of Applied Physics* 89 (2001) 6464–6472.

- [242] P.R. Maloney, N.G. Czakon, P.K. Day, R. Duan, J. Gao, J. Glenn, S. Golwala, M. Hollister, H.G. LeDuc, B. Mazin, O. Noroozian, H.T. Nguyen, J. Sayers, J. Schlaerth, J.E. Vaillancourt, A. Vayonakis, P. Wilson, and J. Zmuidzinas, The MKID camera, AIP Conf. Proc. 1185, 176–179 (2009).
- [243] P.L. Richards, *Journal of Applied Physics* 76 (1994) 1–24.
- [244] Detectors needs for long wavelength astrophysics, A Report by the Infrared, Submillimeter, and Millimeter Detector Working Group, June 2002; <http://safr.gsfc.nasa.gov/docs/ISMDWG_final.pdf>.
- [245] Herschel Space Observatory, <<http://herchel.jpl.nasa.gov/spireInstrument.shtml>>.
- [246] P. Agnese, C. Buzzi, P. Rey, L. Rodriguez, J.L. Tissot, *Proceedings of SPIE* 3698 (1999) 284–290.
- [247] C. Dowell, C.A. Allen, S. Babu, M.M. Freund, M.B. Gardner, J. Groseth, M. Jhabvala, A. Kovacs, D.C. Lis, S.H. Moseley, T.G. Phillips, R. Silverberg, G. Voellmer, H. Yoshida, *Proceedings of SPIE* 4855 (2003) 73–87.
- [248] G.N. Gol'tsman, Yu.B. Vachtomin, S.V. Antipov, M.I. Finkel, S.N. Maslennikov, K.V. Smirnov, S.L. Poluakov, S.I. Svechnikov, N.S. Kaurova, E.V. Grishina, B.M. Voronov, *Proceedings of SPIE* 5727 (2005) 95–106.
- [249] K.S. Il'in, M. Lindgren, M. Currie, A.D. Semenov, G.N. Gol'tsman, R. Sobolewski, S.I. Cherednichenko, E.M. Gershenzon, *Applied Physics Letters* 76 (2000) 2752–2754.
- [250] D.J. Benford and S.H. Moseley, Superconducting transition edge sensor bolometer arrays for submillimeter astronomy, *Proceedings of the International Symposium on Space and THz Technology*, <www.eecs.umich.edu/~jeast/benford_2000_4_1.pdf>.
- [251] K. Irwin, *Applied Physics Letters* 66 (1995) 1998–2000.
- [252] A.J. Walton, W. Parkes, J.G. Terry, C. Dunare, J.T.M. Stevenson, A.M. Gundlach, G.C. Hilton, K.D. Irwin, J.N. Ullom, W.S. Holland, W. Duncan, M.D. Audley, P.A.R. Ade, R.V. Sudiwala, E. Schulte, *IEEE Proceedings Science, Measurement & Technology* 151 (2004) 119–120.
- [253] W.S. Holland, W. Duncan, B.D. Kelly, K.D. Irwin, A.J. Walton, P.A.R. Ade, E.I. Robson, *Proceedings of SPIE* 4855 (2003) 1–18.
- [254] “SCUBA-2,” <<http://www.roe.ac.uk/ukatc/projects/scubatwo/>>.
- [255] A.L. Woodcraft, M.I. Hollister, D. Bintley, M.A. Ellis, X. Gao, W.S. Holland, M.J. MacIntosh, P.A.R. Ade, J.S. House, C.L. Hunt, R.V. Sudiwala, *Proceedings of SPIE* 6275 (2006) 62751F.
- [256] D.J. Benford, Transition edge sensor bolometers for CMB polarimetry, <http://cmbpol.uchicago.edu/workshops/technology2008/depot/cmbpol_technologies_benford_jcps_4.pdf>.
- [257] J. Gildemeister, A. Lee, P. Richards, *Applied Physics Letters* 77 (2000) 4040–4042.
- [258] D.J. Benford, G.M. Voellmer, J.A. Chervenak, K.D. Irwin, S.H. Moseley, R.A. Shafer, G.J. Stacey, and J.G. Staguhn, Thousand-element multiplexed superconducting bolometer arrays, in *Proc. Far-IR, Sub-MM, and MM Detector Workshop*, vol. NASA/CP-2003-211 408, pp. 272–275, edited by J. Wolf, J. Farhoomand, and C.R. McCreight, 2003.
- [259] W. Knap, M. Dyakonov, D. Coquillat, F. Teppe, N. Dyakonova, J. Łusakowski, K. Karpierz., M. Sakowicz, G. Valusis, D. Seliuta, I. Kasalynas, A. El Fatimy, Y.M. Meziani, T. Otsuji, *Journal of Infrared, Millimeter and Terahertz Waves* 30 (2009) 1319–1337.
- [260] M. Dyakonov, M.S. Shur, *Physical Review Letters* 71 (1993) 2465–2468.
- [261] M. Dyakonov, M. Shur, *IEEE Transactions on Electron Devices* 43 (1996) 1640–1646.
- [262] M. Shur, V. Ryzhii, *International Journal of High Speed Electronics and Systems* 13 (2003) 575–600.
- [263] E. Öjefors, U.R. Pfeiffer, A. Lisauskas, H.G. Roskos, *IEEE Journal of Solid-State Circuits* 44 (2009) 1968–1976.
- [264] F. Schuster, D. Coquillat, H. Videlier, M. Sakowicz, F. Teppe, L. Dussopt, B. Giffard, T. Skotnicki, W. Knap, *Optics Express* 19 (2011) 7827–7832.
- [265] F. Schuster, W. Knap, V. Nguyen, *Laser Focus World* (2011).